Developing Time-Resolved Synchrotron Infrared Spectroscopy for Spectroelectrochemical Measurements

A Thesis Submitted to the

College of Graduate and Postdoctoral Studies

in Partial Fulfillment of the Requirements

for the degree of Doctor of Philosophy

in the Department of Chemistry

University of Saskatchewan

Saskatoon

By

Kaiyang Tu

Permission to Use

In presenting this thesis in partial fulfilment of the requirements for a Postgraduate degree from the University of Saskatchewan, I agree that the Libraries of this University may make it freely available for inspection. I further agree that permission for copying of this thesis in any manner, in whole or in part, for scholarly purposes may be granted by the professor or professors who supervised my thesis work or, in their absence, by the Head of the Department or the Dean of the College in which my thesis work was done. It is understood that any copying or publication or use of this thesis or parts thereof for financial gain shall not be allowed without my written permission. It is also understood that due recognition shall be given to me and to the University of Saskatchewan in any scholarly use which may be made of any material in my thesis.

Requests for permission to copy or to make other use of material in this thesis in whole or part should be addressed to:

Dean

College of Graduate and Postdoctoral Studies

University of Saskatchewan

116 Thorvaldson Building, 110 Science Place

Saskatoon, Saskatchewan

S7N 5C9

Canada

Department of Chemistry

University of Saskatchewan

110 Science Place

Saskatoon, Saskatchewan

S7N 5C9

Canada

Abstract

This thesis details my work in developing spectroelectrochemical platforms utilizing synchrotron infrared radiation (SIR) and time-resolved FTIR to study the kinetics of electrochemical reactions on second to millisecond scale with high chemical sensitivity. It will cover development of spectroelectrochemical cells and procedures compatible with the mid-IR beamline at the Canadian Light Source to study irreversible electrocatalytic processes with rapid scan FTIR in reflection mode. The thesis demonstrates application of SIR-based rapid scan FTIR to spatially map catalytic activity on heterogenous PtNi electrode and provides proof-of-principle for its capability for combinatorial screening for binary electrocatalysts. The thesis discusses the development of time-resolved step scan FTIR in attenuated total reflection - surface enhancing infrared absorption spectroscopy configuration (ATR-SEIRAS) to improve signal-to-noise of the measurement for increased detection limits and time-resolution, before demonstrating the utility of the developed step scan ATR-SEIRAS platform by investigation of the kinetics of conformational changes within self-assembled monolayers (SAM) of ferrocene alkanethiols. Overall, the work described in this thesis outlines the advancement of SIR-based spectroelectrochemical platforms within the group to a point, where they can be directly applied to investigation of dynamics processes within electrochemical reaction.

Acknowledgements

I would first like to thank Dr. Ian J. Burgess for being my supervisor and a constant source of help and guidance throughout my graduate studies here. This thesis would not have been possible without his mentorship and support throughout these years. I will always be grateful for this.

A huge thank you goes to all the current and former members of the Burgess group that made every day within the group a joy. It was my greatest pleasure to have worked with you all and I wish you the best of luck whereever it might take you.

Special thanks goes to the many people that made this thesis possible. These experiments would have been impossible without the aid and advices of the Mid-IR beamline Scientists, Dr. Scott Rosendahl, Tim May, Dr. Xia Liu, Dr. Stuart T. Read and Dr. Ferenc M. Borondics. A huge thank you also goes out to the members of the Sylmand facility Dr. Sven Achenbach, Garth Wells, Michael Jacobs as well as Steven Creighton from the SRC. I would also like to thanks the current and former members of the Physics Mashine Shop Ted Toporowski, Blair Chomyshen and Jill Cornish.

Last and most importantly, I would like to thanks my parents. I would not be here, if not for your love, for your support, for your courage and for your steadfastness that took us on a journey to distant shores. For everything and so much more, I am eternally grateful for you two.

In memory of my father, Xincheng Tu.

Contents

List of Tables

List of Figures

List of Abbreviations

2D-COS	2-dimensional Correlation Spectroscopy
AES	Auger Electron Spectroscopy
AFM	Atomic Force Microscopy
AIRES	Anomalous Infrared Enhanced Spectroscopy
ATR	Attenuated Total Reflection
CE	Counter Electrode
CLS	Canadian Light Source
CV	Cyclic Voltammetry
DAC	Data Acquisition Card
DMFC	Direct Methanol Fuel Cell
E/I	Potential/Current
ECA	Electrochemical Annealing
EDL	Electrochemical Double Layer
EM	Electromagnetic
ECSA	Electrocatalytic Active Surface Area
Fc11SH	11-(Ferrocenyl)Undecanoicthiol
FEM	Finite Element Method
FPA	Focal Planar Array
FT	Fourier Transformed
FTIR	Fourier Transformed Infrared Spectroscopy
FWHM	Full-Width Half Maximum
IR	Infrared
IRE	Internal Reflection Element
IRRAS	Infrared Reflection Absorption Spectroscopy
ITO	Indium Tin Oxide
IZO	Indium Zinc Oxide
LSPP	Localized Surface Plasmon Polaritons
MCT	Mercury Cadmium Tellurium
MeOH	Methanol
MOP	4-Methoxypyridine
MOR	Methanol Oxidation Reaction
NHE	Normal Hydrogen Electrode
PVC	Polyvinyl Chloride
QCL	Quantum Cascade Laser
QCM	Quartz Crystal Microbalance
RAIRS	Reflection Absorption Infrared Spectroscopy
RE	Reference Electrode
S/N	Signal-to-Noise
SAM	Self-Assembled Monolayers
SEC	Spectroelectrochemical Cell
SEIRAS	Surface Enhanced Infrared Absorption Spectroscopy

SERS	Surface Enhanced Raman Spectroscopy
SFG	Sum-Frequency Generation
SIR	Synchrotron Infrared Radiation
UME	Ultramicroelectrodes
WDS	Wavelength Dispersive X-ray Spectroscopy
WE	Working Electrode
XPS	X-ray Photoelectron Spectroscopy
XRD	X-ray Diffration Spectroscopy

Chapter 1

Introduction

1.1 Motivations and Objectives

Since its inception with the first batteries over 200 years ago, electrochemistry has remained a vital area of research with modern applications ranging from industrial metal processing, commodity chemical synthesis, sensor applications, energy conversion, to storage solutions in renewable energy. As the common denominator throughout this wide variety of areas, electrochemistry is at its core, the study of chemical reactions occurring primarily at a heterogeneous interface involving charge transfer[1]. Due to the intimate relationship of electrochemical reaction with electricity, purely electrochemical techniques infer information about these heterogeneous reactions through easily quantifiable and measurable parameters such as current and potential. While these techniques remain instrumental for investigating electrochemical processes, complimentary information through more broadly used analytical techniques for molecular changes at the interface have proven to be extremely valuable.

Consider the liquid/solid interface, the most common heterogeneous interface in electrochemistry, as an example. The interfacial reaction is affected by the solute concentration at the interface which in turn depends on thermodynamic considerations that link interfacial concentrations to solute concentrations in the bulk of the liquid phase and kinetic

considerations such as mass transport through the liquid medium. On the solid side, surface topography, crystallinity, composition and changes in electronic properties can drastically alter the kinetics and thermodynamics of chemical reactions and the optimization of these parameters remains a continued focus of electrochemical research.

To study these various aspects, a host of analytical techniques have found application in electrochemistry. Microscopy techniques such as scanning tunneling microscopy[2], atomic force microscopy (AFM)[3] or scanning electrochemical microscopy[4,5] have been instrumental to map the surface topography of the solid surface, while various X-ray[6] or electron microscopy-based techniques[7] allow insight into crystallography, composition and electronic properties. The liquid phase composition can be determined by mass spectroscopy[8], probe microscopy[9] and vibrational spectroscopy techniques[10,11] that provide the chemical identification otherwise lacking in purely electrochemical techniques. It is important to emphasize that surface sensitive variants of these techniques are essential to discriminate surface adsorbed molecules from the large excess of non-participatory molecules residing in the bulk phase[12,13]. It is fair to say that the understanding of electrochemical processes has and will continue to greatly benefit from the integration of more novel or more refined analytical techniques into the electrochemical "toolbox" to compliment classical electrochemical techniques.

Particularly exciting are the developments of various *in situ* spectroscopic techniques that allow parallel acquisition of electrochemical and spectroscopic data of the chemical reaction[14–18]. While *in situ* spectroelectrochemical techniques are experimentally much more challenging to implement than *ex situ* measurements, they can provide unique insight into the reaction under dynamic and equilibrium conditions. Within this context, *in situ* Fourier transformed Infrared (FTIR) spectroscopy has proven to be an excellent compli-

mentary technique as it supplements electrochemically gathered charge transfer information with the chemical identities and structural information of both solution and surface absorbed species. Since its introduction by Bewick and coworkers in the 1980s[19], *in situ* FTIR investigations at equilibrium conditions or of kinetically slow (*i.e.* > 1 s) electrochemical processes with FTIR have become commonplace within the electrochemical literature. One example from Osawa's group is the experimental confirmation of formate as a surface adsorbed intermediate species during methanol oxidation[20]. What is distinctively sparse however, are reports of fast, time-resolved FTIR measurements investigating kinetic processes in the millisecond to microsecond range.

Therein lies the goal of this thesis: the development of a robust methodology to study electrochemical reactions with sub millisecond resolved FTIR techniques.

As will be discussed in depth at later points in the thesis, achieving microsecond time-resolution requires the implementation of small electrodes (generally termed ultramicroelectrodes or UMEs) which in turn generates immense experimental challenges such as very low analyte concentrations, poor signal-to-noise (S/N) ratios and the technical challenges associated with incorporating ultramicroelectrodes in IR compatible electrochemical cells.

The project's goals are not without significant precedent. For example, both rapid scan and step scan FTIR spectroscopy has been reported (albeit very sparsely) in electrochemical studies[21–28]. First reports by Osawa *et al.* had some success using plasmonic enhancement techniques to overcome the limitations of low analyte quantities[23,24]. However, the experimental approach used in these studies was unable to properly implement UMEs which imposes a hard barrier of on the order of $10^{-1} - 10^{-2}$ s on time-resolution. Later work by Sun *et al.* was able to incorporate an UME but were limited in its application due to the

reliance of an abnormal IR effect to provide the surface enhancement necessary to resolve the IR signal[21,22]. In both cases, the experimental shortcomings are a result of compromises needed to compensate for the low brilliance of conventional globar IR sources.

The starting point for the body of work contained in this thesis was the proof-of-concept studies by, Scott Rosendahl, my predecessor in the Burgess research group. During his PhD, Dr Rosendahl demonstrated the unique opportunities that high brilliance synchrotron infrared radiation (SIR) affords IR –based spectroelectrochemistry[27,28]. This thesis expands on that work and applies it to scientifically relevant electrochemical systems.

1.2 Scope of Thesis

The work presented in this thesis will cover the development and application of spectroelectrochemical platforms compatible with the mid-IR beamline at the Canadian Light Source (CLS) for kinetic investigations of electrochemically relevant processes with time-resolved *in situ* FTIR. The overall objectives of the work are twofold. 1) To transition beyond a simple electrochemical model system used within the proof-of-concept study and develop SIR-based *in situ* spectroelectrochemical platforms that can study more complex electrochemical reactions. 2) To utilize such platforms to investigate previously inaccessible kinetic information and demonstrate novel applications of time-resolved *in situ* FTIR for electrochemistry.

As characterization of molecules within bulk solution and at the interface surface require different *in situ* FTIR configurations, this thesis is broadly composed of two parts that address each aspect. Chapters 3 and 4 focus on investigations of the bulk solution phase composition of an irreversible electrochemical reaction and Chapters 5 and 6 focus on surface

absorbed molecules. Each of these two topics are first introduced with method development chapters (Chapters 3 and 5) which describe, in detail, the experimental methods and proof-of-concept measurements. Each of these Chapters is followed with a demonstration of the method (Chapters 4 and 6) applied to a relevant electrochemical system. To accommodate the chosen structure, no overall background chapter will be included in the thesis. Instead, Chapters 3 - 6 possess individual background sections focusing on specific information about electrochemical systems and techniques used within the chapter and information permanent to the discussion of the results. Additionally, Chapter 2 contains a brief introduction into common background elements such as FTIR and its application for electrochemistry with a focus on the experimental challenges of fast time-resolved FTIR that are relevant throughout the thesis.

Specifically, Chapter 3 focuses on the developments required to transition the existing synchrotron FTIR platform I inherited to one that is compatible with an irreversible electrocatalytic system. The methanol oxidation reaction (MOR) on Pt was chosen as the system to demonstrate the new experimental capabilities. This Chapter contains a detailed description of the developmental work on experimental setup and protocols needed to tackle the highly challenging goal of measuring irreversible electrocatalytic systems. The chapter will conclude with a discussion of the feasibility in applying the method to other irreversible systems with higher time-resolution.

Chapter 3 will focus on utilizing the rapid scan FTIR platform developed in Chapter 2 to demonstrate spatial mapping of catalytic activity on heterogeneous Pt-based alloys. This is composed of three parts; PtNi alloy production, SIR-based mapping of catalytic activity, and simulation work to confirm the qualitative nature of the methodology. The chapter

will end with an outlook on improvements to the measurement method using UV-lithography.

Chapter 4 will present the development work conducted to build a step scan FTIR platform for investigating the kinetics of surface adsorbed molecules undergoing electrochemical processes. This encompasses the adaptation of the time-resolved FTIR infrastructure to a new experimental configuration better suited for detection of surface absorbed molecules and improvements required for step scan FTIR measurement with higher time-resolution. The chapter concludes with a demonstration of the developed platform by monitoring the desorption kinetics of 4-methoxypyridine on Au electrode surfaces.

Chapter 5 will demonstrate the utility of the step scan FTIR platform to investigate the kinetics of orientation changes within surface adsorbed molecules. It will be shown that such details are inaccessible through electrochemical and conventional FTIR means. The focus is a study on the kinetics of molecular rearrangement upon oxidation and reduction of 11-(ferrocenyl)undecanoicthiol (Fc11SH) layers on Au. The chapter will end with an outlook on improvement to the measurement method to broaden its application towards more electrochemical reactions.

The final Chapter will conclude the thesis and provide a summary and discussion of the research presented in this thesis, outline the advancement of *in situ* FTIR studies of electrochemical systems and suggest future improvements and applications. Overall the thesis will cover the development from a proof-of-concept starting point to a fully functioning time-resolved *in situ* FTIR platforms for kinetic investigation of electrochemical systems.

1.3 References

[1] Bard, A. J.; Faulkner, L. R. *Electrochemical Methods: Fundamentals and Applications*, 2nd ed.; Wiley New York, 2001; pp 1–43.

[2] Kim, Y.-G.; Baricuatro, J. H.; Javier, A.; Gregoire, J. M.; Soriaga, M. P. The Evolution of the Polycrystalline Copper Surface, First to Cu(111) and Then to Cu(100), at a Fixed CO2RR Potential: A Study by Operando EC-STM. *Langmuir* **2014**, *30*, 15053–15056.

[3] Shen, C.; Hu, G.; Cheong, L.-Z.; Huang, S.; Zhang, J.-G.; Wang, D. Direct Observation of the Growth of Lithium Dendrites on Graphite Anodes by Operando EC-AFM. *Small Methods* **2018**, *2*, 1700298.

[4] Bard, A. J.; Fan, F. R. F.; Kwak, J.; Lev, O. Scanning electrochemical microscopy. Introduction and principles. *Analytical Chemistry* **1989**, *61*, 132–138.

[5] Hiesgen, R.; Wehl, I.; Aleksandrova, E.; Roduner, E.; Bauder, A.; Friedrich, K. A. Nanoscale properties of polymer fuel cell materials—A selected review. *International Journal of Energy Research* **2010**, *34*, 1223–1238.

[6] Nelson, J.; Misra, S.; Yang, Y.; Jackson, A.; Liu, Y.; Wang, H.; Dai, H.; Andrews, J. C.; Cui, Y.; Toney, M. F. In Operando X-ray Diffraction and Transmission X-ray Microscopy of Lithium Sulfur Batteries. *Journal of the American Chemical Society* **2012**, *134*, 6337–6343.

[7] Gu, M. et al. Demonstration of an Electrochemical Liquid Cell for Operando Transmission Electron Microscopy Observation of the Lithiation/Delithiation Behavior of Si Nanowire Battery Anodes. *Nano Letters* **2013**, *13*, 6106–6112.

[8] Baltruschat, H. Differential electrochemical mass spectrometry. *Journal of the American Society for Mass Spectrometry* **2004**, *15*, 1693–1706.

[9] Gewirth, A. A.; Niece, B. K. Electrochemical Applications of in Situ Scanning Probe Microscopy. *Chemical Reviews* **1997**, *97*, 1129–1162.

[10] Iwasita, T.; Nart, F. C. In situ infrared spectroscopy at electrochemical interfaces. *Progress in Surface Science* **1997**, *55*, 271–340.

[11] Kavan, L.; Rapta, P.; Dunsch, L.; Bronikowski, M. J.; Willis, P.; Smalley, R. E. Electrochemical Tuning of Electronic Structure of Single-Walled Carbon Nanotubes: In-situ Raman and Vis-NIR Study. *The Journal of Physical Chemistry B* **2001**, *105*, 10764–10771.

[12] Vezvaie, M.; Brosseau, C. L.; Lipkowski, J. Electrochemical SERS study of a biomimetic membrane supported at a nanocavity patterned Ag electrode. *Electrochimica Acta* **2013**, *110*, 120–132.

[13] Osawa, M. *In-situ Surface-Enhanced Infrared Spectroscopy of the Electrode/Solution Interface in Advances in Electrochemical Sciences and Engineering*; Wiley Online Books; 2008; pp 269–314.

[14] Ye, J. Y.; Jiang, Y. X.; Sheng, T.; Sun, S. G. In-situ FTIR spectroscopic studies of electrocatalytic reactions and processes. *Nano Energy* **2016**, *29*, 414–427.

[15] Tripathi, A. M.; Su, W.-N. N.; Hwang, B. J. In situ analytical techniques for battery interface analysis. *Chemical Society Reviews* **2018**, *47*, 736–851.

[16] Topsoe, H. Developments in operando studies and in situ characterization of heterogeneous catalysts. *Journal of Catalysis* **2003**, *216*, 155–164.

[17] Bak, S.-M.; Shadike, Z.; Lin, R.; Yu, X.; Yang, X.-Q. In situ/operando synchrotron-based X-ray techniques for lithium-ion battery research. *NPG Asia Materials* **2018**, *10*, 563–580.

[18] Wang, H.; Zhou, Y.-W.; Cai, W.-B. Recent applications of in situ ATR-IR spectroscopy in interfacial electrochemistry. *Current Opinion in Electrochemistry* **2017**, *1*, 73–79.

[19] Bewick, A.; Kunimatsu, K.; Pons, B. S. Infra red spectroscopy of the electrode-electrolyte interphase. *Electrochimica Acta* **1980**, *25*, 465–468.

[20] Chen, Y. X.; Miki, A.; Ye, S.; Sakai, H.; Osawa, M. Formate, an Active Intermediate for Direct Oxidation of Methanol on Pt Electrode. *Journal of the American Chemical Society* **2003**, *125*, 3680–3681.

[21] Zhou, Z.-Y.; Lin, S.-C.; Chen, S.-P.; Sun, S.-G. In situ step-scan time-resolved microscope FTIR spectroscopy working with a thin-layer cell. *Electrochemistry Communications* **2005**, *7*, 490–495.

[22] Zhou, Z.-Y.; Tian, N.; Chen, Y.-J.; Chen, S.-P.; Sun, S.-G. In situ rapid-scan time-resolved microscope FTIR spectroelectrochemistry: study of the dynamic processes of methanol oxidation on a nanostructured Pt electrode. *Journal of Electroanalytical Chemistry* **2004**, *573*, 111–119.

[23] Osawa, M.; Yoshii, K.; Hibino, Y.-i.; Nakano, T.; Noda, I. Two-dimensional infrared correlation analysis of electrochemical reactions. *Journal of Electroanalytical Chemistry* **1997**, *426*, 11–16.

[24] Osawa, M.; Yoshii, K.; Ataka, K.-i.; Yotsuyanagi, T. Real-time monitoring of electrochemical dynamics by submillisecond time-resolved surface-enhanced infrared attenuated-total-reflection spectroscopy. *Langmuir* **1994**, *10*, 640–642.

[25] Wisitruangsakul, N.; Zebger, I.; Ly, K. H.; Murgida, D. H.; Ekgasit, S.; Hildebrandt, P. Redox-linked protein dynamics of cytochrome c probed by time-resolved surface enhanced infrared absorption spectroscopy. *Physical Chemistry Chemical Physics* **2008**, *10*, 5276–5286.

[26] Pronkin, S.; Wandlowski, T. Time-resolved in situ ATR-SEIRAS study of adsorption and 2D phase formation of uracil on gold electrodes. *Journal of Electroanalytical Chemistry* **2003**, *550-551*, 131–147.

[27] Rosendahl, S. M.; Borondics, F.; May, T. E.; Pedersen, T. M.; Burgess, I. J. Interface for time-resolved electrochemical infrared microspectroscopy using synchrotron infrared radiation. *Review of Scientific Instruments* **2011**, *82*, 083105.

[28] Rosendahl, S. M.; Borondics, F.; May, T. E.; Burgess, I. J. Step-Scan IR Spectroelectrochemistry with Ultramicroelectrodes: Nonsurface Enhanced Detection of Near Femtomole Quantities Using Synchrotron Radiation. *Analytical Chemistry* **2013**, *85*, 8722–8727.

Chapter 2

Background

2.1 Introduction

The introduction of FTIR in the 1970s is arguably the starting point for more widespread implementation of IR in the field of electrochemistry. While earlier examples of IR for electrochemistry exist, the much better S/N of these instruments were the crucial advantage that lead to its rapid adaptation and particularly Bewick *et al.*[1] pioneered their implementation for studying electrochemical reactions in liquids in 1980. Since then, spectroelectrochemical measurements combining electrochemical methods with FTIR have found a wide range of application in electrochemistry. Examples include the study of heterogeneous electrocatalysis reactions[2], interfacial electrochemistry[3] and *in situ* study of electrochemical processes[4] as highlighted by recent reviews. The wide range of application resulted in the development of many different platforms, each tailored towards the needs of a specific electrochemical system of interest. Despite the tremendous progress spectroelectrochemical *in situ* FTIR made over the last decades, very few platforms have addressed the experimental challenges associated with implementing microelectrodes within a spectroelectrochemical cell, that limits its application for kinetic measurements of electrochemical reaction with milli and microsecond time-resolution.

As the main body of this thesis (Chapter 3 - 6) centers around the development of spectroelectrochemical *in situ* FTIR platforms for kinetics measurements of electrochemical systems, the primary objective of this Chapter 2 is to provide a short introduction into IR spectroscopy, time-resolved FTIR and its *in situ* spectroelectrochemistry implementation with a focus on the experimental challenges that arise from it.

2.2 Infrared Absorption Spectroscopy

IR light is typically defined as electromagnetic radiation with wavelengths ranging from 0.7 μm to 1000 μm. This energy range contains a wealth of molecular vibrational modes that make IR spectroscopy a powerful characterization tool with chemical sensitivity and structural sensitivity[5]. Analogous to other absorption spectroscopy methods, IR light absorption occurs through the excitation of IR active modes within a sample. These modes are molecular vibrations of bonds within a molecule. Whether a vibration is IR active, can be determined from the quantum mechanical transition moment integral M_{ij}. For example, in the case of a simple diatomic molecule, the atomic vibration can be described as a one-dimensional harmonic oscillator and results in normalized quantized vibrational wavefunctions, Ψ_j. The expectation value for the transition dipole moment associated with the absorption of a photon that results in the excitation from Ψ_j to Ψ_i^* is given by the following integral[6,7].

$$M_{ij} = \int \Psi_i^* \mu \Psi_j dx \tag{2.1}$$

Here μ is the electric dipole moment of the vibration along the normal mode coordinate x. For IR active transitions, a qualitative evaluation can be achieved by examining the

case where μ is constant along dx. The electric dipole μ can be expressed through a series expansion, consisting of its permanent dipole μ_0 oriented along the normal coordinate x as well as oscillation of the dipole due to molecular vibrations around its equilibrium position x_0:

$$\mu = \mu_0 + \left(\frac{\delta\mu}{\delta x}\right)_{x=0}(x - x_0) + \left(\frac{\delta^2\mu}{\delta x^2}\right)_{x=0}(x - x_0)^2 + ... \tag{2.2}$$

It is apparent that μ_0 is independent of the molecular vibrations along x and because Ψ_i^*, Ψ_j are orthogonal to each other, the integral of the permanent dipole moment μ_0 component of the expansion must be zero. Within the dipole approximation, any term beyond the first derivatives can be neglected and the Equation 2.1 re-expressed as:

$$M_{ij} = \int \Psi_i^* \left(\frac{\delta\mu}{\delta x}\right)_{x=0}(x - x_0)\Psi_j dx \tag{2.3}$$

Within this model, an IR absorption of a molecule occurs therefore through any vibration that results in a change of the dipole moment upon excitation. In other words, IR spectroscopy does not rely on the existence of a strong dipole within a molecular bond, but a strong change in dipole moment upon excitation through incident IR light. In case of linear molecules, this is exemplified by CO_2, where the permanent dipole between the two C=O bonds cancel each other out. The molecule does however posses a large IR absorption cross section due to the large dipole moment changes upon asymmetric stretching of the O=C=O bonds. A similar principle applies to IR active modes beyond simple one-dimensional cases such as the more complex bending and rocking vibrations or breathing vibration of large molecules such as benzene rings[8].

One crucial aspect of Equation 2.3 is that IR absorption is based on resonant absorption with the energy of the light matching the vibrational energy level differences of the interrogated molecule. In theory, the differences between IR active chemical bonds, their geometric arrangement and strength of chemical bonds should result in a unique IR "fingerprint" for every molecule and this provides IR spectroscopy with its excellent chemical sensitivity for identification of molecular species. In practice, many implementations of IR absorption for chemical identification utilize a more empirical approach through separate evaluation of observed IR modes in the group frequency region and the fingerprint region of IR spectra. While by no means all encompassing, the group frequency region is typically defined as $1500 - 4000\ \mathrm{cm}^{-1}$. This region is comprised of IR absorption signatures from functional groups that remain independent of their molecular environment, allowing quick qualitative and quantitative identification on the existence and ratio of functional groups within the sample molecule of interest. One example is isocyanide which is an excellent IR absorber found within the narrow region between $2065 - 2110\ \mathrm{cm}^{-1}$. The fingerprint region is typically defined as the spectral region $< 1500\ \mathrm{cm}^{-1}$. Most vibrational modes here are strongly affected by their intra- and intermolecular environment, resulting in more complicated IR signatures unique to each molecule. Comparison of an IR fingerprint within this region with a spectral database allows exact identification of the molecule. Overall, the wealth of functional and fingerprint signatures presents in the mid-IR range between $700 - 4000\ \mathrm{cm}^{-1}$ make it well suited for chemical identification. It is, therefore, at first consideration, an excellent tool to determine the identity of molecular species participating in many electrochemical reactions[9].

Also interesting for electrochemical application is the ability of IR absorption to differentiate between solution phase and surface adsorbed molecules, as electrochemical pro-

cesses are intrinsically heterogeneous reactions. The vibrational modes of surface adsorbed molecules can be altered by the electric fields present at the solid surface as well as their adsorption site bond. The resulting change of IR absorption wavenumber from its solution phase counterpart allows differentiation between solution phase and surface absorbed molecules. A good example is the IR signal of surface adsorbed CO on Pt. The frequency of the CO stretching vibration can be used to differentiate between bridge or single atom bonded CO-Pt adsorption site and is highly sensitive to the electrical potential of the metal due to the Stark-shift effect, whereby the surface applied potential affects both the bond order of the CO as well as its dipole[10].

A second crucial aspect not explicitly shown in Equation 2.3 is the dependence of absorption on the polarization of the incident light. Molecules illuminated with polarized IR light will only show IR absorption if a component of the light's electric field vector is parallel to its vibrational dipole moment. Should the light be orthogonal to the change in dipole moment of the molecule, no interaction can occur, resulting in zero change of the dipole moment. For samples with ordered intermolecular structure, such as self-assembled monolayers, illumination with polarized IR light will result in stronger or weaker IR adsorption depending on whether the preferential molecule orientation matches the incident light polarization. For molecules on metal surfaces, this effect can be amplified through interaction of the incident light with the metal[11] and will be utilized in Chapter 5 to follow the orientation changes of a surface absorbed thiol monolayer[12].

While the chemical sensitivity and structural sensitivity of IR outlined above make it an excellent complimentary technique to purely electrochemical measurements, early IR instruments suffered from long measurement times, poor signal quality and limited wavenum-

ber resolution due to their reliance on dispersive elements such as optical gratings. It was the development of Fourier-transformed infrared (FTIR) spectroscopy in the 1970s that spurred a more wide-spread application of IR based spectroelectrochemistry measurements[5]. For any Fourier-transformed (FT) based spectroscopy, differentiation between wavelengths no longer occurs via dispersive based optical elements. Instead, entire spectra are encoded in a single interferogram through a Michelson interferometer. For time-resolved measurements, operating through an FT-based detection scheme introduces technical challenges and requires a more detailed description of an FTIR instrument, schematically shown in Figure 2.1.

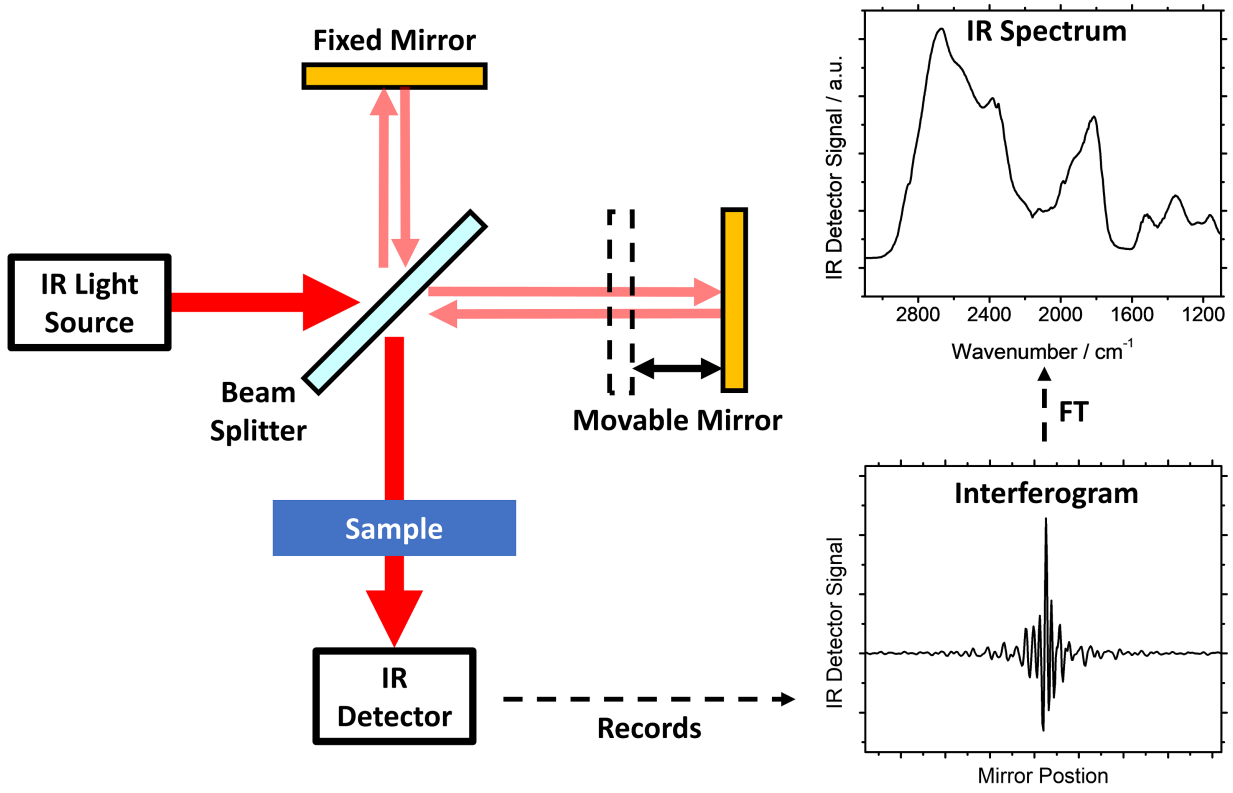

Figure 2.1: Schematic representation of a Michelson interferometer and the post processing of an FTIR spectrometer.

Central to the operation of a FTIR instrument is a Michelson interferometer, composed of a beam splitter and two mirrors. The beam splitter splits the light coming from the

IR source towards the two mirror arms of the interferometer. One arm can vary its optical path length through a moving mirror, while the optical path length of the other arm remains fixed. Depending on the mirror position δ (also commonly denoted as mirror retardation), an optical path difference between two mirror arms introduces a phase shift in one of the two light beams. After reflection, the two light beams are recombined at the beam splitter before passing through a sample onto an IR detector such as a mercury cadmium tellurium detector (MCT). Moving the mirror at constant speed over the entire length of its possible retardation, the instruments records the detector signal as a function of δ. The key to any FT-based spectrometer is the encoding of a wide spectrum of wavelength intensity information into a single interferogram, with its spectral resolution $\Delta\nu$ limited by the maximum mirror retardation length Δ of the interferometer ($\Delta\nu = (2\,\Delta)^{-1}$). FT transformation of an interferogram into wavenumber space produces an IR spectrum. In combination with a reference IR spectrum, an IR absorption spectrum can be calculated. While theoretically a single interferogram is sufficient, in practice, multiple interferograms are coadded together to improve S/N of the measurement. The improvement of coadding spectra is typically estimated to be $\propto \sqrt{M}$, where M is the number of spectra.

2.3 Time-resolution of Fourier Transformed Infrared Spectroscopy

For measurements of dynamic processes, a sample would be perturbed at a time t_0, followed by the collection of multiple interferograms in rapid succession. The time-resolution here is limited by the collection time of sufficient interferograms required for the coadditions as

shown in Figure 2.2a. The time required for the mirror in the interferometer to move multiple times along its maximum retardation. In practice, a state-of-the-art FTIR instrument with a conventional globar IR source typically requires 64 - 1024 coadditions for sufficient S/N for measurements in liquid electrochemical environments due to strong background absorption. The resulting time-resolution will range from a few seconds to up 5 minutes, which is insufficient for many electrochemical processes occurring at faster time scales. Increased temporal resolution can be achieved through either decreasing the maximum pathlength of the interferometer mirror (which comes at a cost of poorer spectral resolution), or increasing the mirror velocity which also leads to poorer S/N. The key to further increase time-resolution into the millisecond range is to circumvent the coaddition of sequentially collected interferogram as shown in Figure 2.2a and 2.2b. The first option is rapid scan FTIR utilized in Chapter 3 and 4 and the second option is step scan FTIR utilized in chapter 5 and 6.

A schematic of the rapid scan FTIR measurement procedure is depicted in Figure 2.2c. A sample is perturbed at time t_0 and a series of interferograms are collected in rapid succession. Instead of coadding immediately, the sample is reset to its initial state and a second series of interferograms are collected. The entire sequence of FTIR measurement and sample reset is repeated as many times as required to build sufficient S/N through co-addition. After data collection, each interferogram in a single FTIR series is given a time element designation starting with t_1, t_2, t_3, etc and IR spectra with the same time designation are coadded to improve S/N. The time-resolution is limited by the collection time of a single interferogram. As an added benefit, higher mirror velocities are less detrimental as the accompanying decrease in S/N can be partially offset by increasing the number coadditions acquired in a given amount of measurement time. Modern FTIR instruments with higher

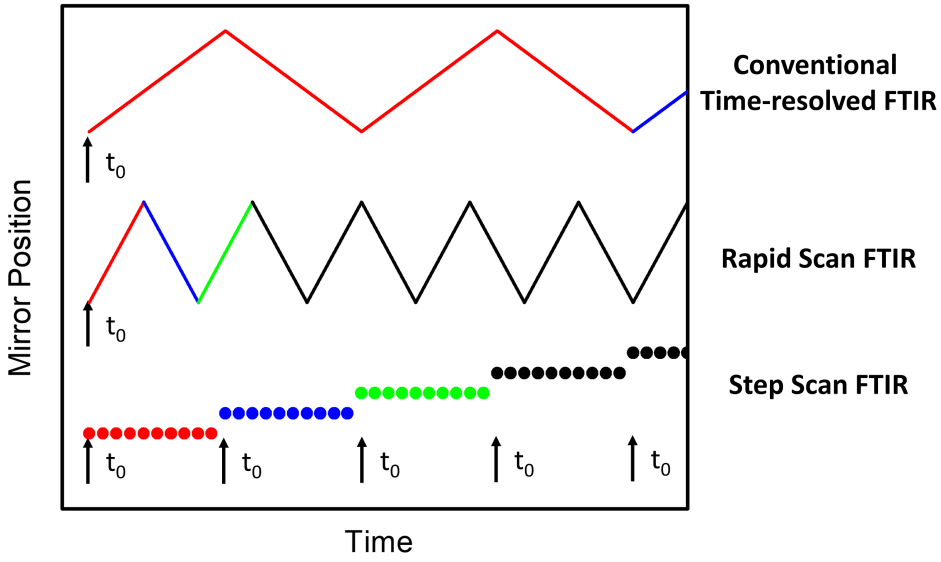

(a) Mirror Movement for various Time-Resolved FTIR

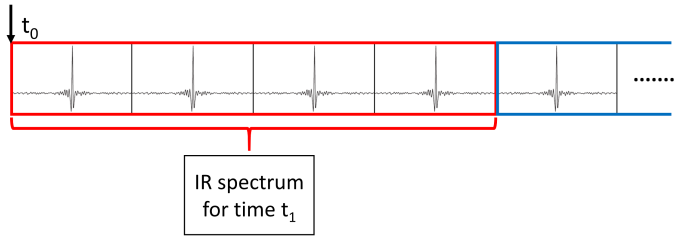

(b) Conventional Time-Resolved FTIR

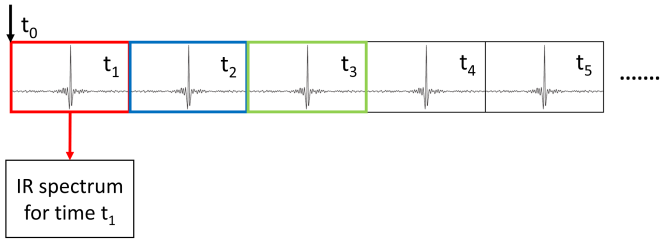

(c) Rapid Scan FTIR

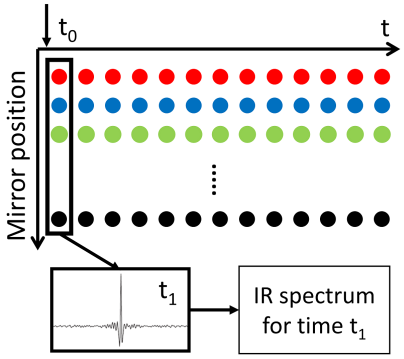

(d) Step Scan FTIR

Figure 2.2: (a) Schematic representation of interferogram mirror movement during conventional time-resolved FTIR, rapid scan FTIR and step scan FTIR. t_0 denotes the start of the sample perturbation, followed by collection of the IR detector signal transient. Schematic representation of the post processing procedure for (b) conventional time-resolved FTIR, (c) rapid scan FTIR and (d) step scan FTIR.

mirror velocities allow time-resolution of 10 - 20 millisecond.

Accessing higher time-resolution beyond the mechanical limits of a moving mirror requires step scan FTIR. Instead of the continuous movement of the mirror of conventional and rapid scan FTIR as shown in Figure 2.2a, the mirror position in step scan FTIR is stepped between stationary positions at consistent distances from each other. For a single step scan measurement, the sample is reset to its initial state before inducing a perturbation at t_0 and collecting the detector response in time for each mirror position. Repeating the process over all mirror position yields a 3D dimensional data block consisting of detector response at different mirror position and time-elements as depicted in Figure 2.2d. Post-measurement processing can now construct the interferograms for each time element and convert them to IR spectra. The time-resolution of this measurement is fully decoupled from the mechanical movement of the mirror and is only limited by the MCT-detector response time and the S/N of the measurement. In practice, step scan IR with recently developed IR lasers can achieve time-resolution down to nanoseconds[13,14]. A major drawback of the step scan technique is the need for a drastically increased number of repeated sample perturbations and overall measurement time compared to rapid scan FTIR. To provide some context, an interferogram collected by a modern FTIR instrument consists of about 1000 mirror positions. Assuming data is acquired for one second at each mirror position, the measurement time for a single step scan data block requires $\sim$17 min. In order to improve S/N, multiple step scan spectra are collected to decrease noise by coaddition. In this example, to acquire 128 coadded interferograms for every time slice, the interrogated system must be stable for 36 h and possess a consistent response to the perturbation over 128,000 iterations.

Since both rapid scan and step scan FTIR demand increased measurement time

and repetition of the reaction, it is crucial during the experimental development within this thesis to evaluate stability and repeatability of the electrochemical reaction and address any challenges originating from it. A second consideration is the optimization of each iteration of the electrochemical reaction to decrease the overall experimental duration.

2.4 Challenges of *in situ* Spectroelectrochemistry

One primary challenge to overcome for all *in situ* implementations is the strong background absorption of IR within liquid environments. Liquids are an excellent IR absorber for their specific IR modes and also diminish light intensity across the entire spectrum through simple dampening. To tackle this challenge, the most common optical setups for *in situ* IR for electrochemistry are shown in Figure 2.3. The external reflection geometry in Figure 2.3a, commonly referred to as infrared reflection absorption spectroscopy (IRRAS)[15], passes light through solution within a thin cavity before the reflected light is collected and guided towards a suitable IR detector for measurement. While not removing background absorption of the liquid, this optical setup minimizes the IR pathlength through solution using thin cavities on the order of 4-40 microns. This limits the background absorption of the liquid, while still retaining sensitivity to solution phase composition. As IR absorption when passing through liquids obeys the Beer-Lambert law, quantitative analysis through known or experimentally measured IR absorption cross section of solution species is possible.

In the attenuated total reflection geometry (ATR) shown in Figure 2.3b[3,16], incident IR light is passed through an internal reflection element (IRE) composed of a material with high refractive index such as germanium or silicon. At the solid-liquid interface, the IR light

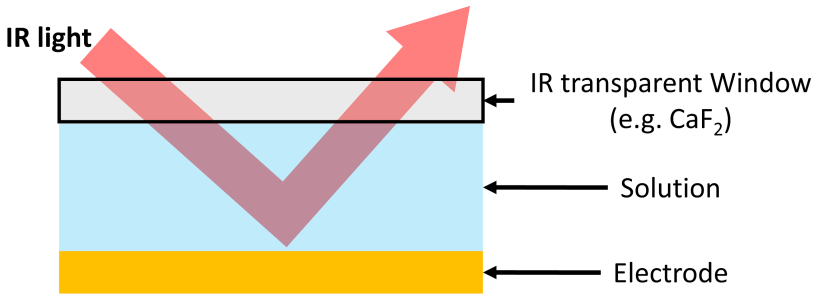

(a) IRRAS

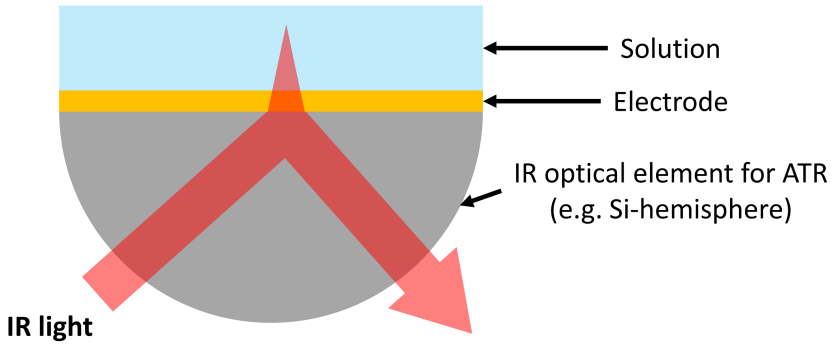

(b) ATR

Figure 2.3: Schematic representation for the optical setup for (a) infrared reflection absorption spectroscopy (IRRAS) and (b) attenuated total reflection spectroscopy (ATR).

can undergo total internal reflection above the critical angle, if the refractive index of the liquid medium has a real component. At the area where IR is totally internal reflected, an evanescent wave extends from the IRE into the medium of interest for a few hundred nanometers to micrometers depending on the refractive indices of the system, the wavelength of the light and the incident angle of the light. For mid-IR light the penetration depth is around 0.5 – 2 μm. Compared to IRRAS geometries, this optical configuration avoids the strong background absorption of liquid media but restricts the volume interrogated by the IR light to the proximity of the interface. This setup is well suited for measurement of thin films, nanoparticle layers or surface adsorbed analytes. The obvious downside is its limited range to the initial few hundreds of nanometers from the interface and a more difficult extraction of quantitative information.

The choice of optical geometry is driven by the electrochemical system and the specific aspect of the reaction of interest. For spectroelectrochemical measurements of solution phase molecules, the IRRAS configuration is better suited and technically simple to implement, but low IR reflection/transparency properties of the sample or poor mass transport conditions related to their thin cavities can necessitate ATR geometries despite their limited range for solution phase molecules[17]. In this thesis, Chapter 3 and 4 will focus on solution phase components of an electrochemical reaction and therefore rely on IRRAS measurements, while Chapter 5 and 6 are interested in observing surface absorbed molecules using the ATR configuration. It should also be noted that IR detection of surface adsorbed molecules often relies on additional signal enhancement due to the low quantities of molecules at the surface compared to the solution. A common approach is the preparation of a surface-enhancing metal structure on the ATR IRE element[11,18]. A more in-depth overview of this subject will

be provided in Chapter 5.

Besides the challenges arising from the liquid media, all experimental platforms developed within this thesis also must address the crucial electrochemical requirement of an ultramicroelectrode (UME). The origin of this requirement necessitates a more detailed examination on how electrochemical processes at the heterogeneous interface respond to fast potential perturbations. For most electrochemical experiments occurring at the liquid-solid interfaces, the solid surface at which the reaction of interest occurs is often referred to as the working electrode (WE). Controlling the WE's electrical potential allows manipulation of both thermodynamic (equilibrium distribution of products and reactants) and kinetic (rate of reactions) aspects of an electrochemical reaction. Conceptually, when a solid surface WE is submerged into solution, a thin electrical double layer (EDL) is formed at the interface to screen the bulk solution from the surface charge of the WE[19]. According to the Stern model shown in Figure 2.4a, the EDL of a positively charged surface consists of a layer of near-surface anions that are attracted from bulk solution to the interface by the surface charge of the WE, followed by a diffuse layer with an net non-equal distribution of anion and cation concentrations. The charge within the EDL effectively balances the electronic surface excess charge on the metal side of the interface.

For time-resolved IR spectroelectrochemical experiments such as Osawa's[20,21] and Sun's[17,22], the WE potential E is stepped from an initial potential E_{init} where the reaction is thermodynamically inhibited to a potential step (E_{step}) where the reaction is thermodynamically favored to induce the electrochemical reaction. In an ideal situation, the potential of the electrode should respond instantaneously to an externally applied E_{step} as shown by the blue line in Figure 2.4b. For real electrodes however, any potential perturbation requires

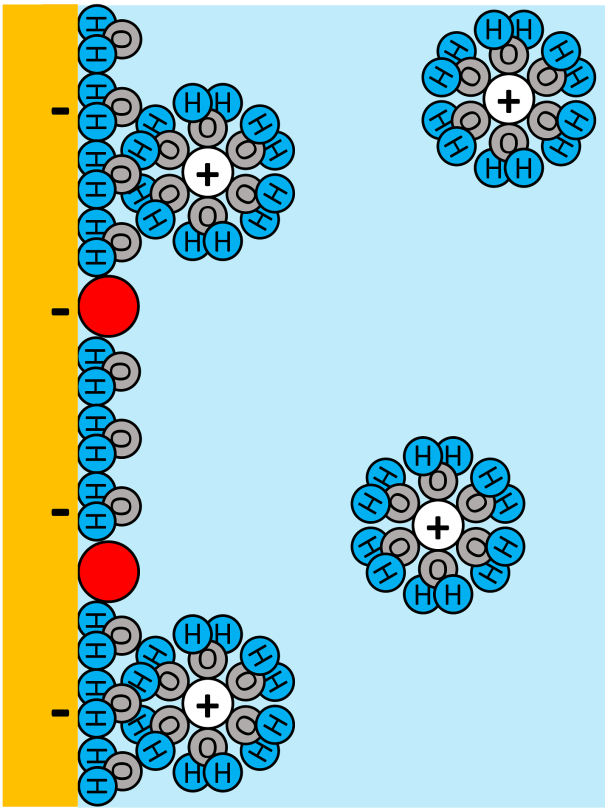

(a) Stern Model of EDL

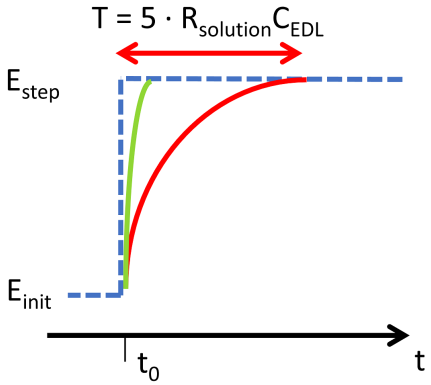

(b) Potential Response Time

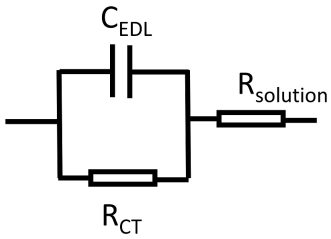

(c) Equivalent Circuit of EDL

Figure 2.4: (a) Schematic representation of the Stern model for the EDL with negative charged electrode surface (yellow area) within aqueous solution (light blue area). Also shown are oriented electrolyte solvent molecules (H_2O), surface absorbed molecules (red) and solvated cation within the inner and diffuse layer. (b) The electrochemical potential response after a potential perturbation from E_{init} to E_{step} at t_0. The dashed blue line represents the ideal behavior and the red and green line represents response of real electrode with large and small surface area respectively. (c) Schematic representation of the equivalent circuit for the EDL.

adjustment of the EDL to the new electric potential[23]. This process is non-instantaneous and occurs over a finite time period as indicated by the red line in the figure. The rise time in the potential response is detrimental to investigation of kinetics as within this initial timeframe the electrode response and interfacial chemical reaction are inseparable.

Conceptually, the electric response of an EDL can be described by an equivalent circuit model, shown in Figure 2.4c, consisting of a double layer capacitance C_{EDL} in parallel to a charge transfer resistance R_{CT} followed by a bulk solution resistance $R_{solution}$. The metal-solution interface reaches the new step potential only after C_{EDL} has been fully charged. In the limiting case of an infinite charge transfer resistance the time dependence of the establishment of the interfacial potential is given by:

$$\frac{\Delta E(t)}{\Delta E_{applied}} = \left[1 - exp\left(- \frac{t}{R_{solution} C_{EDL}} \right)\right] \tag{2.4}$$

In the presence of a charge transfer reaction (for example the reduction or oxidation of a small molecule in solution) the value of R_{CT} is finite and perturbs the establishment of the interfacial potential caused by the charging of the double layer capacitance.

A general rule of thumb is that the electrochemical time constant $T = R_{Solution} E_{EDL}$ defines the minimum temporal resolution of a potential step experiment with the requirement that $T_{min} = 5RC$. It is, therefore, evident that spectroelectrochemical experiments with microsecond resolution require the use of cells that have time constants on the order of 200 ns. As R_{CT} is dependent on the specifics of the system (material of the electrode, solvation of the redox species) only $R_{Solution}$ and C_{EDL} can be modified by changes to the electrochemical cell geometry. To a first approximation, the solution resistance is determined only by the

concentration and mobility of ions in the electrolyte solvent. Beyond working with saturated electrolyte concentrations there is little that can be done to lower $R_{solution}$ much below values in the range of 100 Ω. On the other hand, the capacitance of a metal-solution interface is an extensive property and scales with the dimension of the electrode. For example, the area normalized capacitance of the gold-aqueous electrolyte solution has a nominal capacitance of 50 μF/cm^2. Thus, whereas $5RC$ is on the order of 25 ms for a 1 cm^2 Au electrode, it can be lowered to 25 ns by decreasing the electrode area to 100 μm^2. Compared to a large surface, the potential response of such an electrode is more akin to the green line in Figure 2.4b. Therein lies the key to microsecond resolved electrochemistry; the utilization of working electrodes with length scales in the tens of micrometer domain. Experimentally, this concept was first demonstrated by Wightman and Fleischmann, who showed that ultra microelectrodes with one dimension in micrometer range possess cell time constants of the order of microseconds[24].

While the use of UMEs resolves the electrochemical constraints for fast time-resolved measurements, it introduces considerable spectroscopic challenges. The wavelength of IR radiation is within the micrometer range and focusing light to its diffraction limit < 50 μm severely increases the noise of the measurement. The low S/N with conventional globar IR sources in combination with further experimental difficulties imposed by the spectroscopic demand of rapid scan and step scan FTIR is ultimately responsible for the sparse implementation of *in situ* FTIR to study the kinetics of electrochemical process to date. However, the $\sim 10^3$ higher brilliance of SIR compared to conventional IR sources utilized in the proof-of-principle measurements by Rosendahl *et al.*[25,26] can overcome poor S/N of previous spectroelectrochemical implementation of rapid scan and step scan FTIR. In their study, the

authors were able to perform step scan FTIR measurements to observe femtomolar quantities of ferri/ferrocyanide, a reversible model molecule for electrochemical redox reaction in solution, with 100 μs time-resolution. The challenge of this thesis will be to transition from this simple model system and develop spectroelectrochemical platforms to support more complex electrochemical systems.

2.5 References

[1] Bewick, A.; Kunimatsu, K.; Pons, B. S. Infra red spectroscopy of the electrode-electrolyte interphase. *Electrochimica Acta* **1980**, *25*, 465–468.

[2] Zaera, F. New advances in the use of infrared absorption spectroscopy for the characterization of heterogeneous catalytic reactions. *Chemical Society Reviews* **2014**, *43*, 7624–7663.

[3] Wang, H.; Zhou, Y.-W.; Cai, W.-B. Recent applications of in situ ATR-IR spectroscopy in interfacial electrochemistry. *Current Opinion in Electrochemistry* **2017**, *1*, 73–79.

[4] Ye, J. Y.; Jiang, Y. X.; Sheng, T.; Sun, S. G. In-situ FTIR spectroscopic studies of electrocatalytic reactions and processes. *Nano Energy* **2016**, *29*, 414–427.

[5] Griffiths, P. R.; de Haseth, J. A. *Fourier Transform Infrared Spectrometry*; Wiley Online Books; 2007; pp 1–18.

[6] Aroca, R. *Surface-Enhanced Vibrational Spectroscopy*; Wiley Online Books; 2006; pp 1–33.

[7] Atkins, P.; de Paula, J. *Physical Chemistry*, ninth ed.; Oxford University Press, 2010; pp 481–537.

[8] Larkin, P. *Infrared and Raman spectroscopy: principles and spectral interpretation*; Elsevier, 2017; pp 7–26.

[9] Christensen, P.; Hamnett, A. In-situ techniques in electrochemistry — ellipsometry and FTIR. *Electrochimica Acta* **2000**, *45*, 2443–2459.

[10] Liu, S. X.; Liao, L. W.; Tao, Q.; Chen, Y. X.; Ye, S. The kinetics of CO pathway in methanol oxidation at Pt electrodes, a quantitative study by ATR-FTIR spectroscopy. *Physical Chemistry Chemical Physics* **2011**, *13*, 9725–9735.

[11] Osawa, M. *In-situ Surface-Enhanced Infrared Spectroscopy of the Electrode/Solution Interface in Advances in Electrochemical Sciences and Engineering*; Wiley Online Books; 2008; pp 269–314.

[12] Han, B.; Li, Z.; Wandlowski, T.; Blaszczyk, A.; Mayor, M. Potential-induced redox switching in viologen self-assembled monolayers: An ATR-SEIRAS approach. *Journal of Physical Chemistry C* **2007**, *111*, 13855–13863.

[13] Roedig, C.; Chizhov, I.; Weidlich, O.; Siebert, F. Time-Resolved Step-Scan Fourier Transform Infrared Spectroscopy Reveals Differences between Early and Late M Intermediates of Bacteriorhodopsin. *Biophysical Journal* **1999**, *76*, 2687–2701.

[14] Schultz, B.-J. J.; Mohrmann, H.; Lorenz-Fonfria, V. A.; Heberle, J. Protein dynamics observed by tunable mid-IR quantum cascade lasers across the time range from 10 ns to 1 s. *Spectrochimica Acta Part A: Molecular and Biomolecular Spectroscopy* **2016**, 1–9.

[15] Hollins, P. Infrared Reflection–Absorption Spectroscopy. *Encyclopedia of Analytical Chemistry* **2006**, 1–17.

[16] Mudunkotuwa, I. A.; Minshid, A. A.; Grassian, V. H. ATR-FTIR spectroscopy as a tool to probe surface adsorption on nanoparticles at the liquid-solid interface in environmentally and biologically relevant media. *Analyst* **2014**, *139*, 870–881.

[17] Zhou, Z.-Y.; Tian, N.; Chen, Y.-J.; Chen, S.-P.; Sun, S.-G. In situ rapid-scan time-resolved microscope FTIR spectroelectrochemistry: study of the dynamic processes of methanol oxidation on a nanostructured Pt electrode. *Journal of Electroanalytical Chemistry* **2004**, *573*, 111–119.

[18] Suzuki, Y.; Osawa, M.; Hatta, A.; Suetaka, W. Mechanism of absorption enhancement in infrared ATR spectra observed in the Kretschmann configuration. *Applied Surface Science* **1988**, *33-34*, 875–881.

[19] Bard, A. J.; Faulkner, L. R. *Electrochemical Methods: Fundamentals and Applications*, second edi ed.; wiley New York, 1980; Vol. 2; pp 534–579.

[20] Osawa, M.; Yoshii, K.; Ataka, K.-i.; Yotsuyanagi, T. Real-time monitoring of electrochemical dynamics by submillisecond time-resolved surface-enhanced infrared attenuated-total-reflection spectroscopy. *Langmuir* **1994**, *10*, 640–642.

[21] Osawa, M.; Yoshii, K.; Hibino, Y.-i.; Nakano, T.; Noda, I. Two-dimensional infrared correlation analysis of electrochemical reactions. *Journal of Electroanalytical Chemistry* **1997**, *426*, 11–16.

[22] Zhou, Z.-Y.; Lin, S.-C.; Chen, S.-P.; Sun, S.-G. In situ step-scan time-resolved microscope FTIR spectroscopy working with a thin-layer cell. *Electrochemistry Communications* **2005**, *7*, 490–495.

[23] Bard, A. J.; Faulkner, L. R. *Electrochemical Methods: Fundamentals and Applications*, 2nd ed.; Wiley New York, 2001; pp 1–43.

[24] Heinze, J. Ultramicroelectrodes in Electrochemistry. *Angewandte Chemie International Edition in English* **1993**, *32*, 1268–1288.

[25] Rosendahl, S. M.; Borondics, F.; May, T. E.; Pedersen, T. M.; Burgess, I. J. Interface for time-resolved electrochemical infrared microspectroscopy using synchrotron infrared radiation. *Review of Scientific Instruments* **2011**, *82*, 083105.

[26] Rosendahl, S. M.; Borondics, F.; May, T. E.; Burgess, I. J. Step-Scan IR Spectroelectrochemistry with Ultramicroelectrodes: Nonsurface Enhanced Detection of Near Femtomole Quantities Using Synchrotron Radiation. *Analytical Chemistry* **2013**, *85*, 8722–8727.

Chapter 3

Development of Synchrotron based Rapid Scan FTIR for Methanol Oxidation

3.1 Introduction

While electrochemical processes occurring at heterogenous liquid-solid interfaces are crucial for the development of many technologies ranging from renewable energy application to novel analytical sensors, deciphering and optimizing their reactions has remained challenging. Electrocatalytic oxidation of methanol (MOR) in fuel cells, for example, has remained an active research area almost 60 years after the initial mechanistic descriptions were reported in the 1960s[1,2]. In this way MOR matches fusion reactors by being continually elusive. One central challenge for many electrochemical reactions is the complex nature of chemical reaction occurring on solution-metal interfaces. Accessing interfacial information is not only technically challenging but individual measurement techniques can only characterize certain aspects of the reaction. A multitude of complimentary techniques are required to comprehensively interrogate individual aspects of the reaction. As discussed in Chapter 1, this challenge sparked the development and implementation of a host of new analytical methods, such as electrochemical techniques to measure the charge transfer, X-ray spectroscopy to characterize electrode composition, probe microscopy for surface topography and absorption spectroscopy

for chemical identification of solution phase species just to name a few. As analytical techniques continue to improve, a crucial aspect of electrochemistry is the continued integration and improvement of these techniques.

As discussed in Chapter 2, spectroelectrochemistry refers to the application of spectroscopic techniques such as UV/Vis, Raman or X-ray methods for electrochemical systems. Fourier transformed infrared spectroscopy (FTIR) is a well-established complimentary technique to electrochemistry due to its excellent chemical sensitivity combined with *in situ*/*in operando* capabilities[3]. Since its adoption into electrochemistry in the 1980s[4], various FTIR spectroelectrochemical techniques have been developed to either probe solution phase molecules by passing IR light through the solution or surface adsorbed molecules by enhancing the IR signal of moieties near the electrode surface. While investigations of non-dynamic electrochemical processes with FTIR are commonplace within the literature, the large electrode surfaces areas used in these setups prohibit measurement of dynamic process on the second to millisecond time scale.

The central limitation is the time constant, a value that describes the time delay of any thermodynamic electrode responses (electrode potential) to any perturbation of electrochemical equilibrium, as described more in depth in Chapter 2. With the time constant scaling proportionally with electrode surface area, any increase in time-resolution must be matched with a decrease in electrode surface areas. Due to poor S/N when focussing IR light onto small samples areas for conventional IR sources, very few examples of time-resolution in the milliseconds have ever been reported in the literature[5–9]. Recently, Rosendahl *et al.* have successfully demonstrated that high brilliance synchrotron infrared radiation can provide the S/N ratio needed for time-resolved FTIR measurement with microsecond time-resolution of

a simple electrochemical model system[10,11].

This chapter will focus on the technical developments to transition the existing synchrotron FTIR platform for the model electrochemical system (the reversible ferricyanide/ ferrocyanide redox couple) used by Rosendahl *et al.*[11] to the much more complex MOR on Pt which is a highly irreversible electrochemical system.

3.2 Background

3.2.1 Methanol Oxidation and Direct Methanol Fuel Cell

Since the first description of MOR on Pt electrodes, the electrocatalytic oxidation of methanol (MeOH) has remained a highly researched topic within the literature due to its application in a direct methanol fuel cell (DMFC)[12]. Skipping the conversion into thermal energy within combustion engines, fuel cell devices such as the DMFC can theoretically achieve higher efficiencies by direct conversion of chemical bond energy into electrical current.

Modern fuel cells can be split into two categories by their fuel source, either utilizing hydrogen as fuel or small organic molecules such as MeOH, formic acid and ethanol. While MeOH, compared to hydrogen, is easier to transport and store on a large industrial scale, the widespread implementation is limited due its sluggish kinetics[12,13]. Research efforts within recent years have tackled performance problems of DMFC either through development of better catalysts[14] and fuel cell materials[15,16] or through investigation of the complex reaction mechanism for a better fundamental understanding of the chemical reaction[17–20]. Ultimately, optimization of DMFCs will require both. In this context, the development of a time-resolved

FTIR platform, as described in Chapters 3 and 4 of this thesis, was targeted toward investigations of the MOR. Specifically, whereas Chapter 4 is focused on applying electrochemical IR spectromicroscopy toward catalyst development, this Chapter describes an attempt to investigate the reaction mechanism of MOR on Pt. However, it is important to emphasize that the overarching goal of the research was method development. Specifically, studying the MOR provided the impetus to extend the capability of time-resolved, electrochemical IR spectromicroscopy to important catalytic reactions that are inherently irreversible and much more complex than simple redox systems.

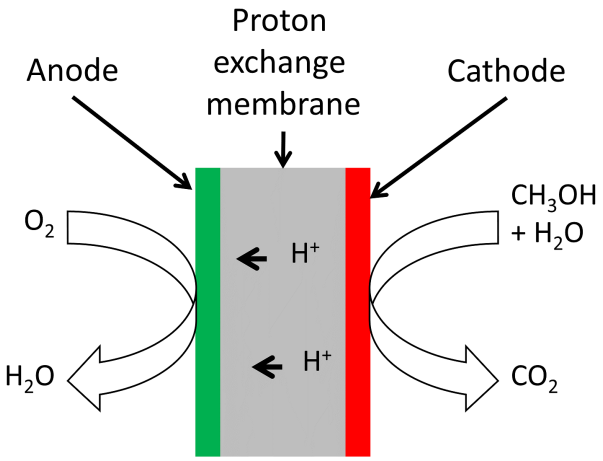

Anode reaction: $CH_3OH + H_2O \rightarrow 6\ H^+ + 6\ e^- + CO_2$

Cathode reaction: $3\ O_2 + 12\ H^+ + 12\ e^- \rightarrow 6\ H_2O$

Total reaction: $2\ CH_3OH + 3\ O_2 \rightarrow 4\ H_2O + 2\ CO_2$

Figure 3.1: Schematic representation of a DMFC and the chemical equation of the MOR within a DMFC.

Within the many possible catalyst materials used for DMFC, Pt and Pt-based alloys remain the most common electrocatalysts for MOR because of the unique ability of platinum to break C−H bonds. The overall reaction and operating principle of a DMFC can be found in Figure 3.1. The main reaction pathway of MOR, also referred to as "indirect" pathway, on

platinum at the anode of a DMFC is through adsorption of MeOH onto reactive sites of the Pt surface, before dehydrogenation to surface adsorbed CO, releasing $4H^+$ and generating $4e^-$. The CO is further oxidized into CO_2 and $2H^+$ by reaction with surrounding H_2O and generating two additional e^-. Within a DMFC, the generated H^+ is transferred to the cathode through a proton exchange membrane where it reacts with O_2 to form H_2O.

3.2.2 Methanol Oxidation Reaction Mechanism on Platinum

The overall oxidation of MeOH into CO_2 catalysed by Pt was described within the initial literature[1,2], but the details of the anode reaction mechanism and pathways remain under investigation to this day due to its sheer complexity. The sluggish kinetics of MOR compared to hydrogen fuel cells is due to the dissociation of hydrogen and reaction with H_2O over multiple steps and the associated energetic barriers. A detailed description of this complex process is far beyond the scope of this background section and better described within the many simulation works and reviews of MOR on Pt in the literature[12,17,19].

Broadly speaking, as early as Breitner in 1976 the completed oxidation of MeOH is considered a "dual path mechanism" where the multiple reaction pathways are categorized into either an "indirect" pathway involving the formation of CO_{ads} as a reaction intermediate and subsequent oxidation to CO_2, or a "direct" oxidation pathway to CO_2 through other intermediate species without the forming CO[2]. Since then, a much more detailed reaction pathway has been deciphered and a schematic overview of the principle methanol oxidation reaction pathways on Pt is depicted in Figure 3.2[12,17,19]. Starting with the dehydrogenation, it is widely accepted that the dissociation of hydrogen from MeOH is a step wise process involving up to three Pt atoms. After adsorption of MeOH onto the catalyst surface, MOR

branches into multiple reaction pathways depending on the dissociation of the initial proton from either a C−H bond or the O−H bond. For the C−H bond, subsequent dissociation will result in either in CO_{ads} or $HCOO_{ads}$ as long-lived intermediates before oxidizing to CO_2. An initial dissociation of the O−H bond will instead lead to H_3CO_{ads} that oxidizes to CO_2 by converting to CO_{ads} or $HCOO_{ads}$. These surface adsorbed MOR intermediates can exist simultaneously on the Pt surface and they possess different oxidation steps towards the final oxidation product CO_2 depending on a host of experimental conditions such as MeOH concentration, mass transport conditions within the electrolyte, reaction temperature, electrode potential, surface texture/structure and catalyst loading[12]. One crucial challenge for optimization are two detrimental processes within DMFC, 1) CO poisoning of catalyst and 2) the incomplete MeOH oxidation into HCOOH, H_2CO and $HCOOCH_3$.

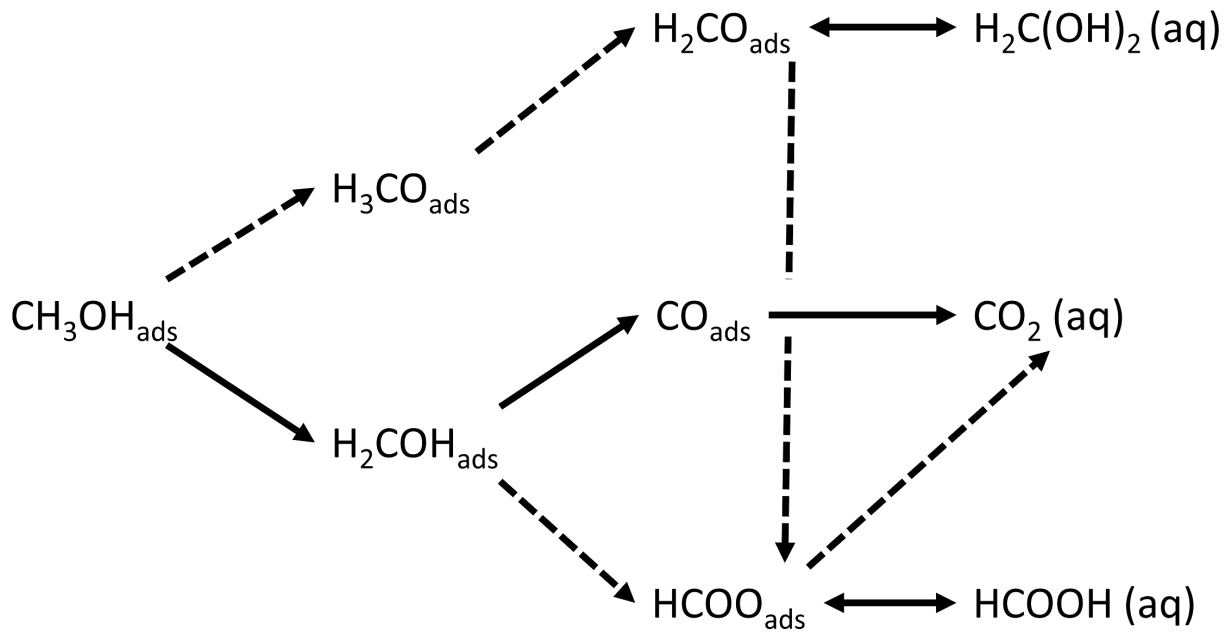

Figure 3.2: Adapted from Liu *et al.*[17]. Reaction pathways of the MOR on a platinum electrode with solid lines indicating the "indirect" pathway and dashed lines the "direct" pathway.

Following the "indirect" MOR path through CO, the subsequent reaction of the surface absorbed CO with H_2O to CO_2 is one of the lynch pins for DMFC performance. CO is strongly bound to the metal surface due to π-back bonding. On pure platinum, the oxidation of CO requires higher overpotential than the dehydrogenation step with ideal reaction conditions at even higher potentials. Large overpotentials decrease the efficiency of the fuel cell, as a higher percentage of generated current is consumed in the operation of the cell. Running DMFC at lower overpotential however can lead to build up of incomplete oxidized CO at the reactive sites of Pt, poisoning the catalyst for further methanol oxidations. A major thrust in DMFC research is mitigating CO poisoning through catalyst material design as will be extensively discussed in Chapter 4 or optimizing the reaction condition to avoid the "indirect" oxidation pathway altogether.

The main aspect of interest here is the incomplete oxidation product of MOR. The long-lived intermediates of MOR, *i.e.* $HCOO_{ads}$ and H_2CO_{ads}, are known to be weakly bonded to the surface compared to CO. These molecules can desorb from the Pt surface as HCOOH and H_2CO respectively without undergoing complete oxidation to CO_2. This results in the products of the MOR being composed of a mixture of CO_2, HCOOH, H_2CO and $HCOOCH_3$, a result of HCOOH reaction with MeOH in solution. The formation of these incomplete reaction products is well known in the literature and various groups have attempted to minimize efficiency losses. Formic acid has even been proposed as an alternative fuel source, allowing more reliable oxidation into CO_2[21–23].

For a long time, studies viewed HCOOH and H_2CO as lost for further oxidation once they diffused away into the double layer after desorbing from the surface. Within recent years however, this assumption was challenged by studies demonstrated varying MOR prod-

uct composition depending solely on catalyst density on the anode. This work culminated in a description of a more complex "desorption-readsorption-reaction" involving HCOOH and H_2CO within fuel cells first proposed by Behm *et al.*[24,25]. As anodes within typical DMFCs consist of many small Pt-nanoparticles, HCOOH and H_2CO created at a nanoparticle can desorb and diffuse to the surface of a different particle. Subsequent oxidation of these intermediates impacts the overall efficiency of the anode. In later experiments by the same group, electrochemical measurements with Pt nanoparticle arrays show transport of these species can be between nanoparticles hundreds of nanometers apart from each other. MOR performance within a single catalyst particle affects the performance of other particles within its surrounding, resulting in changes of overall MOR performance. Further investigation into the contribution of the "desorption-readsorption-reaction" on MOR activity of Pt catalyst can benefit from *in situ* monitoring of solution phase HCOOH and H_2CO concentration. Hence, an objective of this research was to find spectroscopic evidence of these intermediates in the solution surrounding a Pt anode during methanol oxidation.

3.2.3 *in situ* FTIR for the Methanol Oxidation Reaction

In the case of methanol oxidation, FTIR has proven itself to be a very effective technique as all reaction intermediates and products of MOR are IR active[8,9,20,26–28]. The purely optical nature of IR has lent itself to the development of various experimental approaches, each tasked with investigating different aspects of the complex reaction. For instance, Pt catalyst material deposited on ATR elements allow surface sensitive FTIR measurements of the surface adsorbed molecules. *In situ* ATR-SEIRAS measurement performed by Osawa *et al.* were able to clearly identify surface adsorbed HCOO (~ 1320 cm^{-1}) on Pt surfaces alongside CO

(~ 2050 cm^{-1} and ~ 1830 cm^{-1} in linear and bridge bonded configurations respectively)[26]. Solution phase species require passing IR light through the solution which is much more difficult to implement due to the high extinction of infrared light by aqueous based electrolytes. Nevertheless, Smotkin *et al.* were able to identify the solution phase species of the reaction and assigned CO_2 (~ 2340 cm^{-1}), HCOOH (~ 1710 cm^{-1}, $1440 - 1395$ cm^{-1} and $1320 - 1210$ cm^{-1}), H_2CO (~ 1648 cm^{-1}) and H_2COCH_3 (~ 1745 cm^{-1} and $1210 - 1160$ cm^{-1})[29].

While these FTIR measurements under steady state conditions have undoubtably aided in the identification of long-lived solution phase composition, the addition of time-resolved FTIR provides unique opportunities to experimentally extract kinetic rate information about these solution phase molecules. For example, time-resolved FTIR experiments on the second-to-minute scale by Chen *et al.* investigate HCOOH[27] and MeOH[28] oxidation on a Pt electrode surface within the controlled mass-transport environment of a flow-through cell. In both case, kinetics information extracted from the IR transient of the CO_{ads} and $HCOO_{ads}$ intermediates were crucial to differentiate between "direct" and "indirect" oxidation rate and examine the electrocatalytic preference for either reaction pathway based on electrode potential and temperature.

Another important example of the capabilities of time-resolved FTIR is Sun *et al.* work, which is also one of the few examples of rapid scan and step scan FTIR measurement of an electrochemical system in solution in the entire literature[8,9]. In their work, Sun *et al.* utilized a Pt microelectrode of 200 μm diameter to decrease the time constant (see Chapter 2) compared to the typically large electrode surface area used in many of the other FTIR approaches used to study MOR. The FTIR instrument used a conventional globar IR source to interrogate the reaction in an external reflection geometry. Usually, the combi-

nation of strong background water absorption, rapid/step scan FTIR and small electrode size would severely deteriorate the S/N of IR measurement beyond anything recoverable. Sun *et al.* electrochemically nanotextured the Pt microelectrode to create an anomalous infrared enhanced spectroscopy (AIRES) setup that boosts the IR signal of surface adsorbed CO above the noise. This setup was able to measure the electrooxidation of CO at high overpotentials with time-resolution on the hundreds of microsecond range. They were able to determine that CO oxidation to CO_2 occurs with a nucleation and growth mechanism at the boundary between regions of the Pt surface containing CO and oxygen species. These experiments successfully demonstrated the ability of time-resolved FTIR to investigate the mechanism and kinetics of the initial reaction step within an electrocatalytic reactions after an "instantaneous" potential perturbation.

While Sun *et al.*'s work showcased the possibility of time-resolved measurement in this area, the reliance of AIRES to create sufficiently strong IR signal has its limitations. 1) Electrode material selection is limited to nanotextured Pt and 2) Only surface adsorbed species benefit from the surface enhancing effect of AIRES. As Behm *et al.* work showcased the importance of solution phase transport for overall performance of MOR through the "desorption-readsorption-reaction" process[24,25], a different approach must be developed to access the solution phase species with sufficient time-resolution. Recent work by Rosendahl *et al.* used a different approach to acquire high S/N, time-resolved FTIR on micro/ultramicroelectrodes using SIR[10,11]. The next challenge in the development of SIR-based spectroelectrochemistry is an experimental platform that allows time-resolved FTIR measurements for a more complex irreversible electrochemical system such as MOR. The initial implementation will focus on the simpler rapid scan FTIR compared to the much more

technically challenging step scan FTIR.

3.3 Methodology/Discussion

A significant portion of the work presented in this Chapter will be devoted to the development of the spectroelectrochemical setup and measurement procedure required to perform the SIR-based rapid scan FTIR measurement of the MOR on Pt. The first part of this Chapter focuses on the technical aspects such as construction of a spectroelectrochemical cell for MeOH electrocatalysis on Pt, developing a reliable reset procedure for the working electrode and the electrolyte solution, establishing stable electrochemical conditions for the time period required to perform the rapid scan experiment and demonstrating the entire measurement procedure with rapid scan FTIR results. The second part will then present the rapid scan FTIR results of MOR and discuss the utility of the developed platform based on its performance for detecting solution phase intermediate species.

3.3.1 Reagents, Solutions and Instrumentations

H_2SO_4 (ACS grade, Fisher Scientific), methanol (HPLC grade, Fisher Scientific) and KCl (ACS grade, Fisher Scientific) were purchased and used as received. All aqueous solutions were created using Milli-Q water ($>$ 18 MΩ cm).

All FTIR measurements were performed with a Bruker VERTEX 70V FTIR spectrometer with a Hyperion 3000 IR microscope at the Mid-IR beamline end station at the Canadian Light Source (CLS). High brilliance mid-IR beam from the synchrotron was focused onto the sample cell by a 15$\times$ objective and a 20 μm circular aperture contained within the

IR microscope. FTIR signals were collected in reflectance mode using a 100 μm narrowband MCT detector. IR spectra data were collected using Bruker's OPUS software and processed with the software's internal Fourier-transform algorithms.

All purely electrochemical measurements were performed in a standard three electrode configuration using a HEKA PG 590 potentiostat. Collected current and potential data were collected using a USB 6351 X-series multifunction data acquisition card (DAC) (National Instruments) running a custom written LabVIEW program (Appendix I).

3.3.2 Spectroelectrochemical Cell for MOR

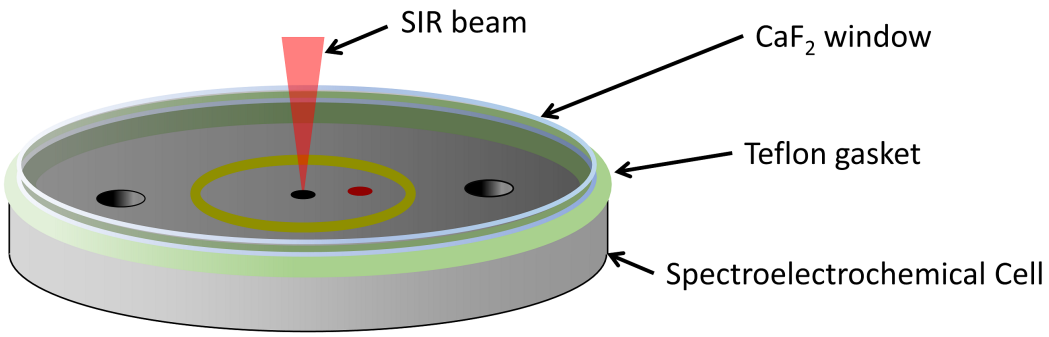

Figure 3.3: Schematic representation of the SEC. SEC liquid volume is sealed by compressing a 25 μm Teflon gasket between a CaF_2 window and the SEC body. Embedded into the SEC are the electrochemical cell components consisting of a Pt WE (black), a Pt RE (red) and a ring Au CE (yellow) as well as an inlet/ outlet (indicated holes) for injection of electrolyte.

A new spectroelectrochemical cell (SEC) had to be constructed specifically for MOR on Pt. A schematic model of the cell is shown in Figure 3.3. The design is adapted from earlier cells used for the reversible redox reaction and allows for IR measurement in an external reflection geometry through a thin cavity of solution.

Spectroelectrochemical Cell Construction

The cell body is machined from a 5 mm thick and 25.4 mm diameter Polyvinyl chloride (PVC) puck. Two 0.3 mm diameter Pt wires and a 0.5 mm diameter Au wire are embedded into the PVC puck with commercial two-part fiberglass resin. Each wire is connected through three small holes to a female electrical pin attached on the backside of the puck. These connections allow the wires to be individually contacted by a potentiostat instrument for electrochemical measurements. Two barbed tubing connectors are attached to the back face of the cell to allow liquid flow in and out of the cell. To expose the wire inside the groove and to create a flat surface for the thin cavity later, the front side of the cell base is mechanically polished with increasingly finer sandpaper until all three wires are exposed. The surface is subsequently polished with sequentially finer diamond polishing slurry (15 μm, 6 μm, 3 μm and 1 μm) to a mirror finish. The finished cell possesses a conventional three-electrode setup consisting of Pt working electrode (WE), Au counter electrode (CE) and a Pt pseudo-reference electrode (RE).

Spectroelectrochemical Cell Assembly

For assembly, the cell base is placed in a metal holder with the front face facing upwards as shown in Figure 3.3. A 25 μm Teflon gasket is placed on top of it followed by an IR transparent CaF_2 window. The gasket and window are pressed onto the polished surface using a thin metal top plate and tightened using four screws to create a thin cavity between the electrode and CaF_2 window. The fully assembled cell in the metal holder fits in the IR microscope stage at the mid-IR beamline. IR light can pass from the top of the assembled

spectroelectrochemical cell through the CaF_2 window and is externally reflected at the Pt working electrode after passing through solution.

Cavity Thickness Measurement

The cavity thickness between cell body and CaF_2 window can be obtained through an IR measurement of a dry assembled SEC. The IR spectra shown in Figure 3.4 collected at the working electrode possesses interference fringes due to overlap of reflection at the CaF_2/Air at the top of the thin cavity and reflection at the metal electrode surfaces. IR light reflected at the CaF_2/Air and the IR light reflected of the WE metal surface create this interference pattern throughout the IR spectra. By selecting the wavenumber of two interference fringe maxima's, the cavity thickness h is calculated through the following Bragg-like Equation:

$$h = \frac{n}{2\Delta\nu} \tag{3.1}$$

Where n is the number of interference fringe maxima between them and $\Delta\nu$ is the wavenumber spacing between the selected maxima. The validity of this method for cavity thickness measurement was demonstrated earlier using IR measurement of D_2O with known absorption coefficient by a previous member of the Burgess group[11].

3.3.3 Electrochemical Performance

The electrochemical performance of the new SEC cells was tested using cyclic voltammetry (CV) and compared against a Pt wire in a conventional electrochemical half cell with an Ag/AgCl reference electrode. Figure 3.5 shows the CV measurement results for the Pt wire

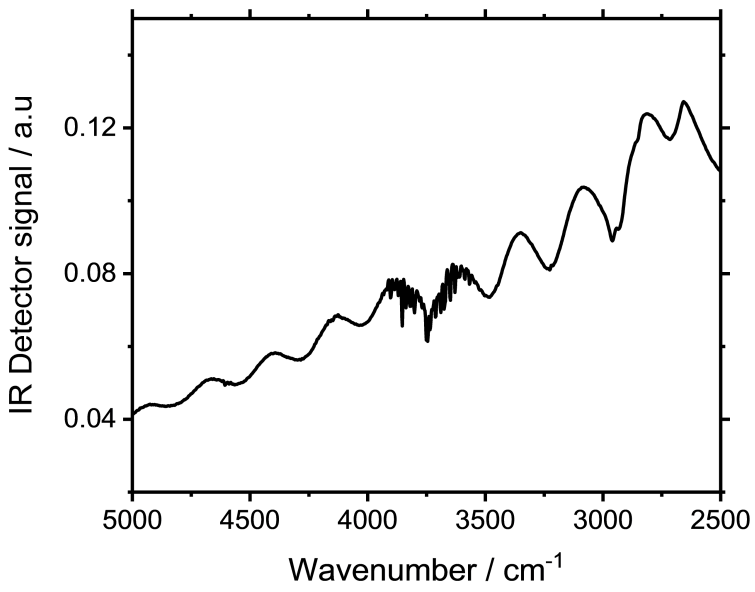

Figure 3.4: Single beam IR spectrum measured by placing the SIR beam spot on top of the WE of the assembled spectroelectrochemical cell without electrolyte. Spectrum shows interference fringes with peak-to-peak distance of ~ 200 cm^{-1}, equaling a calculated thin cavity thickness of ~ 20 μm.

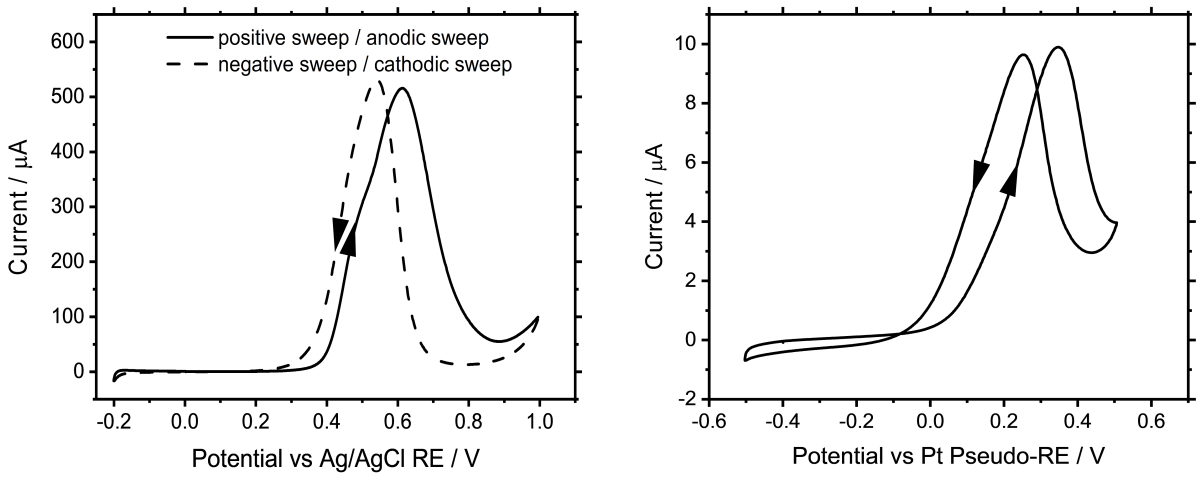

(a) Pt-wire **(b)** Pt-WE in assembled SEC

Figure 3.5: CVs in 0.1 M H_2SO_4 and 1.0 M MeOH of (a) a Pt wire within a bulk electrolyte cell setup and (b) of the Pt WE within the assembled spectroelectrochemical cell for time-resolved FTIR measurement. The sweep rate was 100 mV/s.

in 1 M H_2SO_4 + 1 M MeOH versus the Pt WE of an assembled SEC in 0.1 M H_2SO_4 + 1 M MeOH. The decreased sulfuric acid concentration is used to prevent excessive acid damage to the IR transparent CaF_2 during prolonged experiments. The new concentration is in line with many literature reports on methanol oxidation where supporting electrolyte concentrations typically range from 0.1 M to 1 M[12,30,31]. The potential between these two CV is expected to shift by 198 mV due to the Ag/AgCl reference and an additional 59 mV due to pH change from 1 M down to 0.1 M. This matches very well with the potential offset of ∼250 mV observed between the two CVs, which suggested that the secondary Pt electrode in the SEC can be used as a pseudo-reference electrode. Similarly, comparison of the electrochemical features observed matches favorably. Both anodic and cathodic methanol oxidation peaks are visible at 250 mV $< E <$ 800 mV and -100 mV $< E <$ 500 mV respectively. The two main changes for the assembled SEC is first, a decrease in MOR peak current due to thin cavity mass transport, and secondly, a slight tilt in the baseline of the CV due to the presence of oxygen in the unpurged electrolyte that has to be used in the spectroelectrochemical cell. In short, all differences between the two CVs are well accounted for and matches favorably with the literature[30]. The result demonstrates that the SEC cell is well suited for the MOR. Subsequently, the technical challenge for rapid scan FTIR measurement of the irreversible reaction was the development of a protocol to reset the system after each individual rapid scan iteration as well as guaranteeing its stability for longer measurement times.

3.3.4 Spectroelectrochemical Setup and Procedure for Rapid Scan FTIR of MOR

The development of the setup and procedure for an irreversible electrochemical system such as MOR was a crucial element within this thesis and to the rapid scan FTIR measurements presented in Chapter 4. A description of a single rapid scan iteration will be provided first, before the following paragraphs highlight important elements and discuss challenges during the method development.

Setup

Figure 3.6 is a schematic overview of the measurement platform components, their connections and a sequence of events within a single rapid scan iteration. The measurement is controlled by the OPUS software that operates the Bruker VERTEX 70V FTIR spectrometer with a Hyperion 3000 IR microscope at the Mid-IR beamline end station at the CLS. A macro running on OPUS communicates with the FTIR instrument and sends triggers to the USB 6351 X-series multifunction DAC (National Instruments) running a custom written LabVIEW program (Appendix I). The program in turn controls the electrochemical aspects of the measurement via a HEKA PG 590 potentiostat for electrochemical potential control of the SEC as well as potential/current (E/I) measurements. The program also controls a syringe pump and two solenoid valves through TTL signals. The pumps and valves are required to move fresh electrolyte into the cell after each rapid scan iteration. Each rapid scan iteration can be separated into two distinct parts; 1) resetting the electrochemical system between measurements and 2) inducing MOR via E_{step} and acquisition of IR and E/I data.

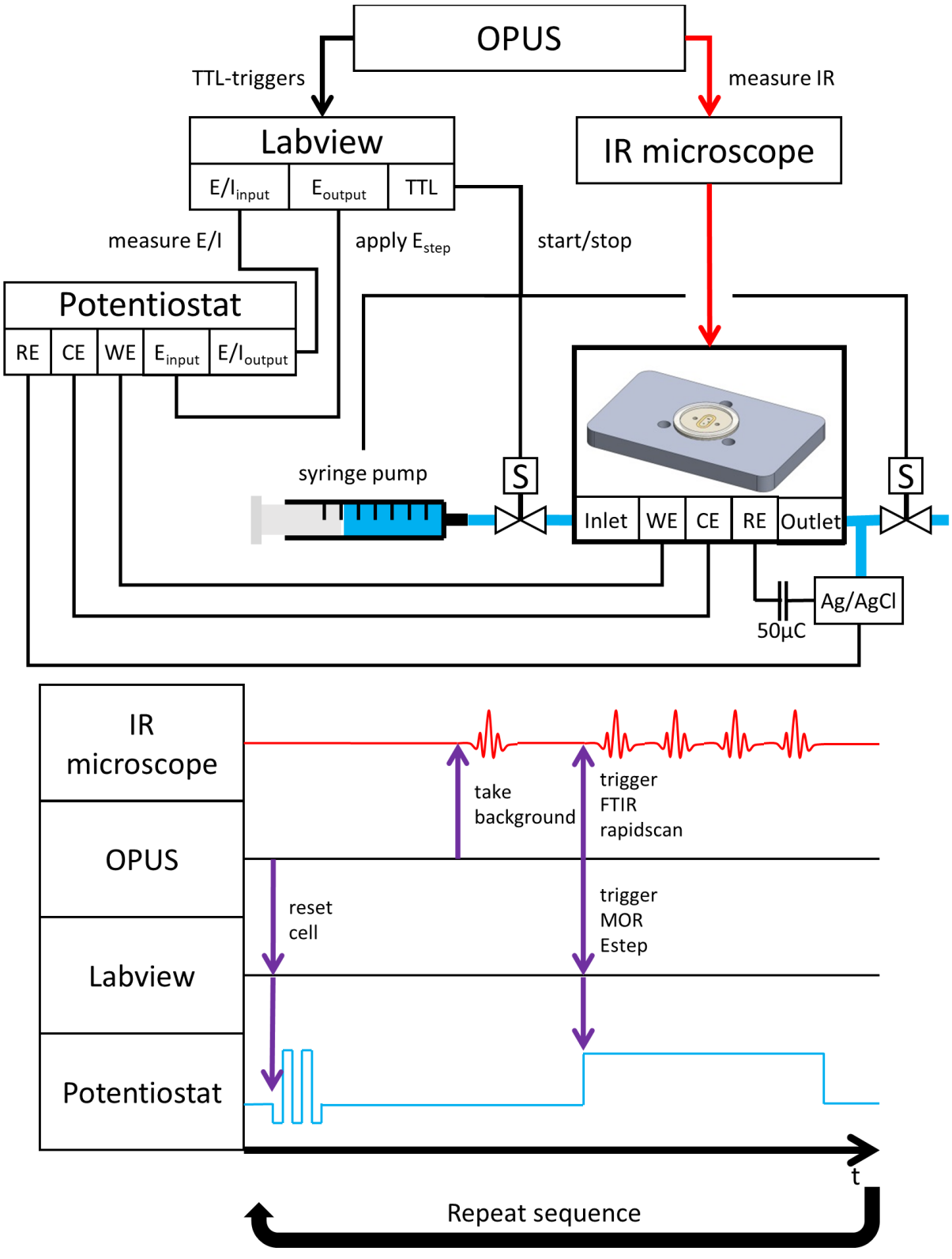

Figure 3.6: Schematic of experimental setup for rapid scan FTIR measurement with SEC. Lower diagram represents the experimental timing sequence.

Electrode and Solution Reset

Unlike the reversible electrochemical system used in earlier SIR-based rapid scan FTIR work by my predecessor, the irreversible MOR reaction requires a reset of both the solution within the cell and a reconditioning of the WE to remove incomplete oxidation products and introduce fresh MeOH reactants into the spectroelectrochemical cell. While conceptually simple, the reset procedure is a critical element within the experimental development as 1) the coaddition of rapid scan spectra will only increase S/N if the reaction conditions are truly identical between each rapid scan iteration and 2) the limited availability of precious synchrotron beamtime necessitates the optimization of the procedure to deliver to the reset within the shortest amount of time.

As mentioned earlier, the MOR is known to generate surface adsorbed CO as an incomplete oxidation product. Poisoning of the Pt catalyst through accumulation of CO at catalytically active sites is well known in the literature and a fundamental challenge for Pt-based DMFC's. To remove the adsorbed CO from the electrode surface, a pulse sequence adopted from Herrero *et al.* work is applied to the surface[30]. The sequence, shown in Figure 3.6, consists of a quick series of potential steps. The potential is alternatively stepped to –0.2 V and + 1.0 V. At + 1.0 V, residual CO on the Pt WE oxidize into CO_2 and desorbs from the surface. The potential steps to –0.2 V reduce any unwanted platinum oxide formed during the high potential. The short pulse duration of 1 s during each potential step limits excessive oxide formation that result in electrochemical roughening of the surface.

After resetting the electrode surface, residual reaction products within the volume of the thin cavity must be removed. Simultaneously, the MeOH concentration must be

refreshed to ensure identical reactant concentration between each measurement. A TTL signal opens the solenoid vales and starts the syringe, injecting fresh electrolyte into the thin cavity from a reservoir at 250 μL/min for 15 s, an amount far exceeding the $\sim$ 6 μL volume of the spectroelectrochemical cell. After pumping and closing of solenoid valves, a wait time is required to allow the solution to reach quiescence. This prevents convective mass transport during the FTIR measurement. Particularly crucial elements for this process are the two TTL-controlled solenoid valves indicated in Figure 3.6 between the syringe pump and the SEC as well as between the SEC and the waste receptacle. Test experiments with the syringe pump and no valves resulted in excessively long wait times of $>$ 5 min for the solution within the cavity to become quiescent. As later experiments in this Chapter utilize 64 scans for coaddition, the total collection time of a single rapid scan FTIR measurement would have exceeded 5 h. Considering a single shift of SIR beamtime at the mid-IR beamline in the CLS is 8 h, only one experiment can be completed within that time frame.

After addition of the solenoid valve, quiescence can be reached within 15 - 30 s depending on pump rate and cavity thickness, reducing the time for each rapid scan iteration to $<$1 min. The difference is likely a result of pressure buildup during pumping due to fluid resistance within the thin cavity. Without the valves, relaxation of this pressure results in residual fluid motion long after the pump has been turned off.

Rapid scan FTIR and Data Acquisition

Once the electrolyte reset is completed, 10 IR background inteferograms are collected while the WE potential is held at 0 V where the MOR is suppressed. After collecting the background IR measurements, OPUS triggers an anodic potential step to +0.7 V which induces

the MOR at the WE. Concurrently, the instrument begins measuring double-sided backward/forward interferograms with 40 kHz mirror velocity and 4 cm^{-1} wavenumber resolution resulting in one complete interferogram being collected every 0.45 s. Faster time-resolution up to 80 ms can be achieved with higher mirror velocity at a cost of S/N, but FTIR results did not warrant such rapid acquisition rates. A simultaneous trigger sent out by OPUS starts the E/I data collection by the potentiostat and DAC. Once both rapid scan and E/I measurements are collected, a single rapid scan iteration is complete. The procedure will be repeated as necessary, so that satisfactory S/N can be achieved by co-adding spectra from individual runs. This required at least 64 rapid scan iterations for the MOR system studied in this Chapter. The collected interferograms are Fourier transformed using OPUS and further processed using a custom written Matlab script (Appendix II).

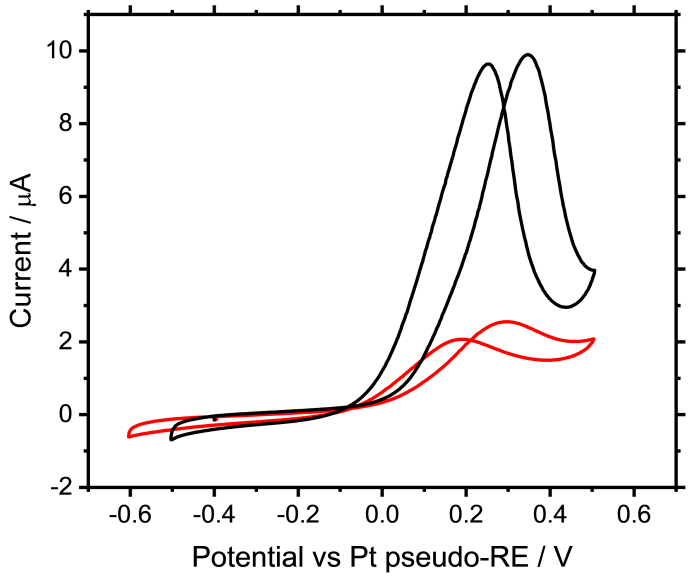

Figure 3.7: CV of MOR on Pt in 0.1 M H_2SO_4 and 1.0 M MeOH within assembled spectroelectrochemical cell at the beginning of an experiment (red line) and 24 h later (black line). The sweep rate was 100 mV/s.

Initial rapid scan FTIR experiments with the setup and procedure described above, showed two issues particular to the Pt-MOR system occurring over longer experimental duration. The two CVs in Figure 3.7 measured 24 h apart show the electrochemical features of the MOR can drastically change over the course of a long experiment. First, the onset of hydrogen evolution at negative potentials, as indicated in the Figure, have shifted from its initial position at -0.6 V to more positive potentials by ∼100 mV. This suggest, that the simple Pt pseudo-reference electrode is unstable over prolonged measurement times. Secondly, the electrocatalytic activity of the Pt WE appears to decrease as the MOR peak current rose by almost an order of magnitude over 24 h. Both processes will cause time dependent changes in the IR measurements and negate the benefits of ensemble averaging. These problems were addressed by further improvements described below.

Potential Stability

The initial choice of Pt wire for the RE is its close resemblance toward the normal hydrogen electrode (NHE), a classic reference electrode used in electrochemistry. In practice, the NHE reference is defined as the potential of a Pt electrode in a 1 M H^+ solution. While the electrolyte system in the SEC with 0.1 M H_2SO_4 anion concentration is not identical to the NHE, pH-dependent potential shifts follow the Nernst equation and equate to +59 mV per pH unit at room temperature. The theoretically known potential coupled with the chemical resistance of Pt towards acidic solution was expected to offer a stable potential, but experiments shown earlier in Figure 3.7 suggest otherwise. The most likely explanation of the potential drift of ∼100 mV over 24 h is the slow autocatalytic conversion of MeOH at the reference potential. While Pt catalysts in DMFC have externally applied overpotential

to induce the MOR, autocatalytic conversion has been reported[32]. Assuming autocatalytic conversion occurs at the Pt electrode, MOR will favor incomplete oxidation products that remain absorbed on the Pt surface. Over the course of several hours, this process could shift the RE potential.

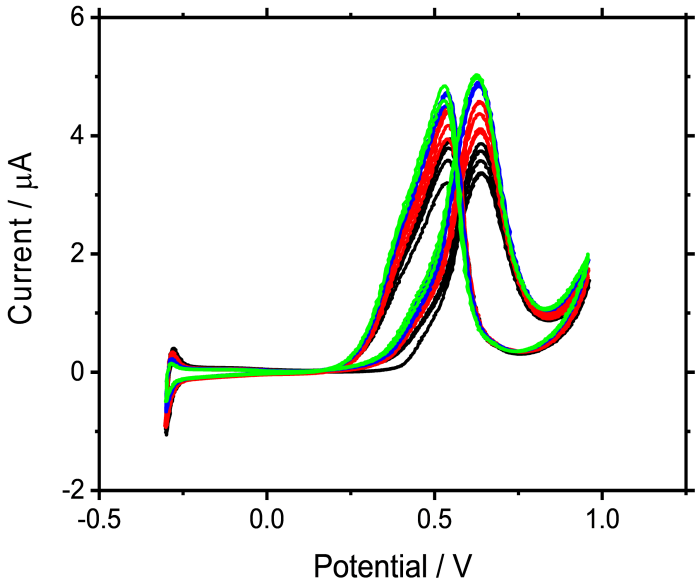

Figure 3.8: CV of MOR on Pt in 0.1 M H_2SO_4 and 1.0 M MeOH within assembled spectroelectrochemical cell at the beginning of an experiment (red line) and 24 h later (black line). The sweep rate was 100 mV/s.

To improve the potential stability, the Pt pseudo-reference electrode was capacitively coupled to an Ag/AgCl reference electrode via a 50 μF capacitor[8]. This Ag/AgCl reference electrode element consists of a small compartment holding an oxidized Ag wire within a saturated KCl solution to provide a stable potential. The reference is placed between the SEC outlet and the solenoid valve as shown in Figure 3.6. A small frit between the reference compartment and the solution within the outlet tubing allows electrical contact between the Ag wire and the SEC without solution exchange. The first iteration of this additional reference electrode was used for the spectroelectrochemical experiment presented

in this Chapter. Measurements over 24 h (Figure 3.8) demonstrate much greater potential stability, decreasing potential shift from ∼100 mV to 20 mV. Experiments in Chapter 4 use an improved reference compartment design with virtually no potential shift by replacing the frit with a three-way valve-based design.

MOR Activity Stability

To better understand the MOR activity increase observed in Figure 3.7 and 3.8, a simulated rapid scan FTIR measurement was used to measure MOR activity changes as a function of rapid scan iterations. To remove any effect of previous experiments on the WE surface, the SEC was repolished with 1 μm diamond slurry. After polishing, a series of simulated rapid scan iteration were applied to the assembled SEC, complete with potential pulses included for CO removal, electrolyte pumping and a potential step to induce MOR. Between each series consisting of 40 rapid scan iterations, a CV is collected (Figure 3.9a) and the respective peak MOR current of each CV is plotted in Figure 3.9b.

The result shown in Figure 3.9b show a drastic increase in MOR current for the initial 40 rapid scan iteration. Afterwards, the MOR peak current increases by ∼5% for every simulated rapid scan experiment before slowing down at the end to <5% over the course of 160 rapid scan iterations. The drastic increase in the beginning is most likely caused by electrochemical cleaning of the surface. Pt is known to accumulate small organic molecules on the surface when exposed to atmosphere. Typical cleaning procedures such as piranha acid or flame annealing before experiments are not possible due to the presence of the surrounding SEC material. The very slight increase of ∼5% at the end of the conditioning stages is likely a result of texturing of the surface due to platinum oxide formation during oxidative removal

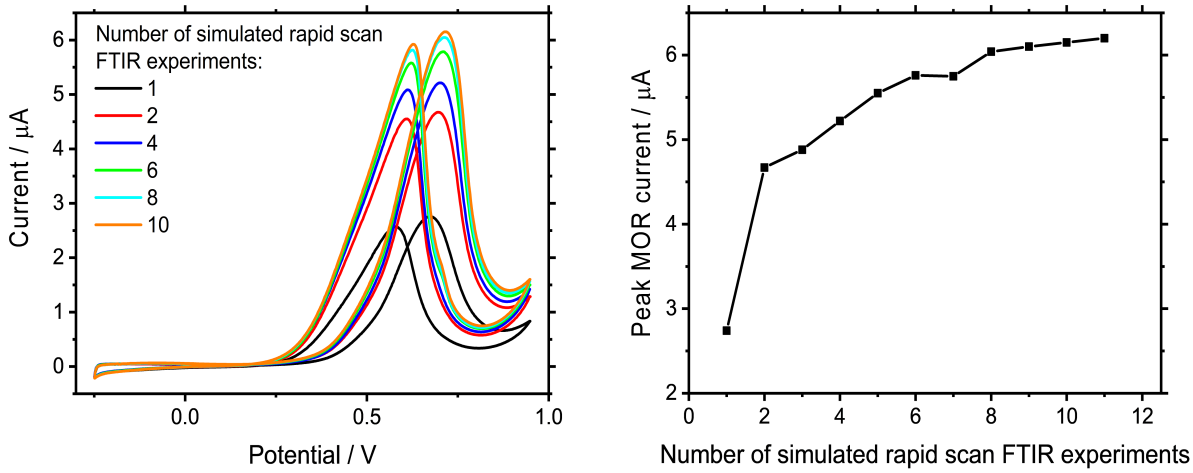

Figure 3.9: (a) CVs in 0.1 M H_2SO_4 and 1.0 M MeOH of the Pt within assembled SEC over the course of 10 simulated rapid scan FTIR experiments. The sweep rate was 100 mV/s (b) shows the change peak MOR current during the positive potential sweep as a function of simulated rapid scan FTIR experiments.

of surface adsorbed CO when resetting the SEC. Short periods of oxide formation followed by rapid reduction roughens the surface and increases the electrocatalytic active surface area. Fortunately, this process appears to taper off over time. The spectroelectrochemical measurement procedure should not include IR measurements made during the initial conditioning of the Pt working electrode. Experimentally, this was achieved by preconditioning the Pt surface through repeated cyclic potential sweeps between -0.2 V to 1.3 V at 50 mV/s for a period of at least 30 minutes before conducting any rapid scan FTIR measurements.

3.3.5 SIR-based Rapid Scan FTIR

Once stability over the entire measurement time can be guaranteed, FTIR-measurements were performed at the CLS using the described spectroelectrochmical setup and procedure. Figure 3.10a shows a representative absorbance spectrum from a rapid scan FTIR measurement at selected times after initiating the MOR with a potential step to +0.6 V. A very strong

absorption peak at 2343 cm^{-1} is seen to clearly increase with time and can be assigned to the complete MOR oxidation product CO_2 in good accordance to the literature[29]. To better represent the time progression of the CO_2 signal, the absorption value at 2343 cm^{-1} is plotted as a function of time in Figure 3.10b. The CO_2 signal shows a linear progression within the first 10 s before a negative deviation from linearity.

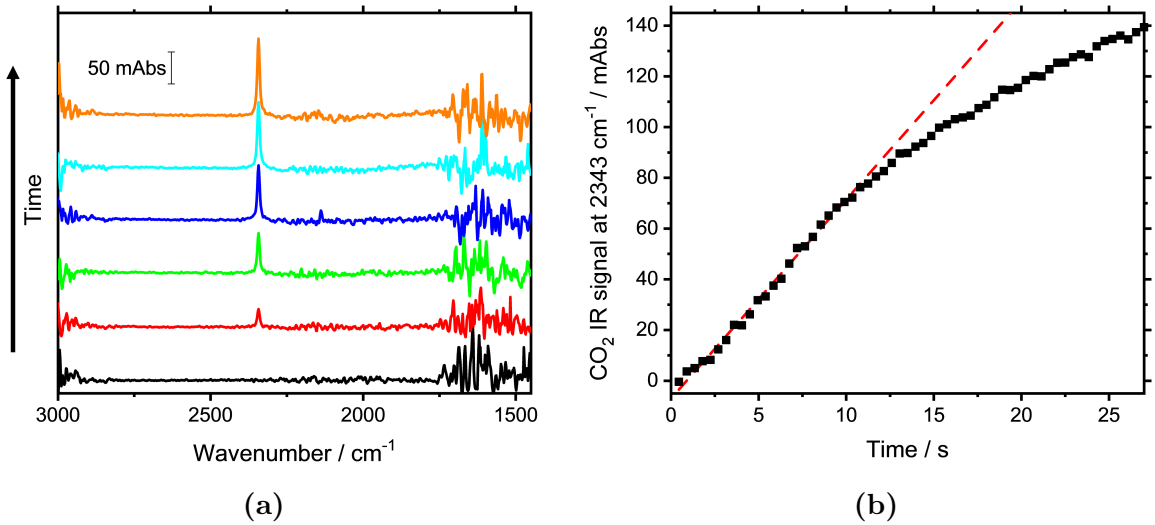

Figure 3.10: (a) Representative rapid scan FTIR spectra (at ∼every 5 s) after inducing MOR through a potential step to +0.7 V showing a clear CO_2 absorption peak at 2343 cm^{-1}. (b) Transient of the CO_2 IR signal at 2343 cm^{-1} with dashed red line representing a linear fit of IR signal within the initial 10 s.

As IR absorbances are proportional to CO_2 concentration, Figure 3.10b suggests CO_2 production and accumulation at a constant rate for the initial 10 s, before a secondary effect is either slowing the rate of CO_2 production or removing CO_2 through mass transport within the thin cavity. Based on simulations which will be described in detail in Chapter 3, the majority of CO_2 produced in the initial seconds will accumulate in the thin cavity between the WE and the CaF_2 window. The linear increase in CO_2 signal is caused by the MOR occurring at a constant reaction rate at the Pt surface. In other words, the production of CO_2 in the thin cavity is kinetically controlled by the MOR reaction rate and the working

electrode is not reactant concentration limited as was the case for the ferricyanide system described by Rosendahl *et al.* The deviation from linearity of the CO_2 signal for time > 10 s can be explained by diffusion losses radially away from the WE into the bulk of the thin cavity. This process is only noticeable at longer times when the IR beam is focused near the center of the WE. However, if the IR microscope is focused near the edge of the WE the deviation can be seen to occur much sooner in the CO_2 transient. This is because diffusion losses start at the edge of the Pt electrode and require time to propagate to the centre.

Beside the strong CO_2 signal, the other species of interest, surface CO as well as the intermediate formic acid and formaldehyde are not visible within the spectrum. Surface adsorbed CO is expected around $1700 - 2100$ cm^{-1} depending on its binding site on the surface. The absence of such signals is likely due to the sub-monolayer coverage of CO (approx. 35 fmol CO for full monolayer[33]) and therefore below our detection limit without a surface-enhancement mechanism such as the AIRES effect relevant to Sun *et al.*'s work[8,9]. The absence of formic acid and formaldehyde is more troubling as measurements at lower overpotential that favor the incomplete MOR into these products were similarly unsuccessful. The aqueous solution in the 20 μm thick cavity possesses enough H_2O absorption within the $1500 - 1750$ cm^{-1} region to absorb almost all the IR signal as seen in Figure 3.11 and the strong background absorption deteriorated all signals < 1500 cm^{-1}. Measurements using D_2O instead of H_2O as the electrolyte solvent were made in an effort to remove the spectral interference from the bending mode of water but, again, no HCOOH or H_2CO signals were detected. The absence of these signals even in the deuterated solution suggest that HCOOH and H_2CO are still below the detection limit. While the molar absorptivity for both species are weaker than CO_2, literature FTIR show the clear presence of HCOOH and H_2CO on

platinum surfaces[26] and should be present within solution according to work by Behm and coworkers[24,25].

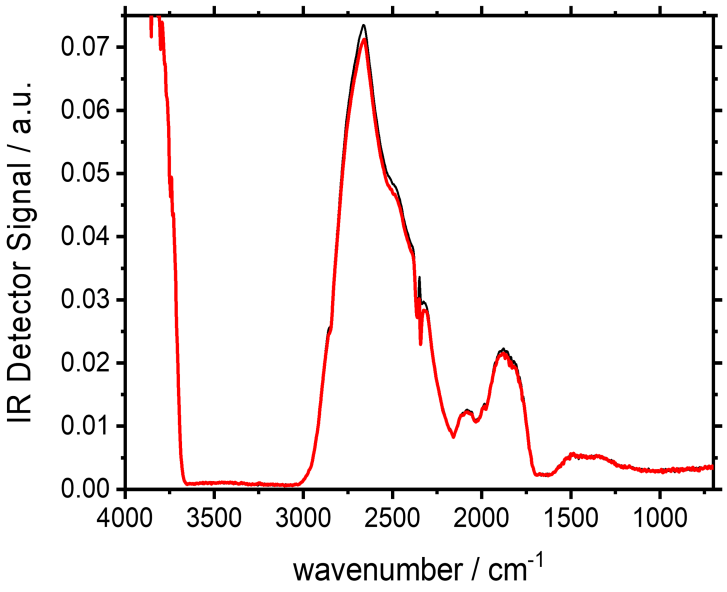

Figure 3.11: Representative single beam IR spectra before (black line) and after (red line) a potential step to +0.7 V.

One explanation for the absence of these intermediates is low IR signals due to the combination of lower IR cross section, stronger background absorption in that wavenumber region and low concentration. Decreasing the cavity thickness of the SEC, typically measured at ~20 μm, could decrease the background absorption within the spectral region of interest, but technical implementation of thinner gasket material proved challenging. A second explanation is the use of a "continuous" Pt electrode compared to the nanodots of Pt on glassy carbon utilized by Behm *et al.*[24,25]. The larger Pt surface increases the probability of HCOOH and H_2CO to reabsorption onto platinum before being fully oxidized into CO_2. Overall, this would imply a very small concentration of reaction intermediates within solution at any given time. Combined with the spectroscopic challenges highlighted above, HCOOH

and H_2CO are likely below the detection limit of the measurement.

3.3.6 Adaptation for Different Electrochemical Systems

While further investigation of solution phase MOR intermediates is obviously unfeasible due to the lack of IR signals, the rapid scan setup and procedure developed in this Chapter can be utilized for different purposes. The CO_2 concentration progression is clearly kinetically limited within the initial seconds. As CO_2 is the complete oxidation product of MOR, it should be possible to track the catalytic activity of the electrode and extract rate information through direct measurement of the product species under *in situ* conditions. The concept of evaluating catalytic activity will be discussed further in Chapter 4.

Looking beyond methanol oxidization, the developed platform and procedure can be utilized for other irreversible electrochemical systems. The measurement platform was easily adjusted to measure diffusion coefficients of the redox couple hydroquinone/benzoquinone by replacing the external reflection SEC with a transmission SEC for diffusion layer mapping. This was the primary focus of Michael Lardner who obtained his MSc in the Burgess group and used many of the technical advances outlined in this Chapter. The hydroquinone/benzoquinone degrades in the presence of oxygen and light and requires influx of fresh electrolyte between rapid scan iterations to guarantee identical starting conditions. The setup, programs and particularly the electrolyte reset protocol devised here were instrumental for time-resolved SIR-based measurements of the effectively "irreversible" hydroquinone/benzoquinone system[34]. Similarly, the rapid scan FTIR platform with small adaptations will be utilized later in Chapter 5 to perform rapid scan FTIR measurement of self assembled ferrocene thiol layers in ATR-SEIRAS configuration.

3.4 Conclusion

The work presented in this Chapter has demonstrated a successful rapid scan FTIR measurement of an irreversible electrochemical system in the form of MOR with SIR. A focus has been the creation of a SEC cell for methanol oxidation, the development of a functional setup and experimental procedure to allow rapid scan FTIR measurement with reliable reset of the electrolyte and electrode surface between individual rapid scan iterations. Resetting the solution has been solved through injection of fresh electrolyte over an automated syringe pump and solenoid valve setup. The accumulation of CO on the WE surface is mitigated through oxidative removal with a short potential step sequence. This however comes at the cost of a slight re-texturing of the surface leading to small catalytic activity increases over a few hours. Potential stability of the measurement is maintained using a capacitively coupled reference electrode configuration consisting of a Pt pseudo-reference electrode within the thin cavity of the SEC and a proper Ag/AgCl reference electrode.

Rapid scan FTIR measurement demonstrated the successful interrogation of the electrolyte above a Pt electrode and the measurement of methanol oxidation into CO_2 with sub-second time-resolution. While the FTIR experiment of the complete oxidation product CO_2 is successful, information regarding the "desorption-readsorption-reaction" through measurement of solution phase MOR intermediates was unsuccessful. The lack on any detectable IR signal from known intermediates could be the combination of strong background absorption of water and low intermediate concentration.

The developed measurement platform was however very successful in rapid scan measurement of a quasi "irreversible" reaction of hydroquinone/benzoquinone, spatial map-

ping of catalytic activity (Chapter 4) and for the measurement of surface absorbed ferrocenethiols (Chapter 6). These results demonstrate the utility of the rapid scan FTIR setup and procedure developed in this Chapter.

3.5 References

[1] Petry, O. A.; Podlovchenko, B. I.; Frumkin, A. N.; Lal, H. The behaviour of platinized-platinum and platinum-ruthenium electrodes in methanol solutions. *Journal of Electroanalytical Chemistry (1959)* **1965**, *10*, 253–269.

[2] Breiter, M. W. On the nature of reduced carbon dioxide. *Electrochimica Acta* **1967**, *12*, 1213–1218.

[3] Zaera, F. New advances in the use of infrared absorption spectroscopy for the characterization of heterogeneous catalytic reactions. *Chemical Society Reviews* **2014**, *43*, 7624–7663.

[4] Bewick, A.; Kunimatsu, K.; Pons, B. S. Infra red spectroscopy of the electrode-electrolyte interphase. *Electrochimica Acta* **1980**, *25*, 465–468.

[5] Osawa, M.; Yoshii, K.; Ataka, K.-i.; Yotsuyanagi, T. Real-time monitoring of electrochemical dynamics by submillisecond time-resolved surface-enhanced infrared attenuated-total-reflection spectroscopy. *Langmuir* **1994**, *10*, 640–642.

[6] Osawa, M.; Yoshii, K.; Hibino, Y.-i.; Nakano, T.; Noda, I. Two-dimensional infrared correlation analysis of electrochemical reactions. *Journal of Electroanalytical Chemistry* **1997**, *426*, 11–16.

[7] Pronkin, S.; Wandlowski, T. Time-resolved in situ ATR-SEIRAS study of adsorption and 2D phase formation of uracil on gold electrodes. *Journal of Electroanalytical Chemistry* **2003**, *550-551*, 131–147.

[8] Zhou, Z.-Y.; Tian, N.; Chen, Y.-J.; Chen, S.-P.; Sun, S.-G. In situ rapid-scan time-resolved microscope FTIR spectroelectrochemistry: study of the dynamic processes of methanol oxidation on a nanostructured Pt electrode. *Journal of Electroanalytical Chemistry* **2004**, *573*, 111–119.

[9] Zhou, Z.-Y.; Lin, S.-C.; Chen, S.-P.; Sun, S.-G. In situ step-scan time-resolved microscope FTIR spectroscopy working with a thin-layer cell. *Electrochemistry Communications* **2005**, *7*, 490–495.

[10] Rosendahl, S. M.; Borondics, F.; May, T. E.; Pedersen, T. M.; Burgess, I. J. Interface for time-resolved electrochemical infrared microspectroscopy using synchrotron infrared radiation. *Review of Scientific Instruments* **2011**, *82*, 083105.

[11] Rosendahl, S. M.; Borondics, F.; May, T. E.; Burgess, I. J. Step-Scan IR Spectroelectrochemistry with Ultramicroelectrodes: Nonsurface Enhanced Detection of Near Femtomole Quantities Using Synchrotron Radiation. *Analytical Chemistry* **2013**, *85*, 8722–8727.

[12] Iwasita, T. Methanol and CO electrooxidation. *Handbook of Fuel Cells* **2003**, *2*, 603–624.

[13] Liu, H.; Song, C.; Zhang, L.; Zhang, J.; Wang, H.; Wilkinson, D. P. A review of anode catalysis in the direct methanol fuel cell. *Journal of Power Sources* **2006**, *155*, 95–110.

[14] Ramli, Z. A.; Kamarudin, S. K. Platinum-Based Catalysts on Various Carbon Supports and Conducting Polymers for Direct Methanol Fuel Cell Applications: a Review. *Nanoscale Research Letters* **2018**, *13*, 410.

[15] Sharma, S.; Pollet, B. G. Support materials for PEMFC and DMFC electrocatalysts—A review. *Journal of Power Sources* **2012**, *208*, 96–119.

[16] Awang, N.; Ismail, A. F.; Jaafar, J.; Matsuura, T.; Junoh, H.; Othman, M. H. D.; Rahman, M. A. Functionalization of polymeric materials as a high performance membrane for direct methanol fuel cell: A review. *Reactive and Functional Polymers* **2015**, *86*, 248–258.

[17] Liu, S. X.; Liao, L. W.; Tao, Q.; Chen, Y. X.; Ye, S. The kinetics of CO pathway in methanol oxidation at Pt electrodes, a quantitative study by ATR-FTIR spectroscopy. *Physical Chemistry Chemical Physics* **2011**, *13*, 9725–9735.

[18] Chen, Y. X.; Miki, A.; Ye, S.; Sakai, H.; Osawa, M. Formate, an Active Intermediate for Direct Oxidation of Methanol on Pt Electrode. *Journal of the American Chemical Society* **2003**, *125*, 3680–3681.

[19] Sakong, S.; Groß, A. The Importance of the Electrochemical Environment in the Electro-Oxidation of Methanol on Pt(111). *ACS Catalysis* **2016**, *6*, 5575–5586.

[20] Chen, D.-J.; Hofstead-Duffy, A. M.; Park, I.-S.; Atienza, D. O.; Susut, C.; Sun, S.-G.; Tong, Y. J. Identification of the Most Active Sites and Surface Water Species: A Comparative Study of CO and Methanol Oxidation Reactions on Core Shell MPt (M = Ru, Au) Nanoparticles by in Situ IR Spectroscopy. *The Journal of Physical Chemistry C* **2011**, *115*, 8735–8743.

[21] Lu, G.-Q.; Crown, A.; Wieckowski, A. Formic Acid Decomposition on Polycrystalline Platinum and Palladized Platinum Electrodes. *The Journal of Physical Chemistry B* **1999**, *103*, 9700–9711.

[22] Park, S.; Xie, Y.; Weaver, M. J. Electrocatalytic pathways on carbon-supported platinum nanoparticles: Comparison of particle-size-dependent rates of methanol, formic acid, and formaldehyde electrooxidation. *Langmuir* **2002**, *18*, 5792–5798.

[23] Xie, R.; Chen, M.; Wang, J.; Mei, S.; Pan, Y.; Gu, H. Facile synthesis of Au-Pt bimetallic nanocomplexes for direct oxidation of methanol and formic acid. *RSC Advances* **2015**, *5*, 650–653.

[24] Chen, Y. X.; Heinen, M.; Jusys, Z.; Behm, R. J. Kinetics and Mechanism of the Electrooxidation of Formic Acid—Spectroelectrochemical Studies in a Flow Cell. *Angewandte Chemie International Edition* **2006**, *45*, 981–985.

[25] Chen, Y.-X.; Heinen, M.; Jusys, Z.; Behm, R. J. Kinetic Isotope Effects in Complex Reaction Networks: Formic Acid Electro-Oxidation. *ChemPhysChem* **2007**, *8*, 380–385.

[26] Chen, Y. X.; Miki, A.; Ye, S.; Sakai, H.; Osawa, M. Formate, an Active Intermediate for Direct Oxidation of Methanol on Pt Electrode. *Journal of the American Chemical Society* **2003**, *125*, 3680–3681.

[27] Chen, Y. X.; Ye, S.; Heinen, M.; Jusys, Z.; Osawa, M.; Behm, R. J. Application of In-situ Attenuated Total Reflection-Fourier Transform Infrared Spectroscopy for the Understanding of Complex Reaction Mechanism and Kinetics: Formic Acid Oxidation on a Pt Film Electrode at Elevated Temperatures. *The Journal of Physical Chemistry B* **2006**, *110*, 9534–9544.

[28] Ye, J. Y.; Jiang, Y. X.; Sheng, T.; Sun, S. G. In-situ FTIR spectroscopic studies of electrocatalytic reactions and processes. *Nano Energy* **2016**, *29*, 414–427.

[29] Fan, Q.; Pu, C.; Smotkin, E. S. In Situ Fourier Transform Infrared-Diffuse Reflection Spectroscopy of Direct Methanol Fuel Cell Anodes and Cathodes. *Journal of The Electrochemical Society* **1996**, *143*, 3053–3057.

[30] Herrero, E.; Wieckowski, A.; Franaszczuk, K. Electrochemistry of Methanol at Low Index Crystal Planes of Platinum: An Integrated Voltammetric and Chronoamperometric Study. *The Journal of Physical Chemistry* **1994**, *98*, 5074–5083.

[31] Mathiyarasu, J.; Remona, A. M.; Mani, A.; Phani, K. L. N.; Yegnaraman, V.; Phani, M. K. L. N. Exploration of electrodeposited platinum alloy catalysts for methanol electrooxidation in 0.5 M H2SO4: Pt-Ni system. *Journal of Solid State Electrochemistry* **2004**, *8*, 968–975.

[32] Batista, B. C.; Sitta, E.; Eiswirth, M.; Varela, H. Autocatalysis in the open circuit interaction of alcohol molecules with oxidized Pt surfaces. *Physical Chemistry Chemical Physics* **2008**, *10*, 6686–6692.

[33] Steckel, J. A.; Eichler, A.; Hafner, J. CO adsorption on the CO-precovered Pt(111) surface characterized by density-functional theory. *Physical Review B* **2003**, *68*, 85416.

[34] Lardner, M. J.; Tu, K.; Barlow, B. C.; Rosendahl, S. M.; Borondics, F.; Burgess, I. J. Quantitative analysis of electrochemical diffusion layers using synchrotron infrared radiation. *Journal of Electroanalytical Chemistry* **2017**, *800*, 184–189.

Chapter 4

Spatial Screening of Electrocatalytic Activity for Methanol Oxidation on heterogeneous PtNi Electrodes

4.1 Introduction

Across multiple research fields, various light-based spatial imaging techniques have emerged as powerful characterization tools that offer insight into various molecular, structural and electronic heterogeneities and their spatial distribution within samples based on the wavelength of the selected light. For infrared light, IR microscopy has emerged as a powerful tool for chemical imaging on more delicate samples such as biological systems due to its excellent high sensitivity and non-destructive nature. The key element behind many imaging applications is the focal plane array (FPA) based IR detector which can be coupled to an IR microscope and used to image chemical composition with approximately micrometer resolution. While effective in imaging large sample areas at once, FPA detection comes with two crucial limitations for time resolved FTIR. First, all IR sensitive detectors are power-based detectors and dividing the total IR power collected by a microscope onto an array detector inherently leads to increased noise levels on each pixel compared to having the light

transduced by a single element of equivalent aggregate area. This is particularly problematic for transmission or transflection experiments in aqueous media where strong, broad-band absorption of water greatly reduces the photon throughput. The secondary limitation is the long read-out time on commercially available FPAs that limits time-resolution to multiple seconds-minute range.

Nevertheless, the high brilliance of SIR offers a secondary approach to gain spatial information using single element detectors. By focusing the SIR beam near its diffraction limits, time-resolved IR signals are confined to a narrow measurement spot. By mechanically moving the sample and performing time resolved FTIR measurement with a single-element MCT detector at different positions, spatial imaging can be achieved, albeit with much poorer spatial resolution. Contemporaneous work within the research group successfully demonstrated this concept for direct measurement of diffusion fronts within solution and allowed extraction of the diffusion constant of a simple redox model system[1]. In this chapter, time-resolved spatial FTIR mapping will not only be applied to an irreversible electrocatalytic system but utilized to map electrocatalytic activity with the aim to extract qualitative rate information of heterogenous catalytically active metal surfaces.

Building upon the rapid scan FTIR for the MOR developed in Chapter 3, Chapter 4 will focus on its utilization as a measurement platform for spatial mapping of electrocatalytic activity on heterogenous electrodes. This is comprised of three parts, 1) production of a PtNi alloy, 2) SIR-based mapping of its catalytic activity and 3) simulation work to confirm the qualitative nature of the methodology. The chapter will end with an outlook on improving the measurement technique using lithography.

4.2 Background

4.2.1 Methanol Oxidation on Pt-based Electrodes

As previously highlighted in Chapter 3, from a research perspective, the application of methanol (MeOH) oxidation on Pt electrodes as a viable energy source in the form of DMFCs is primarily hindered by two challenges[2]: The first one is the accumulation of CO intermediates on Pt catalyst. Due to its high affinity for metal centres through π back-bonding, incompletely oxidized CO can remain at catalytic active sites and block further conversion at its location, effectively poisoning the Pt catalyst. The result is a loss in overall current generated from the MOR and a decrease in efficiency. The second challenge is the heavy reliance on expensive Pt for breaking C-H bonds that leads to high costs for catalytic electrode materials; a factor that strongly affects the economic viability of DMFCs.

Aiming to improve the MOR reaction, binary PtRu alloys were initially suggested as superior electrocatalysts[3,4]. The inclusion of Ru lowers overpotentials (the potential, in excess of the thermodynamics reaction potential, required to drive an electrochemical reaction) and extends the lifetime of the catalyst. The surface Ru strongly promotes the oxidative removal of CO[5]. The oxyphilic nature of the Ru metal provides a source of surface adsorbed OH even in acidic environments[6]. The presence of nearby OH allows CO, that would otherwise block the catalytic site, to fully oxidize to CO_2. While several earlier implementations of PtRu for MOR exist[7–10], Gasteiger *et al.*[11] provided the first qualitative study into the mechanistic importance of the Pt:Ru ratio through their experiments on bulk PtRu electrodes with well characterized surface Ru concentration. With more precise knowledge of Pt:Ru

surface ratios, their work suggested an optimal composition of 10% surface Ru, a balance between maximizing the dehydrogenation reaction sites of Pt and inclusion of sufficient Ru for full oxidation of partial oxidation products.

While this early research addressed the first challenge of CO poising, the second challenge of high cost for commercial application is barely improved through Ru inclusion. Ruthenium easily matches platinum prices, resulting in similar high material cost for construction of electrocatalytic electrodes for DMFC. Within the last decades considerable research effort has been invested into designing Pt-based catalyst for MOR with more abundant metals such as Ni, Co, Cu of similar oxyphilic nature[12]. The move away from Ru however, does come at the cost of material stability in the acidic environments commonly used for MOR. Removal of the secondary metal under operational conditions changes the performance of the material and in the worst case, can cause a complete breakdown of the electrode. An optimal concentration of bulk versus surface composition of Pt_xM_{1-x} has been the aim in many, and often conflicting, studies within the literature[13]. One complication due to acidic leaching of electrode material, is that the corresponding increase in electrocatalytic active surface area (ECSA) must be carefully considered before evaluating effects of the secondary metals on MOR.

MOR research also further expanded the compositional options into tertiary[14], quaternary[15,16] and even quinary combinations[17]. Fine tuning the d-band electron density of the Pt is an important parameter for tuning the catalytic properties of Pt reactive sites for dehydrogenation of MeOH or decreasing its affinity for chCO adsorption to minimize poisoning[18]. The optimization of mixed metal catalysts is further complicated as application focused DMFC research relies on thin film or nanoparticle electrocatalysts. Transitioning into

nanometer size regimes introduces additional variables such as size, shape, crystallography, surface versus core segregations and various electronic effects. Optimization of this wealth of variable space for binary or higher order heterogeneous catalyst is highly challenging. Even for binary bulk, electrodes, maximizing heterogenous electrocatalytic activity requires a balance between increased ECSA, improved oxidation of CO through surface oxyphilic metal site and ensemble effect of the alloy. The challenging nature of catalyst material optimization is by far not isolated to DMFCs but extends to virtually all heterogenous electrocatalytic reactions. To alleviate the research resource demands, recent years have seen an increased interest in high-throughput combinatory screening methods to more effectively tackle these multivariable optimization challenges.

4.2.2 Combinatory Screening for Electrocatalytic Activity

Combinatory screening techniques aim to minimize time-consuming characterization for multiple material compositions through parallel assessment. After its introduction into the area of fuel cells by Redding *et al.*[19], a variety of methodologies have been developed to produce increasingly larger arrays of compositions[20].

Most commonly, sputtered[14,21] or inkjet printed[22,23] libraries are deposited onto conductive substrates. For sputtered libraries, one method to produce varied catalyst composition is to selectively mask different areas of the substrate during sputtering process[14,24]. A secondary method utilizes inherent gradations within the sputtering process, such as sample position in regard to the sputter head, to deposit metal layers heterogeneously onto the surface. Overlap of two or more gradients of different metals creates a matrix with variable binary or higher order compositions[25]. In inkjet printing methods, metal components are

suspended in a liquid phase and mixed into solutions with different metal concentrations that are "printed" onto a substrate[19]. Subsequent drying and annealing removes the organic and liquid component of the ink, leaving behind various composition of metals. One can change the concentrations of the initial metal "inks" during the printing process such that a variety of compositions can be quickly transferred onto a suitable substrate.

Once extensive libraries are created, evaluation of the performance of individual compositions needs to be performed through an experimental methodology that ideally allows for parallel screening to reduce measurement time. If library elements are individually addressable, traditional electrochemical measurement methods that assess catalytic efficiency through voltage-current relationships can be utilized to simultaneously evaluate the entire library[14,21]. Alternatively, direct or indirect measurement of reaction components provide possible avenues for evaluation of catalytic performance. Scanning electrochemical microscope techniques have been proven to be very useful in measuring electrocatalytic currents generated at individual library elements under *in situ* conditions in rapid succession[26]. Optical methodologies are attractive as they can allow parallel assessment without individual electrical connections[22,27,28]. Initial combinatorial screening of electrocatalyst libraries involved the use of pH sensitive fluorescence markers to highlight catalytic activity through increased light signals[28]. A drawback of using fluorescence probe molecules is their possible perturbation of catalytic reactions and their limitation to reactions that occur with certain pH ranges. Other optical methods involve measurement of bubble development using charge-coupled devices or visible lasers[27]. Bubble detection has been applied to the optimization of water splitting catalysts and can be extended to other systems by monitoring bubble development on sacrificial anodes connected to library elements[22]. While these optical methods excel

in speed and quantity of parallel assessment, a major drawback is limited chemical sensitivity compared to the potential chemical information that can be derived from spectroscopic methods.

In principle, infrared spectroscopy allows one to track changes in product distribution with exquisite chemical sensitivity. As a purely optical technique with low intensity light, perturbation of the electrochemical reaction and solution are minimal. To demonstrate proof-of-concept, we intended to adapt the methodology described in Chapter 3 for irreversible electrocatalytic MOR on Pt. A key challenge to this goal was the creation of a compositional library and the development of a measurement protocol to extract electrocatalytic rate information from it.

An on-going issue in combinatory screening of electrocatalysts is variance in performance of libraries based on their production methodology. For example, Strasser's combinatory screening results for PtRu suggested 12% Ru for maximum MOR performance[24], but the combinatory screening studies by Tague *et al.* on an exhaustive binary Pt_xM_{1-x} library suggests an optimal loading of 27% Ru[13]. Surface texture differences that alter MOR performance can be present even when both studies utilize magnetron sputtering. Supplementary methods such as X-ray photoelectron (XPS), Auger electron (AES) and X-ray diffraction spectroscopy (XRD) are required to determine the preferential surface composition and crystallography respectively. Cooper and McGinn in their combinatory screening work of MOR on tertiary PtRuW and PtRuCo catalyst present their result in context of various optimal catalyst compositions determined by other research groups that have Pt-content ranging from 55 - 95% and 30 - 70%[21]. The poor agreement between the results strongly highlighted the need for more thorough characterization of each library before definitive conclusions can be

asserted from analyzing electrocatalysis results.

Despite variance between reports by different groups, the development of Pt-based electrode libraries remains particularly interesting[29], as Pt is not only the key element for energy related electrocatalytic reactions such as fuel (methanol, ethanol, formic acid etc.) oxidation reactions, the oxygen reduction reaction[30,31], and hydrogen evolution reaction[27], but also in the electrocatalytic conversion of multiple small organic molecules for industrial processes[32]. As discussed above, reduction of Pt content is primarily driven by cost incentives and the fact that Pt_xM_{1-x} catalysts with 3d transition metals such as Fe, Ni, Co, Cu have been reported to improve overall performance compared to pure Pt[18,33]. The drive to optimize catalyst activity versus material cost lead to the development of nanoparticle or thin film catalyst materials with increasingly optimized electronic effects[34] and surface structure/composition[31,35]. Comparison between different nanocatalysts however can be challenging due to overlap of multiple reaction promoting effects. To minimize this variance occurring on thin films and nanoparticles, initial studies of electrochemical reaction mechanism often use bulk electrodes with well characterized surface structure. This more "ground up" research approach to optimize electrochemical processes occurs through the study of bulk electrodes with well characterized surface and electronic properties to understand their individual effect on the catalytic activity. Similarly, recent computational studies on the MOR reaction mechanism[36] on PtNi showed the benefit of first examining bulk electrode surfaces to reduce secondary effects before transitioning to thin films or nanoparticle systems. While studying individual bulk electrode compositions is demonstrably beneficial it is very costly in terms of both material and time and becomes impractical. For example, painstaking mechanistic work on well characterized PtRu bulk electrodes by Gasteiger[11] limited them to five samples

of different compositions.

Looking beyond traditional methodologies for generating electrocatalyst library, research into intermetallic diffusion for alloy fabrication offers an alternative way to create a single bulk metal piece with a varied-compositional library. In this approach, the effective diffusion coefficient of two metals is determined through thermal annealing at high temperature below the melting point of either metal. The thermal energy mixes the metal species near the interface of two initially separated pieces to create an interdiffusion layer. Divya *et al.*[37] show heterogenous Pt_xNi_{1-x} and Pt_XCo_{1-X} alloys with a near linear gradient from 100% to 0% Pt within a monolithic metal piece is possible. The controlled change in composition along the gradient allows for evaluation of multiple bulk compositions within a single sample. Karunaratne and Reed provide a theoretical description of the diffusion process under heating[38]. The diffusion for a system such as Pt_xM_{1-x} upon thermal annealing is based on the Fick's second law:

$$\frac{\partial C_M}{\partial t} = \frac{\partial}{\partial x}\left(D_M \frac{\partial C_M}{\partial x}\right) \tag{4.1}$$

In Equation 4.1, the variable t, C_M and D_M are the annealing time, metal concentration and diffusion coefficient of the metal in the second metal based on the annealing temperature respectively. A key aspect for combinatory screening purposes is the fact that the length of the interdiffusion zone that provides a varied-composition gradient is proportional to the square-root of the annealing time. For practical purposes, the size of the compositional library of Pt-M is limited to several hundreds of micrometers for reasonable annealing times of 24 h to a few days. It is important to note that evaluating the electrocatalytic per-

formance of the resulting gradient alloy using traditional current-potential relationships can only provide the average response and spectroscopic or other, spatially resolved techniques are needed to determine electrocatalytic performance along the gradient. Indeed, the dimension of the composition gradient is almost ideal for SIR-based spectromicroscopy and the spectroelectrochemical methodology developed in Chapter 3. To reiterate, the high brilliance of SIR allows for spatial resolution of 20 μm while retaining the IR advantages compared to other spectroscopic or optical screening options. It would, therefore, seem appealing to adopt SIR-based electrochemical spectromicroscopy to study heterogenous bulk electrode libraries for electrocatalysis applications.

4.2.3 Mass Transport in Thin Cavity Spectroelectrochemical Cells

As it will be developed below, it is important to realize that the electrochemical reaction occurring at a particular point along the PtNi gradient is coupled to the same electrochemical reaction occurring at a different rate on nearby regions of the surface. In other words, reaction products produced at one position along the alloy can diffuse through solution into the electrolyte volume above a different PtNi composition. The spatiotemporal overlap of adjacent diffusion zones is important to model in order to assess the time and spatial scales which may perturb the analytical measurements described below.

$$\frac{\partial C_i}{\partial t} = D_i \nabla^2 c_i - \nu \nabla C_i - \frac{z_i F}{RT} D_i C_i \nabla \phi \tag{4.2}$$

For an electrochemical system, mass transport within the aqueous electrolyte is described by an alternative expression of Fick's second law of diffusion shown in Equation 4.2.

The equation describes the change in concentration C_i of a chemical species i through the three main methods of mass transport within an electrolyte environment (diffusion, convection and migration). The first term describes the diffusion for a species due to concentration gradients within the solution and depends on its diffusion coefficient D_i. The second term describes the conventional mass transport between areas of different concentration and depends on the velocity v of the solution. The last term describes the electrostatically driven migration of charged species within solution, which depends on charge of the chemical species z_i, its diffusion coefficient, the temperature T of the environment and the electric potential ϕ.

The rapid scan methodology developed in Chapter 3 measures FTIR spectra after quiescence of the solution is achieved, removing convection from mass transport consideration. As both reactant and products are neutrally charged, mass transport through migration can also be negligible. The main mass transport consideration remaining is concentration gradient driven diffusion. Purely diffusion-driven mass transport has been demonstrated to be a good fit between simulation models and experimental SIR results within the groundwork by Rosendahl *et al.*[39]. Later work utilized diffusion simulation not only as confirmation for IR results, but to extract diffusion coefficients from measurement of the diffusion fronts within electrolytes[1,40].

In the context of this chapter, diffusion simulations are crucial to understand the correlation of time-resolved SIR signals with catalytic activity. Unlike the homogenously active Pt electrode in Chapter 3, spatial FTIR mapping should show catalytic "hotspots" on the PtNi electrode related to the different electrocatalytic productions of CO_2 based on its compositional heterogeneity. As the IR analytical signal corresponds to the accumulation

of CO_2 at different measurement positions along the Pt-gradient, a more detailed analysis of lateral diffusion (parallel to the electrode surface) between different catalytically active positions is vital for the interpretation of measurement results.

4.3 Experimental Methodology

4.3.1 Reagents and Solutions

H_2SO_4 (ACS grade, Fisher Scientific), methanol (HPLC grade, Fisher Scientific), $NiSO_4 \bullet 6H_2O$ (98%, Alfa Aesar), $NiCl_2 \bullet 6H_2O$ (98%, BDH Chemicals Ltd), H_3BO_3 (>99%, Alfa Aesar) were purchased and used as received. All aqueous solution were created using Milli-Q water (> 18 MΩ cm).

4.3.2 Electrochemistry and Binary Alloy Electrode Creation

All purely electrochemical measurements were performed in a standard three electrode configuration using a HEKA PG 590 potentiostat. All electrochemical potentials within this chapter are measured against Ag/AgCl, a saturated KCl reference electrode.

While the creation of the binary alloy electrode will be further elaborated upon within the discussion section of this chapter, this section will provide a brief summary of the experimental steps and parameters during production. The plating experiments were carried out in a heated electrochemical cell connected to a water bath for consistent temperature condition. Nickel plating was performed by electrodepositing a nickel layer onto one side of a Pt-foil using a Watts nickel plating bath (1 M $NiSO_4 \bullet 6H_2O$ + 0.2 M $NiCl_2 \bullet 6H_2O$ +

0.5 M H_3BO_3) with a constant current (1 mA/dm^2) for various times (typically hours) at constant temperature (55° C). To prevent deposition on parts of the Pt foil, and to enhance even deposition, an epoxy mask is applied to the foil. Afterwards the foil is thoroughly rinsed using Milli-Q water. Annealing at 1100° C for 96 hours in a reducing atmosphere (Ar + 5.22% H_2, Praxair) leads to metal inter-diffusion. Annealed electrodes were cooled slowly over 12 h to room temperature. To expose the heterogenous PtNi concentration gradient, electrodes were embedded in resin epoxy and polished. The original edges of the PtNi foil were removed this way to reduce the inhomogeneities of Ni-plating due to edge effects and faults in the original Pt-electrode. Alloys were characterized with wavelength dispersive X-ray spectroscopy (WDS) before further construction. Still embedded into the resin, the PtNi electrode were cut into smaller pieces of heterogeneous PtNi electrode with approximately 300×500 μm size. These substrates were used in electrochemical testing in bulk electrode cells and built into spectroelectrochemical cells for SIR experiments.

4.3.3 Characterization of PtNi Alloy

As electrocatalytic reactions occur at the heterogenous metal/liquid interface, the catalytic activity of a material is strongly affected by its surface composition. For the later discussion of the MOR activity of the PtNi alloy electrodes, it is therefore vital to characterize both its bulk and surface composition. To this end, wavelength dispersive X-ray spectroscopy is utilized to determine the bulk composition of the alloy, while the more surface sensitive Auger electron spectroscopy (AES) provides information on the surface composition. It should be noted that electron probe analysis of the PtNi electrode were performed externally. The information below is provided by the individual facilities and these paragraphs are excerpts

from the published work detailing the results of this chapter[41]:

Electron probe microanalysis was conducted on the Cameca SX-100 microanalyzer at the Advanced Microanalysis Centre of the Saskatchewan Research Council. Each alloy was analyzed for Pt and Ni using wavelength dispersive spectrometers fitted with large area analyzer crystals: LPET for Pt M_α and LLIF for Ni K_α. Each element was analyzed for 30 seconds on peak and 15 seconds for each high and low background with a focused electron beam (<100 nm) at a nominal beam current of 20 nA and an accelerating potential of 20 kV. Raw X-ray counts were converted to concentration using the phi-rho-Z ($\phi - \rho - Z$) correction method of Pichou and Pichoir by comparison to 99.9% pure metal primary standards[42]. A secondary Pt standard was analyzed at the beginning of each run to ensure accuracy.

Auger electron microscopy measurements were carried out using a JAMP-9500F Auger microprobe (JEOL) at nanoFAB, University of Alberta. The instrument is equipped with a Shottky field emitter that produces an electron probe diameter of about 3 - 8 nm at the sample. The accelerating voltage and emission current for both, the SEM and Auger imaging were 15 kV and 8 nA, respectively. The working distance was 24 mm. The sample was rotated 30 degrees away from the primary electron beam to face the electron energy analyzer. M5 lens with 0.6% energy resolution was used for the Auger spectroscopy and imaging. Elemental quantification was achieved by manually selecting peak (Hi) and background intensities and pre-defined elemental sensitivity factors, Z_i (where i = Pt, Ni). Atomic percentages (AP_i) are calculated using the following Equation 4.3.

$$AP_i = \frac{\frac{H_i}{Z_i}}{\sum_i \frac{H_i}{Z_i}} \times 100\% \tag{4.3}$$

4.3.4 Spectroelectrochemical Cell and Setup

New spectroelectrochemical cells, shown in Figure 4.1 are based on the earlier iterations described in detail in Chapter 3 and adapted for the new experimental requirements. The most significant change is the inclusion of two individually addressable WEs. One is the heterogenous PtNi electrode described above and the second is a pure Pt electrode (0.25 mm Pt wire) for comparison and troubleshooting purposes. To compensate for the inclusion of two WEs, the Au CE was redesigned to have a more elliptical form with a WE at each of its two foci.

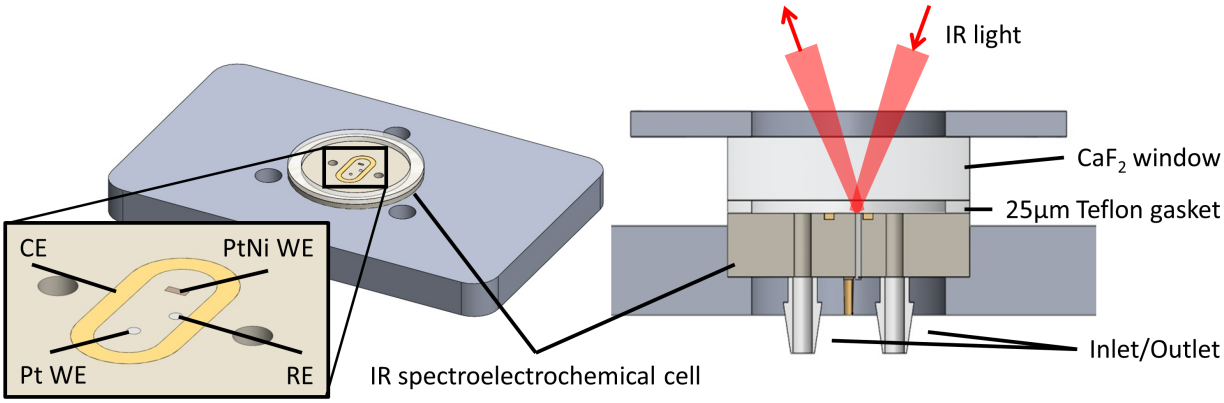

Figure 4.1: Schematic of spectroelectrochemical cell with heterogenous PtNi working electrode.

The spectroelectrochemical measurements are based on experimental procedures developed in Chapter 3. Measurements are all performed using a Bruker VERTEX 70V FTIR spectrometer with a Hyperion 3000 IR microscope at the Mid-IR beamline at the CLS. The high brilliance mid-IR beam from the synchrotron was focused onto the sample cell by a 15× objective and a 20 μm×80 μm blade aperture within the IR microscope. The long axis of the aperture is oriented perpendicular to the PtNi concentration gradient

of the working electrode. Controlled mechanical translation of the sample stage allows for selected measurement positions along the PtNi concentration gradient with spatial resolution defined by the short dimension (20 μm) of the blade aperture. FTIR signals are collected in reflectance mode using a 100 μm narrowband MCT detector. The FTIR interferometer was operated at a mirror velocity of 40 kHz and 4 cm^{-1} resolution that allowed collection of a single double-sided interferograms with $\sim$0.45 s time resolution. IR spectra data were collected using Bruker's OPUS software and processed using the software's internal Fourier-transform algorithms. Rapid scan FTIR data are collected using a custom written macro for the Bruker OPUS software before being subjected to further data processing using custom written Matlab macros.

To coordinate spectroscopic and electrochemical measurement, Figure 3.6 in Chapter 3 shows a detailed schematic of the interface between different instrumentation as well as the timing sequence developed in Chapter 3 and utilized for all MOR experiments in this chapter. The spectrochemical cell is assembled according to Figure 4.1 and placed onto the IR microscope stage with the working electrode in the focus of the IR beam. The internal Pt reference electrode of the cell is capacitively coupled to an Ag/AgCl reference electrode via a 50 μF capacitor for greater potential stability as discussed in Chapter 3. Liquid components are controlled through the syringe pump and two solenoid valves that allow injection of fresh electrolyte into cell as well as removal of previous reaction products into a waste container between rapid scan iterations. The solenoid valves are placed between pump-cell and Ag/AgCl reference-waste to decrease convective relaxation after liquid movement as determined in Chapter 3. Potential control and acquisition of E/I data of the electrochemical cell occurred through a HEKA PG 590 potentiostat. To interface electrochemical components with FTIR

software, potential control, electrochemical data recording and coordinate timing, a custom written program in Labview is used in combination with a USB 6351 X-series multifunction DAC (National Instruments). Fast digital channels between OPUS and the DAC allow for precisely synchronized potential steps and time resolved FTIR measurements.

4.3.5 Experimental Procedure for Spatiotemporal Rapid Scan FTIR

Each measurement of a rapid scan FTIR experiment within this chapter follows an identical experimental procedure. Before each experiment, the electrodes of the spectroelectrochemical cell were mechanically cleaned by polishing with 1 μm diamond slurry, before being rinsed with copious amounts of Millipore water. After assembly of the cell and setup for FTIR described above, working electrodes were further electrochemically cleaned through continuous potential cycling in 1 M MeOH and 0.1 M H_2SO_4 solution between -0.25 – 1.3 V for a minimum of one hour until a stable CV was observed.

Once static FTIR measurements confirmed methanol oxidation on the PtNi working electrode, a series of rapid scan FTIR measurements were performed at different positions along the PtNi gradient of the heterogeneous alloy electrode. Each measurement at a single position consisted of multiple rapid scan sequences. Chapter 3 provides a more in-depth description of the sequence design. In-short: a single sequence consists of a reset portion where surface adsorbed CO is removed from the working electrode and the cell volume is exchanged with fresh electrolyte to remove reaction products formed during the previous sequence. After convective relaxation, the second measurement portion starts with background FTIR spectra measurement before a potential step (E_{step}) is applied to the electrode, inducing methanol oxidation. Simultaneously, a rapid scan FTIR measurement is performed to measure the CO_2

concentration at a specific measurement position. The sequence is completed by stepping the electrode potential back to 0 V to stop the methanol oxidation reaction, before being repeated to increase S/N levels by Nyquist averaging. Once enough rapid scan sequences are collected (usually 128 - 256 repeat sequences) at a measurement position, the IR beam spot is moved to a new position along the PtNi gradient and the rapid scan FTIR measurement is repeated. A total of 10 measurement positions were measured, covering the range of initial Ni content from 0 – 55% with each 20 μm wide beam spot position covering $\sim$6% concentration change.

4.4 Discussion

4.4.1 Development of Heterogenous Pt-based Alloy Electrodes

A key aspect of combinatorial screening platforms for investigating electrocatalytic activity is implementing a large library of metals within a single experiment. The general concept, as shown in Figure 4.2, is to electroplate the secondary metal onto a metal foil before annealing the resulting sample at high temperature. By selecting a high temperature below the melting point of either metal, a concept known and used in literature[37,38], metallic interdiffusion between the metals can occur. This results in a binary phase at the original metal interfaces with varying, but continuous change of metal A to B, which can subsequently be embedded into a spectroelectrochemical cell.

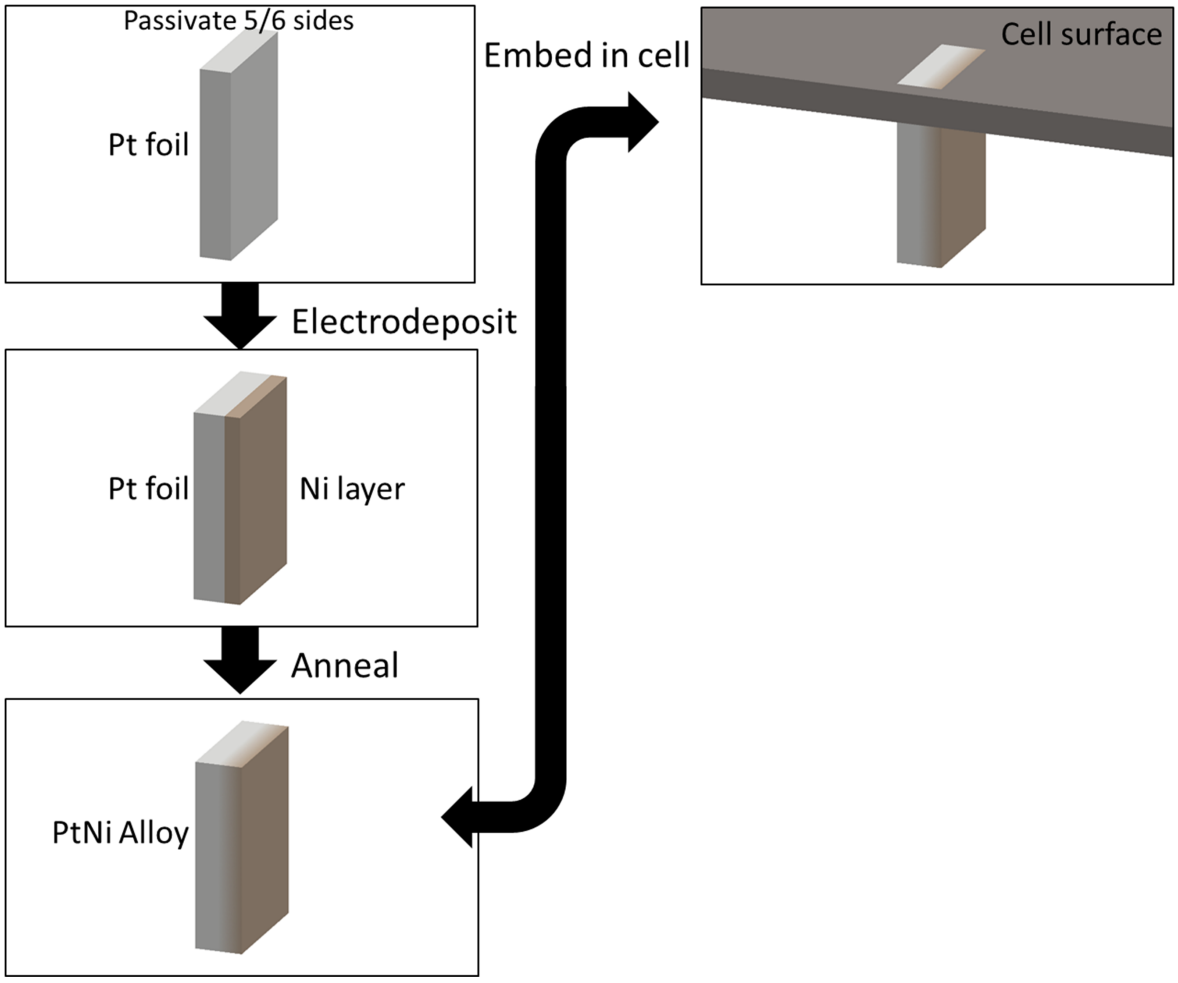

Figure 4.2: Conceptual procedure for creation of heterogenous PtNi alloy through a combination of electrodeposition and annealing at high temperature.

Ruthenium Electroplating on Platinum

Initial attempts to create heterogeneous electrocatalytic electrodes were aimed at fabricating PtRu electrodes. Theoretically, PtRu would be an ideal alloy for proof-of-concept as PtRu alloys have shown increased catalytic activity for methanol oxidation compared to Pt while being less susceptible to degradation due to metal leaching in acidic media compared to 3d metals. Successful implementation would have allowed analysis of the initial result with negligible surface concentration of the metals and topography changes due metal leaching during experimental conditions. Unfortunately, attempts to electroplate ruthenium using literature procedures were discouraging. Multiple ruthenium plating experiments using literature method[43] onto platinum foil electrodes resulted at best in thin sub-micron layers of the secondary metal.

As no literature examples of Ru electrodeposition with layer thicknesses in micron ranges have yet to be reported, alternative options were considered. Development of a new Ru electrodeposition method far exceeds the scope of a proof-of-concept study and alternative methods using Ru metal foils, or Ru deposition through physical deposition methods were cost prohibitive for initial experiments. The best choice was utilizing a known electrodeposition method for a similarly oxyphilic, but less noble metal such as nickel. While surface metal concentration changes had to be considered for discussion of experimental results, nickel electroplating is a widely used in industry and our laboratory has extensive experience in Ni electrodeposition[44,45]. For methanol oxidation, various literature examples showing improved MOR activity with PtNi catalyst have been reported[13,36,46–48].

Development of Monolithic PtNi Alloy Electrode

With the spectroelectrochemical measurements in mind, the resulting PtNi gradient should span from 0% to 50% Ni content (the range where synergistic effects are expected) over at least 200 μm, allowing 10 measurement positions with 20 μm spatial resolution and each position averaging over 5% Ni content change. Translated to the initial electrodeposited Ni layer, the layer needs to be at least 50 μm thick in order to reach Ni concentration of 50% over 200 μm after annealing. Experimentally this was achieved by Ni electroplating using a Watts bath solution in a water-jacketed two-chamber cell at constant current to yield a 100 μm thick layer within 8 h[44,45]. The thickness is well above the requirement and can be easily modified by increasing/decreasing the plating time. Homogeneous layer deposition with only small deviation at the electrode or mask edges can be achieved through constant solution stirring to prevent hydrogen bubble formation on the electrode. In its freshly electrodeposited form, significant nickel oxide and hydroxide contribution are present within the Ni and need to be removed during the subsequent annealing.

The main challenge to solve during electroplating is limiting the Ni layer growth to single side of a platinum foil while preventing mechanical delamination of the deposited layer. To limit deposition areas, an epoxy mask as shown in Figure 4.3a was applied to selected areas of the Pt foil. The top portion allows for complete submersion of the foil into liquid to reduce heterogeneity during electrodeposition due to the liquid-air interface. The unmasked Pt face is aligned parallel to the Ni cathode to improve homogeneity in deposition. Early one-sided plating attempts failed due to delamination of the nickel at the edges either during the drying phase of the sample or during the annealing process due to different thermal

(a) Epoxy mask **(b)** Before annealing **(c)** After annealing

Figure 4.3: (a) Schematic of Pt foil mask during electrodeposition. (b-c) Images of PtNi electrodes (glossy surface is Pt; matt surface is Ni) after Ni deposition (b) and after annealing at high temperature (c).

expansion coefficients of the two metals. The thin perimeter of unmasked electrode arounds its edge and the back face provides enough mechanical stability to the deposited nickel layer on the front side to prevent delamination until the PtNi interface has been properly fused during annealing.

The annealing process was adopted from Karunaratne and Reed's work on inter-metallic diffusion[38]. An inert argon gas with a low hydrogen (5.22%) component was selected to remove oxygen and hydroxide from the bulk of the electrodeposited material over the course of the annealing time. As shown in Figure 4.3b, electrodeposited layer appears grey due to high nickel oxide and nickel hydroxide concentration. By selecting a lightly reducing gas (Argon + 5.22% H_2) oxide and hydroxide were successfully removed during the process, resulting in a shiny metallic PtNi alloy depicted in Figure 4.3c. Overall the process is highly repeatable for creation of heterogeneous PtNi alloys and each alloy composition was further characterized before use in spectroelectrochemical cells.

4.4.2 PtNi Alloy Electrode Characterization

Alloy Composition

The annealed PtNi alloys were extensively characterized with WDS for bulk and AES for surface concentration mapping. Electrochemical techniques were also used to evaluate averaged MOR performance. Before implementation into SECs, WDS determined the bulk Ni and Pt concentration for each alloy. Figure 4.4a is a 2D WDS map created from the Pt M_α counts/s (blue) overlaid with Ni K_α (red) of a representative PtNi alloy annealed for 24 h. A few black spots at the top edge are small defect points within the electrodeposited Ni-layer, but the majority of alloy remains defect free. The map indicates a clear transition from 25% Pt at the top edge to 100% Pt over a span of ∼100 μm. More importantly the PtNi gradient in the horizontal direction parallel to the original PtNi interface remains consistent over the 1.5 mm of mapped PtNi alloy. This simplifies the catalytic activity changes across the PtNi gradient into a one-dimensional problem. By placing the long axis of a 20×80 μm SIR beam spot parallel to the horizontal direction, mapping of catalytic activity can occur at higher S/N while retaining 20 μm spatial resolution along the Ni gradient. Grain formation and associated metal segregation does appear to be present across the entire metal piece. If grains exist, sizes would be smaller than the WDS probe beam size of ∼1.5 μm wide and ∼0.7 μm penetration depth based on Monte Carlo simulations. Coupled with the fact that the Pt_xNi_{1-x} system is known to possess a face-centered cubic structure across the whole range of composition[49], segregated Pt and Ni grains are highly unlikely. The evidence instead supports the formation of a heterogenous PtNi alloy with a one-dimensional Ni gradient.

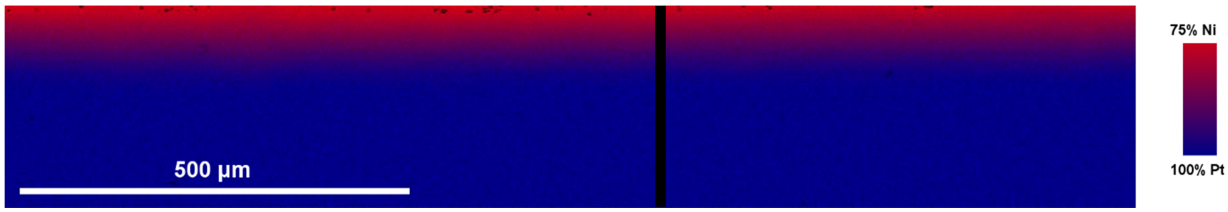

(a) 2D map of X-ray counts/s for Pt and Ni

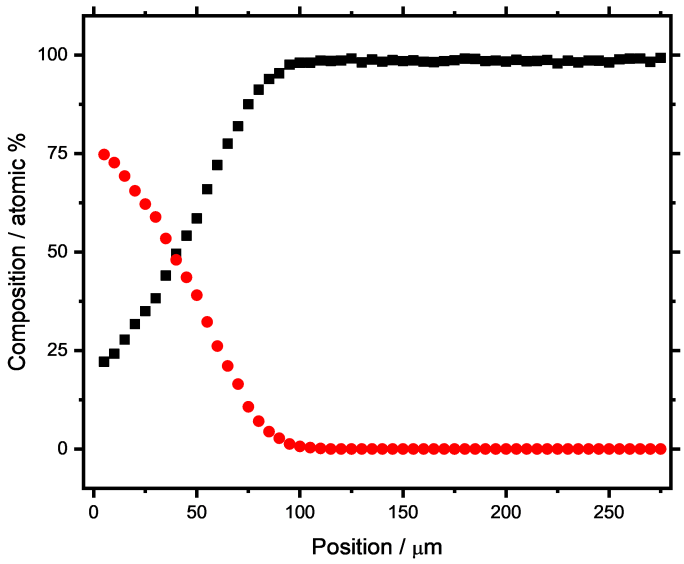

(b) Pt and Ni content

Figure 4.4: (a) 2D map of Pt M_α (blue) and Ni K_α X-ray (red) counts/s of an alloy deposited for 6 h and annealed for 24 h. Scale bar indicates their corresponding PtNi composition based on WDS measurements on the same alloy shown in (b), which is measured along the direction indicated by the black line in (a).

Figure 4.4b shows Pt and Ni content measured across the gradient as indicated by the line in Figure Figure 4.4a. The transition of high Ni to pure platinum occurs smoothly across ∼100 μm in line with the intermetallic diffusion models used in Karunaratne and Reed work[38]. The summation of Pt and Ni content yields consistent 99% composition across the entire alloy. Quantitative Pt and Ni concentrations consistently add up to >99%, suggesting little presence of impurities within the annealed alloy. Due to much higher time cost of 2D-mapping with WDS, most alloy characterizations are limited to single line measurement analogous to Figure 4.4b. To confirm that alloy gradients remained one-dimensional, two or three parallel line measurements on each alloy 500 μm apart were compared. These showed a consistent gradient concentration and only minor variations of 1-2% difference.

While the shape of the concentration gradient is fixed, Nickel concentrations and length of gradient could be freely altered through the initial electrodeposited Ni layer thickness and annealing time respectively. Figure 4.5a shows the results of WDS measurements of the PtNi gradient of two alloys with different annealing time. The gradient length doubles from ∼100 μm (blue) to ∼200 μm (black) by quadrupling the annealing time from 24 h to 96 h, matching with the theoretical predication that the diffusion length, d, and the annealing time, t are related through an inverse square root proportionality, *i.e.* of a $d \propto 1/\sqrt{t}$ proportionality between diffusion length d and annealing time t[38]. PtNi alloys used in spectroelectrochemical cells were consistently annealed for 96 h to achieve a gradient length of 200 μm. While a longer gradient length allows for more precise measurement with smaller Ni-concentration changes, a balance had to be found due to the quadratic increase in annealing time.

Like gradient length, maximum Ni concentrations can be altered through the initial

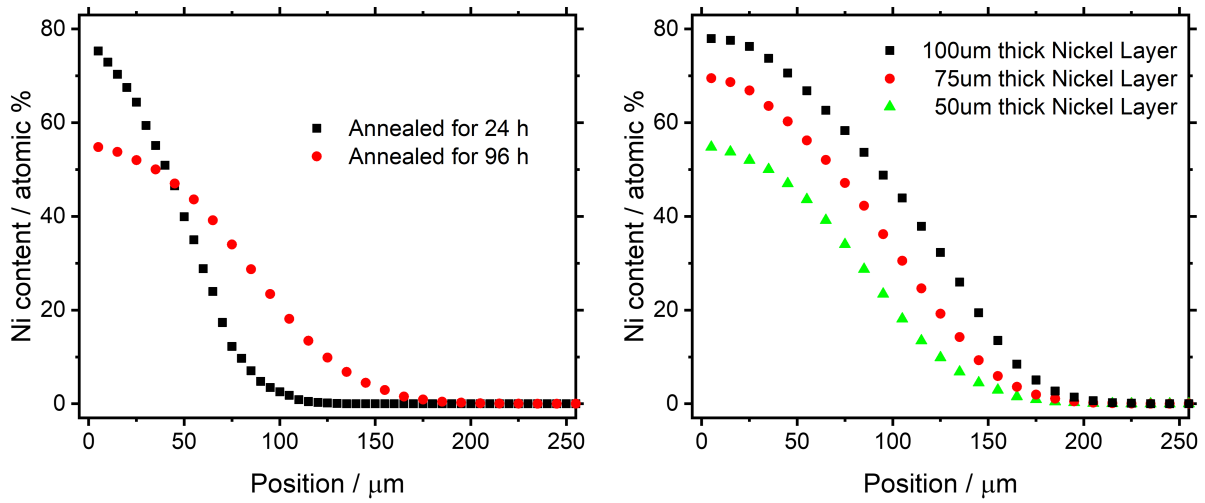

(a) Annealing Time **(b)** Initial Ni-layer thickness

Figure 4.5: Heterogeneous PtNi alloy bulk composition gradient determined through WDS show variance based on (a) annealing time and (b) initial Ni layer thickness as indicated in their respective legends.

electrodeposited Ni layer thickness. Figure 4.5b show WDS measurement of three PtNi alloys with different initial Ni layer thicknesses after annealing for 96 h at the same temperature. While all three alloys show similar Ni-gradient length, maximum Ni content changes linearly with initial Ni layer thickness and are altered by 12% per 25 μm of the electrodeposited nickel thickness. For all following experimental results, PtNi alloys with ~100 μm initial Ni layer annealed for 96 h were selected with a maximum Ni content of 55%. Experiments with maximum nickel content above 60% proved to be unstable during the MOR conditions due to electrode breakdown at the high Nickel content region of the alloy. It was found that acidic Ni-leaching extended beyond the surface layer and into the bulk of the electrode, created a porous Pt skeleton structure which was not mechanically stable. It is important to note that the WDS measurements do not necessarily reflect the outermost surface nickel content even though penetration depth of the electron beam equates to only several hundreds of monolayers. As the MOR is an electrocatalytic reaction, it is imperative to determine the

metal concentrations with a technique that offers greater surface sensitivity.

Bulk versus Surface Ni Composition

A key discussion for any catalytic activity of compositional catalyst is bulk versus surface concentration during operational conditions. In the case of PtNi MOR, it is well established within the literature that Ni surface content changes due to acidic leaching of Ni from the surface[47,50,51]. The extent and its effect on the catalytic activity, however, can change widely between different reports with at times conflicting results. The ubiquitous use of nanoparticle PtNi catalysts with different preparation methods further increases the variance between lab to lab results and further complicates the performance comparison between various Pt_xNi_{1-x} concentrations. One of the key reasons for utilizing bulk electrodes in this study is limiting variance between different PtNi composition. WDS work suggests the PtNi alloy is devoid of larger-sized grains, allowing for evaluation in the absence of any segregation effect often present within nanoparticles. With bulk characterization complete, surface versus bulk concentration before and after operational conditions were required.

Figure 4.6 show the result of Pt and Ni content obtained through AES (black squares and red circles) and WDS (black and red solid lines). The short escape distance of Auger-electrons limits the measured concentration to the initial few atomic layers. In contrast, Monte-Carlo simulation of the electron penetration depth for the WDS measurement show X-ray emission from up to 0.7 μm within the electrode material. The differences in depth of signal generation between AES and WDS allows for a comparison of surface versus bulk concentration.

Before exposure to the acidic electrolyte environment, Figure 4.6a shows the sur-

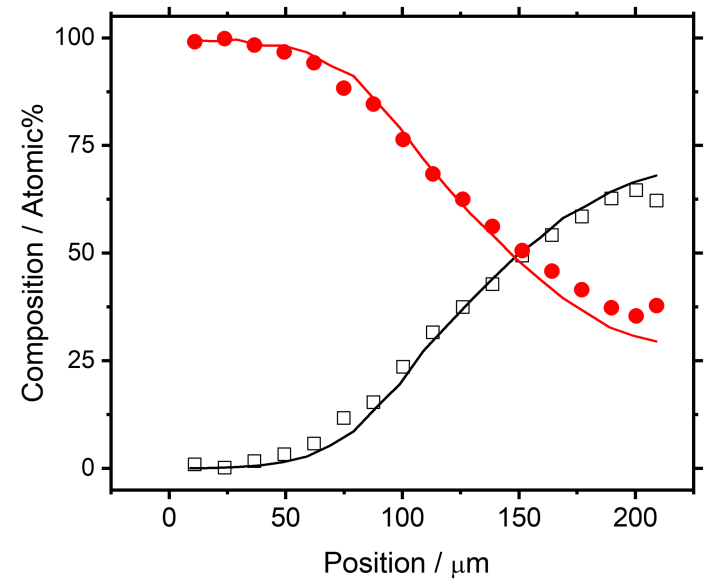

(a) Before acid exposure

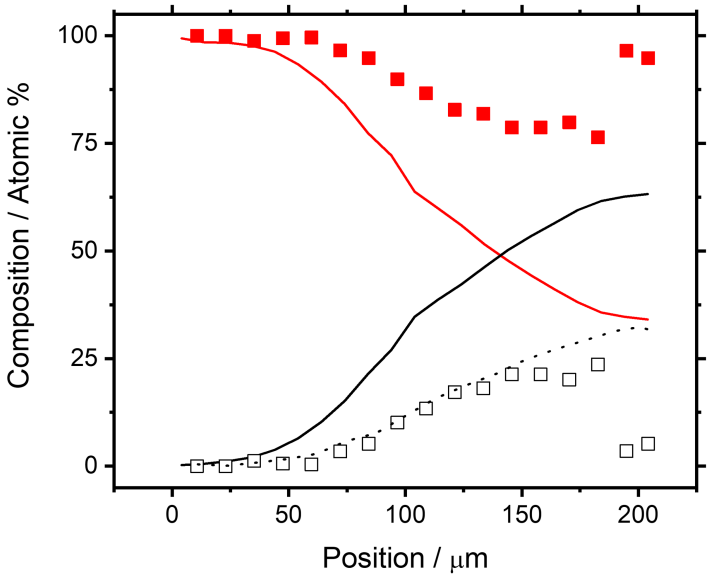

(b) After acid exposure

Figure 4.6: Heterogeneous PtNi alloy composition gradient measured (a) before and (b) after initial treatment in 0.1 M H_2SO_4 and 1.0 M MeOH. WDS determined Ni (black line) and Pt (red line) bulk concentration as well as AES determined Ni (open square) and Pt (red circle) surface concentrations. Dashed line in (b) indicates 50% loss of Ni based on the initial WDS profile.

face and bulk concentration for the heterogenous PtNi are almost identical between AES and WDS. PtNi alloy preparation through intermetallic diffusion between larger metal and subsequent exposure of the bulk gradient through mechanical polishing offers a continuous gradient of PtNi concentration at the bulk as well as the surface. Surface segregation, often reported for nanoparticles, appears completely absent for all PtNi concentrations. Once cycled within the electrolyte (0.1 M H_2SO_4 + 1 M MeOH) for extended periods, the same alloy is characterized again with AES and WDS and the results are shown in Figure 4.6b. The WDS measured consistent bulk Pt (black solid line) and Ni (red solid line) concentrations with virtually no change between before and after exposure to electrolyte. The surface sensitive AES however, shows a decrease in surface Ni for all measurement positions along the entire PtNi gradient. The loss of Ni through acidic leaching matches with general observations from the literature[47,50,51], but due to the conflicting reports within the literature and the variety of initial Ni concentration present on the heterogenous PtNi electrode, a closer examination is warranted.

Broadly speaking, the degree of Ni leaching appears separated into three distinct regions that depend on initial Ni concentration. Regions with 0-50% initial Ni content show a consistent decrease to 50% of the initial value. For 50 - 60% initial Ni concentration, the Ni drops consistently down to ∼25% Ni content. Above 60% initial Ni concentration, a drastic decrease of Ni is observed down to ∼10% Ni content. It should be noted that while significant material is removed, the bulk concentration through WDS remains mostly stable. Unstable PtNi alloy compositions have been observed earlier for Ni content above 75% with clear signs of breakdown. Breakdown of the electrode at above 75% initial Ni content is likely explained by the fact that the remaining Pt is insufficient to form a stable

porous Pt-Pt network. For <50% Ni initial content, the leaching matches very well with Bonakdarpour et al's description for PtNi thin film with 50% loss as indicated by the dotted line in Figure 4.6b[50]. The requirement of statistically higher number of neighboring Pt atoms for Ni to remain chemically stable provides an explanation for the significant decrease at above >50% initial Ni. It should also be noted that several atomic layers contribute to the AES signal. Differentiation between consistent Ni leaching or creation of Pt-skin with underlaying layers with Ni for higher initial Ni content positions can not be excluded without further investigation.

As later results are more invested in demonstration of catalytic activity mapping with SIR, the key take-away is that evaluation of MOR activity for higher initial Ni content must consider the effect of an increased catalytic active surface area due to roughening of the surface through acidic Ni leaching. This effect will be particularly pronounced for measurements at initial Ni content >50%.

Electrochemical Characterization

Before describing electrochemical characterization in detail, it should be noted that all purely electrochemical results are only basic diagnostic information, as MOR performance of the heterogenous PtNi electrode is an average of various Pt_xNi_{1-x} concentrations. Nonetheless, cyclic voltammetry and chronoamperometry measurements are very useful indicators of electrochemical stability and MOR performance over prolonged periods of measurement, a key aspect for the long experimental measurement time of rapid scan FTIR.

Initial electrochemical characterization of the PtNi alloy electrode was performed within a large volume electrochemical cell with de-aerated 0.1 M H_2SO_4 and 1 M MeOH

solution. Binary Pt-alloys in acidic media are known to leach the less noble metal within the initial minutes of operation before arriving at a more stable final concentration. Furthermore, as mentioned in Chapter 3, Pt tends to accumulate loosely bound impurities on its surface that inhibit catalytic activity and require removal through oxidative cycling. To accommodate both processes, the electrode potential was extensively cycled in a bulk solution cell between -0.25 V $<$ E $<$ 1.0 V for a minimum of 30 min to remove impurities from the surface and allow the MOR activity to stabilize. Once the electrode has stabilized, a CV of MOR of the PtNi electrode is collected. A representative CV is shown as black line in Figure 4.7. The onset of hydrogen evolution is present at -0.25 V followed by reversible hydrogen adsorption on Pt between -0.25 V $<$ E $<$ -0.1 V. Continuing onward in the anodic (positive-going) scan direction, MOR starts at 0.25 V with a maximum activity at 0.7 V followed by a current drop due to the formation Pt surface oxides. While detailed analysis of the MOR onset potential and current peak position is limited due to the averaged nature of PtNi electrode, these values compare well to MOR results from pure Pt electrodes in Chapter 3 and the PtNi catalysts reported in the literature[47].

Hydrogen adsorption and methanol oxidation features and their respective onset potentials remain unchanged when the PtNi electrodes is placed in the thin cavity of the fully assembled spectroelectrochemical setup and is shown as the red line in Figure 4.7. CV responses of the assembled spectroelectrochemical cell were all collected under a constant flow of electrolyte to avoid depletion of MeOH within the 25 μm cavity above the electrode. One difference is a decrease in maximum current due to the constrained diffusion geometry within the thin cavity. A second difference is a slight tilt of the CV and current offset at relatively negative potentials. Unlike the bulk electrolyte cell setup, the electrolyte solutions in the

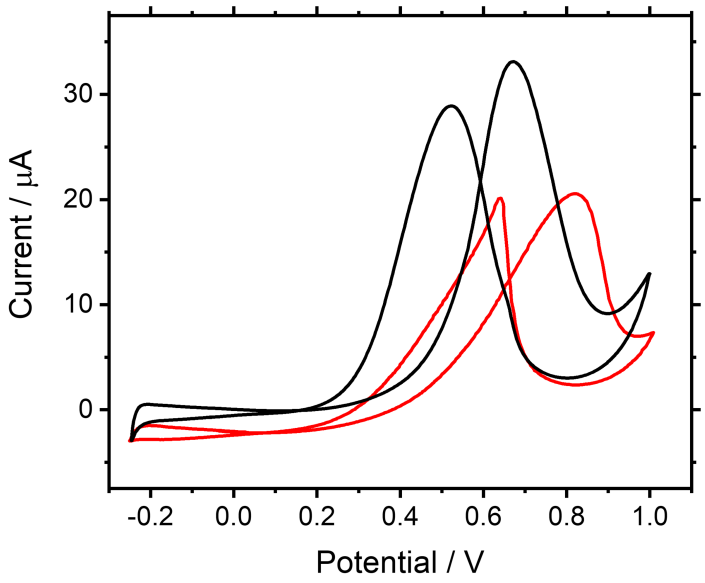

Figure 4.7: CV in 0.1 M H_2SO_4 and 1.0 M MeOH of the PtNi alloy in a bulk electrolyte setup (black) and within assembled SEC (red). The sweep rate is 100 mV/s.

spectroelectrochemical cell were not de-aerated and the parasitic oxygen reduction reaction is the most likely source of these qualitative changes in the CV. In short, the changes in the electrochemical behaviour of the PtNi appears to be limited to predictable effects of the thin cavity setup. Overall the electrochemical results show that the MOR performance of the heterogeneous PtNi electrodes is suited for use in spectroelectrochemical experiments.

4.4.3 Stability Testing of SEC

For the experimental measurement time of 12 – 24 h, the stability of MOR activity of the PtNi electrode is continuously monitored through chronoamperometric measurements occurring simultaneously with the rapid scan FTIR measurements and intermittently collected CVs. Typical examples of these two measurements for a spectroelectrochemical experiment over 24 h is presented in Figure 4.8. The chronoamperometric measurements in Figure 4.8a are

continuously collected parallel to each rapid scan FTIR measurements. The current transients were measured following the working electrode potential being stepped from 0 V to 0.6 V. The step to 0.6 V induces methanol oxidation at the electrode surface and results in a sharp current peak. As the reaction proceeds, the current drops off to a plateau with higher current than initially recorded at 0 V as the mass-transfer limited oxidation of MeOH continues to proceed at timescales larger than the depicted current transient. The initial current response shape and current values during the plateau phase remain almost constant during the full 24 h duration of the experiment, suggesting the average reaction rates on the electrode do not change. A more quantified analysis can be performed by integrating the charge of each individual current transient as a proxy for amount of MeOH converted. The integrated charge values show that changes of the average electrode activity only increase the MOR activity by 6% over the course of 24 h.

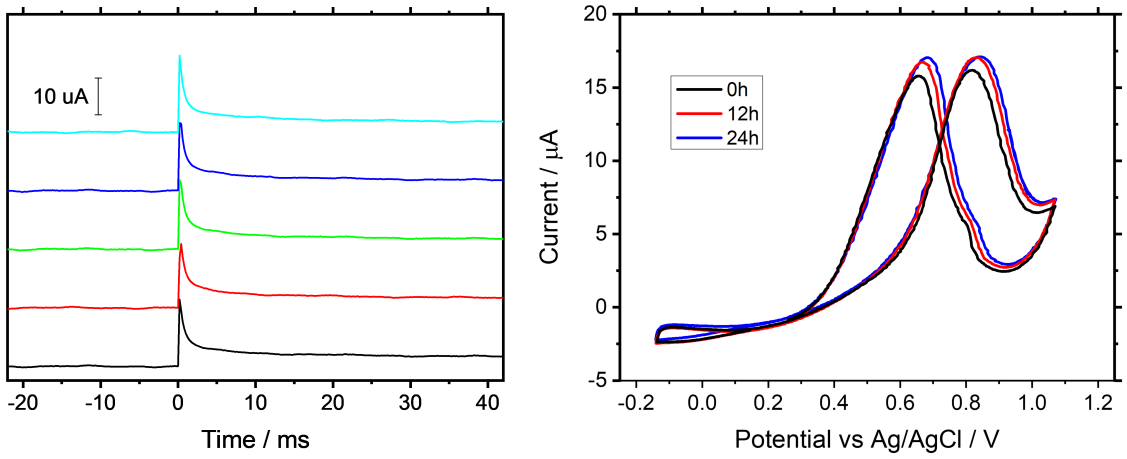

Figure 4.8: Stability of PtNi alloy electrode during a combinatorial screening experiment over 24 h based on (a) current transient of the E_{step} to +0.6 V recorded every 6 h and (b) CVs recorded every 12 h. The sweep rate is 100 mV/s.

This is further supported by the intermittent CVs, collected in-between rapid scan

measurements. The CVs in Figure 4.8b show a similar, very slight, increase in maximum MOR peak currents. As the onset potentials of hydrogen evolution, hydrogen adsorption and methanol oxidation remain stable, it appears this change is not due to drifting potential control, but most likely a small change in surface area due to the repeated short oxidative potential pulse of the platinum surface during the cell reset to remove surface adsorbed CO. A similar process has been described for pure platinum electrodes in Chapter 3. Overall, the depicted current transients and CVs showcase the highly reproducible nature of each methanol oxidation step sequence within the spectroelectrochemical cell.

To further mitigate the small errors caused by systematically increasing electrode activity, the spectroelectrochemical measurements were made with a changing sequence of measurements at each spatial position along the PtNi gradient. Instead of moving between each 10 positions only after collecting 64 rapid scan iterations at a single position, the measurement was split into two passes through the position with 32 iterations on each position. Activity increase between different position are now reduced as they are no longer a maximum of 24 h apart, but rather 12 h. Ideally the measurement would change position after each rapid scan iteration, but at the time of data collection, small manual optical adjustment within the IR microscope when moving position made it untenable. A later upgrade to the optical setup at the mid-IR beamline station with active optics elements should allow the automated measurement with improved positional sequencing.

Overall these results show that the spectroelectrochemical measurement will be stable with a small, but mostly negligible, error due to surface area increase due to roughening during removal of residual CO.

4.4.4 Simulation of Diffusion Profiles within SEC

Understanding the effects of lateral diffusion within the thin cavity is crucial to evaluate the FTIR mapping results along the PtNi gradient. Finite element method (FEM) simulations with FlexDPE (Lite version, Appendix III) were performed to evaluate the influence of diffusion on measured CO_2 concentrations. Simulations were needed as no closed, analytical solutions exist for solving Fick's second law under the thin cavity boundary conditions and the distribution of heterogeneous rate constants along the electrode's metal concentration gradient. However, the unidirectional nature of the PtNi gradient allows the simulation to be reduced to a two-dimensional problem. Figure 4.9 shows the simulation space for all following results, utilizing a 2-dimensional Cartesian coordinate geometry with the z-dimension orthogonal to the electrode surface and the x-dimension parallel to the electrode surface.

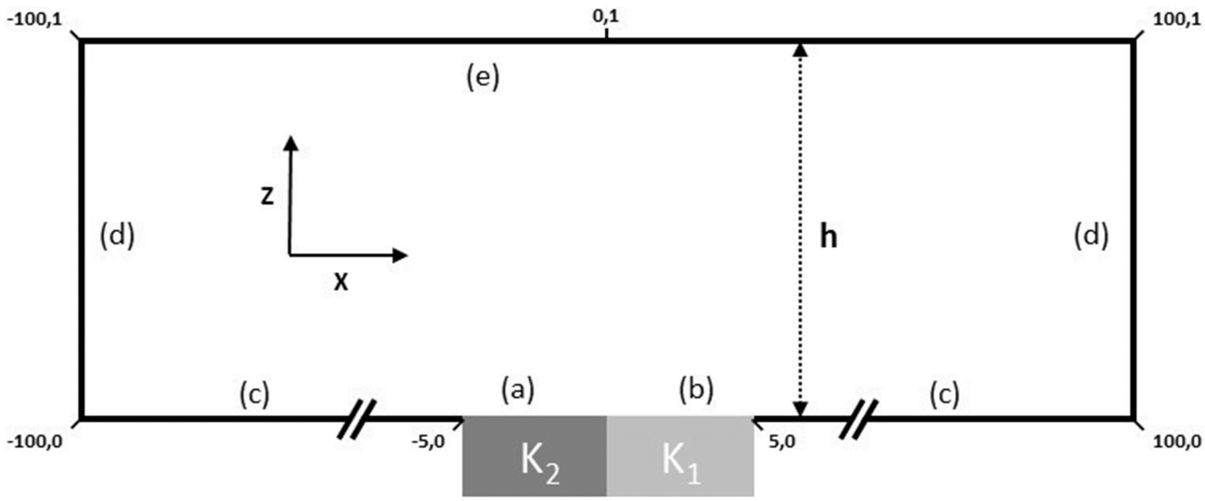

Figure 4.9: Schematic representation of the diffusion space under consideration for numerical simulations.

For simplicity's sake, the most basic simulation model assumes the catalytic activity

of the electrode surface (indicated by grey rectangles in Figure 4.9) consists of two distinct catalytic activity areas with two heterogeneous MOR rate constants (k_1, k_2) and $k_2 = 2k_1$. Dimensionless variables were used with the following definitions:

$$C_{CO_2} = \frac{c_{CO_2}}{c^*_{MeOH}} \tag{4.4}$$

$$t' = \frac{tD}{h^2} \tag{4.5}$$

$$X = \frac{x}{h} \tag{4.6}$$

$$Z = \frac{z}{h} \tag{4.7}$$

$$K = \frac{kh}{D} \tag{4.8}$$

Where t, D, c, h and k are the time, CO_2 (aq) diffusion coefficient, concentration, thin-layer cavity thickness and heterogeneous rate constant respectively. Heterogenous rate constants k are based on the diffusion coefficient D for CO_2 ($\sim\ 2 \times 10^{-5}$ cm^2s^{-1}) and standard heterogenous reaction rate for MOR on platinum from the literature[52]. CO_2 concentrations are normalized by the initial concentration of MeOH c^*_{MeOH}. Ficks' second law for this geometry using the dimensionless variables outline above becomes:

$$\left[\frac{\partial^2}{\partial X^2} + \frac{\partial^2}{\partial Z^2}\right] C_{CO_2} = \frac{C_{CO_2}}{\delta t'} \tag{4.9}$$

The boundary conditions for the system are detailed in Table 4.1. Initial C_{CO_2} is zero throughout the entire electrolyte within the thin cavity. At $t' > 0$, different electrode surface areas are generating CO_2 based on their respective reaction rate K. The inert cell body and

Boundary/region in Figure 4.9	Description	Boundary conditions
(a)	High activity surface of electrode	For $t' > 0$ $n\nabla C_{CO_2} = K_1$
(b)	Low activity surface of electrode	For $t' > 0$ $n\nabla C_{CO_2} = K_2$
(c)	Inert cell body	$n\nabla C_{CO_2} = 0$
(d)	Semi-infinite diffusion conditions at edge of cell cavity space	For $t' \geq 0$ C_{CO_2}
(e)	Inert CaF_2 window	$n\nabla C_{CO_2} = 0$
(f)	Body of electrolyte	For $t' = 0$ $C_{CO_2} = 0$

Table 4.1: Boundary conditions for the FEM simulation space described in Figure 4.9.

CaF_2 window act as hard barriers for CO_2 diffusion within the system. The distance between the electrode and the edge of the cell cavity is sufficient for C_{CO_2} to effectively never reach the boundary within the total timeframe of the simulation and the corresponding boundary condition at (d) guarantees semi-infinite diffusion conditions.

As the IR absorbance signal is proportional to the total number of IR molecules within the measured volume, integration of C_{CO_2} within each 20 μm wide "volume" above the electrode can simulate a corresponding FTIR signal response. Figure 4.10 shows the simulated CO_2 signal over time for three selected positions above the electrode. Position (I) is near the edge to illustrate the effect of CO_2 loss through lateral diffusion away from the electrode surface. Positions (II) and (III) are areas near the region on the simulated electrode where the catalytic activity changes from K_1 to K_2. Simulation of the C_{CO_2} response in these regions evaluates the effect of lateral diffusion between different catalytic active electrodes. For comparison, an idealized response can easily be calculated whereby all lateral diffusion is disregarded. These idealized CO_2 responses are linear over time and each ideal transient is a linear line with slope values of K_1 and K_2 respectively. These are indicated in

Figure 4.10 by the dotted lines.

The resulting numerical simulations that include the effects of lateral diffusion are shown in Figure 4.10a. The CO_2 response at position (I) shows a short linear behaviour at very small time t', but quickly and drastically deviates to lower values. Similar processes have been described in Chapter 3 for pure Pt electrodes. The negative deviation from the expected response is due to mass transport losses of CO_2 away from the electrode into the bulk of the thin cavity. In this case, the closer proximity to the edge and therefore higher concentration gradient creates a much quicker deviation from linear progression. For more central positions on the electrode, *i.e.* position (II) and (III), diffusion due to edge-effects are negligible within the timeframe of the IR experiment. The CO_2 signal remains longer in an initial state due to a lack of strong lateral CO_2 concentration gradients, but at longer t' will show deviation from linear progression. Here interdiffusion between the catalytically more active area (III) to the less active area (II) is responsible for the negative deviation and positive deviation respectively.

While these qualitative changes in simulated CO_2 signal over time are easily visible, the simulations indicate that quantitative values for the MOR rate with insignificantly small errors can only be extracted from very short times ($<0.5\ t'$). Translating from reduced time t' to real time t (Equation 4.5) requires a linear fit of the data within the first 0.8 s of the measurement. The rapid scan FTIR measurement time resolution of 0.45 s would make results from a linear fit of just two datapoints highly flawed. Higher time resolutions are possible with rapid scan but come at a cost of decreased S/N and a requirement of increased measurement time to co-add to the same S/N level. Due to this experimental limitation, a better approach is quantifying the error of the linear fit. To this effect, simulations were

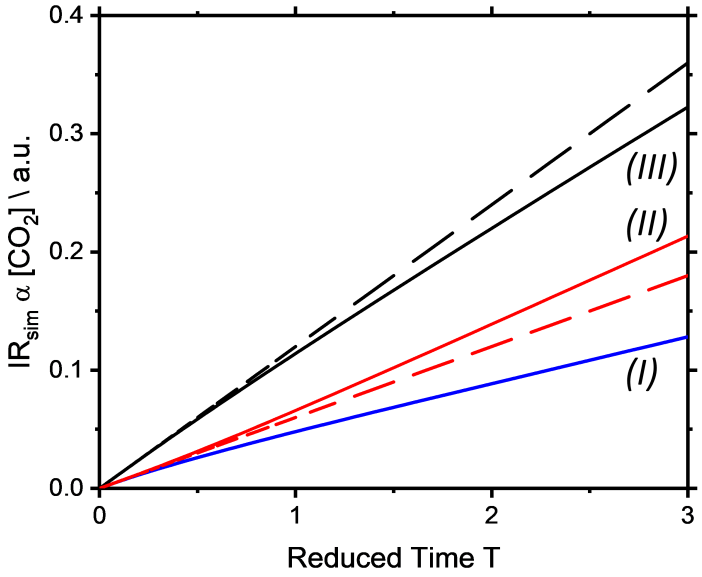

(a) Simulated IR signal transients

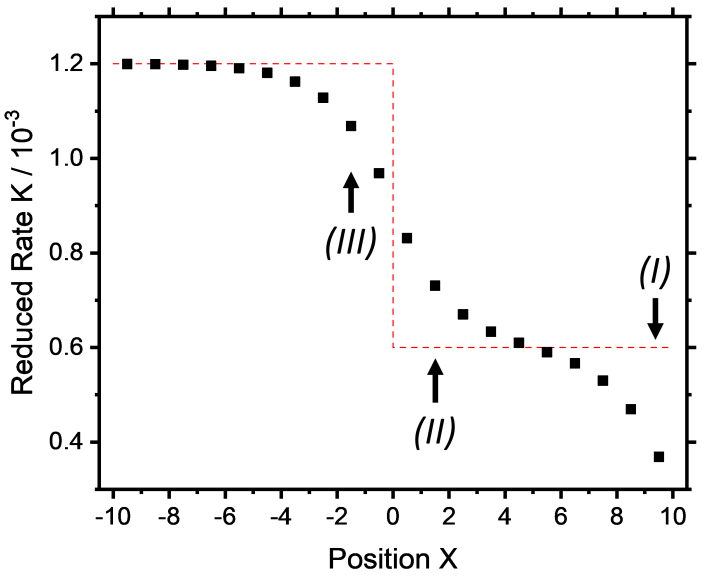

(b) Linear fitted K_{fit} vs actual K_{fit} values

Figure 4.10: (a) Simulated IR absorption response of CO_2 (IR_{SIM}) generated from an electrode with two regions of MOR activity. Evolution of CO_2 signal with time is shown for areas *(I)* (blue line), *(II)* (red line), and *(III)* (black line) on the simulated electrode as indicated in the inset. Dashed lines are the ideal (no lateral diffusion) IR_{SIM} transients for -10 > x ≥ 0 (blue) and 0 > x > 10 (red). (b) Calculated rates K_{fit} (black square) based on linear fitting of simulated IR responses within the initial 4 s for all positions on the electrode. Dashed line indicates actual K values.

run on an electrode with two catalytic regions. Below $X = 10$, the reduced rate constant $K = K_1$ and for X > 10 the value doubles to $K_2 = 2K_1$. Figure 4.10b shows the results of linear fits with different fit time length along the electrode surface. The dashed red line indicates the actual K value of the electrode and the black datapoints are the MOR rate values calculated through a linear fit of the simulated CO_2 IR responses over 4 s. The results of the simulation exercise demonstrate that the calculated rate values will deviate for >5% for the initial three position near any catalytic activity change. *I.e.* the experimental FTIR results will not provide rigorous quantitative results. However, the results will be semi-quantitative with accuracies that depend on how sharply the true MOR reactivity varies across the binary alloy interface. In the limit of gradual changes, the results will be highly accurate and at worst should provide qualitative assessment of the composition effects on MOR activity.

4.4.5 SIR-based Combinatorial Screening of Heterogeneous PtNi

Following the successful creation and characterization of a heterogeneous PtNi electrode, rapid scan FTIR measurements were carried out to measure differences in catalytic activity of the binary alloy electrode by monitoring the formation of CO_2 at different spatial positions along the Ni-gradient. During each rapid scan iteration, the MOR is initiated by a E_{step} from 0 V to 0.6 V at 0 s. Figure 4.11 shows the formation of CO_2 in time over the next 10 s at a position with an average 33% initial Ni content as determined by WDS. A clear peak, assigned as CO_2, develops at 2343 cm^{-1} with little noise visible in the nearby wavenumber region. Like previous experiments in Chapter 3 on MOR on Pt, incomplete oxidation products are not visible due to the combination of their low concentration, smaller IR absorption cross-section and strong H_2O adsorption within the relevant wavenumber region.

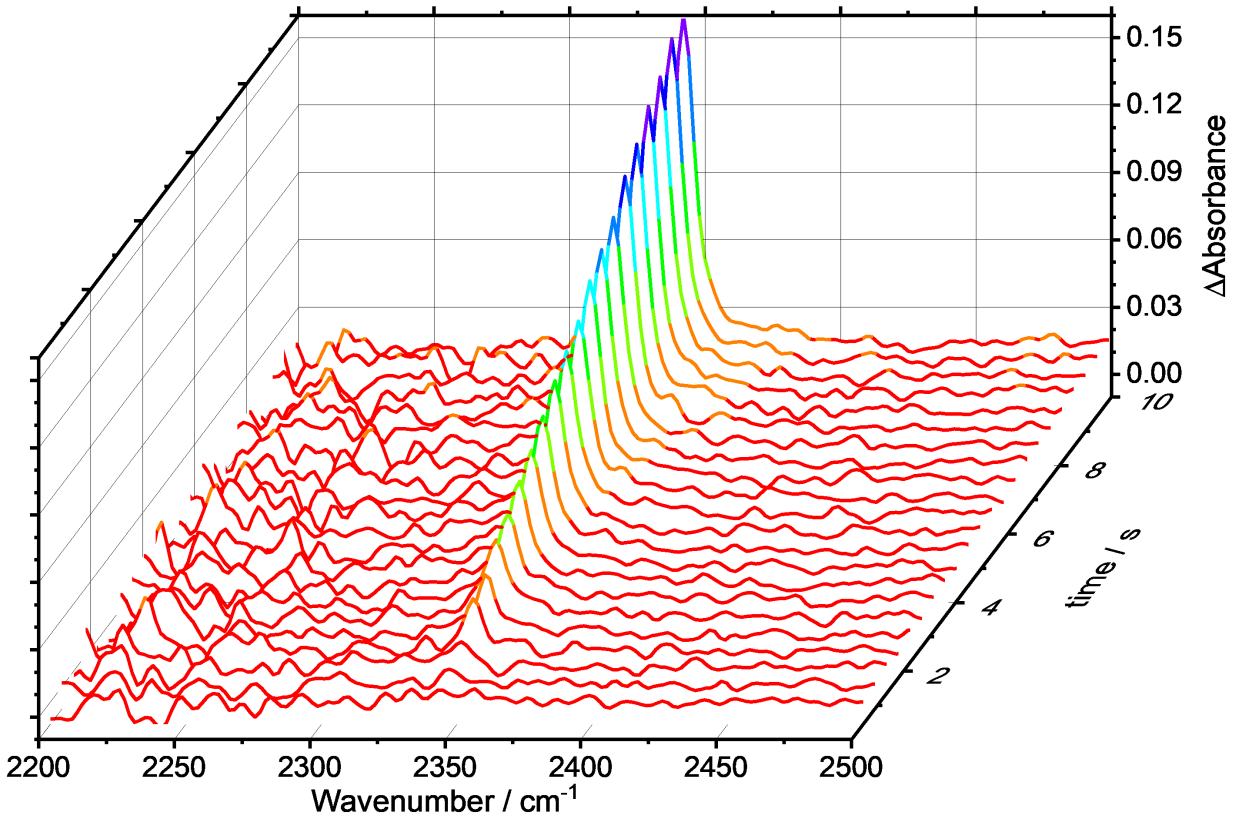

Figure 4.11: Time-resolved IR absorbance change of CO_2 (peak maximum at 2343 cm^{-1}) after inducing methanol oxidation reaction by stepping the potential to +0.6 V. Measurement position on PtNi alloy corresponds to ∼33% initial Ni-content.

As the complete oxidation product of MeOH, the CO_2 signal serves as a proxy for the otherwise not measurable MeOH consumption. To evaluate the kinetics and therefore the catalytic activity, a better representation of the data is the CO_2 peak absorbance over time as shown in Figure 4.12a. CO_2 concentration in the measured volume increases linearly for the initial seconds as indicated by the black line before a deviation occurs at longer times ($t>$ 4 s). The initial linear increase within the initial seconds similar to results obtained on pure platinum electrodes in Chapter 3. However, two important differences are present within rapid scan spectra on PtNi. First, measurements at different positions show different linear increases of CO_2 content in the volume immediately above the electrode. Figure 4.12b shows a wider selection of CO_2 signal progressions for various measurement positions along the Ni content gradient depicted in Figure 4.6. This indicates that the heterogeneous PtNi electrodes possesses different catalytic activity as expected. Secondly, several positions (with low Ni content) show a significant upward deviation at long times compared to the typical downwards deviation observed on pure Pt electrodes.

The linear process within the initial seconds is due to kinetically controlled production of CO_2 at the electrode as has been explained in Chapter 3. The heterogeneous PtNi electrode shows similar linear behaviour within the initial seconds for all measured positions but has different slopes when comparing measurement positions with different initial Ni-content. At longer times, the measured CO_2 concentrations on a pure Pt electrode in Chapter 3 were consistently lower due to lateral diffusional losses away from the electrode into the bulk electrolyte of the thin cavity. However, for PtNi at multiple measurement positions along the Ni-gradient, the FTIR data show a positive deviation from linear CO_2 production at longer times. Effectively these positions gain CO_2 concentration at longer

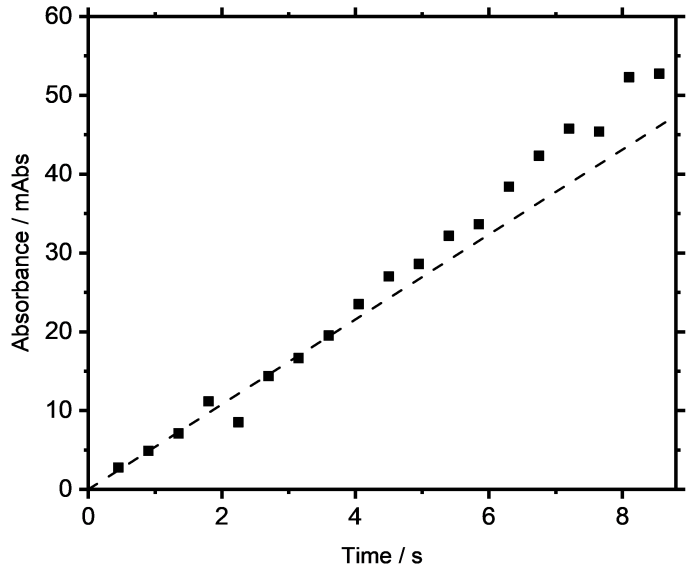

(a)

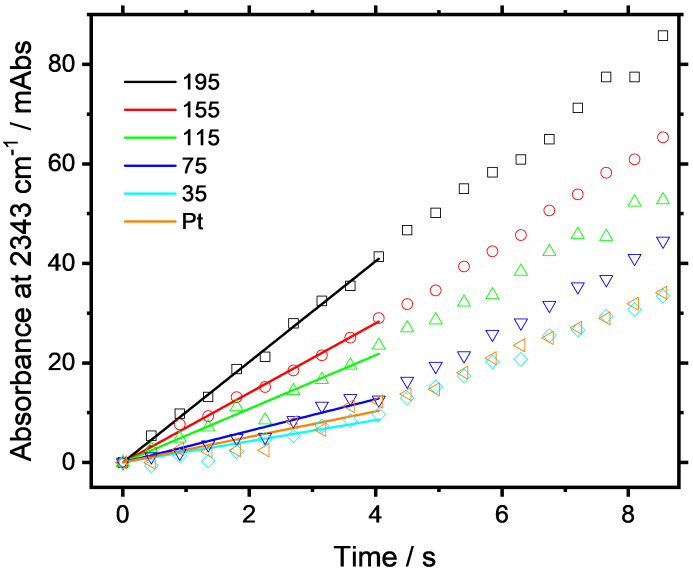

(b)

Figure 4.12: (a) Transient of CO_2 IR signal measured at ∼33% Ni (black square) with CO_2 progression (dashed black line) based on linear fitting the initial 4 s of data. (b) CO_2 (aq) absorbance transients for every second spot along the measured PtNi gradient (legend provides distance along the gradient in microns). Linear fits (solid lines) for the first 4 s of data provide the rate of MOR.

times. Considering the heterogeneous nature of catalytic activity for the electrode surface, this increase is linked to diffusion lateral to the electrodes surface between areas of different activity, allowing more catalytically active areas to positively influence the CO_2 concentration at nearby lower activity areas. This result was demonstrated by the numerical simulations. Based on the numerical simulation work, the CO_2 signal over time is linearly fitted within the initial 4 s. The resulting slope value is divided by the value measured over 100% Pt-content to provide relative heterogenous rate values for MOR for various Pt_xNi_{1-x}.

For better presentation, the relative MOR rate values are plotted against their respective near-surface Ni-content as determined by AES in Figure 4.13. The x-value represents the position on the electrode and horizontal x-error bars for the Ni-content the width of the 20 μm IR beamspot for each measurement. The results show a consistent increase in MOR rate over the entire length with increasing initial Ni content and a particularly strong increase for the last two positions closest to the edge of the electrode. From a qualitative standpoint, the FTIR mapping was clearly able to identify the Pt_xNi_{1-x} electrode area with $\sim$5% surface Ni and initial Nickel content >50% as the most catalytic active composition. On initial comparison with previous reported results by Mathiyarasu *et al.*, 8% Ni has been cited as the optimal concentration for PtNi[47]. This is very much consistent with the present result. Similarly, PtRu screening has suggested 10% Ru maximizes the probability of three surface Pt sites near an oxyphilic surface metal in order to provide optimal MOR reaction condition[11]. While the FTIR measurements match well with these literature reports, the origin of said MOR activity and the quantitative value of this FTIR screening requires a more nuanced discussion.

Based on the numerical simulation discussed earlier, the measured MOR rate value

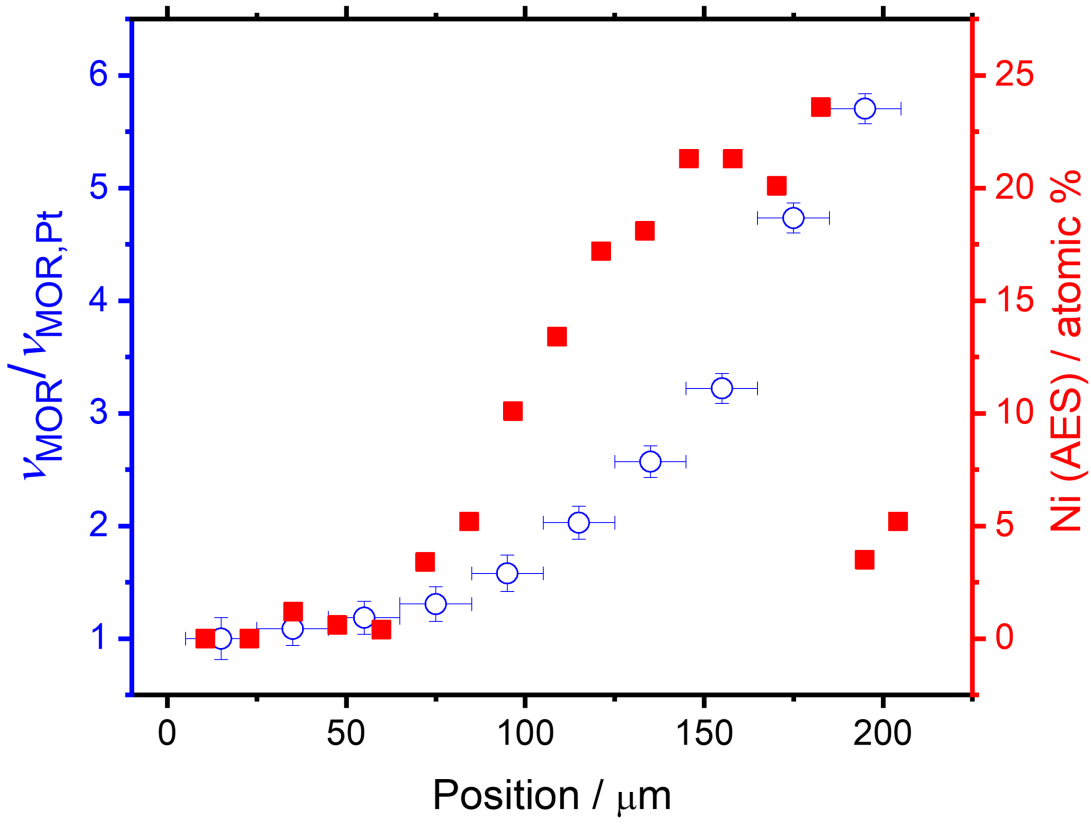

Figure 4.13: Rates of MOR $mathrmv_{MOR}$ $\upsilon_{MOR,Pt}$ (blue outlined circle) measured at different position along the PtNi gradient, normalized to the rate of MOR on pure platinum. Horizontal error bars represent the SIR beam spot dimension, limited by a 20×80 μm blade aperture. Overlaid is the corresponding surface nickel content (red square) as determined by AES.

for the highest position is negatively affected by diffusion both from the position to lower Ni-content areas as well as diffusion due to the "edge-effect" due to its location at the electrode edge. This is further supported by the downward deviation from linear behaviour within its IR transient in Figure 4.12b, which is only seen for this single position. Due to the diffusional losses of CO_2 away from this position, the actual MOR rate is much larger than the measured MOR rate of 6x the value of pure Pt. The stark increase in CO_2 production at this composition, obviously brings up questions about the origin of this strong increase in activity, when considering, that electrode areas with similar $\sim$8% surface Ni-content, but different initial Ni content, are $\sim$15 - 20% less active.

In general, an increase in catalytic activity can be linked to a combination of three separate effects, 1) increase in ECSA 2) improved reaction pathway due to surface Ni and 3) ensemble effects of PtNi[53]. The strong surface Ni-leaching observed in the AES measurement for the most active position points towards a contribution by ECSA increase. Traditional electrochemical methods to determine ECSA such as underpotential hydrogen underpotential deposition measurements[54] are not feasible due to the averaging nature of the electrochemical response from the heterogenous electrode. Ex-situ AFM measurement also proved to be difficult, as surface roughness measurements are dominated by features created during the mechanical polishing. Instead, a more qualitative *in situ* method based on IR reflection of the electrode surface between 4000 - 5000 cm^{-1} wavenumbers was devised, based on the assumption that increased roughness will decrease the specular reflection from the surface. The chosen frequency range is devoid of any chemical feature and the shorter wavelength of light should be more sensitive to smaller surface roughness changes. Comparing the IR signal within this spectral region before and after extensive electrochemical cycling should

provide a surrogate measurement for changes in surface roughness as unstable near-surface Ni content is leached from the electrode. The percent loss of the integrated IR signal within the selected spectral region for each position is then plotted against the Ni content determined by AES is shown in Figure 4.14. The result provides qualitative evidence that catalytic activity increase is at least partially driven by simple ECSA increase as the loss of IR signal strength experiences a jump from a slow increase from 2 - 5% over 180 μm to 10% within the last 20 μm of the electrode.

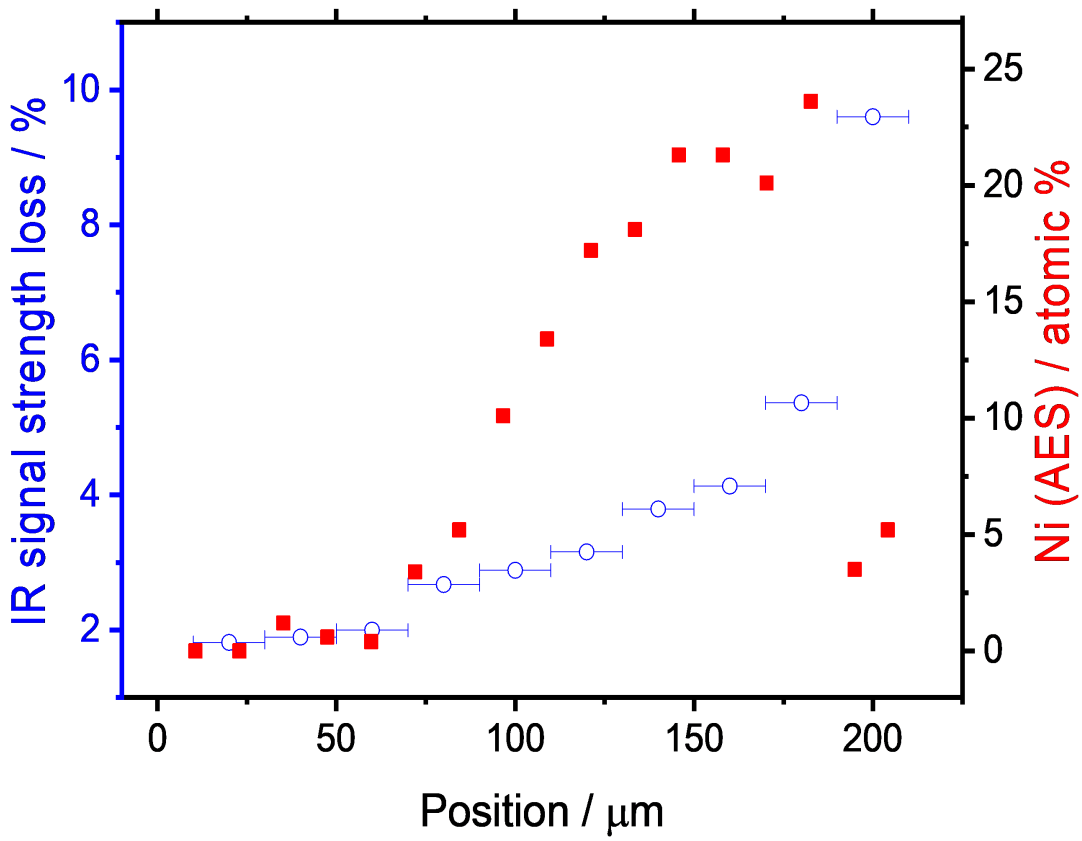

Figure 4.14: IR signal strength changes (blue outlined circle) after electrochemical treatment. X-error bars indicate the SIR beam spot dimension, limited by a 20 μm×80 μm blade aperture. Overlaid are the corresponding final surface concentrations of Ni (red square) as determined by AES.

Overall, the rapid scan FTIR results within this chapter have successfully demonstrated the first qualitative combinatorial screening of a heterogeneous PtNi bulk electrode (with initial Ni content ranging from 0-55%) and its electrocatalytic activity for MOR. Analysis of the screening results in the context of earlier determined bulk and surface compositions, revealed a particularly strong increase in catalytic activity for electrode positions with initial Ni content >50%. While this is later identified to be at least partially credited to an increases in ECSA due to acidic leaching of Ni from the electrode surface, it should be noted that the final surface composition of the electrodes matches of ∼8% Ni matches well with previous cited literature reports with PtNi nanoparticles[47].

4.4.6 Improvements to Combinatorial Screening of Binary Metal Catalysts

With proof-of-concept established for the rapid scan FTIR measurements, two further approaches were attempted to further improve the combinatory mapping methodology. The first aims to expand the possible library of electrode materials and the second attempts to improve the quantitative value of the measurement.

One key lesson learned from the earliest attempts to create a heterogenous electrode described in this chapter is the lack of micrometer thick electrodeposition methods for ruthenium. To solve this issue for metal combinations lacking a well-established electrodeposition methodology, an alternative preparation method for heterogenous bimetallic electrodes by directly fusing thin metal foils together was adopted from Divya et al's work[37]. Thirteen layers of 25 μm thick Pt foil followed by thirteen layers of 25 μm thick Ni foil were sand-

wiched together between two graphite pieces and pressed together through a set of ceramic screw and nut combinations. Through 40 min heating intervals under vacuum condition in an inductive heating oven, the individual layers of metal foils were fused together into a solid block. Subsequently the graphite holder, that aided the inductive heating of the sample, is exchanged for ceramic pieces. Annealing under reducing conditions for 96 h induced intermetallic diffusion. It should be noted that fusion and annealing should theoretically be possible within one vacuum step but was not achievable due to equipment limitations. Figure 4.15a shows an SEM image of the electrode surface. Except for a small defect at the bottom left, all 26 layers of metal thin foils are continuously fused together over millimeter length scales. The slight contrast between darker top and brighter bottom area indicates Ni and Pt respectively and the transition in the middle of the electrode between them is the composition transition from Pt to Ni. WDS measurements performed at multiple points along the alloy confirm a smooth PtNi concentration gradient over 200 μm with compositions varying from 0% Ni to 100% Ni shown in Figure 4.15b. While the work is limited to PtNi, it demonstrates the feasibility of utilizing thin metal films, which opens a much larger library of possible bimetallic combinations for combinatorial mapping.

The main challenge for more quantitative analysis of the extracted heterogenous MOR rate values is the error arising because of lateral diffusion because of the "edge-effect" and/or overlap with other differently catalytically active positions. To minimize this error, individual PtNi compositions within the gradient have to be more spatially separated from each other. For this purpose, an inert mask was created on a PtNi electrode surface through UV-lithography. A PtNi electrode within a spectroelectrochemical cell with a finished photoresist mask is shown in Figure 4.16. The larger electrode with PtNi gradient in the center

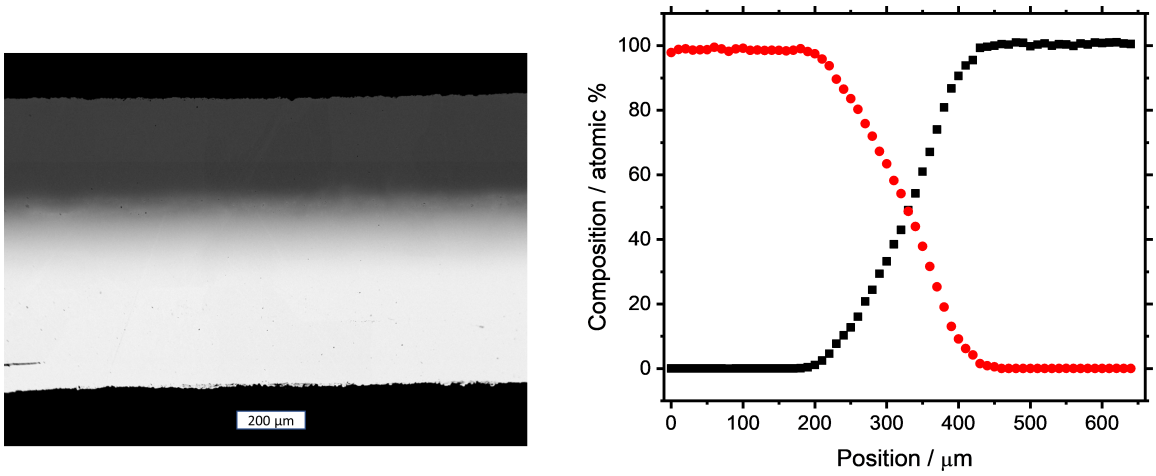

(a) 2D SEM image

(b) Pt and Ni content

Figure 4.15: (a) SEM image of the PtNi alloy created from fusing 13×25 μm Ni + 13×25 μm Pt thin foils within vacuum induction furnace and followed by annealing over 96 h under reducing atmosphere. The scale bar (b) Corresponding WDS determined PtNi concentration measured parallel to the concentration gradient.

created through thin metal film fusion described above has been used, as it provides a larger surface area for UV lithography. The spectroelectrochemical cell was adopted to allow spin coating of a 5 μm thick photoresist layer (SU-8 2005). Subsequent heating to 95° C in an oven for 15 min removes solvent from the film, before cooling down to room temperature. The desired pattern was written using UV-lithography at the SyLMAND facility at the CLS. The UV exposed photoresist layer is heated to continue the UV initiated polymerization before rinsing with developer solvents to remove surplus photoresist. The mask provides an inert cover over most of the electrode surface except for 10 open slots 20×80 μm wide and positioned with their long dimension perpendicular to the PtNi gradient. An individual slot corresponds to Pt_XNi_{1-X} content range of around 5 - 6%, with the total of 10 spots covering the range of 0 - 60% Ni-content. Diffusion error between positions of different Ni content is minimized by placing each open slot at least 150 μm apart. FTIR signals of CO_2 within the initial seconds are now isolated to the MOR reaction of that location, eliminating the

"edge effect". The photoresist mask extends a few hundret microns beyond the electrode for mechanical stability at the transition between metal and electrochemical cell material as well as to prevent defects creating additional electrocatalytic active areas at the edge.

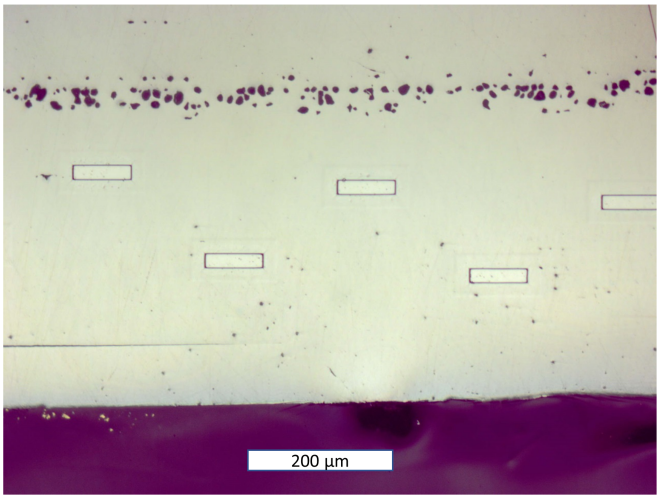

Figure 4.16: PtNi alloy electrode embedded within a SEC. A mask of SU-8 photoresist polymer has been prepared on top through a combination of spin coating, UV lithography and annealing, leaving only small notches of the electrode (20×80 μm) open.

Electrochemical and spectroelectrochemical tests were promising. Individual measurement positions showed no upward deviation from linear behaviour in the initial seconds due to CO_2 diffusion from more active areas. Unfortunately, it was not possible to properly quantify MOR rates for the most interesting composition with initial Ni content of 50 - 60%. The significant increase in acidic leaching of surface Ni weakens the adhesion of the surrounding photoresist layer, leading to creation of small electrolyte cavities under the inert layer at these positions. The increase in geometric surface area artificially raises any quantitative MOR rate values measured for these positions. So, while the implementation of inert masking can improve error in quantitative reaction rate vales, surface leaching posed

a significant challenge for measurement in acidic medium when using the photoresist mask. To demonstrate the improved combinatory mapping, a different electrocatalytic system than MOR on PtNi in sulfuric acid would have been a better choice. One option is to change the metal composition to PtRu, which is more resistant towards degradation within acidic electrolyte. Unlike the unsuccessful earlier attempts in creating PtRu binary electrodes through electrodepositing, the improved electrode production methodology by thin metal foil fusing should make the production of this alloy viable. A second option is a switch of the electrolyte to more neutral/basic conditions, which also have been reported to be viable for MOR[55,56].

4.5 Conclusion

The work presented in this chapter has demonstrated the use of spatially and time resolved FTIR microscopy to map electrocatalytic activity of a heterogenous sample. Methodology to produce monolithic PtNi alloy electrodes with a well-defined continuous Pt_xNi_{1-x} concentration gradient for high throughput screening is described. Compared to sputtered or inkjet-printed libraries, its composition is closer to bulk mixing of two metals, limiting variance between different concentrations between library production methods. The PtNi electrodes were extensively characterized for their electrochemical stability during extended experiment measurement times of up to 24 h as well as for changes in their surface metal composition due to acidic electrolyte environments.

Combinatorial screening of MOR activity was performed through spatial resolved FTIR mapping of different CO_2 production rates based on Pt_xNi_{1-x} compositions at various locations along the electrode. Numerical simulations show that diffusional broadening of the

CO_2 signal between differently catalytic active electrode areas can be mitigated by limiting the measurement to short times through the use of rapid scan FTIR and semi-quantitiative and qualitative assessment of MOR rates is possible. PtNi composition with bulk composition of 60 - 65% and surface concentration of ∼5% after exposure to acidic composition showed the highest MOR rate. Proxy measurements of surface roughness through increased IR scattering indicate an increased surface areas is only partially responsible for the increase in MOR activity.

The last subsection showcased two improvements that can be employed for future combinatorial screening capabilities of spatial IR mapping of catalytic activity. The first one is the production of binary metal alloys through direct fusion of metal thin foils. The removal of electrodeposition simplifies the production of these monolithic alloys and increases the range of possible metal compositions. Secondly, development of UV-lithography compatible spectroelectrochemical cells can mitigate diffusional broadening through partial masking of the electrode surface with electrochemically inert materials. This should improve the qualitative and quantitative comparison between different binary and possibly even tertiary compositions.

Ultimately, while the initial choice of Ni as the secondary component was driven by its ease for production of a heterogenous bimetallic sample, any attempts at quantitative analysis of MOR activity has suffered due to changes in the electrode surface through acidic Ni leaching. Nonetheless, the work within this chapter provides proof-of-concept for SIR-based IR mapping of electrocatalytic materials and provides a solid foundation for future implementation. While the results discussed here focus on combinatorial screening of bimetallic PtNi electrocatalysts for MOR, it should be possible to expand to other bimetallic catalysts

or electrodes systems where heterogeneity is dominated by different effects such as catalyst distribution. Particularly the improvements described in the last paragraph should benefit its application for electrocatalytic systems where surface topography changes are limited.

4.6 References

[1] Lardner, M.; Tu, K.; Rosendahl, S.; Borondics, F.; Burgess, I. Spatiotemporal mapping of diffusion layers using synchrotron infrared radiation. *Electrochimica Acta* **2015**, *162*.

[2] Iwasita, T. Methanol and CO electrooxidation. *Handbook of Fuel Cells* **2003**, *2*, 603–624.

[3] Petry, O. A.; Podlovchenko, B. I.; Frumkin, A. N.; Lal, H. The behaviour of platinized-platinum and platinum-ruthenium electrodes in methanol solutions. *Journal of Electroanalytical Chemistry (1959)* **1965**, *10*, 253–269.

[4] Watanabe, M.; Motoo, S. Electrocatalysis by ad-atoms. *Journal of Electroanalytical Chemistry and Interfacial Electrochemistry* **1975**, *60*, 275–283.

[5] Tong,; Kim, H. S.; Babu, P. K.; Waszczuk, P.; Wieckowski, A.; Oldfield, E. An NMR Investigation of CO Tolerance in a Pt/Ru Fuel Cell Catalyst. *Journal of the American Chemical Society* **2002**, *124*, 468–473.

[6] Jackson, C.; Conrad, O.; Levecque, P. Systematic Study of Pt-Ru/C Catalysts Prepared by Chemical Deposition for Direct Methanol Fuel Cells. *Electrocatalysis* **2017**, 1–11.

[7] Janssen, M. M. P.; Moolhuysen, J. Binary systems of platinum and a second metal as oxidation catalysts for methanol fuel cells. *Electrochimica Acta* **1976**, *21*, 869–878.

[8] Beden, B.; Kadirgan, F.; Lamy, C.; Leger, J. M. Electrocatalytic oxidation of methanol on platinum-based binary electrodes. *Journal of Electroanalytical Chemistry and Interfacial Electrochemistry* **1981**, *127*, 75–85.

[9] Goodenough, J. B.; Hamnett, A.; Kennedy, B. J.; Manoharan, R.; Weeks, S. A. Methanol oxidation on unsupported and carbon supported Pt + Ru anodes. *Journal of Electroanalytical Chemistry and Interfacial Electrochemistry* **1988**, *240*, 133–145.

[10] Swathirajan, S.; Mikhail, Y. M. Electrochemical Oxidation of Methanol at Chemically Prepared Platinum-Ruthenium Alloy Electrodes. *Journal of The Electrochemical Society* **1991**, *138*, 1321–1326.

[11] Gasteiger, H. A.; Markov, N.; Ross, P. N.; Cairns, E. J. Methanol Electrooxidation on Well-Characterized Pt-Ru Alloys. **1993**, 12020–12029.

[12] Greeley, J.; Mavrikakis, M. Alloy catalysts designed from first principles. *Nat Mater* **2004**, *3*, 810–815.

[13] Tague, M. E.; Gregoire, J. M.; Legard, A.; Smith, E.; Dale, D.; Hennig, R.; DiSalvo, F. J.; Bruce van Dover, R.; Abruña, H. D. High Throughput Thin Film Pt-M Alloys for Fuel Electrooxidation: Low Concentrations of M (M = Sn, Ta, W, Mo, Ru, Fe, In, Pd, Hf, Zn, Zr, Nb, Sc, Ni, Ti, V, Cr, Rh). *Journal of The Electrochemical Society* **2012**, *159*, F880–F887.

[14] Strasser, P.; Fan, Q.; Devenney, M.; Weinberg, W. H.; Liu, P.; Nørskov, J. K. High Throughput Experimental and Theoretical Predictive Screening of Materials: A Comparative Study of Search Strategies for New Fuel Cell Anode Catalysts. *The Journal of Physical Chemistry B* **2003**, *107*, 11013–11021.

[15] Gurau, B.; Viswanathan, R.; Liu, R.; Lafrenz, T. J.; Ley, K. L.; Smotkin, E. S.; Reddington, E.; Sapienza, A.; Chan, B. C.; Mallouk, T. E.; Sarangapani, S. Structural and Electrochemical Characterization of Binary, Ternary, and Quaternary Platinum Alloy Catalysts for Methanol Electro-oxidation. *The Journal of Physical Chemistry B* **1998**, *102*, 9997–10003.

[16] Fu, S.; Zhu, C.; Du, D.; Lin, Y. Enhanced Electrocatalytic Activities of PtCuCoNi Three-Dimensional Nanoporous Quaternary Alloys for Oxygen Reduction and Methanol Oxidation Reactions. *ACS Applied Materials & Interfaces* **2016**, *8*, 6110–6116.

[17] Wang, A.-L.; Wan, H.-C.; Xu, H.; Tong, Y.-X.; Li, G.-R. Quinary PdNiCoCuFe Alloy Nanotube Arrays as Efficient Electrocatalysts for Methanol Oxidation. *Electrochimica Acta* **2014**, *127*, 448–453.

[18] Kim, Y. S.; Jeon, S. H.; Bostwick, A.; Rotenberg, E.; Ross, P. N.; Stamenkovic, V. R.; Markovic, N. M.; Noh, T. W.; Han, S.; Mun, B. S. Role of Transition Metal in Fast Oxidation Reaction on the Pt3TM (111) (TM = Ni, Co) Surfaces. *Advanced Energy Materials* **2013**, *3*, 1257–1261.

[19] Reddington, E.; Sapienza, A.; Gurau, B.; Viswanathan, R.; Sarangapani, S.; Smotkin, E. S.; Mallouk, T. E. Combinatorial Electrochemistry: A Highly Parallel, Optical Screening Method for Discovery of Better Electrocatalysts. *Science* **1998**, *280*, 1735–1737.

[20] Potyrailo, R.; Rajan, K.; Stoewe, K.; Takeuchi, I.; Chisholm, B.; Lam, H. Combinatorial and High-Throughput Screening of Materials Libraries: Review of State of the Art. *ACS Combinatorial Science* **2011**, *13*, 579–633.

[21] Cooper, J. S.; McGinn, P. J. Combinatorial screening of thin film electrocatalysts for a direct methanol fuel cell anode. *Journal of Power Sources* **2006**, *163*, 330–338.

[22] Xiang, C.; Suram, S. K.; Haber, J. A.; Guevarra, D. W.; Soedarmadji, E.; Jin, J.; Gregoire, J. M. High-Throughput Bubble Screening Method for Combinatorial Discovery of Electrocatalysts for Water Splitting. *ACS Combinatorial Science* **2014**, *16*, 47–52.

[23] Seley, D.; Ayers, K.; Parkinson, B. A. Combinatorial Search for Improved Metal Oxide Oxygen Evolution Electrocatalysts in Acidic Electrolytes. *ACS Combinatorial Science* **2013**, *15*, 82–89.

[24] Strasser, P. Combinatorial Optimization of Ternary Pt Alloy Catalysts for the Electrooxidation of Methanol. *Journal of Combinatorial Chemistry* **2008**, *10*, 216–224.

[25] Gregoire, J. M.; Van Dover, R. B.; Jin, J.; DiSalvo, F. J.; Abruña, H. D. H. D. Getter sputtering system for high-throughput fabrication of composition spreads. *Review of Scientific Instruments* **2007**, *78*, 72212.

[26] Antolini, E. Evaluation of the Optimum Composition of Low-Temperature Fuel Cell Electrocatalysts for Methanol Oxidation by Combinatorial Screening. *ACS Combinatorial Science* **2017**, *19*, 47–54.

[27] Arabia, S.; Loget, G.; Schmuki, P. H2 Mapping on Pt-Loaded TiO2 Nanotube Gradient Arrays. *Langmuir* **2014**, *30*, 15356–15363.

[28] Welsch, F. G.; Stöwe, K.; Maier, W. F. Fluorescence-Based High Throughput Screening for Noble Metal-Free and Platinum-Poor Anode Catalysts for the Direct Methanol Fuel Cell. *ACS Combinatorial Science* **2011**, *13*, 518–529.

[29] Moura, S. A.; Fajín, L. J.; Mandado, M.; Cordeiro, N. M.; Moura, A.; Fajín, J.; Mandado, M.; Cordeiro, M. Ruthenium–Platinum Catalysts and Direct Methanol Fuel Cells (DMFC): A Review of Theoretical and Experimental Breakthroughs. *Catalysts* **2017**, *7*, 47.

[30] Sui, S.; Wang, X.; Zhou, X.; Su, Y.; Riffat, S.; Liu, C.-j. A comprehensive review of Pt electrocatalysts for the oxygen reduction reaction: Nanostructure, activity, mechanism and carbon support in PEM fuel cells. *Journal of Materials Chemistry A* **2017**, *5*, 1808–1825.

[31] Wang, C.; Markovic, N. M.; Stamenkovic, V. R. Advanced Platinum Alloy Electrocatalysts for the Oxygen Reduction Reaction. *ACS Catalysis* **2012**, *2*, 891–898.

[32] Wain, A. J.; O'Connell, M. A.; Attard, G. A. Insights into Self-Poisoning during Catalytic Hydrogenation on Platinum Surfaces Using ATR-IR Spectroelectrochemistry. *ACS Catalysis* **2018**, *8*, 3561–3570.

[33] Van Der Vliet, D. F.; Wang, C.; Tripkovic, D.; Strmcnik, D.; Zhang, X. F.; Debe, M. K.; Atanasoski, R. T.; Markovic, N. M.; Stamenkovic, V. R. Mesostructured thin films as electrocatalysts with tunable composition and surface morphology. *Nature Materials* **2012**, *11*, 1051–1058.

[34] Shukla, A. K.; Neergat, M.; Bera, P.; Jayaram, V.; Hegde, M. S. An XPS study on binary and ternary alloys of transition metals with platinized carbon and its bearing upon oxygen electroreduction in direct methanol fuel cells. *Journal of Electroanalytical Chemistry* **2001**, *504*, 111–119.

[35] Stamenkovic, V. R.; Fowler, B.; Mun, B. S.; Wang, G.; Ross, P. N.; Lucas, C. A.; Marković, N. M. Improved Oxygen Reduction Activity on Pt3Ni(111) via Increased Surface Site Availability. *Science* **2007**, *315*, 493–497.

[36] Du, P.; Wu, P.; Cai, C. Mechanistic Insight into the Facet-Dependent Adsorption of Methanol on a Pt3Ni Nanocatalyst. *The Journal of Physical Chemistry C* **2015**, *119*, 18352–18363.

[37] Divya, V. D.; Ramamurty, U.; Paul, A. Interdiffusion and the vacancy wind effect in Ni–Pt and Co–Pt systems. *Journal of Materials Research* **2011**, *26*, 2384–2393.

[38] Karunaratne, M.; Reed, R. Interdiffusion of the platinum-group metals in nickel at elevated temperatures. *Acta Materialia* **2003**, *51*, 2905–2919.

[39] Rosendahl, S. M.; Borondics, F.; May, T. E.; Burgess, I. J. Step-Scan IR Spectroelectrochemistry with Ultramicroelectrodes: Nonsurface Enhanced Detection of Near Femtomole Quantities Using Synchrotron Radiation. *Analytical Chemistry* **2013**, *85*, 8722–8727.

[40] Lardner, M. J.; Tu, K.; Barlow, B. C.; Rosendahl, S. M.; Borondics, F.; Burgess, I. J. Quantitative analysis of electrochemical diffusion layers using synchrotron infrared radiation. *Journal of Electroanalytical Chemistry* **2017**, *800*, 184–189.

[41] Tu, K.; Lardner, M. J.; Morhart, T. A.; Rosendahl, S. M.; Creighton, S.; Burgess, I. J. Spatial Mapping of Methanol Oxidation Activity on a Monolithic Variable-Composition PtNi Alloy Using Synchrotron Infrared Microspectroscopy. *The Journal of Physical Chemistry C* **2016**, *120*, 23640–23647.

[42] Pouchou, J.-L.; Pichoir, F. In *Quantitative Analysis of Homogeneous or Stratified Microvolumes Applying the Model "PAP" BT - Electron Probe Quantitation*; Heinrich, K. F. J., Newbury, D. E., Eds.; Springer US: Boston, MA, 1991; pp 31–75.

[43] Jones, T. In *Electrodeposition & Deposition of the Precious Metals: Rhodium, Ruthenium, Iridium, Osmium, Rhenium*; Publication, F., Ed.; 2003.

[44] Barlow, B. C.; Szymanski, G.; Lipkowski, J.; Shobeir, B.; Love, B.; Burgess, I. J. Pulsed Potential Dissolution Reduces Anode Residue Formation during Nickel Electroplating. *Journal of The Electrochemical Society* **2016**, *163*, C164–C170.

[45] Schlesinger, M.; Paunovic, M. *Modern Electroplating*, fifth edit ed.; John Wiley & Sons, 2010; Vol. 55; pp 79–114.

[46] Zhang, B.; Niu, Y.; Xu, J.; Pan, X.; Chen, C.-M.; Shi, W.; Willinger, M.-G.; Schlogl, R.; Su, D. S.; Schlögl, R.; Su, D. S. Tuning the surface structure of supported PtNix bimetallic electrocatalysts for the methanol electro-oxidation reaction. *Chemical Communications* **2016**, 2–5.

[47] Mathiyarasu, J.; Remona, A. M.; Mani, A.; Phani, K. L. N.; Yegnaraman, V.; Phani, M. K. L. N. Exploration of electrodeposited platinum alloy catalysts for methanol electrooxidation in 0.5 M H2SO4: Pt-Ni system. *Journal of Solid State Electrochemistry* **2004**, *8*, 968–975.

[48] Huang, W.; Wang, H.; Zhou, J.; Wang, J.; Duchesne, P. N.; Muir, D.; Zhang, P.; Han, N.; Zhao, F.; Zeng, M.; Zhong, J.; Jin, C.; Li, Y.; Lee, S.-T. T.; Dai, H. Highly active and durable methanol oxidation electrocatalyst based on the synergy of platinum–nickel hydroxide–graphene. *Nature Communications* **2015**, *6*, 10035.

[49] Hansen, M.; Anderko, K. In *Constitution of Binary Alloys,*, 2nd ed.; Schenectady, G. P. G., Ed.; 1985.

[50] Bonakdarpour, A.; Wenzel, J.; Stevens, D. A.; Sheng, S.; Monchesky, T. L.; Lobel, R.; Atanasoski, R. T.; Schmoeckel, A. K.; Vernstrom, G. D.; Debe, M. K.; Dahn, J. R. Studies of transition metal dissolution from combinatorially sputtered, nanostructured Pt1-xMx (M = Fe, Ni; $0 < x < 1$) electrocatalysts for PEM fuel cells. *Journal of the Electrochemical Society* **2005**, *152*, A61–A72.

[51] Wang, S.; Yang, G.; Yang, S. Pt-Frame Ni quasi Core–Shell Concave Octahedral $PtNi_3$ Bimetallic Nanocrystals for Electrocatalytic Methanol Oxidation and Hydrogen Evolution. *The Journal of Physical Chemistry C* **2015**, acs.jpcc.5b10083.

[52] Frank, M. J. W.; Kuipers, J. A. M.; Swaaij, W. P. M. V.; van Swaaij, W. P. M. Diffusion Coefficients and Viscosities of CO2 + H2O, CO2 + CH3OH, NH3 + H2O, and NH3 + CH3OH Liquid Mixtures. *Journal of Chemical & Engineering Data* **1996**, *41*, 297–302.

[53] Maroun, F.; Ozanam, F.; Magnussen, O. M.; Behm, R. J. The Role of Atomic Ensembles in the Reactivity of Bimetallic Electrocatalysts. *Science* **2001**, *293*, 1811 LP – 1814.

[54] Herrero, E.; Buller, L. J.; Abruña, H. D. Underpotential Deposition at Single Crystal Surfaces of Au, Pt, Ag and Other Materials. *Chemical Reviews* **2001**, *101*, 1897–1930.

[55] Yang, Y.-Y.; Ren, J.; Zhang, H.-X.; Zhou, Z.-Y.; Sun, S.-G.; Cai, W.-B. Infrared Spectroelectrochemical Study of Dissociation and Oxidation of Methanol at a Palladium Electrode in Alkaline Solution. *Langmuir* **2013**, *29*, 1709–1716.

[56] Wang, J.; Cheng, N.; Banis, M. N.; Xiao, B.; Riese, A.; Sun, X. Comparative study to understand the intrinsic properties of Pt and Pd catalysts for methanol and ethanol oxidation in alkaline media. *Electrochimica Acta* **2015**, *185*, 267–275.

Chapter 5

Development of an ATR-SEIRAS Platform for time-resolved Investigation of Dynamic Electrochemical Processes with Step Scan FTIR

5.1 Introduction

A crucial class of electrochemical processes are heterogeneous electron transfer reactions involving a molecule and the electrode surface. For complex chemical reactions, such as the methanol oxidation reaction introduced in Chapter 3, optimising the oxidation pathway greatly benefits from direct measurement of the surface adsorbed intermediates with chemical specificity. Various surface sensitive *in situ* vibrational spectroscopy techniques have emerged as powerful tools to directly measure monolayer or even sub-monolayer quantities of molecules absorbed on electrode surfaces. This is quite remarkable given that there are only about 10^{12} adsorbed molecules in a 1 mm^2 area of irradiated surface.

One proven strategy utilized in both surface enhanced Raman spectroscopy (SERS) [1] and surface enhance infrared absorption spectroscopy (SEIRAS) [2,3] is to drastically increase the analytical signal generated at the electrode surface through electromagnetic enhancement

mechanisms. In the case of SERS, electromagnetic effects dominate the enhancement factor and rely on resonance conditions between the Raman excitation line and the localized surface plasmon polaritons (LSPP) of metal islands, colloids, or roughened continuous electrodes. This limits the technique to metals such as Ag and Au and requires surface compositions that can support LSPPs. Alternative methods such as reflection absorption infrared spectroscopy (RAIRS)[4–6] or sum-frequency generation (SFG)[7–10] are more amenable to use of smooth metal electrode surfaces (and are not limited to metals with resonant LSPP modes) with well known crystallographic orientation but come at the cost of less sensitivity. With advantages and disadvantages for every technique, the selection of a tool that offers both electrochemical compatibility and strong enough surface enhancement will be primarily motivated by the system of interest.

For investigating the kinetics of fast electrochemical processes of surface absorbed molecules, very few implementations of the techniques described above have been reported in the literature[11–17]. The central challenge is the electrochemical requirement for UME to allow a fast response to potential perturbations. The decrease in electrode surface dimension(s) into the micrometer range not only negatively effects S/N, but also demands spectroscopic sensitivity to femtomole quantities of molecules which is an experimentally challenging endeavour. Previous work by Rosendahl *et al.* on ferri/ferrocyanide (a model electrochemical system)[18] indicated that high brilliance synchrotron radiation could provide a much broader applicable platform than previous examples in the literature by Sun *et al.*[11,12].

While this initial study showcased microsecond time-resolution of femtomole quantities of analyte, the experiments described in Chapter 3 and 4 of this thesis suggested that even with SIR, further signal enhancement is required to investigate more challenging electro-

chemical systems such as surface adsorbed reaction intermediates with step scan FTIR. It was recognized by this group as early as 2015 that the ultimate goal of performing microsecond time-resolved step scan FTIR studies of electrochemical reactions would require the successful coupling of SIR and a surface enhancing IR technique such as ATR-SEIRAS (attenuated total reflection surface enhanced infrared absorption spectroscopy). An overview of ATR-SEIRAS is provided below, but briefly the technique relies on internal reflection through a suitable IR prism modified by the presence of a metallic film on its principal reflection plane. This film provides both the electrode surface as well as the optical response that generates surface enhancement. Combining the enhancement of SEIRAS with SIR has the potential to provide the required signal amplification to perform fast time-resolved step scan FTIR measurement on UMEs. Performing measurements in ATR-configuration mitigates some of the strong background absorption of IR light by liquid media compared to the IRRAS configuration.

Direct transition from external reflection FTIR geometry to measurements of UMEs in ATR-geometry at the Canadian Light Source is not trivial. Repeated efforts were made by the Burgess group to achieve this goal. It eventually required the design and construction of a new IR microscope end station at the mid-IR beamline. This work was done in parallel by a coworker[19,20], while work described in this Chapter was ongoing. This Chapter describes the author's efforts to address key complexities and technical restrictions associated with combining ATR-SEIRAS with time-resolved FTIR.

5.2 Background

5.2.1 Surface Enhanced Infrared Absorption Spectroscopy

At the center of surface enhanced vibrational spectroscopy techniques is the interaction of incident light with small anisotropic metal structures, resulting in electromagnetic enhancement of the analytical signal of molecules adsorbed on the metal surface. The origin of the surface enhancement is complex and beyond the scope of this thesis and the details can be found in various reviews[3,21] on the subject matter. Here, it will be limited to crucial elements for the experimental work in chapter 5 and 6, based on Osawa *et al.*'s model of the system[3,22–24], who pioneered the development of attenuated total reflection (ATR) - surface enhance infrared absorption spectroscopy (SEIRAS) for electrochemistry.

In Osawa's model for IR signal enhancement of SEIRAS, metal surfaces are composed of ellipsoidal metal island supported upon a thin continuous layer of Au as shown in Figure 5.1. Upon illumination of infrared light, a polarization p is induced into these metal island if one of the dimensions of the metal particles is smaller than the wavelength of incident light, which in turn generates a strongly enhanced electric field intensity in its vicinity. Based on earlier work by the group on isolated surface enhancing Ag islands[24], the resulting enhancement of the IR absorption is due to electromagnetic and chemical enhancement contributions. On the electromagnetic side, the induced polarization generates an additional electromagnetic (EM) field surrounding the island that decays quickly away from the particle. The EM field intensity scale in distance from the surface with a $1/r^6$ dependence such that the effective range of this contribution is limited to $r < \sim$10 nm[24].

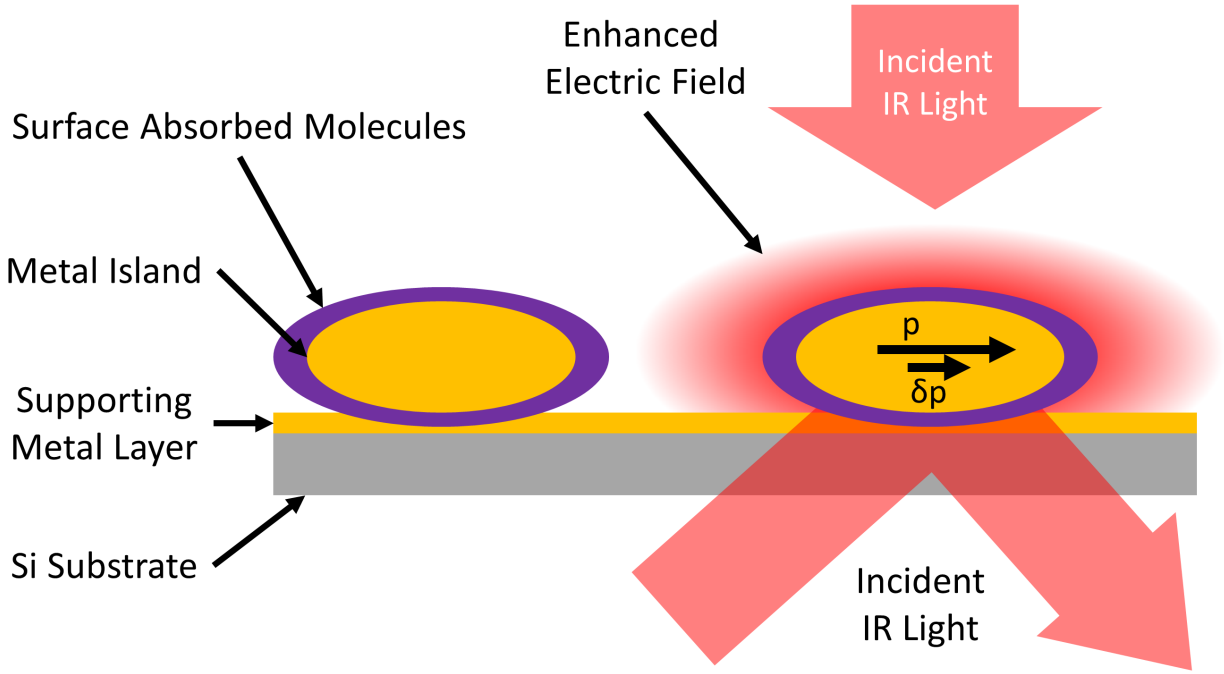

Figure 5.1: Adapted from Osawa[3]. Schematic representation of the metal surface for SEIRAS consisting of ellipsoidal metal island on a thin supporting metal layer. Upon illumination, the induced polarization p generates an enhanced electric field. This in turn causes a polarization perturbation δp in the metal island at frequencies matching the molecular vibration of the surface absorbed molecule.

As IR absorption of molecules is proportional to the electric field intensity, IR absorption of the molecules within the 10 nm is drastically enhanced. Additionally, the EM field generated by the polarized metal island is normal to the metal surface, which results in: 1) Preferentially oriented molecules adsorbed on the surface with vibrational modes that are defined by a transition dipole moment normal to the metal surface will interact with the EM field much more strongly compared to molecules with random orientation; 2) On the chemical side, the vibrational transition dipole moments of absorbed molecules within the enhanced electric field generate a small polarization perturbation δp of the metal polarization p, which results in additional changes of the absorption of the island at the frequency matching the vibrational mode of the particle. Combined, these three effects offer enhancement of vibration absorption cross sections by a factor of about 10^3 for molecules directly adsorbed on the metal surface. The surface normal orientation of the EM field also offers the possibility to detect orientation changes of the absorbed molecules.

5.2.2 Attenuated Total Reflection – Surface Enhanced Infrared Absorption Spectroscopy

Since its introduction, ATR-SEIRAS has become a powerful technique to investigate the chemical and structural composition of surface adsorbed molecules and thin layers. For example, the experimental confirmation of formate as a reaction intermediate of the methanol oxidation reaction was reported by Osawa *et al.* through an ATR-SEIRAS measurement with a textured Pt metal film[22]. The optical arrangement of the technique for spectroelectrochemistry can be found in Figure 5.2. The incident IR light is passed through an IR transparent

internal reflection element (IRE) composed of a material with high refractive index such as germanium or silicon. At the solid-liquid interface, the IR light is totally internal reflected, leaving only an evanescent wave that protrudes from the IRE into the medium of interest. In the absence of a metal film, the evanescent wave extends into the optically rarer medium a distance roughly equal to half of its wavelength $\lambda/2$. However, as described above, a suitably textured metal film can couple with the evanescent wave and lead to localization of the EM field.

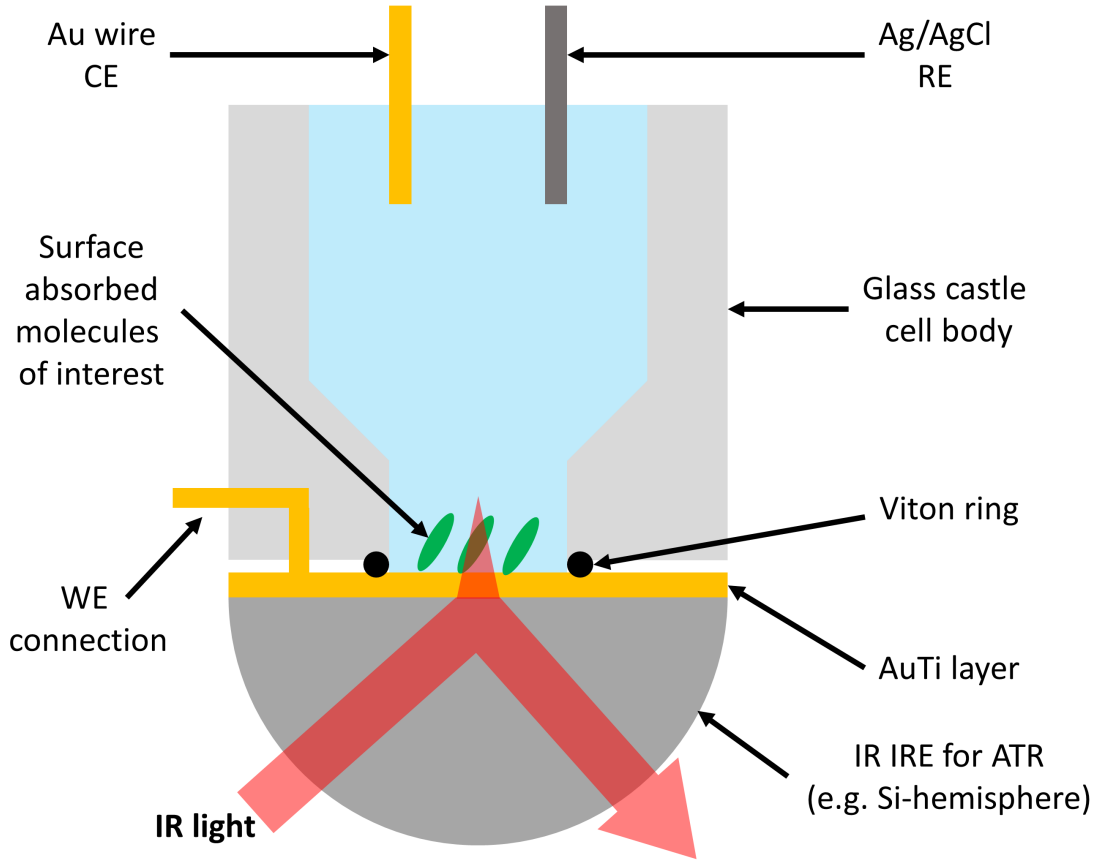

Figure 5.2: Schematic model of the assembled ATR-SEIRAS spectroelectrochemical "glass castle" setup.

A major advantage of the ATR optical configuration is the strongly reduced background absorption of the liquid medium compared to the external reflection geometry used

in Chapters 3 and 4. The most crucial aspect of ATR-SEIRAS is the preparation of thin, textured metallic layers, typically around 20 nm or less in thickness, that are responsible for generating the surface enhancement. ATR-SEIRAS can be performed on a very wide range of metals including those that are highly catalytically active (Pt, Pd)[23,25,26] and 3d transition metals such as Cu, Ni and Fe[27–29]. However, gold is often a preferred metal for electrochemical ATR-SEIRAS due to the relative ease of preparation of thin metal films[2,30]. Furthermore, the inert nature of Au makes it an excellent electrode material for a host of electrochemical systems ranging from fundamental study of double layer composition[31,32] to investigations on functionalized surface[33–35].

While the utility of ATR-SEIRAS Au surfaces for electrochemistry is well known, these layers can be experimentally challenging. Au layers on Si-based IRE's prepared through physical deposition methods (sputtering, thermal evaporation) are known to be mechanically labile due to the weak bonds between Au and Si-oxide surface. Osawa *et al.*[30] developed an alternative, electroless deposition method of Au. In this method the oxide surface layer of silicon is removed before a galvanic reaction between tetrachloraurate ions and hydrogen terminated silicon leads to an Au layer through the formation of Au-Si bonds. Freshly prepared electroless deposited layers show increased mechanical stability compared to physical deposition methods, however, prolonged exposure to air and aqueous electrolytes gradually destabilizes the Au-Si bonds through oxidation. The delamination of these layers can also be further expedited during electrochemical experiments by applying modest potentials to the surface that support either hydrogen evolution or Au-oxide formation. Considering step scan FTIR measurements require up to 100,000 iterations of a potential perturbation sequence to the electrode, the stability of the SEIRAS-active Au layers must be very robust. The two

options are to either remain within a small potential window between 0 - 0.7 V vs Ag/AgCl where Au layers are more stable (as utilized in Chapter 6) or to increase the overall stability of the Au layers through an adhesion layer for measurements outside of this potential window. In this Chapter, option two was explored as the step scan measurement herein will focus on 4-methoxypyridine (MOP) adsorption/desorption kinetics that requires a potential step (E_{step}) to a relatively large potential excursion to fully desorb the MOP.

5.3 Methodology/Discussion

The overall objective of the work present in this Chapter is the development and demonstration of a step scan FTIR measurement in ATR-SEIRAS configuration on an electrochemical system. This can be broken down into three parts. 1) Descriptions of the step scan FTIR setup, the spectroelectrochemical components and preparation of SEIRAS-active AuTi layers. 2) Step scan FTIR measurements of an electrochemical system (MOP) as well as an in-depth description of the subsequent data processing. 3) A discussion and outline of the remaining challenges in the developed of electrochemical step scan FTIR.

5.3.1 Reagents, Solutions and Instrumentations

H_2SO_4 (Fisher Scientific), NaF (Fisher Scientific), KCl (ACS grade, Fisher Scientific) and 4-Methoxypyridine (Fisher Scientific) were purchased and used as received. All aqueous solutions were made using Milli-Q water (> 18 MΩ cm).

All FTIR measurements were performed with a Bruker VERTEX 70 FTIR spectrometer with a conventional globar source. The IR light is directed by a Veemax III variable

angle ATR accessory (PIKE technologies) to illuminate the spectroelectrochemical cell in ATR configuration. The light internally reflected by the sample is subsequently measured by a 100 μm narrowband MCT detector. IR data were collected using Bruker's OPUS software and processed with the software's internal Fourier-transform algorithms.

All purely electrochemical measurements were performed in a standard three electrode configuration using a HEKA PG 590 potentiostat. Current and potential data were collected using a USB 6351 X-series multifunction DAC (National Instruments) controlled through a Labview interface. The Labview program was written by the author and is described in detail in Appendix IV.

5.3.2 Step Scan FTIR Implementation

Arguably the most crucial technical aspect for experiments in Chapter 5 and 6 is the development work on the setup and procedure for step scan FTIR which is described here. The overall setup will be described first, before providing a detailed walkthrough of a single step scan iteration and lastly a demonstration of the synchronous timing between the electrochemistry and IR required for a spectroelectrochemical step scan FTIR measurements.

Figure 5.3 is a schematic overview of the individual components of the step scan FTIR setup. The electrochemical aspects of SEC are controlled by a Labview program (Appendix IV) that controls the potentiostat through a DAC. The WE potential applied to the SEC can be changed through an analog signal from the DAC to the potentiostat. The analog current (I) and potential (E) responses of the cell, as measured/applied by the potentiostat are recorded by the DAC. On the spectroscopy side, the OPUS software operates the step scan FTIR measurement through a custom macro. It should be noted that

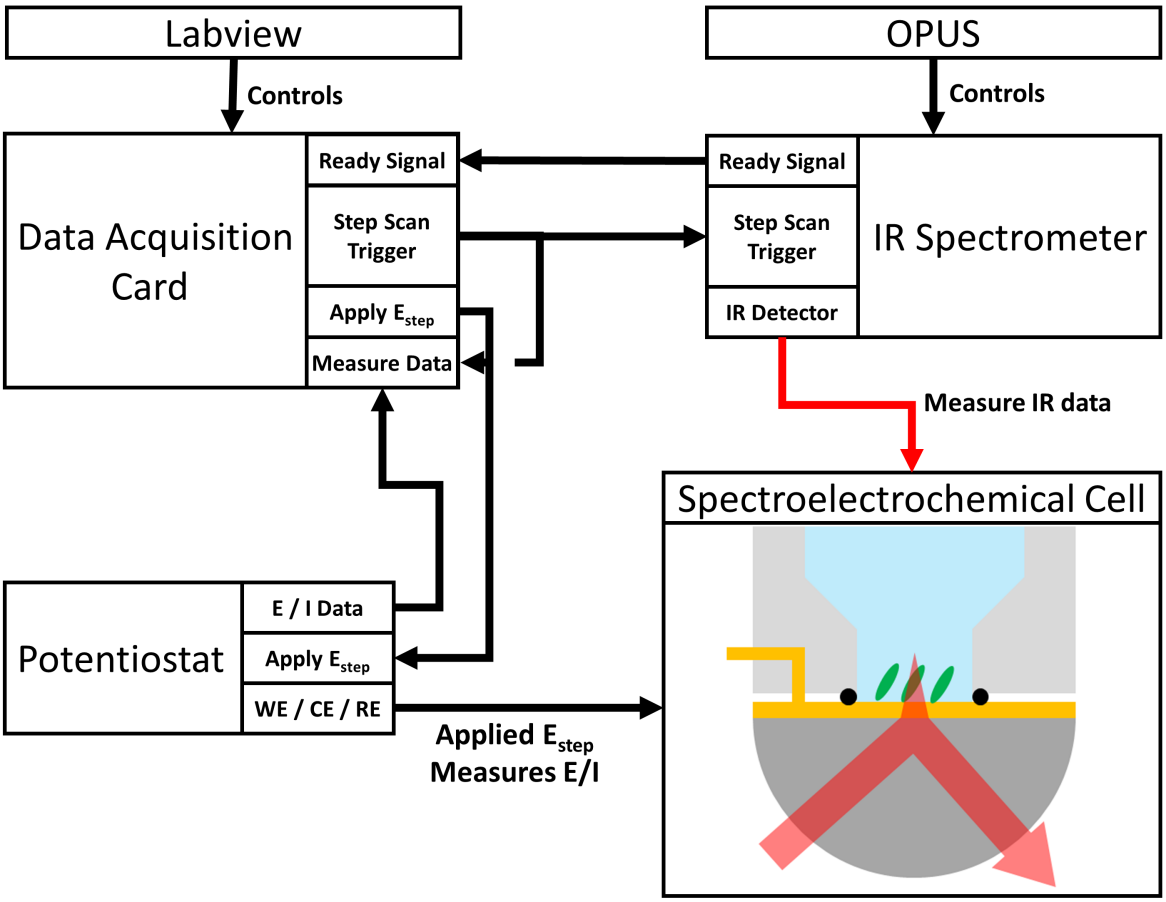

Figure 5.3: Schematic of experimental setup for step scan FTIR measurement with SEC.

while the step scan experiments described in Chapter 5 and 6 had both Labview and OPUS running on the same computer, the communication between IR and electrochemical aspects was intentionally limited to simple TTL signals between the DAC and the spectrometer in order to simulate the interface environment for future step scan experiments at the mid-IR beamline of the CLS.

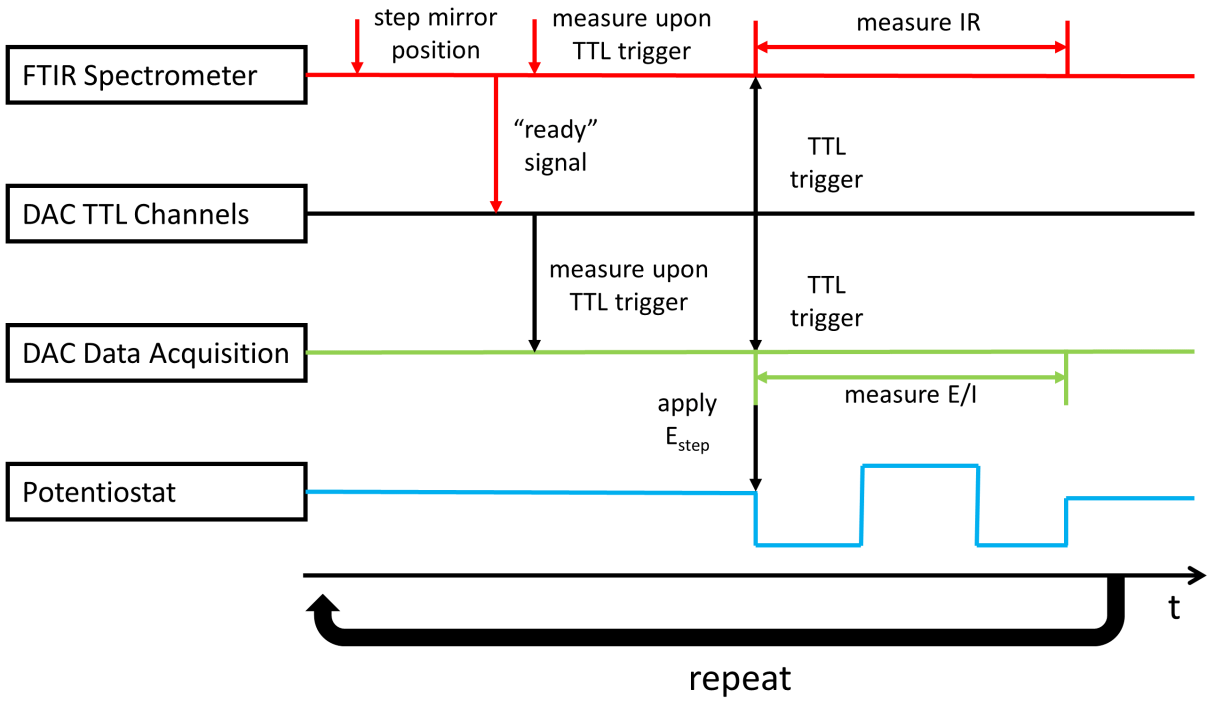

Figure 5.4: Schematic of experimental timing sequence for a single step scan FTIR iteration.

Figure 5.4 is a schematic overview of a single step scan iteration. At the beginning of each iteration, the spectrometer steps the interferometer mirror to the next mirror position. Once stepped, a "ready" signal is sent to the DAC and the spectrometer waits for a rising edge trigger signal to start the IR measurement. The DAC receives the "ready" signal and prepares to measure E/I data upon a rising edge trigger signal. With both DAC and spectrometer ready to measure, the DAC simultaneously generates two potential sequences.

One contains a TTL rising edge and the other the potential sequence that needs to be applied to the WE of the SEC. The first one is split and triggers the E/I and IR measurements, while the second one is sent to the potentiostat. After the measurement, all DAC channels are reset, and the next step scan iteration starts.

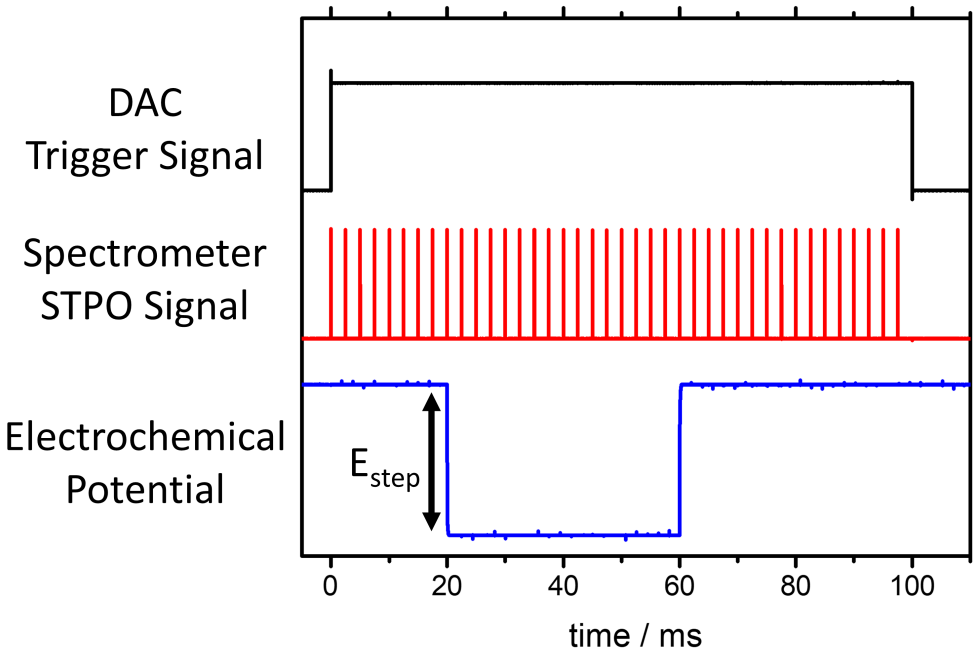

Figure 5.5: Experimental test results for timing accuracy between DAC, FTIR spectrometer and Potentiostat. At $t = 0$, spectrometer is triggered by rising DAC trigger signal and records 40 IR signals with 2.5 ms time-resolution. Spectrometer STPO rising TTL signal correspond to the start of each IR signal in time. Potentiostat accurately applies E_{step} 20 ms after rising DAC trigger signal followed by $-E_{step}$ at 60 ms.

The most crucial aspect is synchronous timing between the IR data collection and the potential perturbation applied to the SEC after initiating the measurement with the TTL trigger. The Labview program and instrumentation were utilized to record three signals as shown in Figure 5.5. The black line is the 5 V rising edge TTL signal generated by DAC to initiate the IR data collection and electrochemical measurement and defines $t = 0$. The

red line is a signal from the spectrometer that indicates start of IR data acquisition for each time element within a single step scan iteration. Here it is set to acquire IR date for 40 time elements with a rather low, 2.5 ms time-resolution for better graphical representation. The blue line shows the potential response of an electrochemical dummy cell to potential perturbation applied by the potentiostat. For this measurement, the potential sequence is set to remain at resting potential for an initial period of 20 ms after receiving the TTL trigger. Afterwards the potential is stepped to a negative potential for 40 ms before returning to resting potential. The results in the figure demonstrate synchronous timing of the setup within the acquisition rate of the DAC, which was set to 500 kHz (*i.e.* 2 μs resolution) during this test.

5.3.3 Spectroelectrochemical Cell

All ATR-SEIRAS experiments in this Chapter were performed in a home-built spectroelectrochemical cell for ATR-SEIRAS experiment developed in the Burgess group[36]. These cells were utilized earlier by Quirk *et al.*[37] to perform potential dependent ATR-SEIRAS experiments on MOP adsorption and orientation on Au surfaces. A schematic representation of the setup is shown in Figure 5.2.

The spectroelectrochemical cell is assembled onto a metal plate that fits the VeeMAX III ATR accessory attached to the FTIR spectrometer. A silicon hemisphere was used as the internal reflection element (IRE) for ATR and sputter coated with a 3 nm thick adhesion layer of Ti followed by a 20 nm thick Au layer. The IRE is placed onto a Delrin holder with the hemisphere centered onto the clearance space in the center to allow IR illumination from below. An 8 mm inner diameter Viton rubber gasket followed by a machined Teflon cell

base is placed on top of the Au film. The IRE, Delrin holder and Teflon base are secured onto the metal plate through multiple screws, creating a watertight seal between the Au film and Teflon base. The remaining glass elements are attached to the Teflon case to create an electrochemical cell with a conventional three electrode arrangement. The AuTi film on the IRE is the WE, with electrical contact made through spring-loaded, retractable pins housed within the Teflon base. An Au wire is used as the CE and Ag/AgCl served as the RE. A long and short glass tube can be used to purge the electrolyte solution of dissolved oxygen and maintains an inert atmosphere of argon within the cell.

5.3.4 ATR-SEIRAS AuTi-Layer Preperation

In order to prepare SEIRAS-active Au surfaces that can withstand the repeated potential steps to -0.9 V required for MOP desorption, a thin (∼3 nm) undercoat of Ti was sputtered onto the silicon oxide IRE substrate before depositing the 20 nm thick Au layers. The primary function of this Ti layer is to improve the mechanical adhesion of the Au to the silicon oxide, by forming a covalent bonds with the underlying oxide while simultaneously creating a thin metal-metal alloy interface with the later deposited gold metal on top. While AuTi layers are commonly found within the literature[38,39], its implementation for SEIRAS is to my knowledge limited to two reports by Ohta *et al.*[40,41]. The primary reason why Ti is not extensively reported for ATR-SEIRAS is that it seems an underlying layer of Ti results in very smooth surface morphologies that are detrimental to the enhancement mechanisms described earlier[42,43]. Here, only the method utilized to obtain AuTi layers will be described. A later part of the chapter will go further in-depth on challenges in the reproducibility of AuTi for SEIRAS and the resulting viability for further experiments.

AuTi layers were prepared on a Si hemisphere IRE for ATR through subsequent magnetron sputtering of first Ti and then Au without breaking vacuum to avoid oxidation of the Ti. Sputtering was done in a Kurt J. Lesker Corp PVD 75 magnetron sputtering chamber with two separate sputter heads at base pressure of $< 3\times10^{-6}$ Torr and sputtering pressure of 5×10^{-3} Torr with argon serving as the sputtering gas. 3 nm thick Ti and 20 nm thick Au layers were deposited at ~ 0.1 nm/s, matching the sputtering conditions for the SEIRAS AuTi layer initially reported by Ohta *et al.*[40]. After assembly into the spectroelectrochemical cells, the AuTi layers required an additional treatment of the Au surface through electrochemical annealing (ECA) in 0.5 M H_2SO_4, by cycling the potential of the AuTi WE between -0.2 V and 1.3 V at 100 mV/s for at least 2 h. Once ECA is completed, the assembled spectroelectrochemical cell is thoroughly rinsed with Millipore water, before the solution of interest (50 mM NaF + 1 mM MOP) was introduced.

5.3.5 IR Characterization of ATR-SEIRAS AuTi-Layers

Before attempting any step scan FTIR measurements, the SEIRAS performance of all freshly prepared AuTi layers was characterized through a conventional IR measurement of the MOP desorption/adsorption. After introduction of MOP into solution, the WE potential is stepped to -0.9 V and +0.6 V to induce desorption/adsorption of the pyridine derivative respectively. A single beam IR spectrum is collected at each potential. Using the spectrum at +0.6 V as reference, a MOP desorption spectrum is calculated and a representative IR spectrum of a SEIRAS-active AuTi layer is shown in Figure 5.6. The three sharp downward going peaks at 1615 cm^{-1}, 1509 cm^{-1} (ring vibrations) and 1310 cm^{-1} (C−O−C stretch) can be assigned to the loss of MOP after stepping to negative potentials as the peak positions compare

favorably with previous literature reports[37]. The increase in the broad H_2O feature around 1700 - 1600 cm^{-1} is likely due to a combination of more H_2O at the electrode surface due to the loss of MOP as well as stronger H_2O ordering due to the more negatively charged electrode surface. The increase in noise within the spectrum at wavenumbers <1500 cm^{-1} is a result of IR absorption due to the Si IRE. The insert in Figure 5.6 shows the single beam spectrum measured by the MCT detector. At around 1500 cm^{-1}, the overall IR light passing through the silicon drops to 20% of its maximum intensity. This results in a decrease of the S/N for the MOP signal at 1509 cm^{-1} and 1310 cm^{-1} and will be detrimental for later step scan FTIR measurements.

Comparing the SEIRAS performance of the AuTi layer to previous results within the group on pure Au layers, the IR signal intensity of the MOP signals is lower by about a factor of ∼2. The decrease is expected as Ti is detrimental to the SEIRAS-activity of the Au layers, even when limited to only a thin layer (∼3 nm) between Au and the Si IRE[42,43]. In exchange for the poorer SEIRAS performance, the mechanical stability of AuTi is drastically improved. No delamination has ever been observed on any sputtered AuTi layers and removal of the metal film from the IRE required the use of concentrated aqua regia and HCl for Au and Ti respectively. In contrast, and as mentioned above, Au films directly deposited on silicon are incredibly fragile and delaminate upon minimal mechanical abrasion.

5.3.6 Step Scan FTIR of MOP Desorption/Adsorption

A step scan experiment was conducted using the AuTi layer to measure the kinetics of MOP desorption/adsorption. The step scan measurement timing and potential sequence is analogous to the one shown in Figure 5.5. On the electrochemical side, the potential was

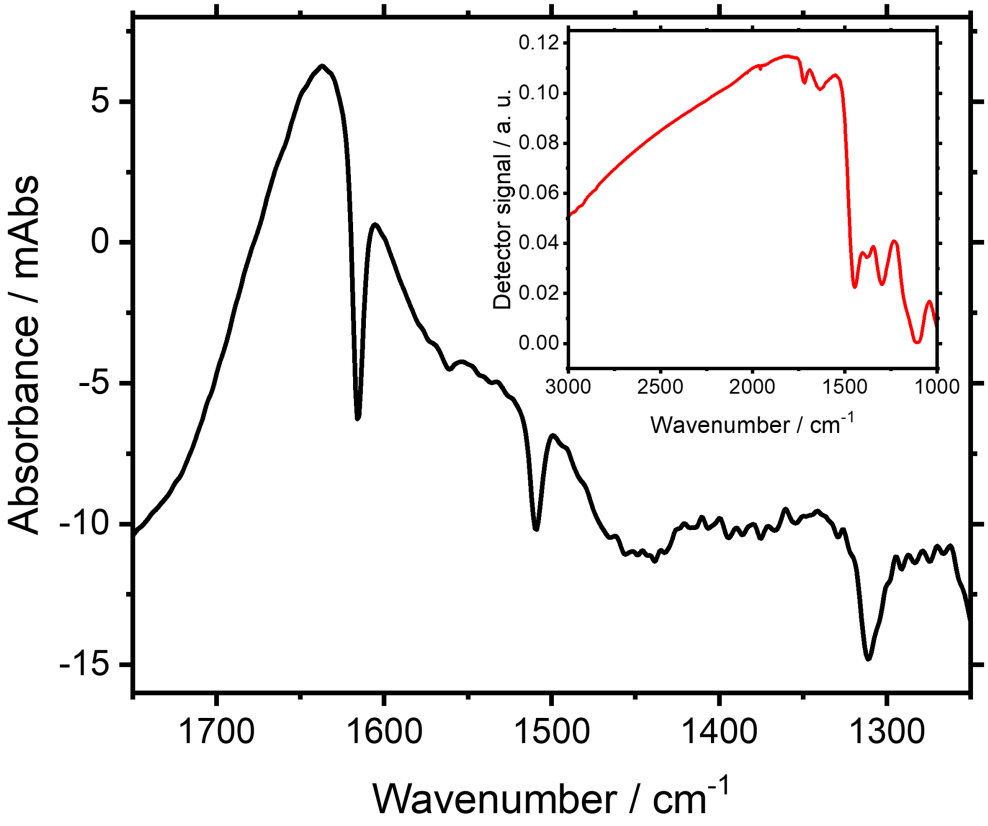

Figure 5.6: ATR-SEIRAS spectra of MOP desorption in 50 mM NaF solution with 0.1 mM MOP after E_{step} to -0.8 V. Sharp IR signals corresponding to MOP are found at 1615 cm^{-1}, 1509 cm^{-1} and 1310 cm^{-1}. The reference spectrum is measured at +0.6 V. Insert shows the corresponding single beam IR spectrum.

initially held at a base potential of +0.6 V for 50 ms during which time an IR measurement was made to establish a background. After this, the potential was stepped to -0.8 V (for 100 ms) to induce MOP desorption, followed by a E_{step} back to +0.6 V (for 100 ms) to reabsorb the MOP. The spectrometer was set to measure IR signal with 2.5 ms time-resolution for 250 ms per step scan iteration, after receiving the TTL trigger. Spectral information was collected from 1000 - 2500 cm^{-1} with a wavenumber resolution of 8 cm^{-1}. With these settings, the collection of a single-sided step scan interferogram required measurements at 740 different mirror positions. The transient recorded at a given mirror position was ∼1 s in duration meaning a single data cube required ∼12 min. In order to achieve sufficient co-adding to lower the noise to an acceptable level, 64 data cubes were required. Thus, the total measurement time for a step scan experiment was ∼12 h.

An important aspect of the analysis of the IR spectra is the data processing that is shown schematically in Figure 5.7. The raw step scan interferograms collected by the spectrometer are FT individually in OPUS and further processed by a custom Matlab script (Appendix V). The script constructs a reference spectrum for each step scan by coadding the spectra of the initial 10 time elements of the measurement. Utilizing the reference spectra, an absorbance spectrum is calculated for each time element of each step scan before coadding the individual step scan spectra. The result are 90 IR absorbance spectra of MOP desorption/adsorption covering a 225 ms window with 2.5 ms time-resolution.

Figure 5.8 shows the results from the step scan FTIR measurement of MOP desorption/adsorption with only spectra at 25 ms intervals shown to reduce graphical clutter. The first spectrum (black line) is taken at $t = 25$ ms after acquisition of the reference spectra where the electrode potential is still at +0.6 V. The spectra suggest a noise level of ∼0.3 mAbs

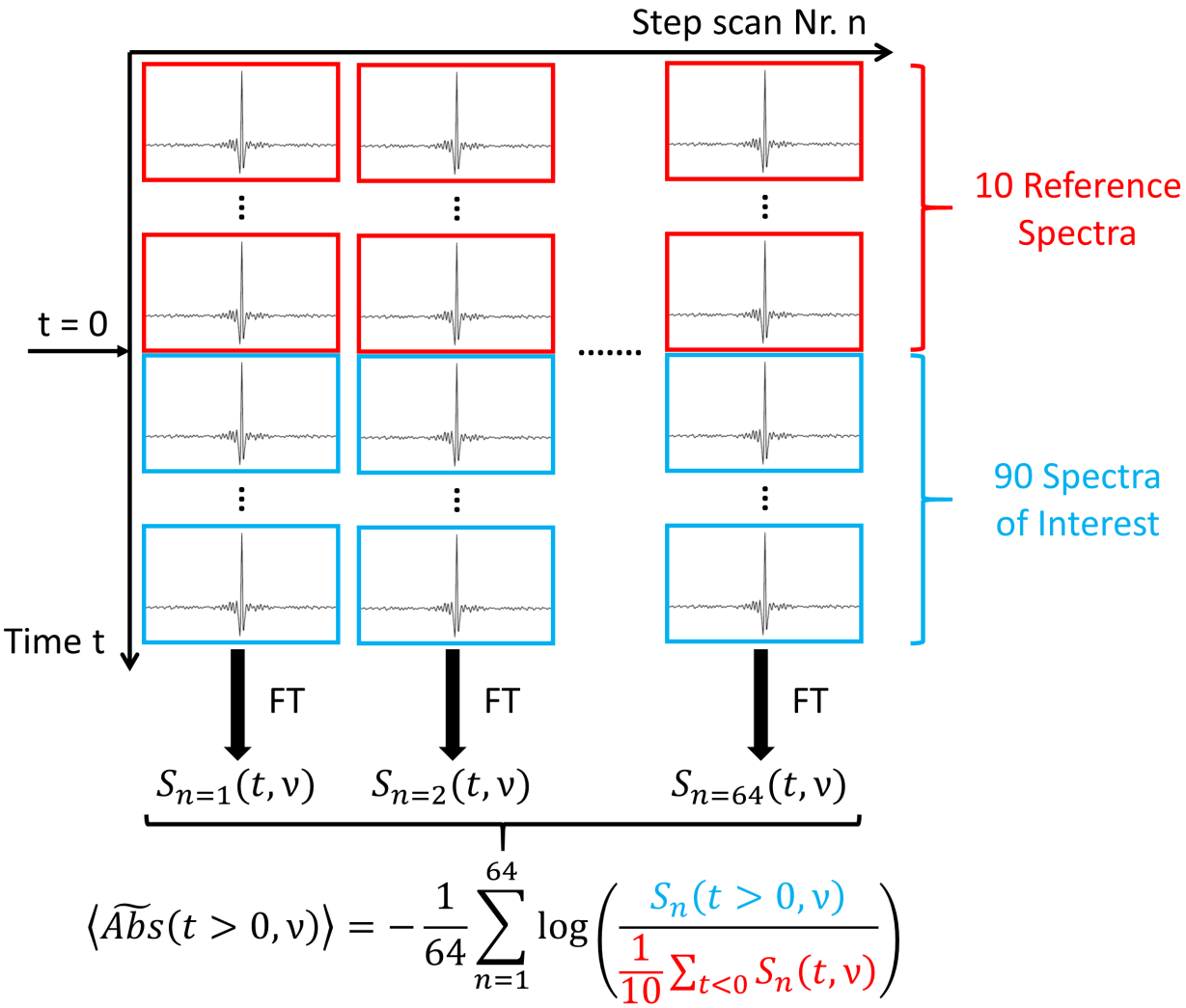

Figure 5.7: Schematic representation of post measurement data processing for a step scan FTIR experiment. The FTIR spectrometer recorded 64 step scan FTIR data cubes. Each interferogram for the 100 time-element within a data cube is Fourier-transformed into a single beam spectrum in wavenumber space. An absorbance spectrum for each data cube is calculated by constructing a reference spectrum from the initial 10 time-elements. Finally, the absorbance spectra for each time element are coadded together to create the final cube of IR spectra over time.

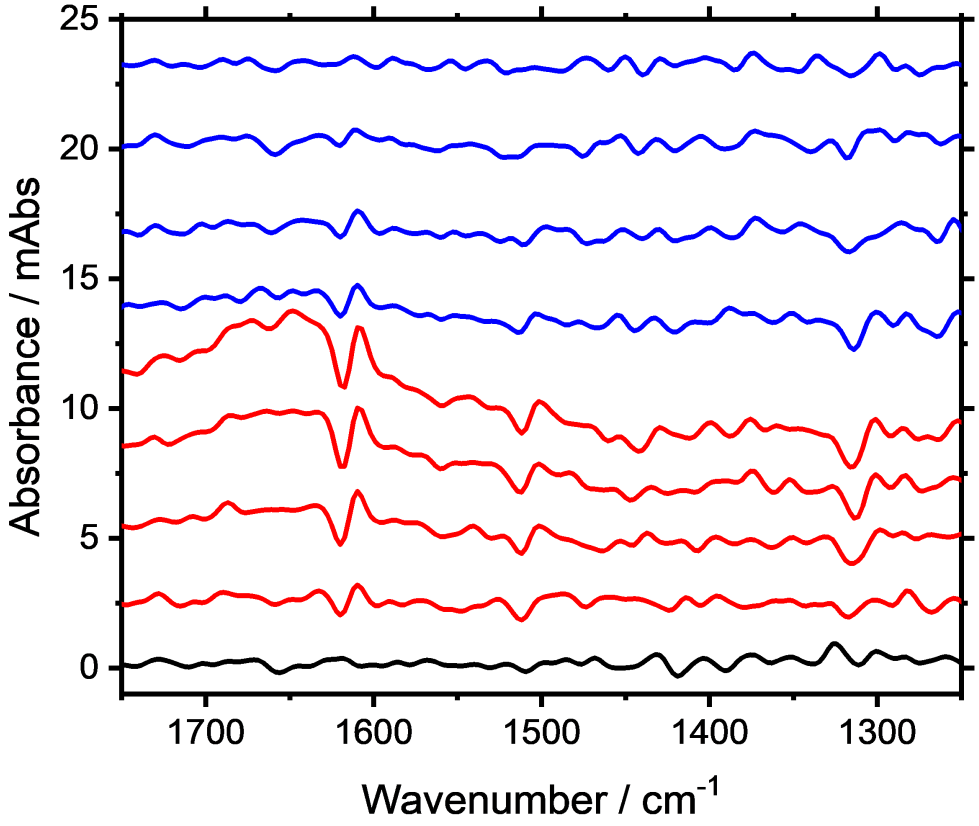

Figure 5.8: Selected step scan FTIR spectra (every 25 ms) of MOP desorption/adsorption with reference spectra at +0.6 V. The spectra correspond to +0.6 V (black), followed by MOP desorption over 100 ms after E_{step} to –0.8 V (red) and subsequent MOP adsorption over 100 ms after E_{step} +0.6 V (red). IR signal corresponding to MOP are found at 1615 cm^{-1}, 1509 cm^{-1} and 1310 cm^{-1}

and ∼0.7 mAbs within the spectral region >1500 cm^{-1} and <1500 cm^{-1} respectively. The higher noise at lower IR frequencies is due to the reduced Si transparency as described above. The next four spectra (red lines) show the decrease in MOP IR signals due to the desorption of the molecule after the E_{step} to -0.8 V at t = 25 ms. All three MOP IR modes at 1615 cm^{-1}, 1509 cm^{-1} and 1310 cm^{-1} are clearly visible and the absolute value of the relative absorption intensities increase over the course of 100 ms before reaching a maximum of 2.5 mAbs, 1 mAbs and 1.3 mAbs respectively. In addition to the MOP signals, an increase of the broad H_2O signal between 1550 and 1750 cm^{-1} can also be observed. The last four spectra (blue lines) show the return to baseline after stepping the potential back to +0.6 V at t = 125 ms which leads to the re-adsorption of MOP on the surface and a net displacement of adsorbed water molecules.

A better graphical representation of the time progression can be achieved by plotting the peak transients of the MOP IR signal in time. Figure 5.9 shows the peak transient for the 1615 cm^{-1} MOP signal. To extract the peak intensities, a baseline fit was required to compensate for changes in IR absorption due to the broad H_2O signal. For the desorption of the MOP (*i.e.* during t = 25 - 125 ms) the IR signal drops rapidly for the initial 75 ms before stabilizing. The adsorption of MOP appears slower, with only a rapid increase in the initial 25 ms, followed by a slow increase for the remainder of the measurement. The difference is likely due to simple mass transport effects. For desorption, the kinetics of the process is less affected by mass transport, as MOP on the electrode surface is fixed. For adsorption however, diffusion limits the transport of MOP from solution to the electrode surface, slowing down the adsorption process. Overall, the step scan FTIR results presented here demonstrates that the developed FTIR setup is fully capable of measuring the kinetics

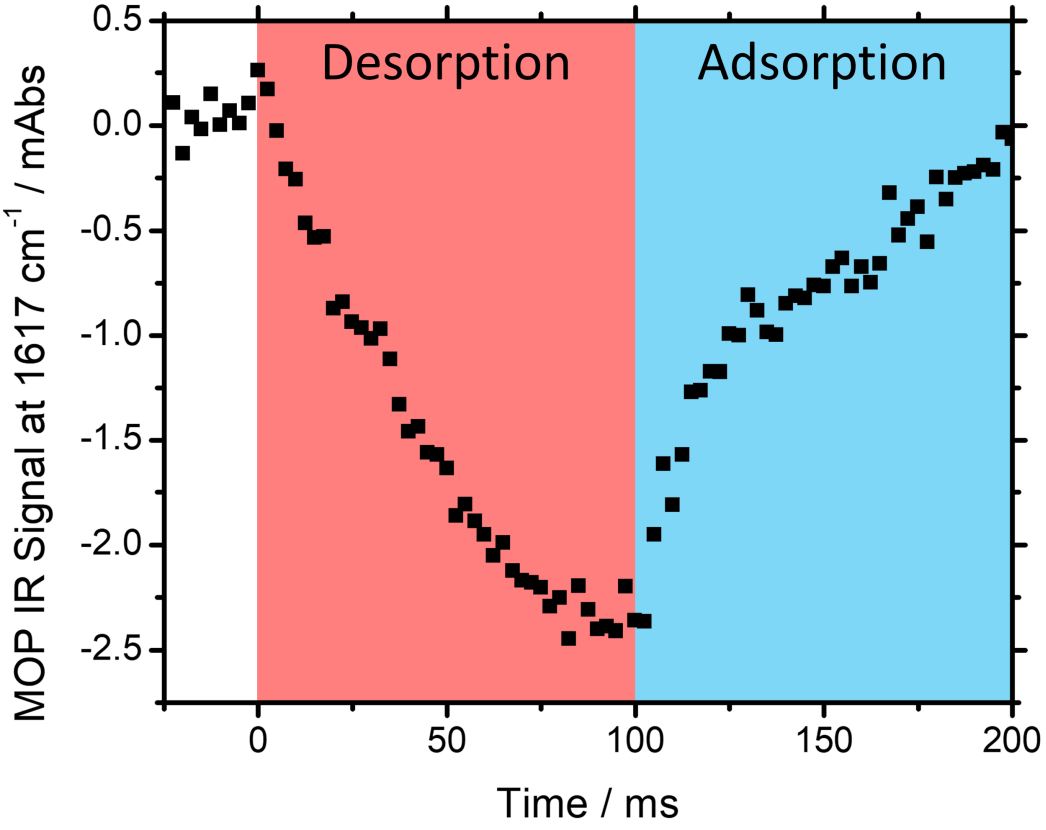

Figure 5.9: Step scan FTIR transient of the MOP IR signal at 1617 cm^{-1}. The red and blue background indicate the region where MOP desorption and adsorption occurs due to E_{step} from +0.6 V to -0.8 V at $t = 0$ and from -0.8 V to +0.6 V at $t = 100$ respectively. The reference is measured at +0.6 V.

of surface adsorbed species.

5.3.7 Challenges with AuTi for ATR-SEIRAS

While the results described above showed great promise, the reliability of the AuTi film preparation method remained a major area of concern. Sputtering and electroless deposition methods, utilized within the literature and this research group to prepare pure Au layers[30,31,37], can be optimized to reliably provide SEIRAS activity. This is not the case with the AuTi films, where the majority of layers are SEIRAS inactive even after significant effort was invested into optimising the preparation. The difficulty of preparing these layer is hinted within the literature, where to the best of my knowledge, only two successful reports of SEIRAS-active AuTi layers have been reported and both came from the same group[40,41]. There are no reports from other research groups using AuTi despite the obvious stability advantages of AuTi-layers.

One explanation for the observed difficulty in obtaining SEIRAS active layers when using Ti adhesion layers is induced surface texturing of the Au through the underlying Ti adhesion layer. As mentioned earlier, sputtered AuTi layers are known to create smoother surface textures compared to rougher pure Au based layers[42,43]. Smooth surfaces are detrimental to the excitation of local plasmonic modes, crucial for surface enhancement of the IR signal. Experimentally, AuTi layers at varying sputtering parameters with average roughness values ranging from 0.96–2.54 nm determined by AFM yielded no improvement, even though the surface roughness value of a SEIRAS active Au layer was measured at 1.20 nm and literature suggests SEIRAS can be achieved with roughness >0.6 nm[30,44,45]. Nevertheless, SEIRAS active AuTi layers were intermittently successful although no correlation could

ever be found between general deposition conditions/film conditioning and SEIRAS activity. Thus, it is likely that only a very narrow range of sputtering conditions are viable.

A compounding issue for AuTi optimization is the instrumentational difficulties originating from the magnetron sputtering device used. AuTi layers require sputtering within a single vacuum chamber to prevent oxidation of the titanium layer. This limited the AuTi layer preparation to a single magnetron sputtering device in the SyLMAND facility at the Canadian Light Source. The sputtering unit possessed two sputtering heads for Au and Ti respectively but lacked a quartz crystal microbalance (QCM) to provide real-time feedback on sputtering rates and layer thicknesses. To compensate, various Ti and Au test layers thickness were measured post-sputtering to provide a calibration curve. The calibration met with only limited success, as sputtering rates under identical instrument parameters will increase as the sputtering targets are used. Significant deviations from calibration curve predictions were measurable less than five sputtering iterations after the establishment of the calibration curve. The situation was further exacerbated as other users of the SyLMAND facility would periodically use the sputtering unit and targets to deposit very thick layers on substrates which effectively completely negated the previous calibration curve.

Although the primary explanation for the deleterious effect of Ti on SEIRAS enhancement is the templating of smooth Au surfaces a second explanation was explored. The incorporation of small quantities of Ti within the Au layer caused either by metallic interdiffusion or cross contamination of the sputtering heads could adversely affect the polarizability of the Au particles. Ti migration along grain boundaries is well known and could occur during deposition and/or the subsequent ECA of the surface[38,46,47]. This would fit experimental observation where the SEIRAS activity of the AuTi layers over long step scan experiments

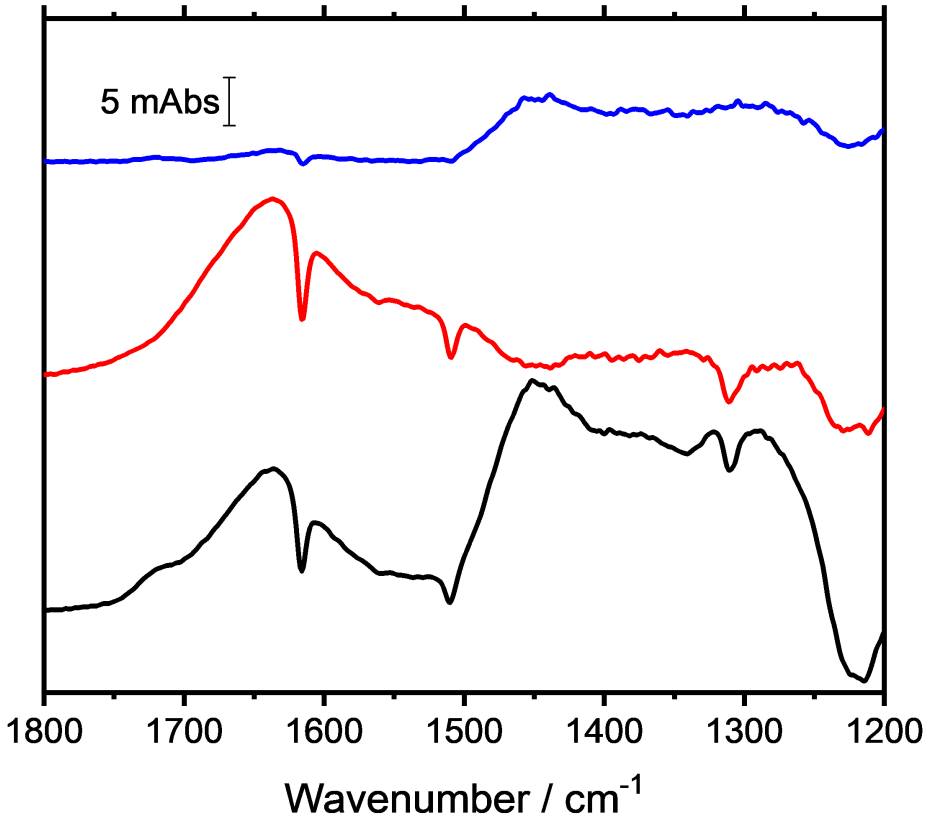

Figure 5.10: FTIR spectra measured during a long (24 h) step scan FTIR experiments showing the degradation of ATR-SEIRAS signal of the AuTi layer over time (black at 0 h, red at 12 h and blue at 24 h). The reference spectrum is measured at +0.6 V.

(24 h) can vary significantly. This is illustrated in Figure 5.10, where normal FTIR spectra are measured at fixed intervals of 12 h during a step scan experiment. While the MOP signatures at 1615 cm^{-1}, 1509 cm^{-1} and 1310 cm^{-1} are clearly visible at $t = 0$ h and change little within the initial 12 h of measurement, the baseline, particularly between 1500 - 1200 cm^{-1} is shifted. Coinciding with the silicon phonon modes that are IR active, it is possible that the Si-Ti layer is slightly altered due to increased oxidation of Ti through imperfections within the Au layer. A more drastic change is observed between 12 - 24 h, where the analytical signal of the MOP for the 1615 cm^{-1} is drastically reduced from 9 mAbs to 1 mAbs and the remaining MOP IR modes fall below the noise level. However, XPS measurements on an electrochemically annealed 20 nm thick Au layer on 3 nm Ti showed no Ti signatures and the exact nature of the stability of the SEIRAS activity was insufficiently investigated due to the difficulty in obtaining SEIRAS active layers when using AuTi. A conclusive answer on what effect is responsible for the difficulties in obtaining reliably SEIRAS active layers remains elusive.

5.4 Conclusion

This Chapter detailed the developmental work on a step scan ATR-SEIRAS platform to measure changes in IR signal of a simple surface adsorbed molecule upon electrochemical potential perturbation. A focus has been placed on the instrumental aspect of the experiment to ensure proper communication and timing between different instrumental components backed up with experimental confirmation. The step scan ATR-SEIRAS measurement of the desorption/adsorption of 4-methoxypyridine upon potential steps demonstrates the ability

of the platform to measure the IR transient signals of the molecules with time-resolution beyond commercially available rapid scan FTIR methodologies.

The experiment also served as a test for the use of AuTi layers, composed of a SEIRAS active Au layer deposited on a thin adhesion layer of Ti. Unfortunately, while the mechanical performance of the AuTi layers was excellent, the SEIRAS activity of the AuTi layers was entirely unreliable and this led to a decision to discontinue the use of these layers for future step scan experiments. This restricts the platform to Au layers directly deposited on Si and means new experiments face an associated much higher likelihood of mechanical failure. This can only be mitigated by the selection of electrochemical systems with a much narrower electrochemical potential window.

With this in mind, the following chapter will aim to utilize the developed step scan ATR-SEIRAS platform to investigate the oxidation/reduction of self-assembled monolayers of ferrocene-alkanethiol.

5.5 References

[1] Aroca, R. *Surface-Enhanced Vibrational Spectroscopy*; Wiley Online Books; 2006; pp 73–184.

[2] Osawa, M. *In-situ Surface-Enhanced Infrared Spectroscopy of the Electrode/Solution Interface in Advances in Electrochemical Sciences and Engineering*; Wiley Online Books; 2008; pp 269–314.

[3] Osawa, M. Dynamic Processes in Electrochemical Reactions Studied by Surface-Enhanced Infrared Absorption Spectroscopy (SEIRAS). *Bulletin of the Chemical Society of Japan* **1997**, *70*, 2861–2880.

[4] Christensen, P.; Hamnett, A. In-situ techniques in electrochemistry — ellipsometry and FTIR. *Electrochimica Acta* **2000**, *45*, 2443–2459.

[5] Wain, A. J.; O'Connell, M. A.; Attard, G. A. Insights into Self-Poisoning during Catalytic Hydrogenation on Platinum Surfaces Using ATR-IR Spectroelectrochemistry. *ACS Catalysis* **2018**, *8*, 3561–3570.

[6] Hinrichs, K. *Reflection Absorption IR Spectroscopy (RAIRS)*; Wiley Online Books; 2011; Chapter 23, pp 367–375.

[7] Chou, K. C.; Markovic, N. M.; Kim, J.; Ross, P. N.; Somorjai, G. A. An in Situ Time-Dependent Study of CO Oxidation on Pt(111) in Aqueous Solution by Voltammetry and Sum Frequency Generation. *The Journal of Physical Chemistry B* **2003**, *107*, 1840–1844.

[8] Lu, G. Q.; Lagutchev, A.; Dlott, D. D.; Wieckowski, A. Quantitative vibrational sum-frequency generation spectroscopy of thin layer electrochemistry: CO on a Pt electrode. *Surface Science* **2005**, *585*, 3–16.

[9] Rupprechter, G.; Bandara, A. *Sum Frequency Generation (SFG) Spectroscopy in Surface and Thin Film Analysis*; Wiley Online Books; 2011; Chapter 27, pp 407–435.

[10] Rey, N. G.; Dlott, D. D. Studies of electrochemical interfaces by broadband sum frequency generation. *Journal of Electroanalytical Chemistry* **2017**, *800*, 114–125.

[11] Zhou, Z.-Y.; Lin, S.-C.; Chen, S.-P.; Sun, S.-G. In situ step-scan time-resolved microscope FTIR spectroscopy working with a thin-layer cell. *Electrochemistry Communications* **2005**, *7*, 490–495.

[12] Zhou, Z.-Y.; Tian, N.; Chen, Y.-J.; Chen, S.-P.; Sun, S.-G. In situ rapid-scan time-resolved microscope FTIR spectroelectrochemistry: study of the dynamic processes of methanol oxidation on a nanostructured Pt electrode. *Journal of Electroanalytical Chemistry* **2004**, *573*, 111–119.

[13] Osawa, M.; Yoshii, K.; Hibino, Y.-i.; Nakano, T.; Noda, I. Two-dimensional infrared correlation analysis of electrochemical reactions. *Journal of Electroanalytical Chemistry* **1997**, *426*, 11–16.

[14] Osawa, M.; Yoshii, K.; Ataka, K.-i.; Yotsuyanagi, T. Real-time monitoring of electrochemical dynamics by submillisecond time-resolved surface-enhanced infrared attenuated-total-reflection spectroscopy. *Langmuir* **1994**, *10*, 640–642.

[15] Wisitruangsakul, N.; Zebger, I.; Ly, K. H.; Murgida, D. H.; Ekgasit, S.; Hildebrandt, P. Redox-linked protein dynamics of cytochrome c probed by time-resolved surface enhanced infrared absorption spectroscopy. *Physical Chemistry Chemical Physics* **2008**, *10*, 5276–5286.

[16] Pronkin, S.; Wandlowski, T. Time-resolved in situ ATR-SEIRAS study of adsorption and 2D phase formation of uracil on gold electrodes. *Journal of Electroanalytical Chemistry* **2003**, *550-551*, 131–147.

[17] Rosendahl, S. M.; Borondics, F.; May, T. E.; Pedersen, T. M.; Burgess, I. J. Interface for time-resolved electrochemical infrared microspectroscopy using synchrotron infrared radiation. *Review of Scientific Instruments* **2011**, *82*, 083105.

[18] Rosendahl, S. M.; Borondics, F.; May, T. E.; Burgess, I. J. Step-Scan IR Spectroelectrochemistry with Ultramicroelectrodes: Nonsurface Enhanced Detection of Near Femtomole Quantities Using Synchrotron Radiation. *Analytical Chemistry* **2013**, *85*, 8722–8727.

[19] Morhart, T. A.; Quirk, A.; Lardner, M. J.; May, T. E.; Rosendahl, S. M.; Burgess, I. J. Femtomole Infrared Spectroscopy at the Electrified Metal–Solution Interface. *Analytical Chemistry* **2016**, *88*, 9351–9354.

[20] Morhart, T. A.; Read, S.; Wells, G.; Jacobs, M.; Rosendahl, S. M.; Achenbach, S.; Burgess, I. J. Attenuated Total Reflection Fourier Transform Infrared (ATR FT-IR) Spectromicroscopy Using Synchrotron Radiation and Micromachined Silicon Wafers for Microfluidic Applications. *Applied Spectroscopy* **2018**, *72*, 1781–1789.

[21] Aroca, R. *Surface-Enhanced Vibrational Spectroscopy*; Wiley Online Books; 2006; pp 1–33.

[22] Chen, Y. X.; Miki, A.; Ye, S.; Sakai, H.; Osawa, M. Formate, an Active Intermediate for Direct Oxidation of Methanol on Pt Electrode. *Journal of the American Chemical Society* **2003**, *125*, 3680–3681.

[23] Miki, A.; Ye, S.; Osawa, M. Surface-enhanced IR absorption on platinum nanoparticles: an application to real-time monitoring of electrocatalytic reactions. *Chemical Communications* **2002**, 1500–1501.

[24] Osawa, M.; Ikeda, M. Surface-enhanced infrared absorption of p-nitrobenzoic acid deposited on silver island films: contributions of electromagnetic and chemical mechanisms. *The Journal of Physical Chemistry* **1991**, *95*, 9914–9919.

[25] Shao, M. H.; Adzic, R. R. Electrooxidation of ethanol on a Pt electrode in acid solutions: in situ ATR-SEIRAS study. *Electrochimica Acta* **2005**, *50*, 2415–2422.

[26] Miyake, H.; Okada, T.; Samjeské, G.; Osawa, M. Formic acid electrooxidation on Pd in acidic solutions studied by surface-enhanced infrared absorption spectroscopy. *Physical Chemistry Chemical Physics* **2008**, *10*, 3662–3669.

[27] Huo, S.-J.; Xue, X.-K.; Yan,; Li, Q.-X.; Ma, M.; Cai, W.-B.; Xu, Q.-J.; Osawa, M. Extending in Situ Attenuated-Total-Reflection Surface-Enhanced Infrared Absorption Spectroscopy to Ni Electrodes. *The Journal of Physical Chemistry B* **2006**, *110*, 4162–4169.

[28] Wang, H.-F.; Yan, Y.-G.; Huo, S.-J.; Cai, W.-B.; Xu, Q.-J.; Osawa, M. Seeded growth fabrication of Cu-on-Si electrodes for in situ ATR-SEIRAS applications. *Electrochimica Acta* **2007**, *52*, 5950–5957.

[29] Huo, S.-J.; Wang, J.-Y.; Yao, J.-L.; Cai, W.-B. Exploring Electrosorption at Iron Electrode with in Situ Surface-Enhanced Infrared Absorption Spectroscopy. *Analytical Chemistry* **2010**, *82*, 5117–5124.

[30] Miyake, H.; Ye, S.; Osawa, M. Electroless deposition of gold thin films on silicon for surface-enhanced infrared spectroelectrochemistry. *Electrochemistry Communications* **2002**, *4*, 973–977.

[31] Ataka, K.-i.; Yotsuyanagi, T.; Osawa, M. Potential-Dependent Reorientation of Water Molecules at an Electrode/Electrolyte Interface Studied by Surface-Enhanced Infrared Absorption Spectroscopy. *The Journal of Physical Chemistry* **1996**, *100*, 10664–10672.

[32] Nishi, N.; Minami, K.; Motobayashi, K.; Osawa, M.; Sakka, T. Interfacial Structure at the Quaternary Ammonium-Based Ionic Liquids—Gold Electrode Interface Probed by Surface-Enhanced Infrared Absorption Spectroscopy: Anion Dependence of the Cationic Behavior. *The Journal of Physical Chemistry C* **2017**, *121*, 1658–1666.

[33] Ataka, K.; Giess, F.; Knoll, W.; Naumann, R.; Haber-Pohlmeier, S.; Richter, B.; Heberle, J. Oriented Attachment and Membrane Reconstitution of His-Tagged Cytochrome c Oxidase to a Gold Electrode: In Situ Monitoring by Surface-Enhanced Infrared Absorption Spectroscopy. *Journal of the American Chemical Society* **2004**, *126*, 16199–16206.

[34] Ataka, K.; Stripp, S. T.; Heberle, J. Surface-enhanced infrared absorption spectroscopy (SEIRAS) to probe monolayers of membrane proteins. *Biochimica et Biophysica Acta (BBA) - Biomembranes* **2013**, *1828*, 2283–2293.

[35] Zhang,; Imae, T. Hydrogen-Bonding Stabilized Self-Assembled Monolayer Film of a Functionalized Diacid, Protoporphyrin IX Zinc(II), onto a Gold Surface. *Nano Letters* **2001**, *1*, 241–243.

[36] Rosendahl, S. M.; Danger, B. R.; Vivek, J. P.; Burgess, I. J. Surface Enhanced Infrared Absorption Spectroscopy Studies of DMAP Adsorption on Gold Surfaces. *Langmuir* **2009**, *25*, 2241–2247.

[37] Quirk, A.; Unni, B.; Burgess, I. J. Surface Enhanced Infrared Studies of 4-Methoxypyridine Adsorption on Gold Film Electrodes. *Langmuir* **2016**, *32*, 2184–2191.

[38] Goss, C. A.; Charych, D. H.; Majda, M. Application of (3-mercaptopropyl)trimethoxysilane as a molecular adhesive in the fabrication of vapor-deposited gold electrodes on glass substrates. *Analytical Chemistry* **1991**, *63*, 85–88.

[39] Hoogvliet, J. C.; van Bennekom, W. P. Gold thin-film electrodes: an EQCM study of the influence of chromium and titanium adhesion layers on the response. *Electrochimica Acta* **2001**, *47*, 599–611.

[40] Ohta, N.; Nomura, K.; Yagi, I. Electrochemical Modification of Surface Morphology of Au / Ti Bilayer Films Deposited on a Si Prism for in Situ Surface-Enhanced Infrared Absorption (SEIRA) Spectroscopy. **2010**, *26*, 18097–18104.

[41] Ohta, N.; Nomura, K.; Yagi, I. Adsorption and Electroreduction of Oxygen on Gold in Acidic Media: In Situ Spectroscopic Identification of Adsorbed Molecular Oxygen and Hydrogen Superoxide. *The Journal of Physical Chemistry C* **2012**, *116*, 14390–14400.

[42] Futamata, M. Characterization of the first layer and second layer adsorbates on Au electrodes using ATR-IR spectroscopy. *Journal of Electroanalytical Chemistry* **2003**, *550-551*, 93–103.

[43] Aroca, R. F.; Ross, D. J.; Domingo, C. Surface-Enhanced Infrared Spectroscopy. *Applied Spectroscopy* **2004**, *58*, 324A–338A.

[44] Noda, H.; Wan, L.-J.; Osawa, M. Dynamics of adsorption and phase formation of p-nitrobenzoic acid at Au(111) surface in solution: A combined surface-enhanced infrared and STM study. *Physical Chemistry Chemical Physics* **2001**, *3*, 3336–3342.

[45] Merklin, G. T.; Griffiths, P. R. Effect of Microscopic Surface Roughness in Surface-Enhanced Infrared Absorption Spectrometry. *The Journal of Physical Chemistry B* **1997**, *101*, 5810–5813.

[46] Ashwell, G. W. B.; Heckingbottom, R. Interdiffusion of Titanium and Gold: A Comparison of Thin Films Deposited in Technical Vacuum and Ultrahigh Vacuum. *Journal of The Electrochemical Society* **1981**, *128*, 649–654.

[47] Josowicz, M.; Janata, J.; Levy, M. Electrochemical Pretreatment of Thin Film Platinum Electrodes. **1988**, *135*, 112–115.

Chapter 6

Investigating Molecular Dynamics within 11-(Ferrocenyl)undecanethiol Self-Assembled Monolayers through Time-Resolved Step Scan FTIR

6.1 Introduction

Functionalized electrode surfaces are a consistent theme of interest within electrochemistry spanning many high priority topics such as catalysis[1,2], battery technology[3,4], corrosion[5,6] and molecular sensing[7,8]. Modifying surfaces is a potent way to tailor electrochemical properties in order to optimize performance by introducing new chemical functionalities and/or improving sensitivities/selectivity of the electrochemical reaction of interest. Common strategies are either the adjustment of electrode surface topography and composition of the electrodes or the introduction of new functional groups onto the surface, or a combination of both.

There is great interest in the development of electrochemical sensors based on the integration of tailored organic molecules or biological components as the sensing moiety onto the electrode surface[9–11]. Once developed, these sensors are often simple, scalable and easy to integrate into combinatorial platforms such as lab-on-a-chip or mobile devices for point-

of-care testing[12,13]. One of the most crucial aspects for this kind of functionalization is the anchoring of the organic or biological components through a secondary molecule serving as bridge between the sensing moieties to the commonly metal or semiconducting electrode surface. Designing a bridge is not limited to the physical anchoring of the sensing moiety but must also consider the electron transfer between electrode-bridge-sensor as well as orientational concerns, steric interaction between the individual components and the effects of the electrochemical environment. Within this context, alkanethiols are an important and versatile group of bridge molecules due to their ability to form highly organized self-assembled monolayers (SAM) on various electrode materials through their thiol end group[14–16]. The crucial advantage of self-assembly, is the simple and reliable creation of various monolayer compositions based on incubation conditions, thiol mixture and electrode surface topography[17].

ATR-SEIRAS has proven to be an excellent technique to study these thiols-based SAMs under *in situ* conditions due to its ability to supplement electrochemical measurement with chemical identification of the molecules as well as providing insight on structural changes within the SAMs[18–20]. While many ATR-SEIRAS studies of thiols SAMs exist in the literature, direct measurement of the kinetics of rearrangement within these SAMs upon an electrochemical perturbation are absent due to the lack of time resolution.

Chapter 6 presents the investigation on the kinetics of rearrangement upon oxidation and reduction of 11-(ferrocenyl)undecanethiol (Fc11SH) layers on Au. The work demonstrates the utility of the time-resolved ATR-SEIRAS platform introduced in Chapter 5 to investigate the kinetic changes of 11-(ferrocenyl)undecanethiol, a commonly used model system for investigation of heterogenous electron transfer within thiols SAMS, that

are inaccessible through electrochemical measurement and conventional FTIR.

6.2 Background

6.2.1 Self-Assembled Monolayers

Self-assembled monolayers are composed of organic molecules, which spontaneously organize into single molecule layers on surfaces[17,21]. Since the discovery of organic disulfide-based SAM on Au surfaces by Nuzzo and Allara in the 1983[22], the area saw incredible growth in research efforts as both a model system for the study of intermolecular interactions and self-organization as well as a flexible platform to assemble organized structures at various interfaces. This section will provide a brief primer on the subject area with a focus on SAMs at metal-liquid interfaces, as it is most pertinent to the research in this chapter. An overview of the much broader research invested into fundamental understanding[17,21] as well as the many applications of SAMs in materials[23], analytics[24,25] and biological sciences[26] can be found in the many reviews published on the subject area over the years.

Figure 6.1 shows the general preparation and molecule orientation within the SAM at a solid - liquid interface[17]. The preparation of these structures is simple immersion of a suitable substrate into an incubation solution containing the SAM components for a period of time, often referred to as immersion time or incubation time. The formation at the surface is initiated through a surface-active head-group within the molecule that chemisorbs onto the substrate surface. In this initial state, the few molecules on the surface are primarily flat on the substrate surface. As more and more molecules adsorb onto the surface, the molecules

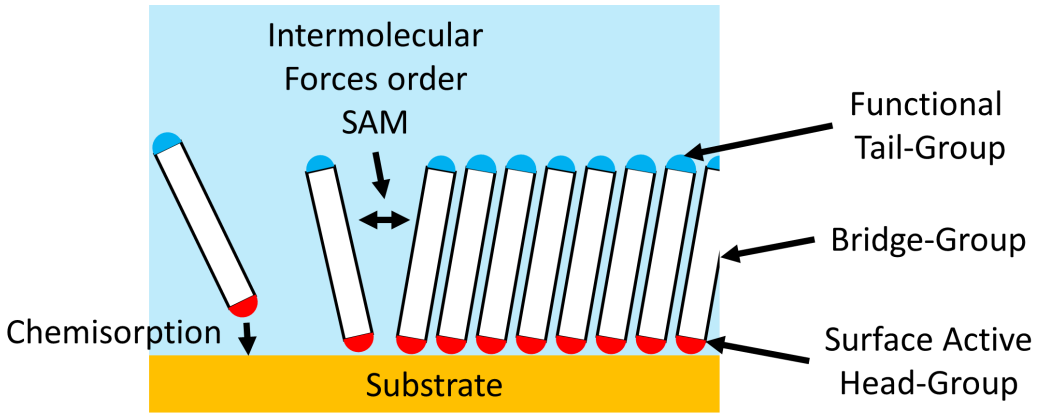

Figure 6.1: Adopted from Ulman[17]. Schematic representation of the preparation and structure of SAM. Submersion of suitable substrate into incubation solution containing SAM moieties. Chemisorption of surface-active head-group to the substrate. Assembly into ordered structure over minutes-hours due to intermolecular interaction with the substrate surface and neighboring SAM moieties.

reorient into a more vertical position for more dense packing. Intermolecular van der Waals forces between the bridge-groups of neighbouring molecules organize the overall layer into consistently oriented 2D or 3D structure on the surface. The tail group or functional groups that terminate the molecules are functionalized for the individual application of the SAM.

The simple principle of SAM formation allows an incredible variety of options for the individual components. The selection of the specific surface-active head-group is primarily motivated by the substrate. Thiols are arguably the most utilized surface-active head-group due to their excellent absorption properties for many metal substrates. A one electron one proton oxidation of the thiol end group leads to the formation of a sulfur-metal bond with metal substrates such as Au, Ag, Cu[27], Pd[28], and Hg[29] as well as some semiconductors[30]. Some alternative head-groups are silanes[31] and fatty acids[32] for solid-liquid interface or hydrophobic/hydrophilic head-groups for SAM formation at liquid-air or liquid-liquid interfaces[33].

Similar to the head-groups, functional tail-groups are primarily selected for the spe-

cific purpose of the SAM. One consideration however is its influence on SAM formation, as particularly bulky tail-groups can interfere with the organization between the individual molecules[34]. One effective strategy to mitigate this effect is adding non-functionalized molecules as a dilutant into the incubation solution, allowing functionalized tail-groups to be spaced apart from each other. This can be further improved by installing bulky functional groups to the SAM after formation, by selecting SAM molecules terminated with chemically accessible head-groups, such as carboxylic acid for ECD-coupling[19] or azide for "click" chemistry[35].

The bridge-group of the molecule is arguably just as crucial as the head group and tail group in determining SAM properties. The formation of organized SAMs as well as determining its properties such as thickness, orientation, packing and electronic properties are all primarily based on the bridging section of the molecule[21]. Long alkane chains as bridge-groups create well organized and densely packed SAMs with modifiable layer thickness based on the alkane chain length[36]. Highly conjugated aliphatic chains provide more rigid orientation and higher electron conductivity useful for their use as thin film transistors[14]. For investigations of biological processes, peptide[37] and even nucleic acid bridges[38] have been reported in the literature for attaching biological functional groups or for more fundamental study of the properties of the bridge elements themselves.

Many applications of SAMs particularly in the area of analytical chemistry utilize SAMs to anchor small organic or biological sensors to otherwise incompatible substrates. Thiol-based SAMs are an attractive and common option to link molecules electronically to highly conductive gold surfaces. The heterogenous electron transfer from the sensing moiety to the electrode is a central property of interest for many of these applications. Here,

electrochemistry is interesting as SAMs offer unique opportunities to create highly organized interfaces for electrochemical study and application. Vice versa, electrochemistry is well suited to study charge transfer mechanisms and layer organization within SAMs, particularly when incorporating redox-active centers into the monolayer whose electrochemical response is strongly influenced by the local environment.

6.2.2 Redox-Active Self-Assembled Monolayers and Ferrocene Terminated Alkanethiols

SAMs with redox-active centers as functional groups have been excellent model systems for studying the fundamental properties of SAMs. The attachment of a redox center at the terminal end of a SAM molecule creates a simple donor/acceptor system with the SAM substrate. Since their introduction as a model system, incorporating redox-active SAM molecules has become a common strategy to investigate SAM properties. A recent review by Meade *et al.* provides an excellent overview of this topic[21]. For the purposes of this chapter, it is worthwhile to showcase the possibility of electrochemical investigation such as determining the heterogenous electron transfer rate k_{ET}[39], the effects of local environment changes upon electron transfer[40–44] and self-organization of SAMs using ferrocene-terminated alkanethiols.

Ferrocene-terminated alkanethiols ($Fc(CH_2)_nSH$) were the first group of redox-active SAMs in the literature. Introduced by Chidsey *et al.* in 1990[34], they are arguably the most commonly used redox-active SAM[21]. Part of their appeal is the ease of forming well organized monolayers due to strong intermolecular interaction between alkane chains and the small ferrocene functional group that decreases interference with SAM organization. For instance,

densely packed and well organized $Fc(CH)_nSH$ with varying n were utilized by Smalley *et al.* to investigate changes in k_{ET} as a function of SAM thickness to determined the exponential decay constant $\beta = -d(ln(k_{ET}))/dn$ that links alkane chain length n with k_{ET}[39,45]. While it is tempting to view the heterogenous electron transfer as a simple function of distance between redox center and substrate surface, a variety of additional influencing factors are well established within the literature.

SAM defects such as pinholes, disorder, domains and islands are one of the most common challenges for accurate determination of k_{ET} resulting in a distribution of various electron transfer rates also known as kinetic dispersion[46]. As electrochemical current and voltage responses are a composition of all SAM structures on the surface, accurate measurement of k_{ET} of a specific SAM composition can only be performed with homogenous monolayers without defects. Even the addition of a single carbon into the alkane chain of a ferrocene-terminated alkanethiol from an even to odd number of methyl groups has been shown to significantly alter the electrochemical behaviour by altering the angle of the terminal methyl group[47–50]. While the strong sensitivity of the electrochemical response of the redox center to the local environment is an experimental challenge, it can be exploited to investigate SAM ordering or the influence of surrounding solution phase solvent and the nature of electrolyte anions.

Lennox *et al.* were able to utilize $Fc(CH_2)_{12}SH$ as a probe for heterogeneity in binary alkanethiol SAMs[51]. In their work, asymmetry in the redox response of $Fc(CH_2)_{12}SH$ were observed by cyclic voltammetry and the result of an overlap of two current peaks, one associated with well-ordered thiols and a second peak at lower electrochemical potential with dis-ordered thiols. Deconvoluting the redox signal into the two contributions offered

information about the ratio of disordered and well-ordered SAMs. Since then, this strategy has become more common to differentiate between well-ordered and disordered SAMs[49]. Similarly, sensitive changes in k_{ET} of $Fc(CH_2)_nSH$ have been observed for different anion concentrations and speciation within solution[40–43]. Work within this aspect was able to relate this difference to the various propensities of anionic species to form ion pairs with the redox center upon oxidation. When a ferrocene in the SAM is oxidized, its positive charge will interfere with the electron transfer of neighbouring redox center until its charge is "neutralized" by ingress and coupling to a solution phase anion. Leech *et al.*[43] measured k_{ET} in solutions with different anions and were able to associate the decrease in k_{ET} values to the hydrophobicity difference of the individual anions. Within their results, they were able to observe up to a 25% difference in k_{ET} values going between hydrophobic ClO_4^- anions compared to more hydrophilic SO_4^{2-}. This is further supported by more recent ATR-SEIRAS measurement by Wandlowski *et al.*[41,52], that provides direct spectroscopic evidence of very little water penetration into the SAM for hydrophobic PF_6^- and ClO_4^-, but strong interfacial H_2O signal upon oxidation of a $Fc(CH_2)_{11}SH$ SAM in SO_4^{2-} and NO_3^- containing solution.

The ATR-SEIRAS on SAMs measured by Wandlowski *et al.* and others also highlight the benefits of combining electrochemical measurements of redox-active SAMs with surface-sensitive FTIR techniques[41,52]. In the case of $Fc(CH_2)_nSH$, multiple early experiments were able to measure an increase in SAM thickness upon oxidation[39]. Ye *at al.*[53,54] proposed a more vertical alignment of the alkane-bridge due to electrostatic repulsion between the oxidized ferrocene head and the positively charged electrode surface. Viana *et al.*[55] however, proposed a rotation of the ferrocene head-group. Wandlowski *et al.*[41,52] observed both mechanisms, providing direct evidence of both rotation of the ferrocene head and

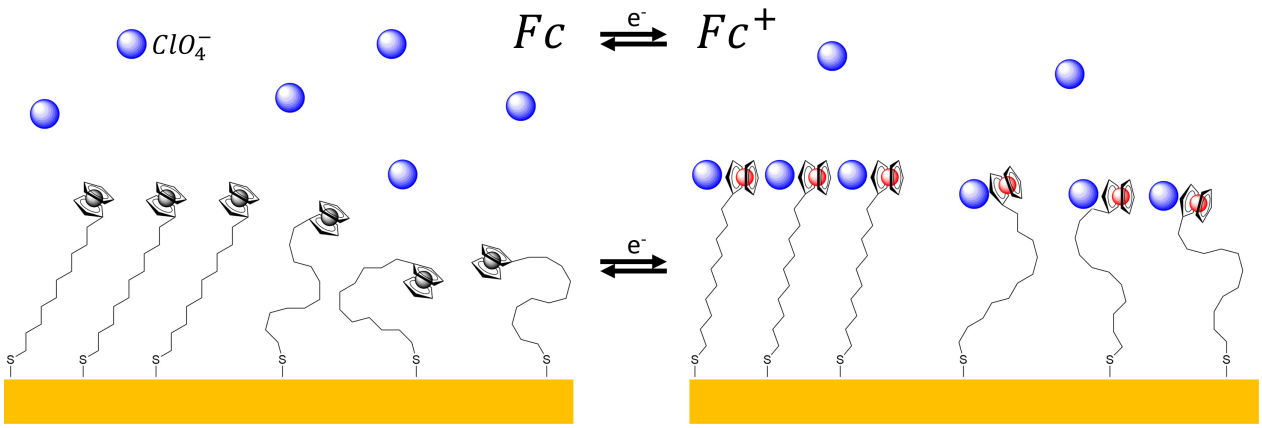

Figure 6.2: Adapted from Rudnev *et. al.*[41,52]. Schematic model of Fc11SH SAM on Au substrate in ClO_4^- anions containing electrolyte. Fc11SH can assemble into either well-ordered or disordered layers. Oxidation and reduction of Ferrocene tail-group will result in orientational change as well as ingress of ClO_4^- anions, followed by ion pairing with positively charge Fc11SH.

tilt motion of the alkane bridge upon oxidation as well as the dependence of these motions on the anion species, a schematic of which is shown in Figure 6.2.

While the effect and process of ion pairing with $Fc(CH)_nSH$ and other redox-active SAMs have remained an active area of research, no literature reports to my knowledge have investigated the relationship between the kinetics of anion ingress from solution to the SAM, conformational changes and heterogenous electron transfer within the SAM upon oxidation/reduction. Ion pairing is a well-established contributing factor in electron transfer within SAMs and direct measurement of the kinetics of ingress could provide a better understanding of how fast electric charge at the redox centers are screened by the anions.

The impact of such new knowledge warrants some consideration. Successful experiments of this nature open up the possibility that the measurement platform could be utilized to investigate electron transfer for more complex redox-active SAMs. For example, Takeda *et al.*[56] noted in their study on k_{ET} of ferrocene terminated SAMs with identically

long helical peptide bridge-groups can range between 50 - 1300 s^{-1}. The large variance of k_{ET} was proposed to be a result of three different molecular dynamic effect that can occur based on molecular arrangement and packing of SAM. In this case, Takeda *el al.* proposed, that the drastic change in k_{ET} is a result of different molecular dynamics of the SAM during oxidation/reduction. Depending on the composition of helical peptide bridge-groups within the SAM, peptides can undergo different combinations of contraction, bending and helix conversion changes. For purely electrochemical measurements, it will be difficult to distinguish between the individual cases, as electrochemical techniques are sensitive to the charge arriving at the electrode surface, but not how it got there. While combination with a secondary technique or computational calculations were reported in the literature as being able to differentiate these cases, there is a strong argument for direct observation of these conformational change within the time resolution of their fast electron transfer. The main experimental challenge would be measurement of the kinetics of the Fc11SH SAM components with enough chemical specificity and time resolution on the order of the electron transfer rate (μs $-$ ms range). Here the step scan ATR-SEIRAS setup developed and discussed in Chapter 5 is capable, in principle, to measure the kinetics of these redox-active SAMs. For this initial attempt, Fc11SH was selected due to the wealth of information on the system available in the literature.

6.3 Methodology

6.3.1 Reagents and Solutions

Anhydrous sodium acetate (ACS grade, Fisher Scientific), perchloric acid (Fluka), acetic acid (Glacial, Fisher Scientific) and KCl (ACS grade, Fisher Scientific) were purchased and used as received. Potassium perchlorate (ACS grade, Fisher Scientific) was recrystallized and stored in a desiccator to limit degradation. 11-(Ferrocenyl)undecanethiol used was either purchased (Sigma Aldrich) or synthesised by the Badia group (Université de Montréal). All aqueous solutions were created using Milli-Q water (> 18 MΩ cm).

6.3.2 ATR-SEIRAS Layer Preparation

Au layers were prepared on a μ-groove Si wafers IR optic element by IRUBIS GmBH. The μ-groove Si wafers are a new low-cost IR IRE that offers much higher IR throughput <1500 cm^{-1} compared to conventional silicon IREs[57,58]. IREs are Au-coated with a Kurt J. Lesker Corp PVD 75 magnetron sputterer at base pressure of $<3\times10^{-6}$ Torr and sputtering pressure of 5×10^{-3} Torr with argon as sputtering gas. 20 nm thick Au layer are deposited at $\sim$0.1 nm/s, matching sputtering condition for SEIRAS Au layer initially reported by Osawa *et al.*[59]. While some sputtered Au-layers can be inherently SEIRAS active, ECA can introduce and improve SEIRAS activity by roughening the Au surface. For all FTIR measurement described in this chapter, Au layers are electrochemically annealed in 0.1 M acetic buffer solution (sodium acetate + acetic acid pH 6).

6.3.3 Assembly of Spectroelectrochemical Cell

As discussed in Chapter 5, Au coated IREs were assembled in a home-built spectroelectrochemical cell for ATR-SEIRAS experiment developed in the Burgess group, also referred to as "glass castle cell" [60]. A schematic representation of the finished setup is shown in Figure 5.2. The spectroelectrochemical cell is assembled on a metal plate that fits the VeeMAX III ATR accessory attached to the FTIR spectrometer. The IRE, shown in Figure 5.2 is placed on a Delrin holder with μ-grooves centered onto the clearance space in the center to allow IR illumination from below. A 6.07 mm inner diameter Viton rubber gasket followed by a machined Teflon cell base is placed on top of the Au film. The IRE, Delrin holder and Teflon base are secured onto the metal plate through multiple screws, creating a watertight seal between the Au film and the Teflon base. The remaining glass elements are attached onto the Teflon case to create an electrochemical cell with a conventional three electrode arrangement. The Au film on the IRE is the WE, with electrical contact through retractable pins within the Teflon base. An Au wire is used as the CE and an Ag/AgCl in saturated KCl serves as the RE. A long and short glass tube can be used to purge the solution and the atmosphere respectively with a steady stream of argon.

To obtain a SEIRAS active metal surface, the sputtered Au needs to be ECA in degassed 0.1 M acetate buffer solution (pH 6) to texture the surface through repeated formation and reduction of gold oxide. Compared to the ECA of AuTi in Chapter 5, the use of acetate buffer provides a spectroscopic handle on the SEIRAS-activity during the procedure, as acetate can adsorbed onto the Au surface. ECA is achieved by potential cycling the Au surface at 20 mV/s, initially between –0.2 V to +0.2 V for 3 cycles before

incrementally increasing potential window by 100 mV for every 3 cycles each until a final ECA potential window of -0.3 V to 0.9 – 1.1 V is reached. Once the positive potential sweep shows the onset of gold oxidation (oxidation onset ∼+0.9 V), FTIR measurement at +0.6 V with -0.3 V as a reference spectrum is collected after every 3 cycles before further increasing the potential limit. For SEIRAS active surfaces, surface adsorbed acetate can be observed at 1400 cm^{-1}. If the acetate IR signal is missing or weak (<2 mAbs), potential cycling is continued with a positive potential limit increased by 50 mV. A lower maximum potential is preferable since stronger oxide formation can decrease the mechanical stability of the metal film resulting in higher likelihood for delamination during the ECA or subsequent measurements.

6.3.4 11-(Ferrocenyl)undecanethiol SAM Incubation

After completing the preparation for ATR-SEIRAS, Fc11SH SAM incubation must occur within the assembled spectroelectrochemical cell as disassembly will result in delamination of the Au-layer. To this end, the ECA solution is removed and the cell is thoroughly rinsed with Millipore water followed by a secondary rinse in ethanol. Lastly, the ethanol solution is exchanged for an ethanol solution containing 1 mM Fc11SH. The thiol layer self-assembles overnight with the cell tightly sealed and covered with aluminum foil to limit degradation of thiol or evaporation of the solvent. Before the spectroelectrochemical experiments, solution phase and weakly physisorbed Fc11SH is removed from the cell by a rinse with ethanol, followed by a second rinse with Millipore water to remove the solvent. Lastly, the electrolyte of interest (0.1 M $KClO_4$ + 10 mM $HClO_4$) is added to the cell. The presence of a Fc11SH SAM is initially evaluated using electrochemical cyclic voltammetry using a HEKA PG 590

potentiostat. Current and potential data were collected using a National Instruments USB 6351 X-series multifunction DAC.

6.3.5 Spectroelectrochemistry and Step Scan FTIR

All FTIR measurements were conducted using a Bruker VERTEX 70 FTIR spectrometer with a liquid nitrogen cooled MCT-detector. The assembled spectroelectrochemical cell fits a PIKE Technologies VeeMAX III ATR accessory set to 55° angle, an optimal angle for the Si IRE. Non-time resolved and rapid scan FTIR measurement were performed with 4 cm^{-1} wavenumber resolution. Step scan FTIR measurements were performed with 8 cm^{-1} resolution to decrease the overall measurement time.

Rapid Scan FTIR

Rapid scan FTIR measurements were performed utilizing a modified LabVIEW program first introduced in Chapter 3. In short, a custom LabVIEW program interfaces the FTIR spectrometer with the potentiostat. Each rapid scan iteration starts with acquisition of 10 background spectra followed by a rapid scan FTIR measurement with 120 kHz mirror velocity and 4 cm^{-1} wavenumber resolution, resulting in 76 ms time resolution. Upon initiation of rapid scan IR acquisition, a potential step is simultaneously applied to the WE to start oxidation/reduction of the Fc11SH SAM. For this redox process, a rapid scan iteration measuring the oxidation is immediately followed by a rapid scan iteration of the reduction. The reduction measurement also acts as a reset to the initial film condition. This improves the time efficiency of the measurement resulting in typically 1 - 2 h for a full rapid scan FTIR experiment.

Step Scan FTIR

The step scan FTIR setup and procedure was developed in detail in Chapter 5 and a schematic representation can be found in Figure 5.3 and 5.4 of said chapter. The FTIR instrument is setup to perform step scan FTIR measurements, collecting 650 time elements with 1 ms time resolution with 8 cm^{-1} wavenumber resolution. Compared to the MOP system (see Chapter 5), that has IR signature bands between and 1200 - 1600 cm^{-1}, the Fc11SH system exhibits IR absorbances over a much wider spectral range. The Cl−O stretch of ClO_4^- at 1100 cm^{-1} represents the low frequency limit whereas the hydrocarbon stretches of the alkane tail and ferrocenyl ring between 2800 - 3150 cm^{-1} represent the high frequency region of interest. The larger range of wavenumbers require a total of 1110 single step scan iterations for acquisition of a single interferogram. Each step scan iteration is triggered by an external rising edge TTL-signal from the DAC and controlled with a custom-written LabVIEW program. The triggering of the IR measurement, potential control of the WE and acquisition of current and potential data occurs within the same LabVIEW program. A TTL signal is simultaneously sent to the IR instrument to start IR signal acquisition, while a sequence of potential steps is applied to the electrode. The potential sequence is shown later in Figure 6.10. An initial period of 20 ms at a standby potential of +0.1 V is used for the background spectra. The following 20 ms is used to diagnose whether the SAM has been returned to initial state from the last step scan iteration. After the initial 20 ms, a positive potential step is applied to the WE and held for 300 ms to oxidize the ferrocene. Afterwards, a negative potential step is applied to reduce the ferrocene back to its initial state. Acquiring 620 ms worth of IR data captures the background, oxidation and reduction of the

system within every single iteration. Based on the 620 ms acquisition time and additional instrument dead time, a single step scan iteration is collected in ∼1 s. For 1110 iterations per single spectra, the collection time for a single step scan interferogram is ∼20 min. The total experimental time for collection of 128 - 256 scans ranges from 48 - 96 h. To confirm stability over time, cyclic voltammetry measurements and static FTIR measurements are taken in 8 h intervals during LN_2 refills of the MCT-detectors. Once acquisition is completed, single interferograms are reconstructed and FT using the IR-instrument software. The resulting data was processed using custom MATLAB and Python scripts (Appendix V, VI) to coadd individual spectra, subtract background, baseline fit absorbance spectra and calculate 2D correlation maps.

6.4 Discussion

6.4.1 Characterization of Fc11SH SAM on ATR-SEIRAS Au-layers

Before measuring time-resolved FTIR spectra of the redox processes of Fc11SH, all freshly prepared SAMs were characterized through cyclic voltammetry and potential dependent FTIR measurements to confirm the presence of the molecule on the Au surface.

Electrochemical Characterization of Fc11SH SAM

Within the literature, cyclic voltammetry is a well-established method to differentiate well-ordered, disordered and mixed (both well-ordered and disordered domains existing on the surface) Fc11SH SAMs as well as to determine the surface coverage[51]. Before discussing the electrochemical cyclic voltammetry measurements of SAMs prepared on the ATR-SEIRAS

Au films, it is beneficial to first establish the electrochemical response of a Fc11SH SAM on a more electrochemical 'ideal' Au surface. For electrochemical characterization of surface assembled thiols, Au-bead electrodes are commonly used in the literature. These electrodes can be acid cleaned and flame annealed before assembly of the thiols layer to create an Au surface composed of large flat terraces with few surface defects. A Fc11SH SAM layer was prepared on an Au bead electrode by submerging the electrode into ethanol solution containing 1 mM Fc11SH overnight.

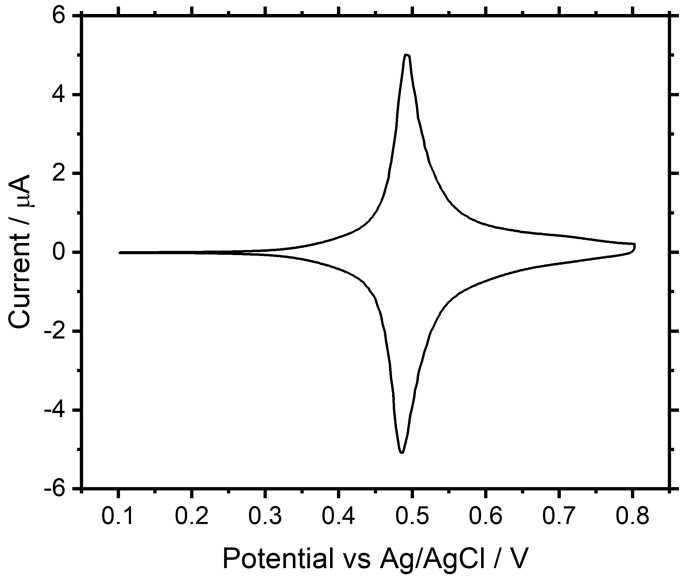

Figure 6.3: CV of Fc11SH SAM assembled on Au bead electrode in 0.1 M $KClO_4$ + 10 mM $HClO_4$, showing the redox reaction of the ferrocene tail-group. The sweep rate was 20 mV/s

.

Figure 6.3 shows the CV of a freshly prepared SAM on an Au-bead electrode in 0.1 M $KClO_4$ + 10 mM $HClO_4$ solution. The CV is dominated by a single redox feature between +0.4 - 0.6 V with the peak position of the anodic oxidation of the ferrocene head group at +494 mV and the corresponding cathodic reduction at +483 mV. The deviation

of the full-width half maximum (FWHM) of the redox process (61 mV) process in the CV compared to the ideal, non-interacting surface redox FWHM value of 90 mV predicted by purely Nernstian reaction, fits the expected peak shape predicted for a surface adsorbed species with Frumkin intermolecular interaction between the redox centers[61].

This result compares favorably with literature reports of purely well-ordered Fc11SH SAMs on Au[51]. A single pronounced redox feature and absence of secondary redox features indicated Fc11SH SAM formation exclusively into a well ordered and densely packed thiol layers. The presence of surface areas with disorganized ferrocene thiols (shown in Figure 6.2) would result in an additional redox peak at more negative potentials. Coverage of the Fc11SH SAMs can be estimated by calculating the redox charge by integrating the CV peak features. As the oxidation/reduction of each ferrocene transfers a single electron, division by the Faraday constant provides the molar values of Fc11SH on the surface. The Au surface area is assumed to be the geometric area of 0.13 cm^2 multiplied by a roughness factor. For the smooth Au bead here, roughness is assumed to be 1, but the rougher SEIRAS-active Au layers used later (geometric area of 0.28 cm^2) are assumed to have a roughness factor of 2.5, based on literature estimates[62]. The surface coverage can then be compared to the theoretical maximum surface coverage value of 4.5×10^{-10} mol/cm^2 based on the closed packing diameter of 0.66 nm for the bulkier ferrocene head-group[34]. The calculated surface coverage of 4.3×10^{-10} mol/cm^2 suggest almost complete coverage of the Au surface with SAM. This is further supported by the very low double layer capacitance visible below +250 mV in the CV.

Ferrocene thiol layers on ATR-SEIRAS Au-surfaces within the spectroelectrochemical cells across multiple experiments have shown a much wider variety of electrochemical

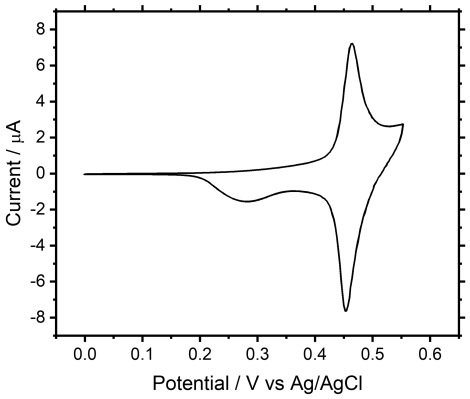

(a) Well ordered

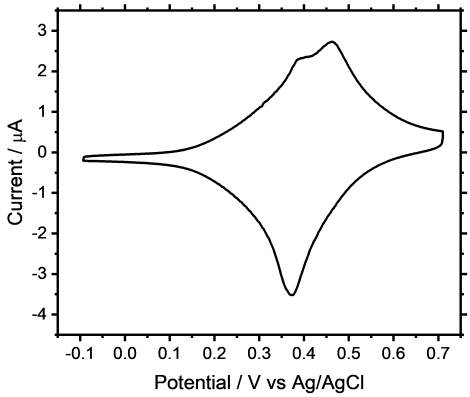

(b) Slightly mixed ordered

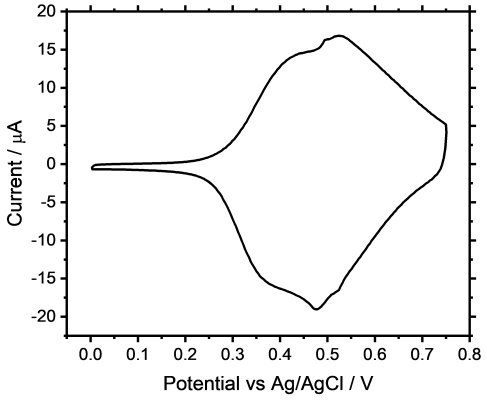

(c) Mixed ordered

Figure 6.4: Various representative CVs of Fc11SH SAM assembled on SEIRAS-active Au layer in 0.1 M $KClO_4$ + 10 mM $HClO_4$. SAM ordering range from (a) highly ordered to (b) less strongly ordered to (c) a mixture of ordered and highly disordered. The sweep rate was 20 mV/s

responses. Figure 6.4 showcases the range of CVs of Fc11SH SAMs observed on SEIRAS-active Au layers. The Fc11SH incubation results can range from a single sharp redox feature as shown in Figure 6.4a, to CV's with lower current and small secondary redox feature in Figure 6.4b, to CV's with essentially two redox peak features that are strongly overlapped with each other in Figure 6.4c. Fc11SH SAM layers with a single pronounced redox feature shown in Figure 6.4a are analogous to well-ordered Fc11SH SAMs formed on Au-bead electrodes. It is also important to note that surface coverage calculated based on the ferrocene redox current is well below the surface area of the Au-film. Together, the CVs suggest the Au surface is only partially covered with Fc11SH, but that the surface areas with adsorbed thiol are tightly packed and well-ordered. In contrast, the double peak features in Figure 6.4c suggest a combination of areas with well-ordered Fc11SH and areas with disordered Fc11SH on the surface of the gold. Here, currents from both redox processes strongly overlap and peak current deconvolution suggests a ∼60:40 mixture of well-ordered to disordered Fc11SH. The electrochemical properties of a freshly assembled Fc11SH layer can fall in the middle of these two limiting results as shown in Figure 6.4b. Such CVs suggest the predominant presence of well-ordered Fc11SH with a minor contribution of disordered Fc11SH. It is also important to note, that surface coverage of all Fc11SH SAM layers was never close to full coverage but instead ranged from 20 - 50% of the estimated surface area. Discussion of the FTIR results below will have to consider that in addition to Fc11SH, surface areas with bare Au will be affecting the measurements.

In an ideal situation, thiol incubation on SEIRAS-active Au-films would benefit from being able to selectively create SAMs with varying ratios of well-ordered and disordered Fc11SH. In practise however, the described Fc11SH assembly procedure allows for reliable

assembly of a Fc11SH SAM onto the gold but controlling the ratio between well-ordered and disordered thiols is currently not possible. As mentioned in Chapter 5, reliable preparation of SEIRAS active Au-films is challenging. Small variations within the surface texture between individual SEIRAS-active Au layers are the most likely reason for the variation in Fc11SH assembly highlighted by the CVs in Figure 6.4. One improvement can be made by developing a more consistent procedure for preparing SEIRAS-active Au-films with more consistent surface texture. A secondary or complimentary option can be found in the literature where the ratio between well-ordered and disordered Fc11SH can be modified through addition of varying amounts of non-ferrocene terminated thiols of similar chain length into the solution. Both options would require significant time investment and were not pursued. Instead, FTIR experiments were repeated multiple times and most Fc11SH SAMs on SEIRAS active Au layers consisted of a mixture of well-ordered and disordered Fc11SH similar to Figure 6.4c. The FTIR results presented in this Chapter will be limited to FTIR data collected of these "mixed-ordered" Fc11SH SAMs.

FTIR Characterization of Fc11SH SAM

Potential dependent FTIR measurements are crucial to confirm that the Au-films remained SEIRAS active during incubation. A secondary function is to judge IR signal strength of the ferrocene thiol as step scan FTIR requires IR absorption signals of >0.2 mAbs to be above the noise level of the measurement. Figure 6.5 is a representative ATR-SEIRAS FTIR spectrum of Fc11SH thiol on Au, showing multiple IR absorption features. The spectrum was recorded at +0.7 V vs Ag/AgCl after oxidation of the ferrocene according to the CVs shown in Figure 6.4c. The reference spectrum was recorded at +0.1 V where all ferrocene is

in its original uncharged state.

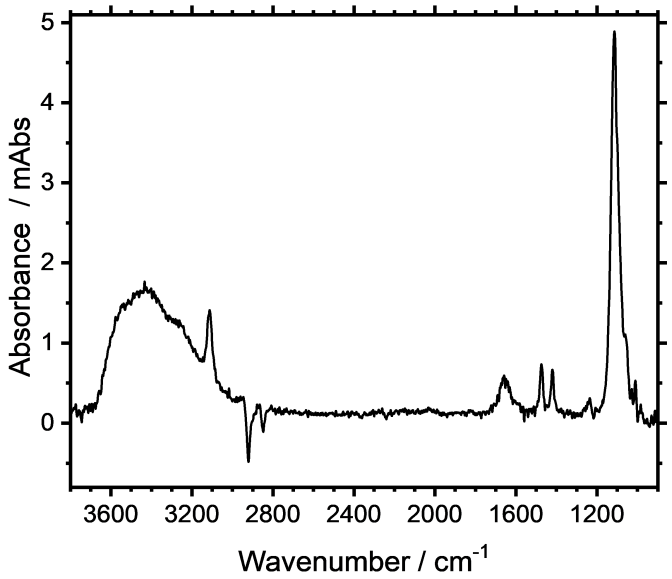

Figure 6.5: Representative ATR-SEIRAS spectrum of mixed-ordered Fc11SH in 0.1 M $KClO_4$ + 10 mM $HClO_4$ upon E_{step} from +0.1 V to +0.7 V. IR signal visible at 1420 cm^{-1}, 1476 cm^{-1}, 2850 cm^{-1}, 2920 cm^{-1} and 3112 cm^{-1} are assigned to Fc11SH. Broad features at 1100 cm^{-1} as well as at 1650 cm^{-1} and 3000 - 3600 cm^{-1} are assigned to ClO_4^- and H_2O respectively. Reference at +0.1 V.

Five bands at 1420 cm^{-1}, 1476 cm^{-1}, 2850 cm^{-1}, 2920 cm^{-1} and 3112 cm^{-1} are assigned to various IR modes of the Fc11SH molecule. The direction of the individual Fc11SH bands is a result of changes in the orientation of the ferrocene rings and the alkyl chains upon oxidation of the iron centre. IR measurements in ATR configuration are sensitive to the orientation of surface adsorbed molecules due to the p-polarization of the evanescence wave. Dipole transition moments parallel to the surface are invisible, while those perpendicular to the surface are surface allowed. The two negative going bands at 2850 cm^{-1} and 2920 cm^{-1} are the C−H stretches of the alkyl chain and the result of the hydrocarbon chain of Fc11SH molecules tilting into a more upright position upon oxidation of the ferrocene head. The more parallel orientation of the C−H symmetric and asymmetric stretching transition dipole

moments within the chain results in a decreased IR absorption. Before oxidation of the redox center, the carbon rings of the ferrocene head are in a slightly tilted orientation towards the surface. Upon oxidation, the entire ferrocene rotates until the rings are vertically aligned with the surface. The rotation results in an increased vertical alignment of the changes in dipole moments associated with the C−H stretch at 3112 cm^{-1}, C−C ring breathing at 1420 cm^{-1} and either H−C−H or Fe−C stretch at 1476 cm^{-1} [41,52].

The strongest IR band at 1100 cm^{-1} is due to the Cl−O stretch of ClO_4^- and the result of an influx of ClO_4^- from solution to charge balance the positive charge of oxidized Fc11SH as well as excess surface charge accumulated on the Au surface. Assuming one-to-one correlation of ClO_4^- with oxidized ferrocene due to ion pairing, the stronger IR cross section of the perchlorate results in a much larger IR signal from the anion relative to those arising from orientational changes of the Fc11SH molecule. The two broad IR bands, one around 1650 cm^{-1} and the other between 3000 - 3600 cm^{-1} are assigned to H_2O and indicate an increased hydration of the thiol layer at more anodic potentials.

For more detailed potential dependence information, IR spectra corresponding to a mixed Fc11SH SAM (*i.e.* a SAM exhibiting a CV such as that shown in Figure 6.4c) were collected at 50 mV intervals. For this experiment, the potential is increased in the positive direction between FTIR measurements and held at each potential to allow the surface to adjust to the new potential before collecting an IR spectrum. Figure 6.6 shows the resulting IR spectra from +0.3 V to +0.7 V with a reference spectrum taken at +0.1 V. Going towards more positive potentials, the ClO_4^- peak at 1100 cm^{-1} is the first peak to appear at potentials $>$ +350 mV. This corresponds well with the onset of the oxidation of disordered Fc11SH in the CV and increases in intensity with more anodic potential. Similar behavior can be

observed for all five Fc11SH IR modes, that appear in the IR spectra at +450 mV and whose IR signals increase with further oxidation of the ferrocene.

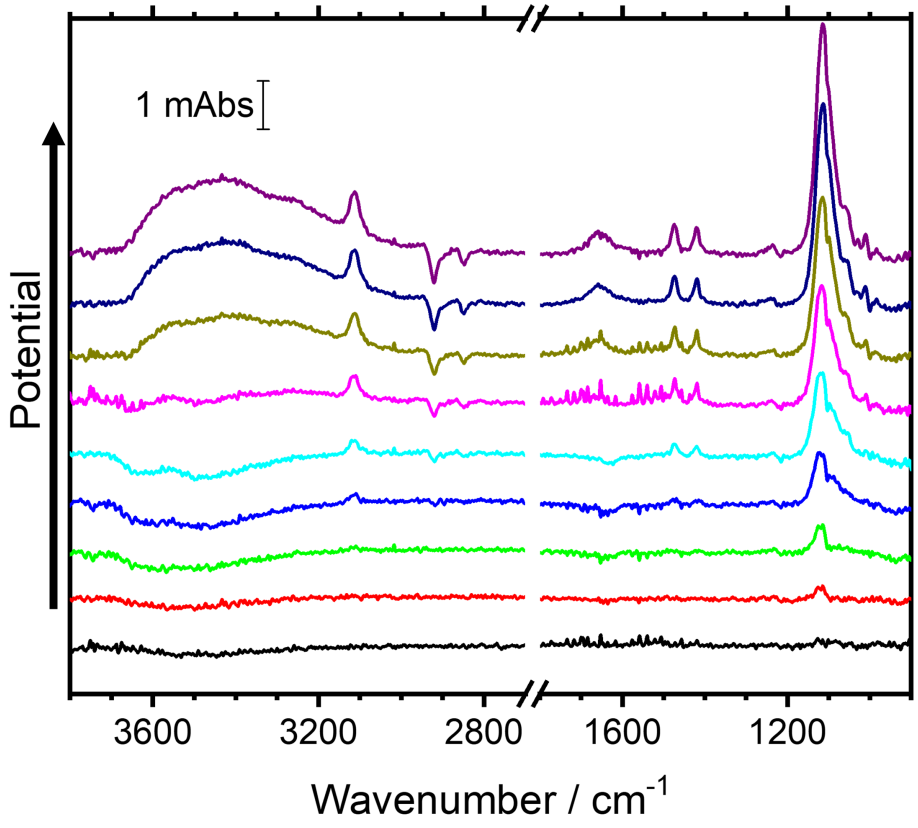

Figure 6.6: ATR-SEIRAS spectra of mixed-ordered Fc11SH in 0.1 M $KClO_4$ + 10 mM $HClO_4$ upon positive sweep from +0.1 V to +0.7 V. Spectra collected every 50 mV. Reference at +0.1 V.

In contrast to the IR signal related to the Fc11SH oxidation, H_2O stretches at 3500 cm^{-1} and bending modes at 1650 cm^{-1} show an initial decrease in IR signal for potentials from +0.3 V to +0.5 V before increasing at potential >+0.5 V to an increase in water IR signal at +0.7 V. To explain this behaviour, it is important to consider that both bare Au surface and Fc11SH oxidation are contributing to the IR signal of H_2O. For the initial potentials from +0.3 – 0.5 V, little Fc11SH oxidation has occurred and the IR response of

H_2O is dominated by contributions from bare Au surface. This results in a decrease in H_2O absorbance, due to potential driven reorientation of water close to the surface. Once Fc11SH oxidation commences at more positive potentials, the influx of hydrated ClO_4^- ions occurs.

Combined with the electrochemical data, the SEIRAS data clearly establishes: 1) the presence of Fc11SH SAMs on a SEIRAS active Au layer; 2) FTIR signals are linked to the oxidation of Fc11SH and compare very favorable with the literature such as the ATR-SEIRAS work on Fc11SH SAMs by Wandlowski *et al.*[41,52]; 3) the IR spectra in Figure 6.5 and 6.6 show S/N ratios good enough to allow time-resolved FTIR measurements.

6.4.2 Rapid Scan FTIR of Fc11SH SAM Oxidation/Reduction

Before committing to a time intensive step scan FTIR measurement, a rapid scan FTIR measurement was performed. This allowed confirmation that the Fc11SH SAM signals and the SEIRAS-active Au-layer remain stable during potential steps. Secondly, rapid scan results allow an estimation of the time scale needed to observe complete oxidation/reduction of the Fc11SH. Any small reduction of measurement time for each step scan iteration results in a large reduction of overall measurement time over the course of 50,000 – 100,000 potential step iterations. Figure 6.7 shows the rapid scan FTIR result for the oxidation of Fc11SH upon an anodic step from +0.1 V to 0.7 V. The spectra were collected with 8 cm^{-1} resolution and a mirror velocity of 160 kHz, resulting in the collection of a double-sided, forward-backward interferogram within 76 ms. In post-processing of the data, the interferograms were split into forward and backward interferograms, resulting in a time-resolution of 38 ms. All Fc11SH IR signals at 1420 cm^{-1}, 1476 cm^{-1}, 2850 cm^{-1}, 2920 cm^{-1} and 3112 cm^{-1} are clearly visible within the rapid scan spectra, along with the ClO_4^- anion band at 1110 cm^{-1} and the two H_2O

bands at 3500 cm^{-1} and 1600 cm^{-1}. Similar spectra are recorded for the cathodic reduction of Fc11SH, but not shown here. The spectra show little noise within 256 repeated scans, but a slight baseline shift within the initial few spectra (particularly pronounced between the IR spectrum for 38 ms to 76 ms) and further analysis required baseline correction using a custom Python script.

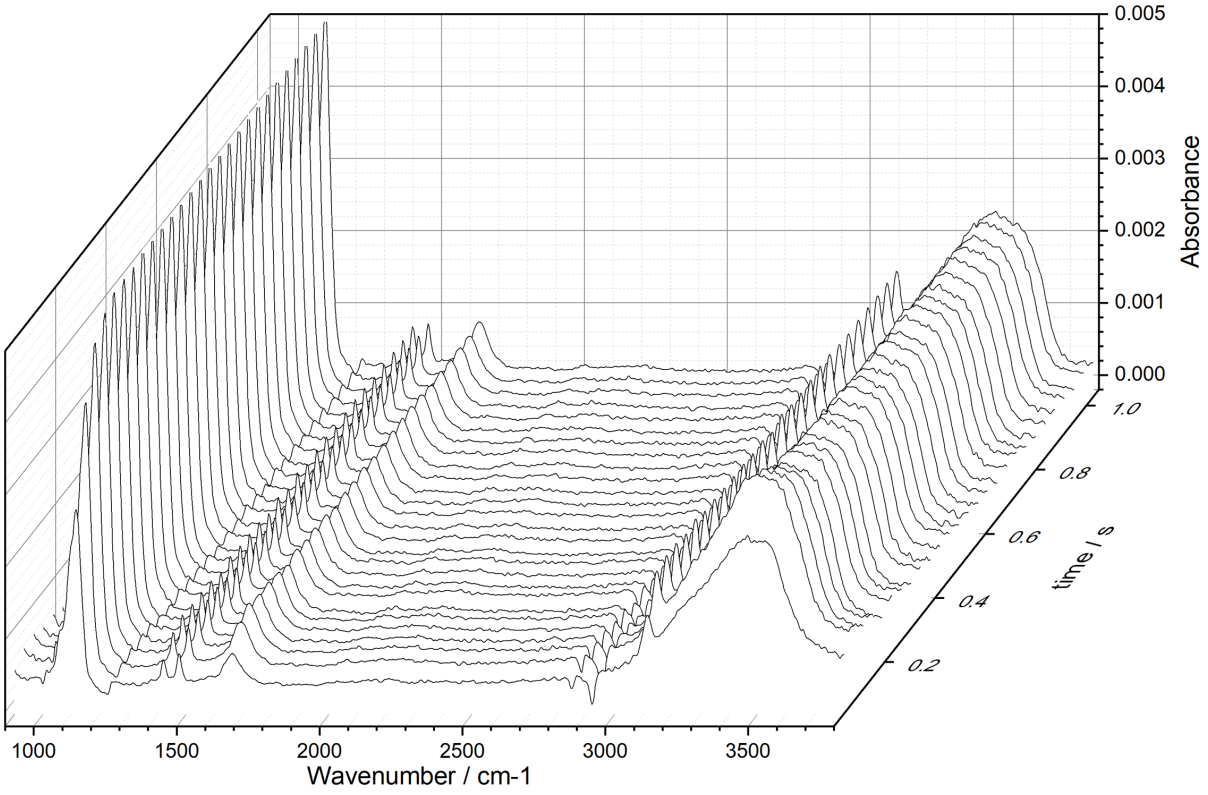

Figure 6.7: Time-resolved rapid scan FTIR spectra of mixed-ordered Fc11SH after E_{step} from +0.1 V to +0.7 V. Time resolution of 76 ms.

For better representation of the time progression of the IR modes of interest, Figure 6.8a and Figure 6.8b show the IR peak absorbance transients extracted from the rapid scan spectra for the oxidation and reduction reaction respectively. For better graphical presentation, the ClO_4^- IR signal within both figures were scaled down by a factor of 5. Examining the IR signal progression in Figure 6.8a for a potential step from +0.1 V to +0.7 V reveals

that all IR signals are visible within the initial 38 ms and reach a new steady state between 150 - 200 ms. Comparing the IR signals, there appears to be no difference between the individual IR peak signal progression within the time resolution of the measurement.

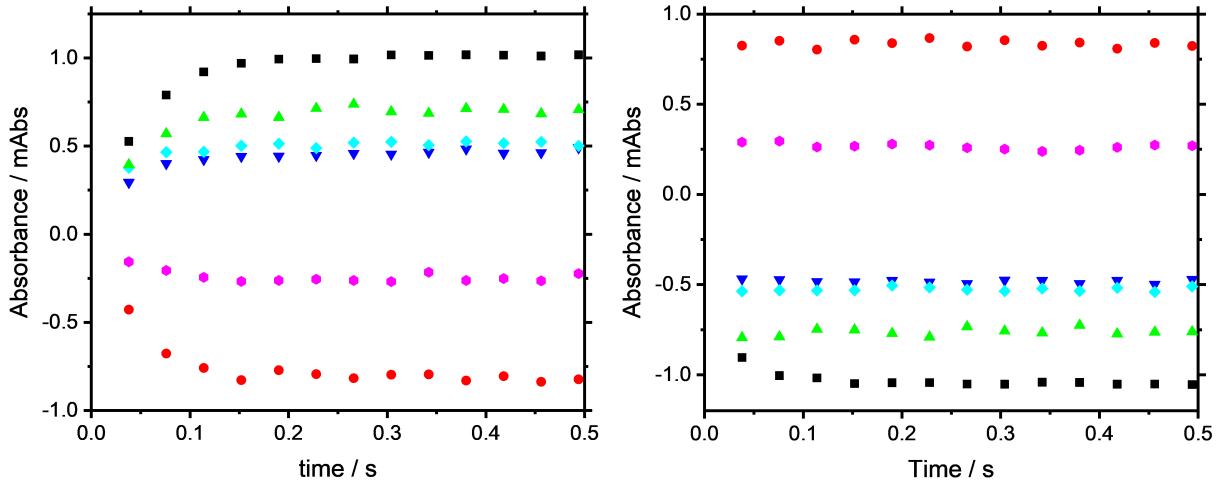

(a) Fc11SH oxidation **(b)** Fc11SH reduction

Figure 6.8: Rapid scan FTIR transients of IR signals at 1110 cm^{-1}, 1420 cm^{-1}, 1476 cm^{-1}, 2850 cm^{-1}, 2920 cm^{-1} and 3112 cm^{-1} for oxidation (a) and reduction (b) of mixed-ordered Fc11SH during E_{step} from +0.1 V to +0.7 V.

The reduction of oxidized Fc11SH shown in Figure 6.8b shows a faster process, with all IR signals reaching a new steady state within the initial two spectra and therefore less than ∼100 ms. The opposite direction of the IR signals is due to the collection of the background spectrum at +0.7 V, compared to the background spectrum collected at +0.1 V for the oxidation. It is important to keep in mind that according to the CV shown in Figure 6.4c, the cathodic reduction occurs at +200 mV higher overpotential. Assuming the charge transfer from the ferrocene to the electrode is identical for the anodic and the cathodic reaction (*i.e.* its charge transfer coefficient $\alpha = 0.5$), the fundamental relationship between a heterogenous transfer rate and the electrochemical overpotential η of an electrochemical process can be derived from a simplified Butler-Volmer equation (Equation 6.1):

$$k = k_0 exp\left(\frac{\pm \alpha z F \eta}{RT}\right) \tag{6.1}$$

Here, k_0, z, F, R and T are the rate constant, number of electrons involved in the reaction, the Faraday constant, universal gas constant and the temperature of the system, which are all constant during this experiment. The charge transfer, is therefore proportional to e^{η}. With an additional 200 mV during the cathodic reaction, the faster kinetics observed in the IR signal progression is likely due to the higher overpotential rather than a fundamental difference in the oxidation and reduction kinetics of the Fc11SH.

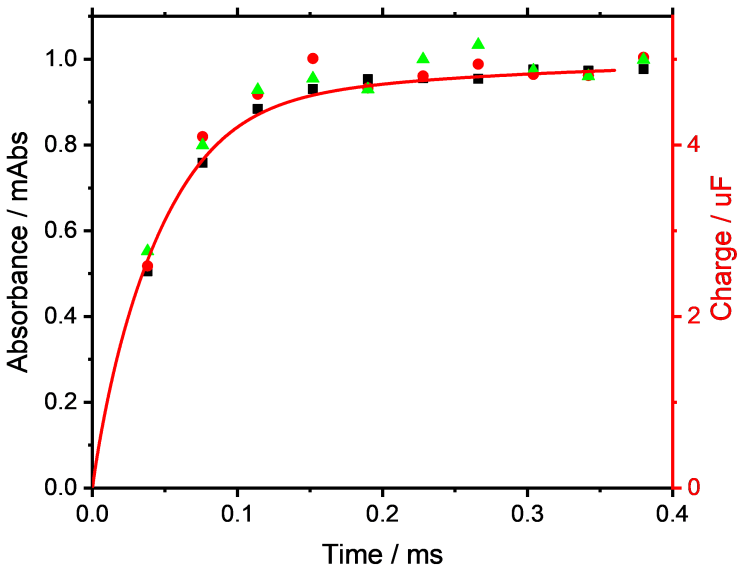

Figure 6.9: Selected normalized IR transients of the Fc11SH IR signals (1110 cm^{-1}, 2920 cm^{-1} and 3112 cm^{-1}) during oxidation, overlaid with the corresponding charge. Integrated charge calculated from current transients collected parallel to rapid scan FTIR data.

One of the main objectives of this study was a comparison between the kinetics of conformational change versus the rate of electron transfer in Fc11SH. Assuming the electrochemically measured current upon potential perturbation is primarily a result of the Fc11SH

oxidation/reduction, then the extent of completion of the charge transfer reaction can be obtained by integrating the measured current transient over time. The calculated charge is plotted versus selected normalized IR transients in Figure 6.9. This figure also shows the IR absorbance transients for the ferrocene ring (3112 cm^{-1}), alkane bridge (2920 cm^{-1}) and perchlorate (1110 cm^{-1}). The strong overlap of all three IR transients with each other and the integrated charge suggest that the charge transfer process is not differentiable from any of the conformational processes within the 38 ms time resolution of the rapid scan FTIR measurement.

Overall, the rapid scan measurements indicate: 1) Fc11SH SAM on SEIRAS active Au-layers are stable for repeated potential steps; 2) Fc11SH and the ClO_4^- anion signal should be of sufficient signal-to-noise to be visible in step scan FTIR measurements; 3) for potential steps between 100 mV to 700 mV, IR observable perturbation will reach a new state within 150 ms; 4) better comparison between individual IR signals as well as between IR and electrochemical data will require higher time-resolution of step scan FTIR to be fully resolved.

6.4.3 Step Scan Potential Sequence and Measurement Stability

Based on the result of the rapid scan FTIR measurements, a potential sequence was designed for the step scan FTIR measurement to capture both oxidation and reduction of Fc11SH within a single FTIR measurement. The black line in Figure 6.10 shows the potential sequence of the step scan measurement. Before each iteration, the potential is held at +0.1 V. Upon initiation of the IR data collection, the potential is continually held at +0.1 V for the initial 20 ms to collect 20 IR spectra with 1 ms time resolution. As the initial 20 spectra are later

used to create the background spectrum for each step scan iteration, the origin of the time scale in Figure 6.10 coincides with the end of background collection. Upon completion of the background measurements, the potential is stepped to +0.7 V to induce the oxidation of Fc11SH. The rapid scan results presented above suggests oxidation at these potentials should reach the new equilibrium within 150 - 200 ms. An extra 100 ms are added to ensure completion of the process for a total measurement time of 300 ms at +0.7 V. Once oxidation is complete, the potential is stepped back to 100 mV and the IR signal is collected for another 300 ms. This provides the IR response for the reduction process as well as resets the potential for the next mirror position iteration.

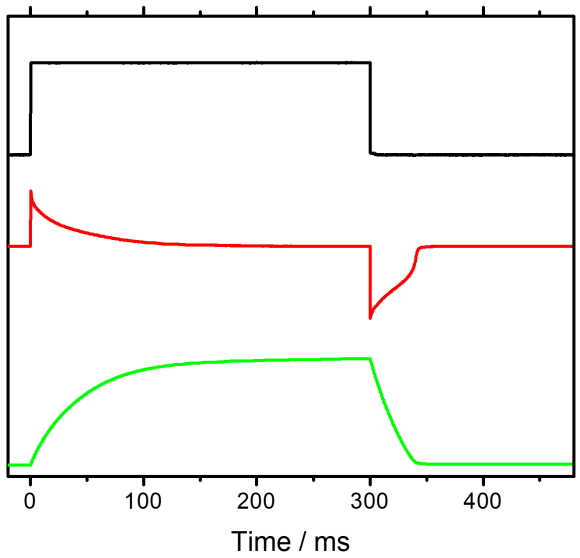

Figure 6.10: Representative transient of electrochemical sequence recorded during a single step scan iteration. At $t = 0$ ms, potential (black) is stepped from +0.1 V to +0.7 V for 300 ms, followed by a E_{step} back at $t = 300$ ms. The corresponding current transient (red) is recorded to calculate the charge (green) through integration.

In addition to the purely spectroscopic IR measurements, electrochemical information is simultaneously collected in the form of current transients. The red line in Figure 6.10 shows a typical current transient of the Fc11SH SAM in response to the potential pertur-

bation described above. Upon stepping to more positive potentials, the current transient will increase due to the combination of current generated from oxidizing the ferrocene as well as from capacitive charging of the interface due to molecular rearrangements. This currents drops, eventually reaching zero, as all Fc11SH molecules are fully oxidized and the electrode/liquid interface has adjusted to the new conditions.

The overall measurement procedure is composed of 620 ms of IR data collection with an additional ∼300 ms of dead time due to the software/instrumentation, resulting in a total measurement time for a single step scan iteration just below 1 s. As the Fc11SH system exhibits IR signals ranging over nearly 2000 cm^{-1} of frequency, space time resolved measurements at many fixed mirror positions must be made to generate accurate interferograms. In experimental terms, this means that for a double-sided interferogram with 8 cm^{-1} wavenumber resolution to be collected, a total of 1100 step scan iterations must be measured which means ∼18 min is needed to obtain a single interferogram. The step scan FTIR results presented below are 128 co-added step scan spectra collected over 48 h of measurement time.

Before discussing the step scan FTIR results, it is important to address the stability of the electrochemical and IR responses of the measured system over the course of the measurement. Figure 6.11a show the current transients collected simultaneously with the IR measurement at 12 h intervals. Current transients remain constant over the entire period of measurement and the maximum value of the integrated charge for the positive potential step remain within 5% of each other. Figure 6.11b shows IR absorption spectra calculated from conventional FTIR measurements taken intermittently during the step scan experiment at 24 h intervals. The IR spectra compare favorably with each other, with all IR signals directly associated with the Fc11SH possessing comparable peak absorbance values. The

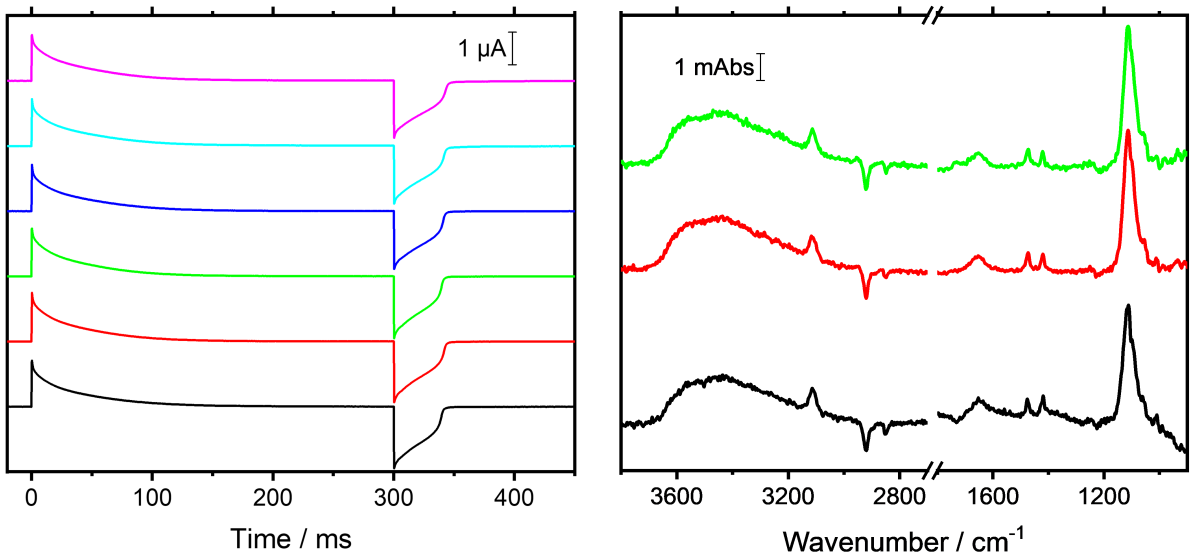

(a) E/I transients **(b)** IR spectra

Figure 6.11: Stability of Fc11SH reaction and corresponding ATR-SEIRAS spectra during step scan FTIR experiment over 60 h based on (a) current transients recorded every 12 h and (b) conventional FTIR spectra of Fc11SH oxidation intermittently collected every 24 h.

results presented in Figure 6.11 provide sufficient evidence that both the electrochemical and IR aspects of the measured system remain consistent over the entire duration of the step scan FTIR experiment.

6.4.4 Step Scan FTIR of Fc11SH SAM Oxidation/Reduction

Figure 6.12 shows the step scan FTIR spectra collated from 128 step scan spectra and based on the potential step sequence described earlier. The results are split into the first 300 ms after the positive potential step in Figure 6.12a and the 300 ms after the negative potential step in Figure 6.12b. Within these step scan FTIR spectra, almost all IR signals observed in earlier FTIR measurements are clearly resolved. The only exception is the weaker C−H stretch of the thiol chain at 2850 cm^{-1}, which is below the increased noise of the step scan measurement due to its weaker IR absorption cross-section.

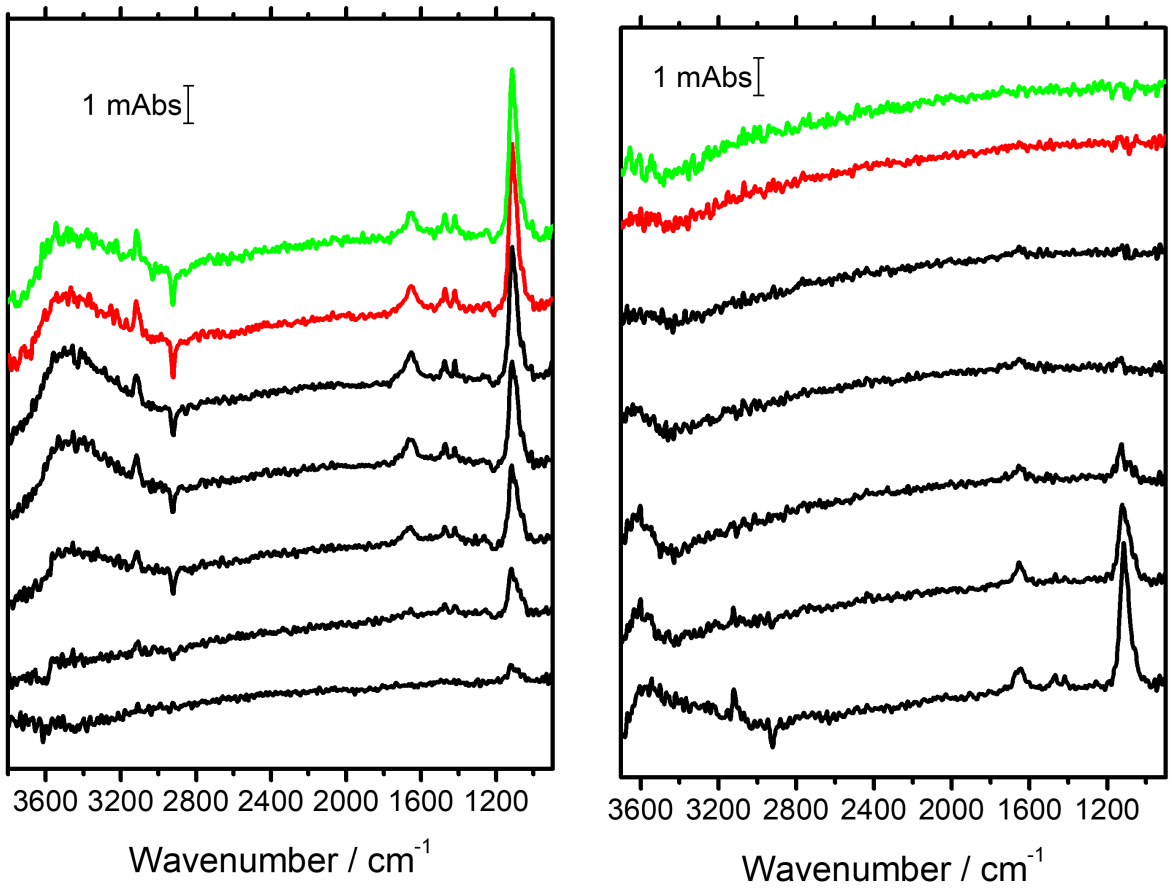

(a) Fc11SH oxidation

(b) Fc11SH reduction

Figure 6.12: Selected step scan FTIR spectra during Fc11SH oxidation (a) and reduction (b) during E_{step} between +0.1 V and 0.7 V. To minimize visual clutter, black shows IR spectra every 20 ms during the initial 100 ms, green spectrum is collected at 200 ms after potential perturbation and red at 300 ms.

Since each potential step encompasses 300 spectra with 1 ms time resolution, the Figure 6.12 shows only selected spectra to minimize clutter. As the rapid scan FTIR showed that the initial 100 ms are the most crucial to Fc11SH redox reactions, the figure shows a spectrum every 20 ms for the initial 100 ms after the potentials step (black lines). Two further spectra at 200 ms (red) and 300 ms (green) are also shown to indicate that a new state has been essentially reached after the initial 100 ms.

IR spectra of the Fc11SH oxidation in Figure 6.12a show increases in the ClO_4^- IR signal as well as indication of the C-H stretches of the ferrocene ring and thiol chain within the first 10 ms. These signals reach maximum values within ∼100 ms. Later spectra at 200 ms and 300 ms suggest very little further changes in the IR signal peak intensities, indicating the oxidation reaction is completed within ∼100 ms. For the reduction shown in Figure 6.12b, the spectra show a more rapid decrease of IR peak intensities compared to the oxidation. Within 50 ms almost all IR signals have returned to baseline. Only small signal changes from ClO_4^- and H_2O are visible at t >50 ms.

To provide a more detailed time-progression of the peak intensity of the individual IR signals of the Fc11SH, all step scan FTIR spectra were baseline fitted using a custom-written Python script to remove the influence of any baseline shift in Figure 6.12. The baseline fitting was straightforward for the sharper IR signal from 1000 - 3200 cm^{-1} but fitting the broad water feature ranging from 3000 - 3700 cm^{-1} were flawed. The broad IR signal overlaps with an increasing downward slope for high wavenumbers as well as drastically increased noise at >3200 cm^{-1}. Any fits were strongly subjective and will therefore not be considered for further analysis. Instead, the H_2O signal at 1650 cm^{-1} will be used to discuss the kinetics of water upon oxidation/reduction of the Fc11SH. Similarly, the stronger IR

signals at 2920 cm^{-1} and 3112 cm^{-1} will be used as indications of the ferrocene ring and thiol chain.

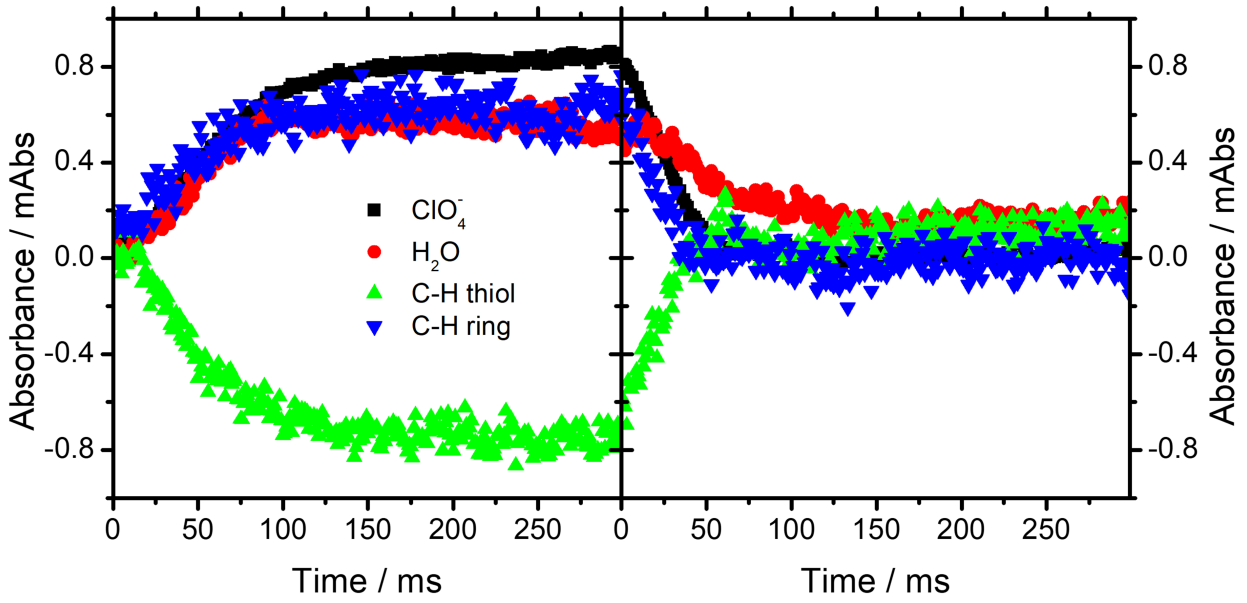

Figure 6.13: Step scan FTIR transients of IR signals at 1110 cm^{-1}, 1650 cm^{-1}, 2920 cm^{-1} and 3112 cm^{-1} for oxidation followed by reduction of mixed-ordered Fc11SH.

Figure 6.13 shows the time progression of peak IR intensity for selected IR signals representing orientation changes of the ferrocene ring (2910 cm^{-1}) and thiol chain (3112 cm^{-1}) as well as the ingress of H_2O (1650 cm^{-1}) and ClO_4^- anions (1110 cm^{-1}, scaled by factor of /5 for better graphical representation). The oxidation in Figure 6.13 shows an immediate increase in all IR signals for the initial 100 - 150 ms before reaching a plateau once the new state has been reached. The cathodic reduction process, shown in Figure 6.13, displays comparable behaviour for the C−H and Cl−O stretch, but with faster kinetics compared to the oxidation. The kinetic differences are again likely due to the differences in the overpotential for the forward and reverse reactions. These results compare favorably to step scan spectra shown in Figure 6.12 and rapid scan results in Figure 6.9. The H_2O signal during

the reduction, however, shows a significant delay compared to the remaining IR signals and will require a more in-depth discussion.

6.4.5 Step Scan FTIR vs Electrochemistry

With successful measurement of Fc11SH step scan FTIR spectra, it is possible to provide a more accurate comparison of the kinetics observed with IR versus the kinetics determined through electrochemical means. Figure 6.14a compares the IR transient of selected and normalized IR signals (2920 cm^{-1} for Fc11SH alkane, 3112 cm^{-1} for Fc11SH ring, 1110 cm^{-1} for ClO_4^- anions) with the charge transient measured during the positive potential step. Unlike the earlier rapid scan results in Figure 6.9, the step scan data show a clear delay between the electrochemically measured process and the individual FTIR modes of the Fc11SH. Based on the charge, half of the Fc11SH is oxidized ∼15 - 20 ms earlier than the FTIR signals associated with the rearrangement of the molecule and influx of the ion pairing anion. The delay is well below the time resolution of 38 ms of the rapid scan FTIR measurement and highlights the temporal resolution benefits of the step scan technique. A similar trend is also visible for the negative potential step shown in Figure 6.14b, where the electrochemical measured charge is overlaid with the highest S/N IR transient of the ClO_4^- anions. While the negative potential step is driven by 200 mV higher overpotentials, the FTIR signal is still ∼10 ms delayed comparted to the charge.

To further quantify the kinetics of the process, the individual IR transients were fitted with an exponential function ($y = 1 - A\ e^{1-k_0 t}$) to calculate their respective rate constant k_0. The fitting results are shown in Table 6.1. The corresponding rate constants of the current transient are calculated by averaging the time constant of the 11 current

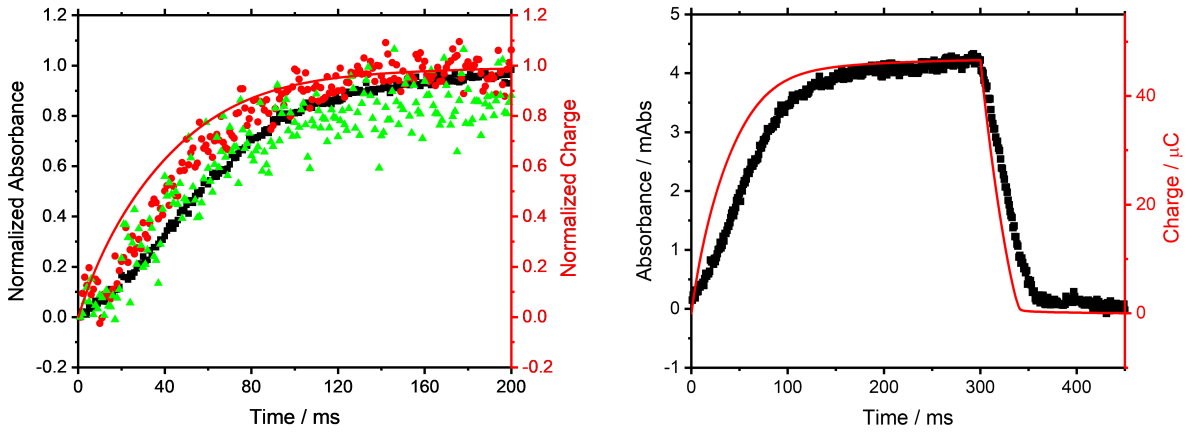

(a) **(b)**

Figure 6.14: (a) Selected normalized IR transients of step scan IR signals at 1110 cm^{-1}, 2920 cm^{-1} and 3112 cm^{-1} during oxidation of Fc11SH, overlaid with the corresponding charge. Integrated charge calculated from current transients collected parallel to step scan FTIR data. (b) Comparison between IR transient of the ClO_4^- anions IR signal during oxidation and reduction and the measured charge.

Rate Constants Calculated from	For Positive Step	For Negative Step
Integrated Current Transient	23.5 s^{-1}	55.6‘s^{-1}
IR Signal at 1110 cm^{-1} (ClO_4^- anion)	15.5 s^{-1}	39.2 s^{-1}
IR Signal at 1650 cm^{-1} (H_2O)	24.4 s^{-1}	18.0 s^{-1}
IR Signal at 2920 cm^{-1} (Fc11SH Alkane)	19.8 s^{-1}	47.3 s^{-1}
IR Signal at 3112 cm^{-1} (Fc11SH Ring)	21.6 s^{-1}	50.6 s^{-1}

Table 6.1: Fc11SH oxidation/reduction rate constants based on exponential fitting of step scan FTIR experimental data.

transients shown in Figure 6.11a.

As with earlier results, the H_2O data will be excluded from the initial discussion. During the Fc11SH oxidation/reduction, the individual rate constants suggest that the electron transfer (charge), influx of anions for ion pairing (1110 cm^{-1}) and molecular reorientation (2920 cm^{-1} and 3112 cm^{-1}) occur at three different rates, decreasing in the order of: 1) electron transfer; 2) ring and alkane reorientation; 3) ion pairing with the anions. While the rate constant of the thiol does suggest the ferrocene rotation to be slightly faster than tilting of the alkane, the low S/N of these IR modes should caution against definitive conclusions.

Similarly, the comparatively slower ClO_4^- anions influx and ion pairing could be affected by the low S/N of the Fc11SH ring and alkane. In order to support this conclusion, a 2D correlation analysis of the step scan FTIR result was performed as a secondary confirmation for the time delay between the different IR signals.

6.4.6 2D Correlation Analysis of Step Scan FTIR Results

Two-dimensional correlation spectroscopy (2D-COS) was first introduced by Noda in 1990[63]. Since its inception, it has gained application for a wide range of absorption techniques including IR, Raman, UV-vis and X-ray spectroscopy as well as encompassing non-absorption-based spectroscopy techniques such as fluorescence, chromatography and NMR. A comprehensive description of the theory of 2D-COS is beyond the scope of this thesis but can be found in multiple reviews[64,65] as well as a textbook on the subject area by Noda and Ozaki[66]. At its core, 2D-COS is an analysis technique that determines correlations of different spectroscopic signals within multiple spectra as a result of an external perturbation. In the case of the step scan FTIR results discussed here, the external perturbation is the potential step between 100 mV and 700 mV. As the spectral data follows the adjustment of the Fc11SH SAM and the EDL over time, 2D-COS will determine which IR signals are correlated with each other as well as their relative correlation to each other (*i.e.* the order of appearance after the potential perturbation). 2D-COS calculation of the dynamic IR spectra $y(\upsilon, t)$ with IR signal for the time elements between T_{min} and T_{max} through a custom MATLAB program (Appendix VIII) will produce two (one for the positive step and another for the negative potential step) 2-dimensional maps called the synchronous $\phi(\upsilon_1, \upsilon_2)$ and asynchronous $\psi(\upsilon_1, \upsilon_2)$ 2D spectrum utilizing the following set of equations:

$$\phi(\upsilon_1, \upsilon_2) + i\psi(\upsilon_1, \upsilon_2) = \frac{1}{\pi(T_{min} - T_{max})} \int_0^\infty \tilde{Y_1}(\omega)\tilde{Y_2^*}(\omega)d\omega \tag{6.2}$$

$$\tilde{Y_j}(\omega) = \int_{-\infty}^{\infty} \tilde{y_j}(\upsilon_j, t)e^{-i\omega t}dt \tag{6.3}$$

$$\tilde{y}(\upsilon, t) = \tilde{y}(\upsilon, t) - \frac{1}{(T_{min} - T_{max})} \int_{T_{min}}^{T_{max}} y(\upsilon, t)dt \tag{6.4}$$

Once calculated, both the synchronous and asynchronous correlation functions can each be plotted as map consists of identical wavenumber ranges plotted on both the abscissa and ordinate of a Cartesian plane. The value of the synchronous $\phi(\upsilon_1, \upsilon_2)$ and asynchronous correlation function $\psi(\upsilon_1, \upsilon_2)$ is usually plotted on the plane in the form of colour-coded heat map as seen in Figure 6.16 and 6.17. If an IR signal with wavenumber υ_1 on the x-axis is correlated to an IR signal of wavenumber υ_2 on the y-axis, the 2D correlation spectrum will possess a cross-correlation peak (also referred to as cross peak) with non-zero value at [υ_1,υ_2]. Further interpretation of the data relies on the following a set of rules, commonly referred to as Noda's rules.

1. If the intensity of the signal at wavenumber υ_1 and υ_2 in the original spectra are correlated and changing in the same direction, the synchronous 2D spectrum will posses a positive cross peak at [υ_1,υ_2]

2. If the intensity of the signal at wavenumber υ_1 and υ_2 in the original spectra are correlated and changing in the opposite direction, the synchronous 2D spectrum will posses a negative cross peak at [υ_1,υ_2]

3. If the change at wavenumber υ_1 mainly precedes the change at wavenumber υ_2, the

asynchronous 2D spectrum will possess a positive peak at [υ_1,υ_2]

4. If the change at wavenumber υ_1 mainly follows the change at wavenumber υ_2, the asynchronous 2D spectrum will possess a negative peak at [υ_1,υ_2]

5. If the synchronous 2D spectrum at [υ_1,υ_2] is negative, interpretation of rules 3 and 4 must be reversed

One challenge for 2D-COS with the Fc11SH IR spectra is the stark signal intensity differences between the weaker IR Fc11SH and H_2O signals compared to the strong ClO_4^- signal. Without any further data processing, the 2D-COS spectrum will only showcase the correlation of the weaker IR signals with the anion IR signal, but not of the weaker IR signals with each other. To tackle this issue, a threshold of >0.3 mAbs was applied to spectral regions surrounding the known Fc11SH peaks to identify six wavenumber regions associated with the reaction. Once peak regions were determined, the absorbances within each region were normalized according to the minimum and maximum absorbance value within each region.

Figure 6.16 and 6.17 shows the results of the 2D-COS analysis. Positive and negative correlation peaks are indicated in red and blue respectively. For the positive potential step from 100 mV to 700 mV, the synchronous spectrum (Figure 6.16a) shows consistently positive cross peaks with maxima centered at any combination of [υ_1,υ_2] with υ_1,υ_2 = 1113 cm^{-1}, 1419 cm^{-1}, 1473 cm^{-1}, 1653 cm^{-1} and 3116 cm^{-1}. According to the first of Noda's rules, these IR signals are correlated with each other and change in the same direction. All cross peaks with the alkane C−H stretch at 2924 cm^{-1} show negative correlations. According to the second rule, the 2924 cm^{-1} stretch is correlated with all other signals but changes in the

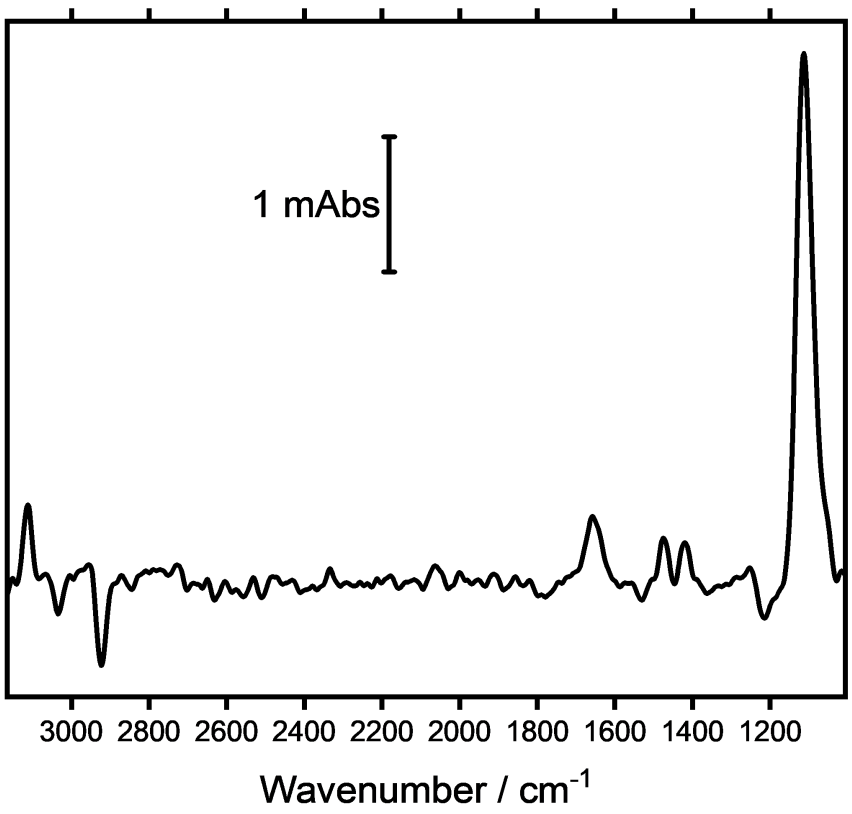

Figure 6.15: Representative step scan FTIR spectra after baseline correction of Fc11SH oxidation/reduction, that was utilized for 2D correlation maps. Spectra contains multiple spectral features around 1113 cm^{-1} (ClO_4^-), 1419 cm^{-1} (ferrocene C−C), 1473 cm^{-1} (ferrocene H−C−H or Fe−C), 1653 cm^{-1} (H_2O), 2924 cm^{-1} (alkane C−H) and 3116 cm^{-1} (ferrocene C−H) that exceed the >0.3 mAbs threshold utilized during the calculation of the correlation maps.

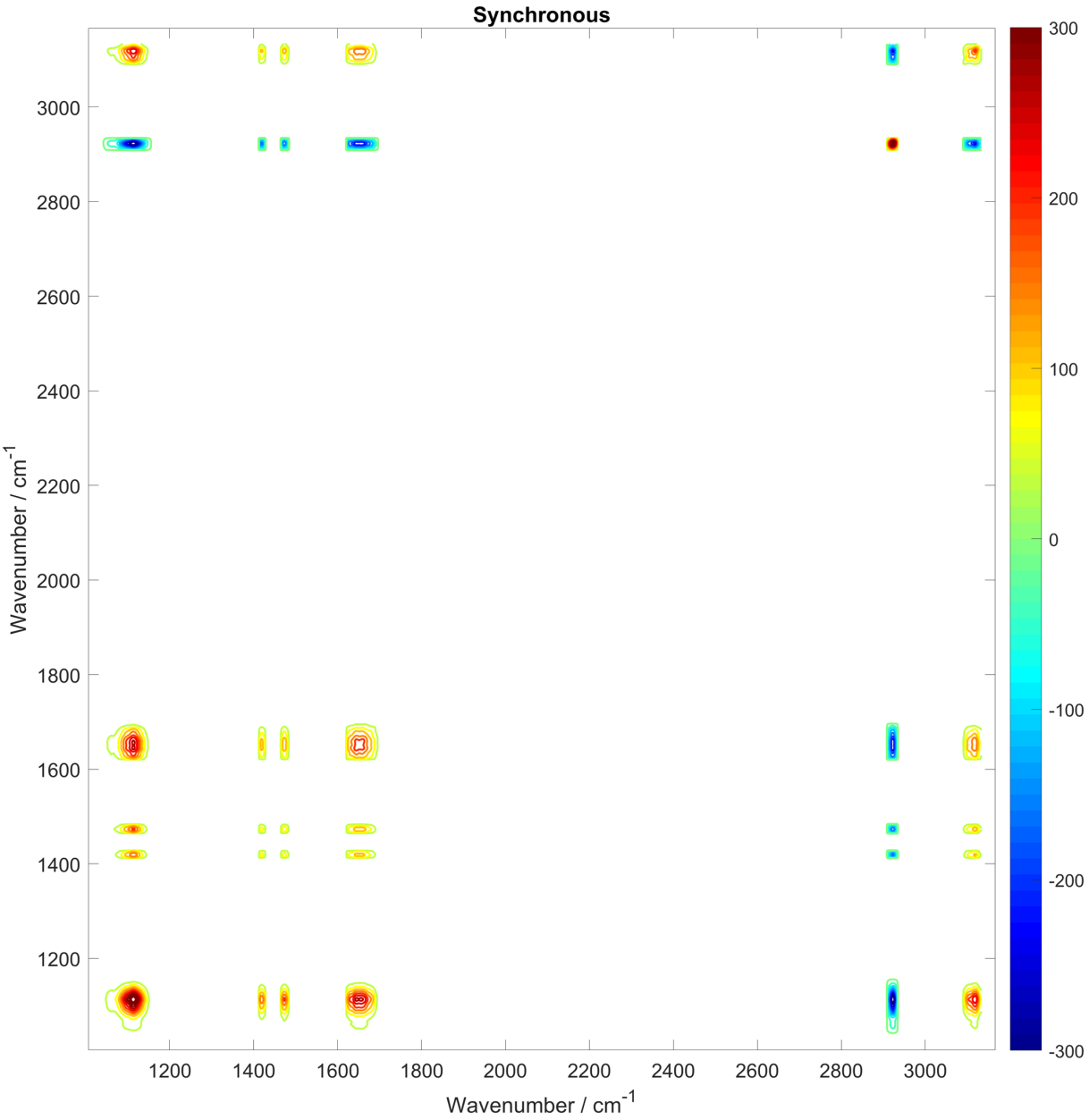

(a) Synchronous Fc11SH oxidation

Figure 6.16: Synchronous (a) and asynchronous (b) 2D correlation maps based on step scan FTIR measurement of Fc11SH oxidation upon E_{step} from +0.1 V to +0.7 V.

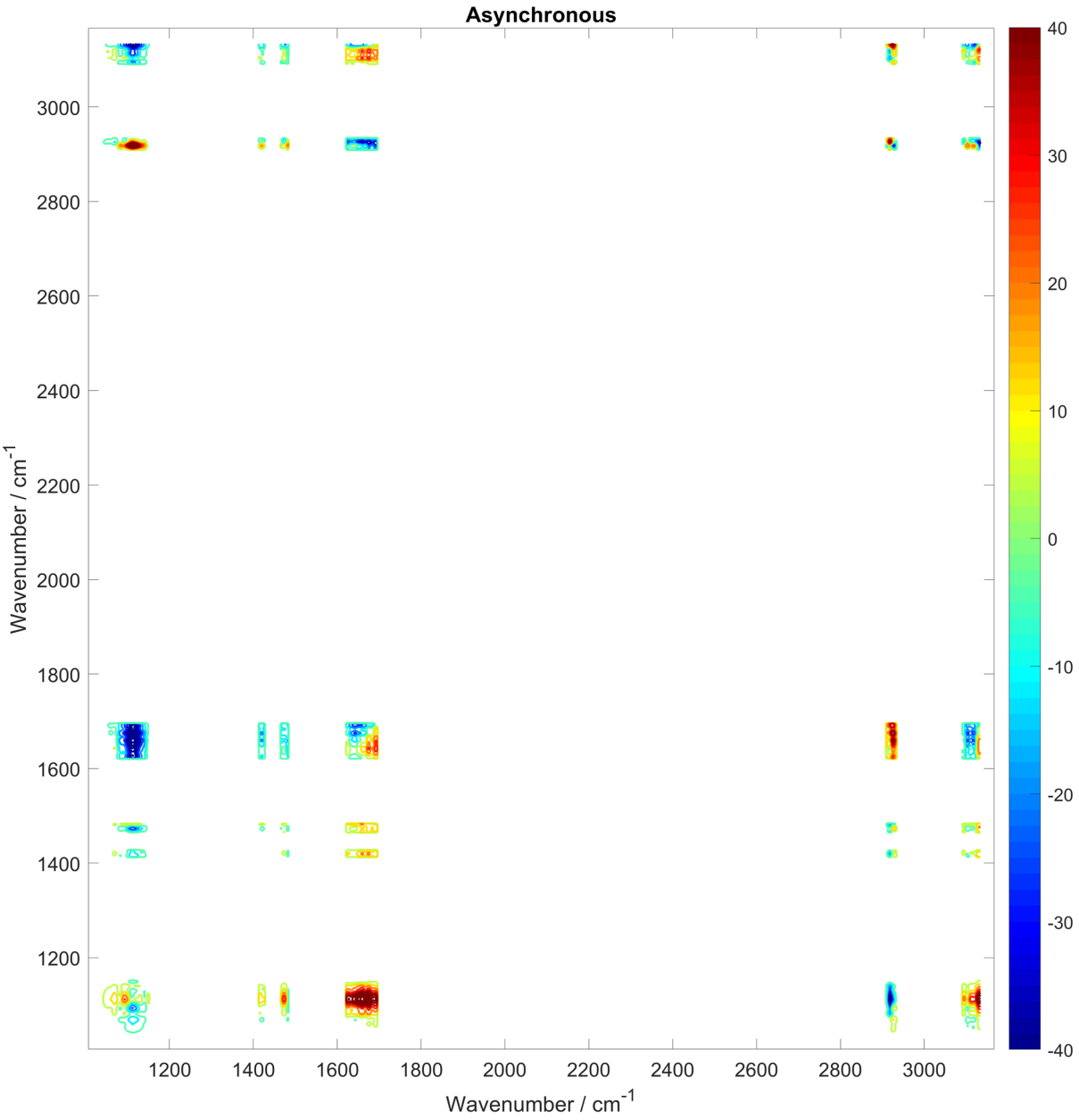

(b) Asynchronous Fc11SH oxidation

Figure 6.16: Synchronous (a) and asynchronous (b) 2D correlation maps based on step scan FTIR measurement of Fc11SH oxidation upon E_{step} from +0.1 V to +0.7 V. (cont.)

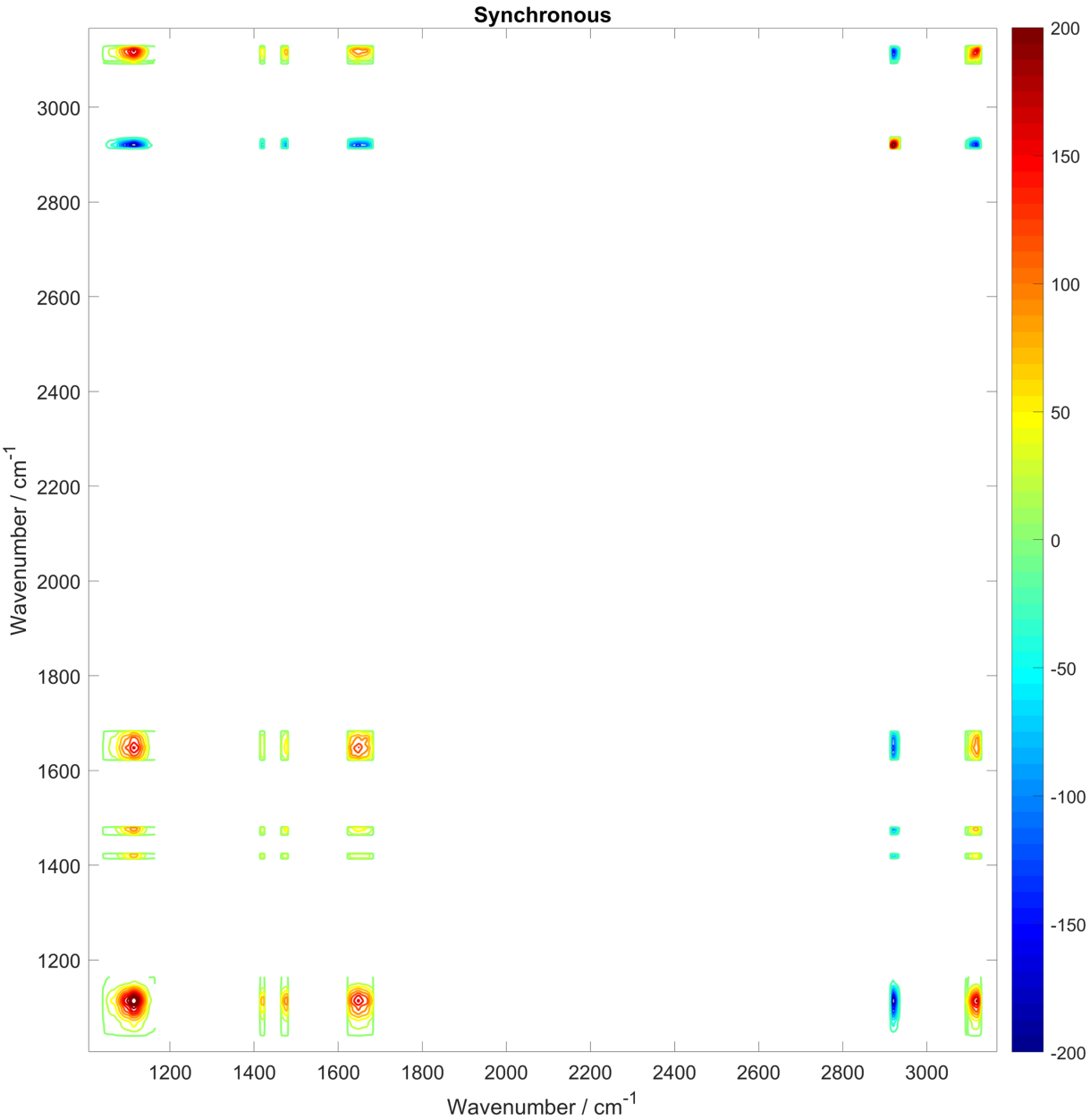

(a) Synchronous Fc11SH reduction

Figure 6.17: Synchronous (a) and asynchronous (b) 2D correlation maps based on step scan FTIR measurement of Fc11SH reduction upon E_{step} from +0.7 V to +0.1 V.

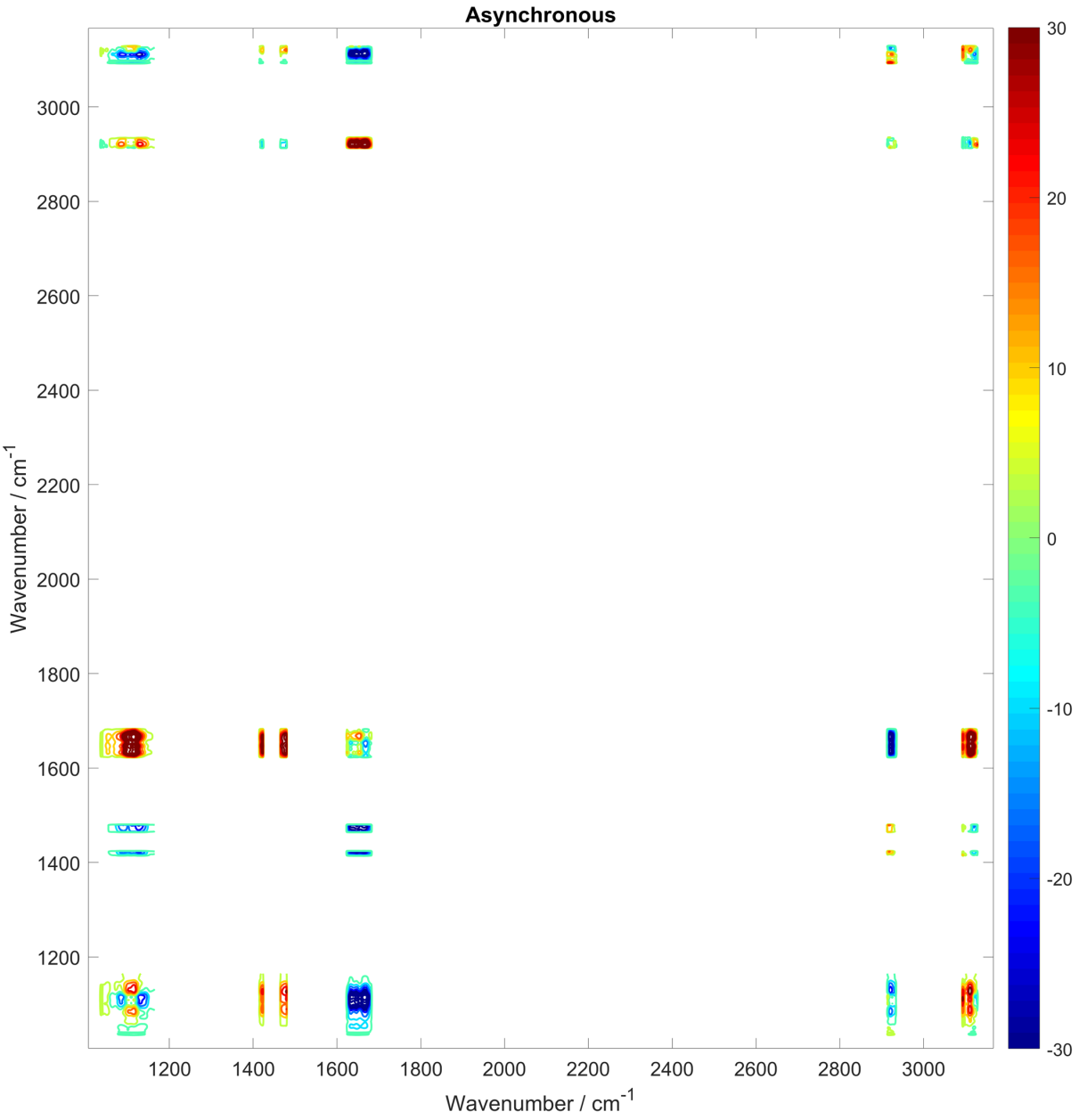

(b) Asynchronous Fc11SH reduction

Figure 6.17: Synchronous (a) and asynchronous (b) 2D correlation maps based on step scan FTIR measurement of Fc11SH reduction upon E_{step} from +0.7 V to +0.1 V. (cont.)

opposite direction. Virtually identical correlations can be found in the synchronous spectrum of the negative potential step from 700 mV to 100 mV in Figure 6.17a. While these results are unsurprising as the same qualitative information can be extracted by inspection of Figure 6.14, the synchronous spectra are still important for determining the order of appearance after the initial perturbation. This can be done in combination with the asynchronous spectrum in Figure 6.16b and 6.17b for the two potential step measurements.

Before discussing individual peaks, it is important to note that all cross-correlation peaks in both asynchronous spectra are much less well defined than those found in the synchronous spectra. A good example of an ill-defined correlation are the cross peaks between the C−H stretch in the ring (3116 cm^{-1}) and alkane (2924 cm^{-1}) in Figure 6.16b. Based on the synchronous spectrum, if either the ring rotation or alkane tilt is preceding the other, the asynchronous spectrum should show two cross peaks with maximum/minimum value centered at [2924 cm^{-1}, 3116 cm^{-1}] and [3116 cm^{-1}, 2920 cm^{-1}]. Instead, the spectrum shows a maxima (red) and minima (blue) in close proximity (<10 cm^{-1} apart) and the values at the exact coordinates of the IR signals are midway between the nearby maxima/minima. While a wavenumber shift of the IR peak in time could explain this result, the absence of any wavenumber shift in the potential dependent FTIR in Figure 6.6 and rapid scan FTIR measurement in Figure 6.7 makes no asynchronous correlation within the noise of these two low S/N IR signal a much more likely explanation. The result will therefore be viewed as no asynchronous correlation between these two IR signals within the noise of the measurement. Similar situations can be found for virtually all cross peak between IR signals related to the conformation of the Fc11SH (*i.e.* signal at 1419 cm^{-1}, 1473 cm^{-1}, 2924 cm^{-1} and 3116 cm^{-1}). In contrast, cross peaks including either the ClO_4^- anions at 1116 cm^{-1} or H_2O at 1653 cm^{-1}

have a maxima/minimum centered around the exact IR signal location. Further analysis of the asynchronous spectra will therefore be limited to correlations of IR signals with either ClO_4^- or H_2O.

The asynchronous spectrum for the positive potential step in Figure 6.17a shows negative cross peaks for correlation between the ClO_4^- anions at υ_1 = 1118 cm^{-1} with IR signals at υ_2 = 1419 cm^{-1}, 1473 cm^{-1}, 1653 cm^{-1} and 3116 cm^{-1}. As earlier synchronous cross peaks at these coordinates are positive, the fourth of Noda's rule applies and states that ClO_4^- signal follows all these IR signals. For the positive cross peak at [1113 cm^{-1}, 2920 cm^{-1}], the interpretation of the fourth of Noda's rule must be inverted due to the negative cross peak in the synchronous spectrum in accordance to the fifth of Noda's rules. The 2D-COS analysis of the positive potential step therefore suggests that ClO_4^- is the slowest of the IR signals. A different situation is visible for the H_2O signal at 1650 cm^{-1}. Here, cross peaks at υ_1 = 1650 cm^{-1} show strong positive correlation, mirrored by cross peaks at υ_2 = 1650 cm^{-1} with strong negative correlations. The exception are cross peaks at [1650 cm^{-1}, 2920 cm^{-1}] and [2920 cm^{-1}, 1650 cm^{-1}] that are negative and positive respectively. Combined with the synchronous spectrum, the 2D-COS suggest that H_2O is preceding all other Fc11SH signals.

A similar analysis was performed for the asynchronous spectrum of the negative potential step shown in Figure 6.17b. Without going further into details, the results are summarized in Figure 6.18. For the positive potential step (Figure 6.18a), the order of appearance is H_2O → Fc11SH orientational modes → ClO_4^-. For the negative potential step (Figure 6.18b), the order of appearance is Fc11SH orientational modes → ClO_4^- → H_2O. The conclusions of 2D-COS analysis results are therefore identical with those based on the rate constants in Figure 6.18. Fc11SH reorientation appears to be consistently earlier than

	ClO_4^- anion	C-C ring	H-C-H ring	H_2O	C-H thiol	C-H ring
C-H ring	After	Same	Same	Before	Same	
C-H thiol	After	Same	Same	Before		Same
H_2O	After	After	After		After	After
H-C-H ring	After	Same		Before	Same	Same
C-C ring	After		Same	Before	Same	Same
ClO_4^- anion		Before	Before	Before	Before	Before

(a) Fc11SH oxidation sequence: $H_2O \rightarrow$ Fc11SH $\rightarrow ClO_4^-$

	ClO_4^- anion	C-C ring	H-C-H ring	H_2O	C-H thiol	C-H ring
C-H ring	After	Same	Same	After	Same	
C-H thiol	After	Same	Same	After		Same
H_2O	Before	Before	Before		Before	Before
H-C-H ring	After	Same		After	Same	Same
C-C ring	After		Same	After	Same	Same
ClO_4^- anion		Before	Before	After	Before	Before

(b) Fc11SH reduction sequence: Fc11SH $\rightarrow ClO_4^- \rightarrow H_2O$

Figure 6.18: Summary of 2D correlation map analysis for Fc11SH oxidation (a) and reduction (b). Blue indicates the change in IR signal of the column occurs after the IR signal of the row. Red indicates before and green indicated a timing difference is not discernable.

the anion signal for both oxidation and reduction of the molecules. H_2O appears either as the first process or the last depending on whether it is the positive potential step with lower overpotential or the negative step with higher overpotential.

6.4.7 Preliminary Model for the Dynamics of Fc11SH SAM

It is well established in the literature that the oxidation/reduction of Fc11SH SAM includes the following three processes[41,52]: 1) oxidation/reduction of Fe^{2+} and Fe^{3+} due to electron transfer between the ferrocene and the electrode surface; 2) rotation of the ferrocene moiety and tilting of the alkane chain between an angled position and a more vertical position; 3) ingress/egress of anions for ion pairing with the oxidized Fc11SH. The known initial and final orientation of the Fc11SH and composition of the EDL is schematically shown in Figure 6.2, but the specific sequence of events were so far only indirectly inferred from experimental measurements lacking the time resolution and/or the ability to directly observe the sequence of events in the solution phase. This was the main motivation for fast time resolved FTIR measurement of the Fc11SH redox, as it can directly follow the kinetics of these processes through their individual IR signals. The combination of electrochemical information from current transients and spectroscopic from step scan FTIR results discussed in this chapter provided the encompassing picture of the reaction needed to propose a possible sequence of events upon oxidation/reduction of the molecule shown by a schematic model in Figure 6.19.

The comparison between the positive step charge transient and the IR peak transient in Figure 6.14 suggest that heterogenous electron transfer from the ferrocene to the electrode is the first event upon an oxidizing potential perturbation. This is further supported by the slightly faster rate constant of the charge transient (23.5 s^{-1}) in Table 6.1 versus the

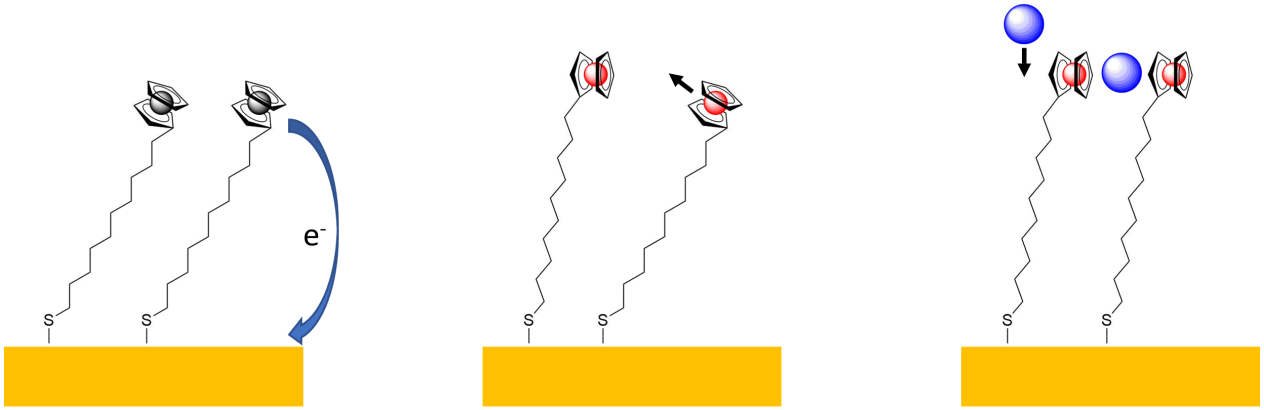

(a) Model for Fc11SH oxidation

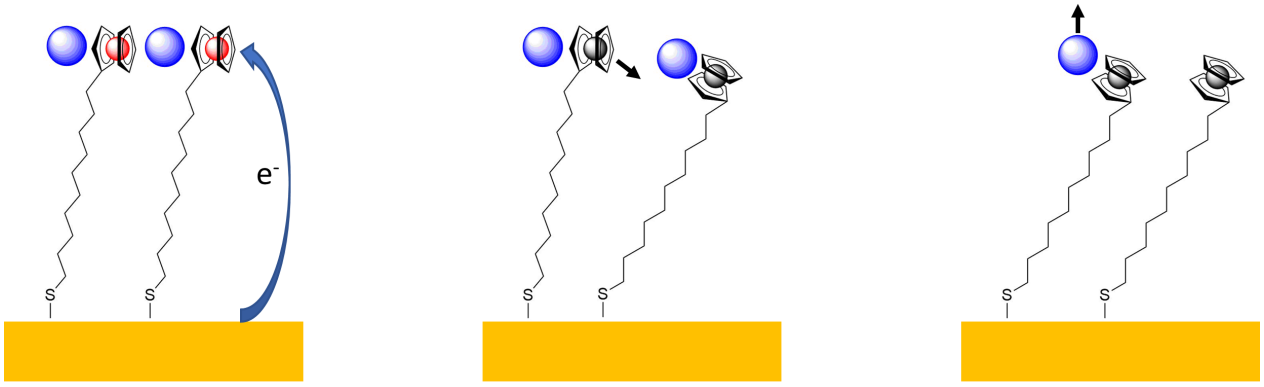

(b) Model for Fc11SH reduction

Figure 6.19: Schematic representation of the proposed sequence-of-events during Fc11SH oxidation (a) and reduction (b) based on analysis of step scan FTIR results.

Fc11SH reorientation (19.8 s^{-1} and 21.6 s^{-1}) and ClO_4^- anions (15.5 s^{-1}) IR signals. The faster rate constant of Fc11SH reorientation versus the ClO_4^- influx is also supported by the 2D-COS analysis. Figure 6.19a contains the schematic model for the oxidation of Fc11SH based on the combination of this information. The Fc11SH is initially in a neutral charged state with tilted orientation compared to the electrode surface. Following a positive potential perturbation of the electrode surface, the heterogenous electron transfer occurs first, followed by the reorientation of the oxidized molecule into a more vertical orientation and lastly the influx of ClO_4^- and ion paring of the anions with the oxidized ferrocene.

In case of the reduction of the oxidized Fc11SH, the heterogenous charge transfer appears to be the first process. Both the charge transfer transient and rate constant values are faster compared to conformational and anion changes in the step scan IR measurement. Rate constant values and 2D-COS suggest that Fc11SH reorientation is also faster than the egress of ClO_4^-. This results in the schematic model shown in Figure 6.19b for the reduction of Fc11SH. Starting from oxidized Fc11SH with ion paired ClO_4^-, the heterogenous electron transfer occurs first in the vertical orientation, followed by rearrangement of the reduced Fc11SH to the tilted position and lastly a slow outflux of ClO_4^- anions.

Before there is any further discussion of this preliminary model, it should be noted that there are a few shortcomings present within the experiments that will be discussed later in this chapter. Nevertheless, assuming the validity of the proposed model, the step scan FTIR measurement within this thesis provides direct spectroscopic evidence of the proposed sequence of events for ferrocene-terminated thiol oxidation and reduction that compares favorably with the literature[41,52–54]. Conformation changes of the Fc11SH upon oxidation was proposed to be the result of electrostatic repulsion between positively charged redox

centers and the positively charged electrode surface. IR signal changes of the ferrocene ring and alkane bridge should therefore follow the electron transfer. Once in the upright position, the positively charged thiols will ion pair with anions from solution. The ingress of the anion should follow the conformational changes as it is limited by the mass transport of the anion resulting in the delayed increase in ClO_4^- IR signal. The reverse process occurs for the reduction. Here the charge neutral Fc11SH, after initial electron transfer from the electrode to the redox center, will immediately relax back into its tilted position. Separation and egress of the ion paired anions is delayed as it is limited by mass transport.

Beyond supporting the model of conformational and ion pairing of Fc11SH in the literature, the sequence of events also has one implication for the symmetry of electron transfer between oxidation and reduction of Fc11SH. It is well established in the literature that electron transfer is strongly dependent on the distance between the redox center and electrode surface[39]. The proposed model assumes electron transfer is the initial step in both oxidation and reduction. As the initial conformation the Fc11SH during reduction is in a more upright position compared to the oxidation, the barrier for electron transfer between the two processes is divergent due to a 0.3 nm difference in electron transfer distance as a result of the thicker SAM layer in the more upright confirmation. This has implications on the transfer coefficient α that describes the symmetry of the potential barrier for the electron transfer of redox process. The transfer coefficient α is an important value for the often used Laviron model-based approach to determine k_{ET} of redox-active SAMs[67,68]. Based on the results of this chapter, α for non-diluted ferrocene alkanethiol SAMs should deviate from a perfectly symmetrical value (*e.g.* $\alpha = 0.5$) to be slightly weighted towards the anodic electron transfer (*e.g.* $\alpha > 0.5$).

6.4.8 Shortcomings, Improvements and Outlook

The value of the interpretation of the step scan FTIR results and proposed model are currently hampered by some shortcomings with the measurement, namely the relatively poor SAM coverage of the Au surface and the poor ordering of the redox-active Fc11SH SAM. It is therefore worthwhile to discuss the influences of these shortcomings and possible options to address them in future measurements.

Shortcomings

Arguably the most detrimental influence on the FTIR measurements is the large presence of bare Au surface after Fc11SH incubation. Based on the CV measurement shown in Figure 6.4 and subsequent calculation of the Fc11SH surface coverage, redox-active SAM coverage can currently range from 20% to 50% of the Au surface. Any electrochemical and IR measurement is therefore the average combination of Au-Fc11SH-electrolyte and Au-electrolyte response to potential perturbations.

For the electrochemical chronoamperometric measurements during time-resolved experiments, the effects of incomplete FcSH coverage are twofold. 1) The integrated charge used to compare oxidation/reduction of the ferrocene redox center is more a combination of ferrocene redox and double layer charging of the bare Au-electrolyte interface. 2) The time constant of the system is also increased due to the presence of bare Au-electrolyte interface. As discussed in Chapter 2, the time-constant T of any electrochemical system can be describe by $T \propto 5R_{solution}C_{EDL}$ where $R_{solution}$ is the solution resistance and C_{EDL} the electrochemical double layer capacitance of the system. With double layer capacitance of bare Au being much

larger than Fc11SH, the combined C_{EDL} and therefore time constant T of the system will increase at low Fc11SH coverage. As a result, any potential response of the electrode within the step scan FTIR measurement is subject to a larger time constant.

On the spectroscopy side, IR signal and time-progression can be negatively affected by additional potential dependent IR signals from the bare Au surface areas. While Fc11SH signals can be directly attributed to the SAM, the IR signals of the H_2O and ClO_4^- could theoretically be affected by potential dependent changes of H_2O orientation and ClO_4^- anions concentration in the double layer. Osawa *et al.* performed ATR-SEIRAS measurement of potential dependent changes at bare Au electrodes in 0.1 M ClO_4^-[59]. In their work, only weak ClO_4^- signal were noticeable at electrode potential E >0.6 V vs Ag/AgCl compared to potential dependent signal of H_2O. For the IR measurements in this chapter, their result strongly suggests that the ClO_4^- contribution of bare Au is negligible compared to the much stronger IR signal from ingress of ClO_4^- from the solution due to ion-pairing with the positively charged Fc11SH.

For the H_2O, however, Osawa *et al.* reported strong IR signal changes across the entire potential range from -0.1 V to +1.0 V. The convolution of H_2O signals from bare Au surface area and areas containing Fc11SH SAM could explain the anomalous time constant of H_2O found in the step scan FTIR measurement results in Table 6.1 and the 2D-correlation analysis in table 6.2. While the Fc11SH and ClO_4^- related time constants increase between the two potential steps as a result of the large overpotential applied to the negative potential step, the H_2O time constant decreases. As a result, the H_2O signal does not arise solely to the Fc11SH redox process and should be improved in future experiments since the H_2O IR signals can contain valuable information about hydrogen bonding.

A secondary shortcoming within the current measurements is the heterogeneity of Fc11SH ordering within the SAM. As mentioned earlier, the combination of poor coverage of the Fc11SH on the Au surface and rough surface texture of SEIRAS-active Au resulted in a large fraction of disorder in the monolayer. Few SAM incubations were able to produce well-ordered monolayers such as those characterized by a CV such as that shown in Figure 6.4a. Most were better described by the double-peaked CV in Figure 6.4c that shows separate electrochemical responses from well-ordered and disordered Fc11SH. As mentioned in the background, the heterogeneity in redox-active SAM ordering is known to introduce so called kinetic dispersion[46]. Electron transfer measured from mixed-ordered monolayers is effectively the average of the various electron transfer rates of disordered and well-ordered Fc11SH. The combination of kinetic dispersion and overlap with bare Au surface charging is most likely responsible for the slower time constant observed within the chronoamperometric measurement on the order of 20 - 50 s^{-1} compared to an order of magnitude higher literature values[43]. Better homogeneity in Fc11SH SAM ordering and better coverage would allow future measurements to narrow the electrochemical response to specific SAM orientation and improve the analytical value of the step scan FTIR platform.

Improvements

Based on the described shortcomings, the most crucial aspect of future experiments should address Fc11SH SAM ordering and coverage by improving the incubation procedure and/or electrode surface texture. The incubation procedure utilized for the experiments within this chapter have yet to undergo any optimization. Modifying Fc11SH concentration and incubation can provide a more complete and homogenous SAM formation on the rough SEIRAS-

active SAM surface[51]. A second consideration is the inclusion of undecane thiols as a so called "diluent" into the incubation solution. Binary SAMs created through the mixture of functionalized and non-functionalized thiols have been a common strategy within the literature to adjust the ordering of SAMs through variation of the Fc11SH to diluent alkanethiol concentration in the incubation solution[34,39]. During SAM formation, the non-functionalized thiols can occupy gaps within the monolayer caused by intermolecular interaction between bulky headgroups to form more densely packed monolayers and/or prevents clustering of the redox-active thiols through dilution.

The crucial challenge for optimizing the electrode surface texture of the sputtered Au-layers for SAM incubation is the opposing nature of more SEIRAS enhancing Au layer that demand rougher surface texture while less defects within SAMs require smoother surfaces. Coupled with the issues of metal sputtering consistency discussed in Chapter 5, optimizing purely through sputtering conditions will most likely be highly challenging. Motivated by the problem observed with AuTi layers described in Chapter 5, separate research within the group by Andvaag *et al.* reported electrodeposited Au nanostructure on sputtered IZO substrate for ATR-SEIRAS, that are a promising avenue to improve Au-surface texture for future experiment[69]. The novel approach to preparing SEIRAS-active Au surface on silicon IR-optic elements utilizes a thin layer of sputtered IZO to provide a conductive surface for electrodepositing Au from a solution. Not only do the authors report stronger ATR-SEIRAS signal compared to conventional sputtered Au-layers, but electrodeposition also has the significant advantage over sputtering that shape, size and preferential crystallography of the Au can be reliably directed through variation in deposition charge, potential and solution composition. While the Au surface crystallography was reported as polycrystalline, the use

of shape directing surfactants during electrodeposition in future experiment could improve Fc11SH SAM formation by providing predominantly (111) faceted surfaces that are favored for defect free SAM formation of alkanethiol[41,52]. An additional benefit of these IZO/Au layers is the improved stability of the SEIRAS-active films which prevents Au-layer delamination during prolonged step scan experiment and possibly improves SAM formation by allowing disassembly of the IRE for SAM incubation outside of the spectroelectrochemical cell in cleaner solutions.

Outlook

With the discussed improvements, it is likely that future experiment will mitigate the two most significant shortcomings (Fc11SH coverage and ordering) currently affecting the step scan FTIR measurements. Reducing the influence of bare the Au surface areas and kinetic dispersion on the chromoamperometric measurement would allow for more accurate comparison of time progressions between redox-charge transfer and the IR signal of the Fc11SH SAM. On the spectroscopy side, removal/reduction of bare Au surface areas would allow for analysis of the H_2O signal that is currently not possible. Information on whether H_2O ingresses into the SAM and its hydrogen bonding environment could greatly improve the analytical quality of the measurement platform to study kinetics of conformational changes within the SAM that are inaccessible by purely electrochemical means. An interesting series of experiments would be investigating the ion pairing kinetics of various anions as it is well established in the literature that the nature of the anion can significantly affect heterogenous electron transfer rates[40–43]. A second avenue could be comparison of conformational change kinetics related to odd-even effects of the alkane chain length[47–50]. Here, differences in elec-

trochemical behaviour were identified as a result of difference in tilt angle of the terminal CH_3-CH_2 bond of the alkane thiols that affects orientation and accessibility of anions to the ferrocene head-group. Time-resolved IR measurement of the ferrocene ring modes could quantify the kinetic changes in the rotational confirmation of the ferrocene head-group upon oxidation/reduction.

Expanding the measurement beyond the narrow focus of $Fc(CH)_nSH$ SAMs, the research presented in this Chapter is an important step for the continued development of time-resolved FTIR measurements with synchrotron mid-IR radiation at the CLS within the Burgess research group. While the time-resolved measurements in this Chapter and Chapter 5 were performed on a conventional FTIR spectrometer, they provide a great testing ground for the experimental setup and procedure for step scan FTIR in ATR-SEIRAS on micro-grooved silicon wafers and have helped develop analysis methods for the results such as 2D-correlation analysis. Kinetics of conformational and anion ion-pairing of Fc11SH SAMs is a viable system to pursue in future experiments. These μ-grooved silicon wafers are a highly attractive option for internal reflection elements compared to conventional silicon IR optics due to a combination of factors[58]. 1) Shorter pathlength through silicon improves the IR signal at wavenumbers below the silicon cut-off <1200 cm^{-1} which is important for measurement of the ClO_4^- anion. 2) Lower cost per IRE allows acquisition and preparation off multiple wafers for higher experiment throughput. 3) Comparable thicknesses to conventional silicon wafers used for semiconductors eases the use of various lithography techniques to create ultramicroelectrodes on these wafers. Parallel research effort within the Burgess group by Morhart *et al.* developed an optical setup at the mid-IR beamline to focus synchrotron-IR light onto a single groove within the μ-grooved wafers to selectively interro-

gate small surface areas in the ATR-configuration[70]. Combining the step scan FTIR setup and procedure described in this chapter, the new horizontal microscope setup at the CLS and the improved ATR-SEIRAS layer of electrodeposited Au on ITO with microelectrodes on the microgroove IRE through UV-lithography should allow step scan FTIR measurements of femtomole quantities of surface-absorbed molecules with microsecond time resolution.

6.5 Conclusion

The work presented in this chapter utilized the rapid scan and step scan FTIR setup and procedures developed in Chapter 3 and 5 respectively to perform time resolved ATR-SEIRAS measurements of Fc11SH SAMs. Methodologies to incubate Fc11SH within the spectroelectrochemical setup were developed and described. Freshly prepared Fc11SH layers were extensively characterized with CV and potential-dependent FTIR measurements to quantify their coverage and quality of their SEIRAS signal respectively. Subsequent rapid scan FTIR experiment with 36 ms time resolution provided preliminary information on the kinetics of the system upon oxidation/reduction of the ferrocene redox center in ClO_4^- anion containing solution. The results also provided the information needed to optimize the measurement time and time resolution of the step scan FTIR experiments.

The central contribution of the chapter is the first step scan FTIR measurement of the conformational change occurring within a redox-active SAM upon oxidation/reduction with millisecond time resolution. The measurement results capture the complete change in Fc11SH orientation as well as ingress/egress of ion paired ClO_4^- anions within the initial 150 ms after a potential perturbation. Based on exponentially fitted time constants for the

chronoamperometric charge and IR signal progression as well as a 2D correlation analysis of the step scan IR spectra, a model for the sequence of event upon oxidation/reduction of Fc11SH SAM in ClO_4^- solution consisting of electron transfer $\rightarrow$ conformational change of thiol $\rightarrow$ ingress/egress of ClO_4^- for ion pairing was proposed. Comparison of the model based on the time resolved IR data matches well with literature proposals. This strongly suggests that the developed step scan FTIR setup and procedure is an effective tool to directly measure the kinetics of interfacial changes within SAMs. For further investigation of the Fc11SH system however, it will be vital to improve the ordering and coverage of the SAM on the SEIRAS-active substrate through a combination of better incubation conditions and improved SEIRAS substrate currently under development.

Ultimately, the experiments presented and discussed within this chapter will aid the continued development of time resolved FTIR measurements in the Burgess research group and the mid-IR beamline at the Canadian Light Source. While no direct synchrotron IR light was utilized, the experimental setup, protocol and programs for analysis of the step scan FTIR results will aid implementation of step scan FTIR measurement at the beamline. The results highlight redox-active SAMs and the Fc11SH system as a viable and interesting system for initial experiments at the CLS. The combination of this work, with parallel development within the Burgess research group will likely be able to provide proof-of-concept for SIR based, fast time resolved IR measurement of surface adsorbed molecules in the near future.

6.6 References

[1] Cao, Z.; Kim, D.; Hong, D.; Yu, Y.; Xu, J.; Lin, S.; Wen, X.; Nichols, E. M.; Jeong, K.; Reimer, J. A.; Yang, P.; Chang, C. J. A Molecular Surface Functionalization Approach to Tuning Nanoparticle Electrocatalysts for Carbon Dioxide Reduction. *Journal of the American Chemical Society* **2016**, *138*, 8120–8125.

[2] Niazov, T.; Shlyahovsky, B.; Willner, I. Photoswitchable Electrocatalysis and Catalyzed Chemiluminescence Using Photoisomerizable Monolayer-Functionalized Surfaces and Pt Nanoparticles. *Journal of the American Chemical Society* **2007**, *129*, 6374–6375.

[3] Yuan, F.-W.; Yang, H.-J.; Tuan, H.-Y. Alkanethiol-Passivated Ge Nanowires as High-Performance Anode Materials for Lithium-Ion Batteries: The Role of Chemical Surface Functionalization. *ACS Nano* **2012**, *6*, 9932–9942.

[4] Jaffe, A.; Saldivar Valdes, A.; Karunadasa, H. I. Quinone-Functionalized Carbon Black Cathodes for Lithium Batteries with High Power Densities. *Chemistry of Materials* **2015**, *27*, 3568–3571.

[5] Peng, S.; Zhao, W.; Li, H.; Zeng, Z.; Xue, Q.; Wu, X. The enhancement of benzotriazole on epoxy functionalized silica sol–gel coating for copper protection. *Applied Surface Science* **2013**, *276*, 284–290.

[6] Banerjee, I.; Pangule, R. C.; Kane, R. S. Antifouling Coatings: Recent Developments in the Design of Surfaces That Prevent Fouling by Proteins, Bacteria, and Marine Organisms. *Advanced Materials* **2011**, *23*, 690–718.

[7] Caucheteur, C.; Guo, T.; Albert, J. Review of plasmonic fiber optic biochemical sensors: improving the limit of detection. *Analytical and Bioanalytical Chemistry* **2015**, *407*, 3883–3897.

[8] Mayer, K. M.; Hafner, J. H. Localized Surface Plasmon Resonance Sensors. *Chemical Reviews* **2011**, *111*, 3828–3857.

[9] Frasconi, M.; Tel-Vered, R.; Riskin, M.; Willner, I. Surface Plasmon Resonance Analysis of Antibiotics Using Imprinted Boronic Acid-Functionalized Au Nanoparticle Composites. *Analytical Chemistry* **2010**, *82*, 2512–2519.

[10] Akram, M. S.; Rehman, J. U.; Hall, E. A. H. Engineered Proteins for Bioelectrochemistry. *Annual Review of Analytical Chemistry* **2014**, *7*, 257–274.

[11] Gooding, J. J. Nanostructuring electrodes with carbon nanotubes: A review on electrochemistry and applications for sensing. *Electrochimica Acta* **2005**, *50*, 3049–3060.

[12] Mohammed, M.-I.; Desmulliez, M. P. Y. Lab-on-a-chip based immunosensor principles and technologies for the detection of cardiac biomarkers: a review. *Lab on a Chip* **2011**, *11*, 569–595.

[13] Pelaz, B.; Charron, G.; Pfeiffer, C.; Zhao, Y.; de la Fuente, J. M.; Liang, X.-J.; Parak, W. J.; del Pino, P. Interfacing Engineered Nanoparticles with Biological Systems: Anticipating Adverse Nano–Bio Interactions. *Small* **2013**, *9*, 1573–1584.

[14] DiBenedetto, S. A.; Facchetti, A.; Ratner, M. A.; Marks, T. J. Molecular Self-Assembled Monolayers and Multilayers for Organic and Unconventional Inorganic Thin-Film Transistor Applications. *Advanced Materials* **2009**, *21*, 1407–1433.

[15] Love, J. C.; Estroff, L. A.; Kriebel, J. K.; Nuzzo, R. G.; Whitesides, G. M. Self-Assembled Monolayers of Thiolates on Metals as a Form of Nanotechnology. *Chemical Reviews* **2005**, *105*, 1103–1170.

[16] Schreiber, F. Structure and growth of self-assembling monolayers. *Progress in Surface Science* **2000**, *65*, 151–257.

[17] Ulman, A. Formation and Structure of Self-Assembled Monolayers. *Chemical Reviews* **1996**, *96*, 1533–1554.

[18] Han, B.; Li, Z.; Wandlowski, T.; Blaszczyk, A.; Mayor, M. Potential-induced redox switching in viologen self-assembled monolayers: An ATR-SEIRAS approach. *Journal of Physical Chemistry C* **2007**, *111*, 13855–13863.

[19] Wisitruangsakul, N.; Zebger, I.; Ly, K. H.; Murgida, D. H.; Ekgasit, S.; Hildebrandt, P. Redox-linked protein dynamics of cytochrome c probed by time-resolved surface enhanced infrared absorption spectroscopy. *Physical Chemistry Chemical Physics* **2008**, *10*, 5276–5286.

[20] Ataka, K.; Stripp, S. T.; Heberle, J. Surface-enhanced infrared absorption spectroscopy (SEIRAS) to probe monolayers of membrane proteins. *Biochimica et Biophysica Acta (BBA) - Biomembranes* **2013**, *1828*, 2283–2293.

[21] Eckermann, A. L.; Feld, D. J.; Shaw, J. A.; Meade, T. J. Electrochemistry of redox-active self-assembled monolayers. *Coordination Chemistry Reviews* **2010**, *254*, 1769–1802.

[22] Nuzzo, R. G.; Allara, D. L. Adsorption of bifunctional organic disulfides on gold surfaces. *Journal of the American Chemical Society* **1983**, *105*, 4481–4483.

[23] Nie, Z.; Petukhova, A.; Kumacheva, E. Properties and emerging applications of self-assembled structures made from inorganic nanoparticles. *Nature Nanotechnology* **2010**, *5*, 15–25.

[24] Mirsky, V. M. New electroanalytical applications of self-assembled monolayers. *TrAC Trends in Analytical Chemistry* **2002**, *21*, 439–450.

[25] Gooding, J. J.; Ciampi, S. The molecular level modification of surfaces: from self-assembled monolayers to complex molecular assemblies. *Chemical Society Reviews* **2011**, *40*, 2704–2718.

[26] Samanta, D.; Sarkar, A. Immobilization of bio-macromolecules on self-assembled monolayers: methods and sensor applications. *Chemical Society Reviews* **2011**, *40*, 2567–2592.

[27] Laibinis, P. E.; Whitesides, G. M.; Allara, D. L.; Tao, Y. T.; Parikh, A. N.; Nuzzo, R. G. Comparison of the structures and wetting properties of self-assembled monolayers of n-alkanethiols on the coinage metal surfaces, copper, silver, and gold. *Journal of the American Chemical Society* **1991**, *113*, 7152–7167.

[28] Carvalho, A.; Geissler, M.; Schmid, H.; Michel, B.; Delamarche, E. Self-Assembled Monolayers of Eicosanethiol on Palladium and Their Use in Microcontact Printing. *Langmuir* **2002**, *18*, 2406–2412.

[29] Demoz, A.; Harrison, D. J. Characterization and extremely low defect density hexadecanethiol monolayers on mercury surfaces. *Langmuir* **1993**, *9*, 1046–1050.

[30] Gaponik, N.; Rogach, A. L. Thiol-capped CdTe nanocrystals: progress and perspectives of the related research fields. *Physical Chemistry Chemical Physics* **2010**, *12*, 8685–8693.

[31] Sagiv, J. Organized monolayers by adsorption. 1. Formation and structure of oleophobic mixed monolayers on solid surfaces. *Journal of the American Chemical Society* **1980**, *102*, 92–98.

[32] Ogawa, H.; Chihara, T.; Taya, K. Selective monomethyl esterification of dicarboxylic acids by use of monocarboxylate chemisorption on alumina. *Journal of the American Chemical Society* **1985**, *107*, 1365–1369.

[33] Schönherr, H.; Johnson, J. M.; Lenz, P.; Frank, C. W.; Boxer, S. G. Vesicle Adsorption and Lipid Bilayer Formation on Glass Studied by Atomic Force Microscopy. *Langmuir* **2004**, *20*, 11600–11606.

[34] Chidsey, C. E. D.; Bertozzi, C. R.; Putvinski, T. M.; Mujsce, A. M. Coadsorption of ferrocene-terminated and unsubstituted alkanethiols on gold: electroactive self-assembled monolayers. *Journal of the American Chemical Society* **1990**, *112*, 4301–4306.

[35] Collman, J. P.; Devaraj, N. K.; Chidsey, C. E. D. "Clicking" Functionality onto Electrode Surfaces. *Langmuir* **2004**, *20*, 1051–1053.

[36] Porter, M. D.; Bright, T. B.; Allara, D. L.; Chidsey, C. E. D. Spontaneously organized molecular assemblies. 4. Structural characterization of n-alkyl thiol monolayers on gold by optical ellipsometry, infrared spectroscopy, and electrochemistry. *Journal of the American Chemical Society* **1987**, *109*, 3559–3568.

[37] Arikuma, Y.; Takeda, K.; Morita, T.; Ohmae, M.; Kimura, S. Linker Effects on Monolayer Formation and Long-Range Electron Transfer in Helical Peptide Monolayers. *The Journal of Physical Chemistry B* **2009**, *113*, 6256–6266.

[38] Long, Y.-T.; Li, C.-Z.; Sutherland, T. C.; Chahma, M.; Lee, J. S.; Kraatz, H.-B. A Comparison of Electron-Transfer Rates of Ferrocenoyl-Linked DNA. *Journal of the American Chemical Society* **2003**, *125*, 8724–8725.

[39] Smalley, J. F.; Feldberg, S. W.; Chidsey, C. E. D.; Linford, M. R.; Newton, M. D.; Liu, Y.-P. P. The Kinetics of Electron Transfer Through Ferrocene-Terminated Alkanethiol Monolayers on Gold. *The Journal of Physical Chemistry* **1995**, *99*, 13141–13149.

[40] Valincius, G.; Niaura, G.; Kazakevičiene, B.; Talaikyte, Z.; Kažemekaite, M.; Butkus, E.; Razumas, V.; Kazakevičienė, B.; Talaikytė, Z.; Kažemėkaitė, M.; Butkus, E.; Razumas, V. Anion Effect on Mediated Electron Transfer through Ferrocene-Terminated Self-Assembled Monolayers. *Langmuir* **2004**, *20*, 6631–6638.

[41] Rudnev, A. V.; Yoshida, K.; Wandlowski, T. Electrochemical characterization of self-assembled ferrocene-terminated alkanethiol monolayers on low-index gold single crystal electrodes. *Electrochimica Acta* **2013**, *87*, 770–778.

[42] Nguyen, K.-L. L.; Dionne, E. R.; Badia, A. Redox-Controlled Ion-Pairing Association of Anionic Surfactant to Ferrocene-Terminated Self-Assembled Monolayers. *Langmuir* **2015**, *31*, 6385–6394.

[43] Ju, H.; Leech, D. D. Effect of electrolytes on the electrochemical behaviour of 11-(ferrocenylcarbonyloxy)undecanethiol SAMs on gold disk electrodes. *Physical Chemistry Chemical Physics* **1999**, *1*, 1549–1554.

[44] Nikitina, V. A.; Rudnev, A. V.; Nazmutdinov, R. R.; Tsirlina, G. A.; Wandlowski, T. Solvent effect on electron transfer through alkanethiols. *Journal of Electroanalytical Chemistry* **2018**, *819*, 58–64.

[45] Smalley, J. F. et al. Heterogeneous Electron-Transfer Kinetics for Ruthenium and Ferrocene Redox Moieties through Alkanethiol Monolayers on Gold. *Journal of the American Chemical Society* **2003**, *125*, 2004–2013.

[46] Rowe, G. K.; Carter, M. T.; Richardson, J. N.; Murray, R. W. Consequences of Kinetic Dispersion on the Electrochemistry of an Adsorbed Redox-Active Monolayer. *Langmuir* **1995**, *11*, 1797–1806.

[47] Tao, F.; Bernasek, S. L. Understanding Odd-Even Effects in Organic Self-Assembled Monolayers. *Chemical Reviews* **2007**, *107*, 1408–1453.

[48] Yuan, L.; Thompson, D.; Cao, L.; Nerngchangnong, N.; Nijhuis, C. A. One Carbon Matters: The Origin and Reversal of Odd–Even Effects in Molecular Diodes with Self-Assembled Monolayers of Ferrocenyl-Alkanethiolates. *The Journal of Physical Chemistry C* **2015**, *119*, 17910–17919.

[49] Feng, Y.; Dionne, E. R.; Toader, V.; Beaudoin, G.; Badia, A. Odd–Even Effects in Electroactive Self-Assembled Monolayers Investigated by Electrochemical Surface Plasmon Resonance and Impedance Spectroscopy. *The Journal of Physical Chemistry C* **2017**, *121*, 24626–24640.

[50] Dionne, E. R.; Dip, C.; Toader, V.; Badia, A. Micromechanical Redox Actuation by Self-Assembled Monolayers of Ferrocenylalkanethiolates: Evens Push More Than Odds. *Journal of the American Chemical Society* **2018**, *140*, 10063–10066.

[51] Lee, L. Y. S.; Sutherland, T. C.; Rucareanu, S.; Lennox, R. B. Ferrocenylalkylthiolates as a Probe of Heterogeneity in Binary Self-Assembled Monolayers on Gold. *Langmuir* **2006**, *22*, 4438–4444.

[52] Rudnev, A. V.; Yoshida, K.; Wandlowski, T. Electrochemical characterization of self-assembled ferrocene-terminated alkanethiol monolayers on low-index gold single crystal electrodes. *Electrochimica Acta* **2013**, *87*, 770–778.

[53] Ye, S.; Sato, Y.; Uosaki, K. Redox-Induced Orientation Change of a Self-Assembled Monolayer of 11-Ferrocenyl-1-undecanethiol on a Gold Electrode Studied by in Situ FT-IRRAS. *Langmuir* **1997**, *13*, 3157–3161.

[54] Ye, S.; Haba, T.; Sato, Y.; Uosaki, K. Coverage dependent behavior of redox reaction induced structure change and mass transport at an 11-ferrocenyl-1-undecanethiol self-assembled monolayer on a gold electrode studied by an in situ IRRAS – EQCM combined system. **1999**, 3653–3659.

[55] Viana, A. S.; Jones, A. H.; Abrantes, L. M.; Kalaji, M. Redox induced orientational changes in a series of short chain ferrocenyl alkyl thiols self-assembled on gold(111) electrodes. *Journal of Electroanalytical Chemistry* **2001**, *500*, 290–298.

[56] Takeda, K.; Morita, T.; Kimura, S. Effects of Monolayer Structures on Long-Range Electron Transfer in Helical Peptide Monolayer. *The Journal of Physical Chemistry B* **2008**, *112*, 12840–12850.

[57] Schumacher, H.; Künzelmann, U.; Vasilev, B.; Eichhorn, K.-J.; Bartha, J. W. Applications of Microstructured Silicon Wafers as Internal Reflection Elements in Attenuated Total Reflection Fourier Transform Infrared Spectroscopy. *Applied Spectroscopy* **2010**, *64*, 1022–1027.

[58] Morhart, T. A.; Unni, B.; Lardner, M. J.; Burgess, I. J. Electrochemical ATR-SEIRAS Using Low-Cost, Micromachined Si Wafers. *Analytical Chemistry* **2017**, acs.analchem.7b03509.

[59] Ataka, K.-i.; Yotsuyanagi, T.; Osawa, M. Potential-Dependent Reorientation of Water Molecules at an Electrode/Electrolyte Interface Studied by Surface-Enhanced Infrared Absorption Spectroscopy. *The Journal of Physical Chemistry* **1996**, *100*, 10664–10672.

[60] Quirk, A.; Unni, B.; Burgess, I. J. Surface Enhanced Infrared Studies of 4-Methoxypyridine Adsorption on Gold Film Electrodes. *Langmuir* **2016**, *32*, 2184–2191.

[61] Bard, A. J.; Faulkner, L. R. *Comprehensive Sampling and Sample Preparation*, second edi ed.; wiley New York, 1980; Vol. 2; pp 580–630.

[62] Miki, A.; Ye, S.; Osawa, M. Surface-enhanced IR absorption on platinum nanoparticles: an application to real-time monitoring of electrocatalytic reactions. *Chemical Communications* **2002**, 1500–1501.

[63] Noda, I. Two-Dimensional Infrared (2D IR) Spectroscopy: Theory and Applications. *Applied Spectroscopy* **1990**, *44*, 550–561.

[64] Noda, I. Progress in two-dimensional (2D) correlation spectroscopy. *Journal of Molecular Structure* **2006**, *799*, 2–15.

[65] Noda, I. Techniques of two-dimensional (2D) correlation spectroscopy useful in life science research. *Biomedical Spectroscopy and Imaging* **2015**, *4*, 109–127.

[66] Noda, I.; Ozaki, Y. *Two-dimensional correlation spectroscopy: applications in vibrational and optical spectroscopy*; John Wiley & Sons, 2005.

[67] Laviron, E. The use of linear potential sweep voltammetry and of a.c. voltammetry for the study of the surface electrochemical reaction of strongly adsorbed systems and of redox modified electrodes. *Journal of Electroanalytical Chemistry and Interfacial Electrochemistry* **1979**, *100*, 263–270.

[68] Laviron, E. General expression of the linear potential sweep voltammogram in the case of diffusionless electrochemical systems. *Journal of Electroanalytical Chemistry* **1979**, *101*, 19–28.

[69] Andvaag, I. R.; Morhart, T. A.; Clarke, O. J. R.; Burgess, I. J. Hybrid Gold–Conductive Metal Oxide Films for Attenuated Total Reflectance Surface Enhanced Infrared Absorption Spectroscopy. *ACS Applied Nano Materials* **2019**, *2*, 1274–1284.

[70] Morhart, T. A.; Read, S.; Wells, G.; Jacobs, M.; Rosendahl, S. M.; Achenbach, S.; Burgess, I. J. Attenuated Total Reflection Fourier Transform Infrared (ATR FT-IR) Spectromicroscopy Using Synchrotron Radiation and Micromachined Silicon Wafers for Microfluidic Applications. *Applied Spectroscopy* **2018**, *72*, 1781–1789.

Chapter 7

Conclusion and Future Work

7.1 Conclusion

The work detailed within this thesis is part of the ongoing development within the Burgess research group to advance *in situ* FTIR spectroelectrochemistry to measure the kinetics of electrochemical processes with sub millisecond time-resolution. As discussed in Chapter 1, FTIR investigations of equilibrium and kinetically slow processes have been widely reported in the literature, but earlier implementations of rapid scan and step scan FTIR techniques for the investigation of kinetically fast spectroelectrochemical systems were limited due to electrochemical and spectroscopy constraints[1–6]. Scott Rosendahl, my predecessor in the research group, demonstrated that synchrotron infrared radiation is an effective means to overcome the challenges of lower analyte quantities, lower S/N ratios and an electrochemical requirement for UME in earlier implementations of fast time-resolved FTIR[7,8]. Building upon Rosendahl's proof-of-concept study on a simple, reversible redox system, each of 3 - 6 in this thesis improves upon aspects of the initial spectroelectrochemical platform to facilitate its application using more complex electrochemical systems.

Chapter 3 successfully tackled the experimental challenges imposed by irreversible electrochemical reactions for rapid scan FTIR measurement in IRRAS geometry of solution

phase molecules with millisecond time-resolution. The system of choice for the initial demonstration is the electrocatalytic methanol oxidation reaction on Pt, a complex reaction with application in DMFC that has remained an active area of electrochemical research for over 60 years. From a developmental perspective, the system was an effective proving ground to tackle the experimental challenges of irreversible electrochemical systems. The MOR requires reliable resetting of both the solution and electrode surface after every rapid scan FTIR measurement. Fully automated solution reset was achieved through injection of fresh electrolyte into the thin cavity and the integration of an TTL-controlled fluid system into the spectroelectrochemical platform. The removal of electrochemical residue from previous reaction on the electrode is facilitated through an oxidative potential pulse[9], controlled through a custom-written interface in LabVIEW. A side-effect of the additional elements is an increase in overall measurement time (>12 h) resulting in potential stability concerns. To address the potential stability, a capacitively coupled reference setup consisting of a Pt pseudo-reference electrode was included within the thin cavity of the SEC with a proper Ag/AgCl reference electrode. The combination of these three additions lead to the successful demonstration of rapid scan FTIR measurements of the irreversible MOR with millisecond time-resolution with SIR.

While the results of Chapter 3 were encouraging, two limitations were clearly highlighted: 1) measurements of irreversible electrochemical systems in IRRAS configuration with higher time-resolution through step scan FTIR is not advised due to the long duration of the reset procedure (>30 s per single reset of the spectroelectrochemical cell) and 2) both decrease in solution background absorption and signal enhancement will be required to resolve the kinetics of low quantity reaction intermediates. This sparked a reassessment of future

SIR-based spectroelectrochemical developments in the Burgess group in 2015. In the short term, my objectives focused on the application of the existing rapid scan FTIR platform and the results are presented in Chapter 4. Here, the platform was refined to utilize the small dimension of the SIR beam to achieve spatial mapping of solution phase components of an electrochemical reaction with 20 μm spatial resolution. This ultimately resulted in its application as a combinatory screening method for binary electrocatalysts. A prospectus on what this tool could be used for is provided later in this chapter.

As a result of my work in the Burgess group, a major objective of the laboratory's research program became the mitigation of the limitations I identified, through the development of a means to achieve surface enhanced infrared detection levels at the mid-IR beamline at the CLS through the implementation of ATR-SEIRAS. Briefly, the two main elements for achieving this goal are: 1) The construction of an ATR microscope beamline end station spearheaded by Tyler Morhart[10], a fellow student in the Burgess group; 2) the development of step scan FTIR infrastructure for the ATR-SEIRAS platform and preliminary investigation of reaction kinetics of a more complex electrochemical systems. This thesis described my efforts to address the latter point in Chapters 5 and 6. Chapter 5 described the modifications to the spectroelectrochemical platform for rapid scan FTIR in IRRAS configuration to step scan FTIR in ATR-SEIRAS and subsequent testing. A primary focus was the development and testing of the communication and timing elements between the various instruments to be compatible for the more stringent demands of faster time resolution. Step scan ATR-SEIRAS measurements on the desorption/adsorption of 4-methoxypyridine upon potential steps were performed with the new platform to demonstrate its timing accuracy within 2 μs. Additional efforts were also invested to improve the stability of the mechanically labile SEIRAS-active

Au layer through addition of a ∼3 nm adhesion layer of Ti. Unfortunately, while the mechanical performance of the AuTi layers was excellent, the SEIRAS activity of the AuTi layers was entirely unreliable and this led to the decision to discontinue the use of these layers for future step scan experiments. Chapter 6 further expands the scope of the step scan FTIR platform beyond simple adsorption/desorption studies of molecules to investigations of the redox kinetics of thiol based SAMs, a crucial bridge element for many advanced functionalized surfaces[11–15].

Besides the progress on the developmental side, this thesis also marks the transition from solving purely experimental challenges toward applications for scientific research. The research in Chapter 4 and 6 were able to highlight two electrochemical applications of time-resolved FTIR as a combinatorial screening platform and for the investigation of redox-active SAM kinetics respectively.

Chapter 4 demonstrates spatial mapping of heterogenous catalytic activity with application for combinatory screening of binary electrocatalysts. High-throughput combinatorial screening has become an increasingly important option for tackling multivariant optimization challenges of electrocatalysts with industrial relevance[16–18]. An ongoing challenge within this area is the large variance between reported catalytic activity between various research groups, based on the production method of nanoparticle libraries. Here the platform developed in Chapter 4 offers catalytic activity assessments of binary metal catalysts ratios on heterogenous bulk electrodes, offering a qualitative pre-screening of metal composition ratios with the excellent chemical sensitivity of IR. While the results described in that chapter are limited to MOR on PtNi alloys, the utilization of thin metal foil for production of heterogenous electrodes in the later stages of the project opens a much larger library of

possible bimetallic combinations for combinatorial mapping. Similarly, the adaptation of the spectroelectrochemical platform for diffusion mapping experiments on the quasi-irreversible hydroquinone by Lardner *et al.* showcase how the methodology is easily adapted to other electrochemical systems[19]. Future combinatorial screening experiments will likely include UV-lithography masks on the electrode surface that will further improve the qualitative value of the measurement results.

Chapter 6 highlights the application of a spectroelectrochemical platform for a kinetic investigation of processes involving a self-assembled monolayer. While the choice of Fc11SH was primarily driven by experimental concern regarding stability, the redox-active SAM proved to be an excellent test system. The well-known electrochemical behaviour and non-dynamic IR responses of the FcSH monolayer offered simple validation of experimental results through comparison with previous literature reports, while simultaneously leaving research opportunities into the kinetics of changes within the SAM upon oxidation/reduction of the ferrocene redox center. The experiments in this chapter culminated in a successful step scan FTIR measurement of the Fc11SH redox process with 1 ms time-resolution. Subsequent analysis of the molecular rearrangement and ion pairing kinetics provided a preliminary model for the sequence of events within the SAM upon oxidation/reduction. Compared to earlier implementations of surface sensitive step scan FTIR, the ATR-SEIRAS measurement is not reliant on the abnormal surface enhancement utilized by Sun *et al.*[1,2]. After the completion of the experimental work contained in this thesis, the method I developed was combined with a custom-built horizontal ATR microscope end station at the mid-IR beamline at CLS. Although it falls outside the domain of this thesis, the experiment relied heavily on the capabilities developed and described herein to perform microsecond resolved measurements on

a true UME. There is much more to come from this approach as will be described in the Future Work section below.

In summary, the research presented in this thesis contributes significantly to the on-going pursuit of the Burgess research group to advance *in situ* FTIR spectroelectrochemistry for the measurement of kinetic aspects of electrochemical processes. Building upon the initial proof-of concept measurements by my predecessor for a reversible model system[7,8], this body of work has demonstrated its application for irreversible electrochemical systems (Chapter 3), spatial mapping of electrocatalytic heterogeneity (Chapter 4), adsorption/desorption kinetics of surface absorbed molecules (Chapter 5) and dynamic changes within self-assembled monolayers (Chapter 6). Beyond the developmental progress, the combinatorial screening of MOR activity on PtNi (Chapter 4) and kinetics investigation of Fc11SH (Chapter 6) also demonstrated the successful utilization of developed spectroelectrochemical platforms towards research application. While experiments in both chapters were limited to a single example, each was selected to represent a large group of relevant electrochemical systems. In the same vein, the experimental setup and methodology was intentionally designed to allow rapid expansion of the research scope to other fuel cell catalysts and SAMs.

7.2 Future Developments, Applications and Outlook

From a development perspective, on-going work within the Burgess group is expected to address current shortcomings in the step scan ATR-SEIRAS setup and expand its viability for future applications. The concerns regarding the electrochemical limit on the time-resolution encountered in Chapter 6 will very likely be successfully overcome through a combination of

UV-lithography to produce UMEs on disposable, Si-wafer IREs[20] and the recently completed ATR-microscope end station at the Canadian Light Source[10]. At the time of writing, the first step scan FTIR experiments with SIR at the mid-IR beamline have been successfully completed. The results demonstrate a successful step scan ATR-SEIRAS measurement of 4-methoxypyridine desorption/adsorption on a 500 μm wide band electrode with 12.5 ms time-resolution, the current spectrometer software limitation. Preliminary results are highly encouraging. However, it should be noted that the DC-coupled detector required to make these measurements was terribly sensitive to vibrational and electronic noise inherent to the CLS. Interestingly, the same detector was employed in DC-coupled mode in the Burgess laboratory and reported at least an order of magnitude lower noise levels. Efforts are underway to ameliorate the inherent high noise environment of a synchrotron beamline hutch. It has already been determined that most of this noise is mechanically coupled vibrational noise from various sources (mainly pumps) and the noise floor will be improved either by improved mechanical isolation or Fourier filtering of the discrete noise frequencies.

Supporting these ongoing and future step scan FTIR experiments are recently developed SEIRAS active Au layers on conductive metal oxide layers[21]. These hybrid layers of SEIRAS active Au structures electrodeposited on a thin supporting layer of annealed IZO or ITO boast stronger surface enhancement, better mechanical stability and more reliable production. Recent step scan FTIR experiments with an UME fabricated from these hybrid layers demonstrated consistent SEIRAS activity over more than four days. In contrast, a SEIRAS layer deposited directly on a Si IRE is likely to delaminate after several days of electrochemical experiments, or, at best, will show an evolving SEIRAS response that makes it difficult to coadd spectra.

Going forward, the option to prepare SEIRAS layers through electrodeposition on conductive metal oxides provide an interesting avenue to modify the material or properties of the working electrode for future time-resolve ATR-SEIRAS experiments. For instance, a wide range of metals, including highly catalytically active (Pt, Pd) and 3d transition metals such as Cu, Ni and Fe, are known to be both SEIRAS active[22–24] and can easily be electroplated from solution[25]. Successful development of the electrodeposition procedure for these electrocatalysts would allow the investigation of the kinetic aspects of surface adsorbed intermediates for irreversible catalytic processes such as methanol oxidation on Pt. Alternatively, literature reports also reported ATR-SEIRAS experiments where nanometer thick layers of electrocatalytic materials are directly electrodeposited on top of surface enhancing gold layers[26]. This strategy provides a second more direct approach to adopt the spectroelectrochemical platform for the investigation of surface processes which are the essential to all electrocatalytic reactions.

For observation of solution phase species participating in electrocatalytic reactions, the successful combinatorial screening of catalytic activity of MOR for PtNi electrocatalyst compositions in Chapter 4 is an obvious avenue for future experiments. Based on the proof-of-concept demonstration with MOR on PtNi, subsequent experiments can utilize the improved electrode production discussed in Chapter 4 based on fused metal thin foils to generate large libraries of Pt-based electrocatalysts for high-throughput screening. In the case of the MOR, other 3d transition metals such as Fe, Co and Cu are known to improve the catalytic activity while decreasing material costs[27–29]. This is also supported by improved spectroelectrochemical cell designs that can integrate up to four different working electrodes into a single setup to minimize lab-to-lab and experiment to experiment variance. It is also

worth noting that the working electrode surface of these spectroelectrochemical cells can be reset through mechanical polishing of the surface layer. In other words, once a single cell with multiple electrocatalytic electrodes has been constructed, the transition to the investigation of alternative fuel sources for fuel cells such as formic acid[30,31] or ethanol[32,33] or supporting electrolytes is simplified to an exercise in optimization of the electrode reset procedures. Changing the supporting electrolyte to neutral or basic conditions can be particularly beneficial, as early transition metals are more dimensionally stable in basic solutions and reduced surface degradation would improve the quantitative value of the measurement methodology. These types of studies would be even further improved through the inclusion of UV-lithographed masks as discussed in Chapter 4.

The combination of ATR-SEIRAS with step scan methodologies is the most important development of this thesis. The excellent structural and chemical sensitivity of IR coupled with the time-resolution of step scan offers a unique opportunity to directly observe changes within monolayers as the technical developments described herein can now readily be applied to a large variety of thiol-based systems. A short-term objective is a more in-depth study on the correlation between the dynamics of structural changes within SAMs and their heterogeneous electron transfer rates. Fundamental investigations regarding the validity of the Marcus theory on heterogeneous electron transfer reactions relied on redox active SAMs where the length of the alkyl chain was used as a meter stick to define the tunneling distance between the electrode and the redox moiety[34]. Since then, it is generally accepted that the heterogenous electron transfer requires additional consideration regarding the molecular dynamics of SAMs, but experimental observation of the kinetics processes within these layers is highly challenging. The work detailed in Chapter 6, showcases the utility of step

scan FTIR in this respect and demonstrates its ability to provide a sequence of events and rate constants based on direct observation of changes within the SAM and suggests subtle changes in electron transfer rates between oxidation and reduction. Future experiments can explore the difference between redox-active SAMs with various thiol bridge elements that alter their orientational alignment and dynamics through steric hindrance. In the long term, this can be further expanded to other thiol-based systems such as functionalized surfaces with analytical[13,15] and biological sensor application[5,12].

The future of IR spectroelectrochemistry, like all aspects of IR spectroscopy, is poised to benefit from a new wave of technological changes. Primary to this will be the increasing popularity of mid-IR lasersources such as quantum cascade lasers (QCL)[35] or supercontinuum fiber lasers[36]. In recent years these sources have moved from the domain of specialized groups to commercially available instruments. The brightness of these sources relative to both globars and synchrotrons[37], will drastically increase the viability of IR spectroscopy on previously challenging samples as well as allow the use of new measurement paradigms[38–40]. These new IR sources will allow IR experiments with superior S/N with much shorter experimental times and can be smoothly integrated into the existing measurement platforms utilized in this thesis. Considering the current limitation of time-resolved *in situ* spectroelectrochemical measurements encountered by Osawa[3,4], Sun[1,2] as well as in Chapter 4 and 5 of this thesis are a result of low S/N, it is fair to say that these high brilliance IR laser sources will greatly improve the detection limit and accessibility of future spectroelectrochemical experiments. The main drawback of laser-based IR sources compared to SIR are the much narrower spectral range, which currently, is limited to a few hundred wavenumbers. While optical setups combining multiple tunable QCL sources, have been demonstrated

to cover the entirety of the mid-IR fingerprint region (700 - 1500 cm^{-1})[37], true broadband measurement covering a bandwidth of more than 2000 cm^{-1} wavenumber will likely remain the prerogative of synchrotron sources for at least a few more years. Beyond that time frame it is highly conceivable that laser-based spectrometers will begin to outcompete synchrotrons for mid-IR applications.

A particularly interesting option for time-resolved measurements is the recent development of QCL-based dual comb spectrometers[39]. One of the first commercial instruments of this kind is currently being commissioned at the Canadian Light Source. Compared to step scan FTIR system utilized in this thesis, these QCL-based systems with multiheterodyne detection schemes offer a drastically improved acquisition time and superior S/N. At the center of these new IR spectrometers are two frequency comb QCLs with slight frequency offset line spacing. The two spectral combs are combined at a suitable detector to generate a heterodyne beat pattern in the radiofrequency wavelength domain. This allows for collection of a complete IR spectrum within a single measurement. In other words, while the time-resolution of step scan FTIR and dual-comb based IR instruments are both limited by the electronics of their respective detectors, the second option can collect an entire spectrum within a single shot. In terms of experimental measurement time, the step scan FTIR measurement of Fc11SH in Chapter 5 required $> 10^5$ repetitions over a 48 h period in order to collect 128 scans for coaddition. In comparison, the heterodyne collection scheme can collect the same data in just a few minutes. This drastic improvement in experimental time and required repetition will greatly aid the implementation of time-resolved FTIR for electrochemical systems that are either less stable or require long dead times for resetting the system after each electrochemical perturbation.

The developments and applications discussed in this chapter are just a few examples illustrating how electrochemical applications of *in situ* time-resolved FTIR will likely progress in the near to intermediate future. This thesis has significantly advanced the experimental capabilities for time-resolved FTIR within the Burgess group to a crucial level. Future research in the group can rely less on method and technique development and is no longer limited to proof-of-concept measurements but can directly utilize the existing spectroelectrochemical platforms to investigate scientifically and societally relevant questions.

7.3 References

[1] Zhou, Z.-Y.; Lin, S.-C.; Chen, S.-P.; Sun, S.-G. In situ step-scan time-resolved microscope FTIR spectroscopy working with a thin-layer cell. *Electrochemistry Communications* **2005**, *7*, 490–495.

[2] Zhou, Z.-Y.; Tian, N.; Chen, Y.-J.; Chen, S.-P.; Sun, S.-G. In situ rapid-scan time-resolved microscope FTIR spectroelectrochemistry: study of the dynamic processes of methanol oxidation on a nanostructured Pt electrode. *Journal of Electroanalytical Chemistry* **2004**, *573*, 111–119.

[3] Osawa, M.; Yoshii, K.; Hibino, Y.-i.; Nakano, T.; Noda, I. Two-dimensional infrared correlation analysis of electrochemical reactions. *Journal of Electroanalytical Chemistry* **1997**, *426*, 11–16.

[4] Osawa, M.; Yoshii, K.; Ataka, K.-i.; Yotsuyanagi, T. Real-time monitoring of electrochemical dynamics by submillisecond time-resolved surface-enhanced infrared attenuated-total-reflection spectroscopy. *Langmuir* **1994**, *10*, 640–642.

[5] Wisitruangsakul, N.; Zebger, I.; Ly, K. H.; Murgida, D. H.; Ekgasit, S.; Hildebrandt, P. Redox-linked protein dynamics of cytochrome c probed by time-resolved surface enhanced infrared absorption spectroscopy. *Physical Chemistry Chemical Physics* **2008**, *10*, 5276–5286.

[6] Pronkin, S.; Wandlowski, T. Time-resolved in situ ATR-SEIRAS study of adsorption and 2D phase formation of uracil on gold electrodes. *Journal of Electroanalytical Chemistry* **2003**, *550-551*, 131–147.

[7] Rosendahl, S. M.; Borondics, F.; May, T. E.; Pedersen, T. M.; Burgess, I. J. Interface for time-resolved electrochemical infrared microspectroscopy using synchrotron infrared radiation. *Review of Scientific Instruments* **2011**, *82*, 083105.

[8] Rosendahl, S. M.; Borondics, F.; May, T. E.; Burgess, I. J. Step-Scan IR Spectroelectrochemistry with Ultramicroelectrodes: Nonsurface Enhanced Detection of Near Femtomole Quantities Using Synchrotron Radiation. *Analytical Chemistry* **2013**, *85*, 8722–8727.

[9] Herrero, E.; Wieckowski, A.; Franaszczuk, K. Electrochemistry of Methanol at Low Index Crystal Planes of Platinum: An Integrated Voltammetric and Chronoamperometric Study. *The Journal of Physical Chemistry* **1994**, *98*, 5074–5083.

[10] Morhart, T. A.; Read, S.; Wells, G.; Jacobs, M.; Rosendahl, S. M.; Achenbach, S.; Burgess, I. J. Attenuated Total Reflection Fourier Transform Infrared (ATR FT-IR) Spectromicroscopy Using Synchrotron Radiation and Micromachined Silicon Wafers for Microfluidic Applications. *Applied Spectroscopy* **2018**, *72*, 1781–1789.

[11] Love, J. C.; Estroff, L. A.; Kriebel, J. K.; Nuzzo, R. G.; Whitesides, G. M. Self-Assembled Monolayers of Thiolates on Metals as a Form of Nanotechnology. *Chemical Reviews* **2005**, *105*, 1103–1170.

[12] Samanta, D.; Sarkar, A. Immobilization of bio-macromolecules on self-assembled monolayers: methods and sensor applications. *Chemical Society Reviews* **2011**, *40*, 2567–2592.

[13] Mirsky, V. M. New electroanalytical applications of self-assembled monolayers. *TrAC Trends in Analytical Chemistry* **2002**, *21*, 439–450.

[14] Nie, Z.; Petukhova, A.; Kumacheva, E. Properties and emerging applications of self-assembled structures made from inorganic nanoparticles. *Nature Nanotechnology* **2010**, *5*, 15–25.

[15] Gooding, J. J.; Ciampi, S. The molecular level modification of surfaces: from self-assembled monolayers to complex molecular assemblies. *Chemical Society Reviews* **2011**, *40*, 2704–2718.

[16] Reddington, E.; Sapienza, A.; Gurau, B.; Viswanathan, R.; Sarangapani, S.; Smotkin, E. S.; Mallouk, T. E. Combinatorial Electrochemistry: A Highly Parallel, Optical Screening Method for Discovery of Better Electrocatalysts. *Science* **1998**, *280*, 1735–1737.

[17] Strasser, P.; Fan, Q.; Devenney, M.; Weinberg, W. H.; Liu, P.; Nørskov, J. K. High Throughput Experimental and Theoretical Predictive Screening of Materials: A Comparative Study of Search Strategies for New Fuel Cell Anode Catalysts. *The Journal of Physical Chemistry B* **2003**, *107*, 11013–11021.

[18] Potyrailo, R.; Rajan, K.; Stoewe, K.; Takeuchi, I.; Chisholm, B.; Lam, H. Combinatorial and High-Throughput Screening of Materials Libraries: Review of State of the Art. *ACS Combinatorial Science* **2011**, *13*, 579–633.

[19] Lardner, M. J.; Tu, K.; Barlow, B. C.; Rosendahl, S. M.; Borondics, F.; Burgess, I. J. Quantitative analysis of electrochemical diffusion layers using synchrotron infrared radiation. *Journal of Electroanalytical Chemistry* **2017**, *800*, 184–189.

[20] Morhart, T. A.; Unni, B.; Lardner, M. J.; Burgess, I. J. Electrochemical ATR-SEIRAS Using Low-Cost, Micromachined Si Wafers. *Analytical Chemistry* **2017**, acs.analchem.7b03509.

[21] Andvaag, I. R.; Morhart, T. A.; Clarke, O. J. R.; Burgess, I. J. Hybrid Gold–Conductive Metal Oxide Films for Attenuated Total Reflectance Surface Enhanced Infrared Absorption Spectroscopy. *ACS Applied Nano Materials* **2019**, *2*, 1274–1284.

[22] Huo, S.-J.; Xue, X.-K.; Yan,; Li, Q.-X.; Ma, M.; Cai, W.-B.; Xu, Q.-J.; Osawa, M. Extending in Situ Attenuated-Total-Reflection Surface-Enhanced Infrared Absorption Spectroscopy to Ni Electrodes. *The Journal of Physical Chemistry B* **2006**, *110*, 4162–4169.

[23] Wang, H.-F.; Yan, Y.-G.; Huo, S.-J.; Cai, W.-B.; Xu, Q.-J.; Osawa, M. Seeded growth fabrication of Cu-on-Si electrodes for in situ ATR-SEIRAS applications. *Electrochimica Acta* **2007**, *52*, 5950–5957.

[24] Huo, S.-J.; Wang, J.-Y.; Yao, J.-L.; Cai, W.-B. Exploring Electrosorption at Iron Electrode with in Situ Surface-Enhanced Infrared Absorption Spectroscopy. *Analytical Chemistry* **2010**, *82*, 5117–5124.

[25] Schlesinger, M.; Paunovic, M. *Modern Electroplating*, fifth edit ed.; John Wiley & Sons, 2010; Vol. 55; pp 79–114.

[26] Yan,; Li, Q.-X.; Huo, S.-J.; Ma, M.; Cai, W.-B.; Osawa, M. Ubiquitous Strategy for Probing ATR Surface Enhanced Infrared Absorption at Platinum Group Metal Electrolyte Interfaces. *The Journal of Physical Chemistry B* **2005**, *109*, 7900–7906.

[27] Cooper, J. S.; McGinn, P. J. Combinatorial screening of thin film electrocatalysts for a direct methanol fuel cell anode. *Journal of Power Sources* **2006**, *163*, 330–338.

[28] Kim, Y. S.; Jeon, S. H.; Bostwick, A.; Rotenberg, E.; Ross, P. N.; Stamenkovic, V. R.; Markovic, N. M.; Noh, T. W.; Han, S.; Mun, B. S. Role of Transition Metal in Fast Oxidation Reaction on the Pt3TM (111) (TM = Ni, Co) Surfaces. *Advanced Energy Materials* **2013**, *3*, 1257–1261.

[29] Tague, M. E.; Gregoire, J. M.; Legard, A.; Smith, E.; Dale, D.; Hennig, R.; DiSalvo, F. J.; Bruce van Dover, R.; Abruña, H. D. High Throughput Thin Film Pt-M Alloys for Fuel Electrooxidation: Low Concentrations of M (M = Sn, Ta, W, Mo, Ru, Fe, In, Pd, Hf, Zn, Zr, Nb, Sc, Ni, Ti, V, Cr, Rh). *Journal of The Electrochemical Society* **2012**, *159*, F880–F887.

[30] Miyake, H.; Okada, T.; Samjeské, G.; Osawa, M. Formic acid electrooxidation on Pd in acidic solutions studied by surface-enhanced infrared absorption spectroscopy. *Physical Chemistry Chemical Physics* **2008**, *10*, 3662–3669.

[31] Chen, Y. X.; Heinen, M.; Jusys, Z.; Behm, R. J. Kinetics and Mechanism of the Electrooxidation of Formic Acid—Spectroelectrochemical Studies in a Flow Cell. *Angewandte Chemie International Edition* **2006**, *45*, 981–985.

[32] Wang, J.; Cheng, N.; Banis, M. N.; Xiao, B.; Riese, A.; Sun, X. Comparative study to understand the intrinsic properties of Pt and Pd catalysts for methanol and ethanol oxidation in alkaline media. *Electrochimica Acta* **2015**, *185*, 267–275.

[33] Shao, M. H.; Adzic, R. R. Electrooxidation of ethanol on a Pt electrode in acid solutions: in situ ATR-SEIRAS study. *Electrochimica Acta* **2005**, *50*, 2415–2422.

[34] Eckermann, A. L.; Feld, D. J.; Shaw, J. A.; Meade, T. J. Electrochemistry of redox-active self-assembled monolayers. *Coordination Chemistry Reviews* **2010**, *254*, 1769–1802.

[35] Faist, J.; Capasso, F.; Sivco, D. L.; Sirtori, C.; Hutchinson, A. L.; Cho, A. Y. Quantum Cascade Laser. *Science* **1994**, *264*, 553 LP – 556.

[36] Domachuk, P.; Wolchover, N. A.; Cronin-Golomb, M.; Wang, A.; George, A. K.; Cordeiro, C. M. B.; Knight, J. C.; Omenetto, F. G. Over 4000 nm Bandwidth of Mid-IR Supercontinuum Generation in sub-centimeter Segments of Highly Nonlinear Tellurite PCFs. *Optics Express* **2008**, *16*, 7161–7168.

[37] Weida, M. J.; Yee, B. Quantum cascade laser-based replacement for FTIR microscopy. *Progress in Biomedical Optics and Imaging - Proceedings of SPIE* **2011**, *7902*, 79021C.

[38] Mayet, C.; Dazzi, A.; Prazeres, R.; Allot, F.; Glotin, F.; Ortega, J. M. Sub-100 nm IR spectromicroscopy of living cells. *Optics Letters* **2008**, *33*, 1611–1613.

[39] Villares, G.; Hugi, A.; Blaser, S.; Faist, J. Dual-comb spectroscopy based on quantum-cascade-laser frequency combs. *Nature Communications* **2014**, *5*, 5192.

[40] Bai, Y.; Zhang, D.; Li, C.; Liu, C.; Cheng, J.-X. Bond-Selective Imaging of Cells by Mid-Infrared Photothermal Microscopy in High Wavenumber Region. *The Journal of Physical Chemistry B* **2017**, *121*, 10249–10255.

Appendix

Appendix I: LabVIEW rapid scan FTIR program

rapidscan_framework_template.vi
Labview Main VI: Main interface that controls the potentiostat, syringe pump and solenoid valves as well as records electrochemical E/I data through the DAC. Timing off individual elements is based on TTL-signals from the spectrometer to the DAC.

basic_apply_pulse_sequence.vi
Labview Sub VI: Applies a potential sequence created by the "basic_define_pulse.vi" to an analog output of the DAC. This is connected to the external potential input of the potentiostat and subsequenctly applied to the WE of the spectroelectrochemical cell to remove residual MOR products from electrode surface.

basic_define_pulse.vi
Labview Sub VI: Creates potential pulse array utilized by "basic_apply_pulse_sequence.vi" based on an input 2D array of ([time1 / ms, potential1 / mV], [time2 / ms, potential2 / mV], ...).

basic_labview_to_opus_AO.vi
Labview Sub VI: Communication from labview to spectrometer through analog output channel of DAC. The output simulates a rising edge TTL signal, followed by a falling edge TTL signal.

basic_rapidscan_step_falling.vi
Labview Sub VI: Awaits a falling edge TTL signal from spectrometer to apply potential step E_{Step} through the potentiostat over its external potential input channel. Simultaneously record E/I data from the potentiostat.

basic_rapidscan_step_rising.vi
Labview Sub VI: Wait for rising edge TTL signal from spectrometer to apply potential step E_{Step} through the potentiostat over its external potential input channel. Simultaneously record E/I data from the potentiostat.

basic_set_E.vi
Labview Sub VI: Change the potential applied by the potentiostat through its external potential input channel.

basic_trigger_falling.vi
Labview Sub VI: Waits for a falling edge TTL signal from the spectrometer.

basic_trigger_rising.vi
Labview Sub VI: Waits for a rising edge TTL signal from the spectrometer.

basic_TTL_OFF.vi
Labview Sub VI: Changes a digital output channel for TTL signals within the DAC to its low state (0V). Important to control solenoid valves and syringe pumps.

basic_TTL_ON.vi
Labview Sub VI: Changes a digital output channel for TTL signals within the DAC to its high state (5V). Important to control solenoid valves and syringe pumps.

rapidscan_framework_template.vi
Z:\Public Shares\Kaiyang Shared\time resolved FTIR\rapidscan basic components\rapidscan_framework_template.vi
Last modified on 11/18/2019 at 1:38 PM
Printed on 11/18/2019 at 2:47 PM

Block Diagram

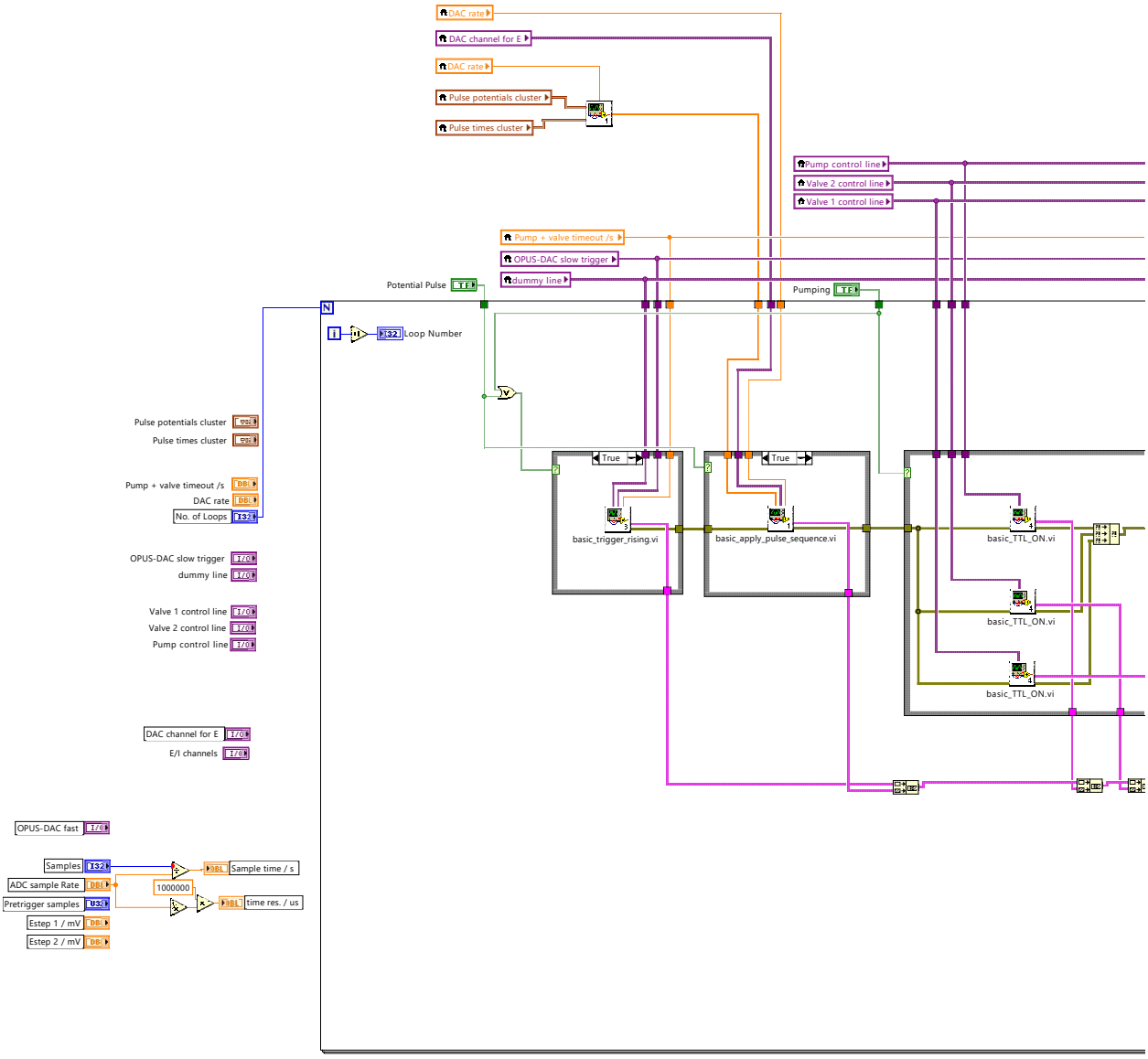

rapidscan_framework_template.vi
Z:\Public Shares\Kaiyang Shared\time resolved FTIR\rapidscan basic components\rapidscan_framework_template.vi
Last modified on 11/18/2019 at 1:38 PM
Printed on 11/18/2019 at 2:47 PM

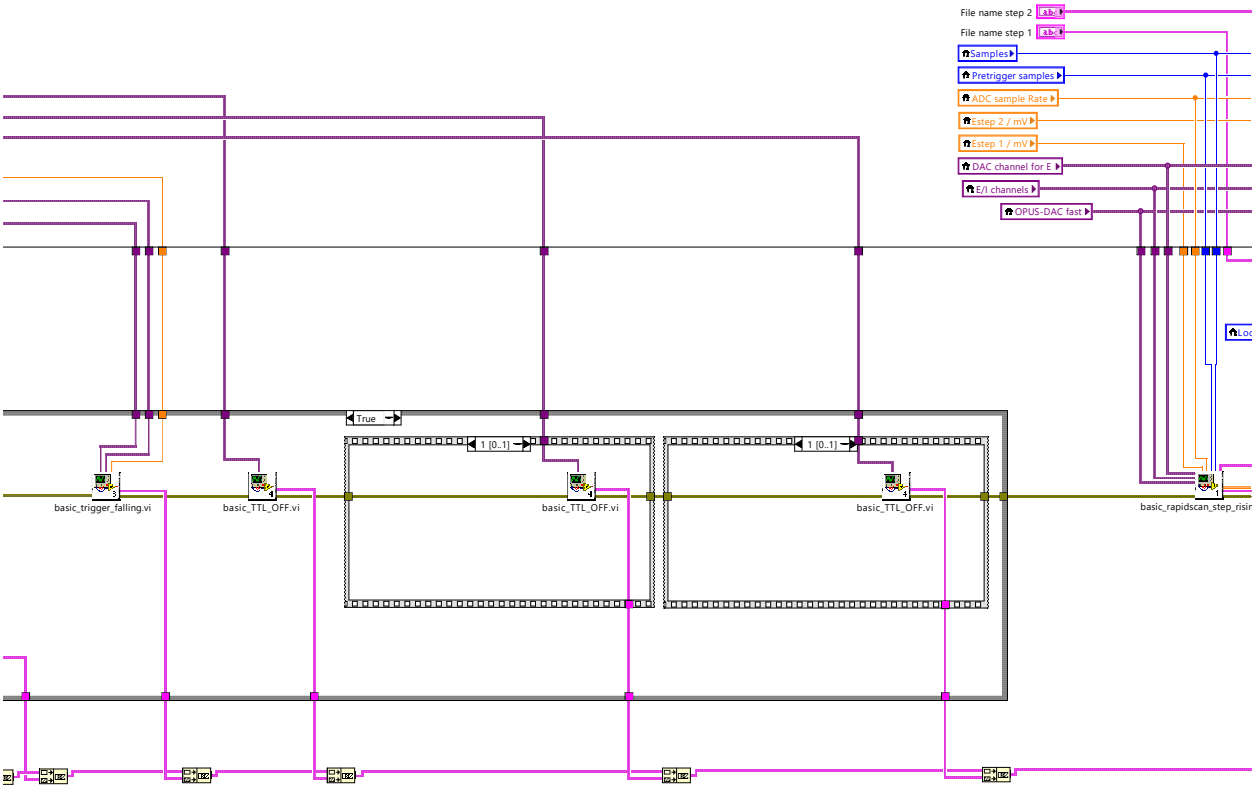

rapidscan_framework_template.vi
Z:\Public Shares\Kaiyang Shared\time resolved FTIR\rapidscan basic components\rapidscan_framework_template.vi
Last modified on 11/18/2019 at 1:38 PM
Printed on 11/18/2019 at 2:47 PM

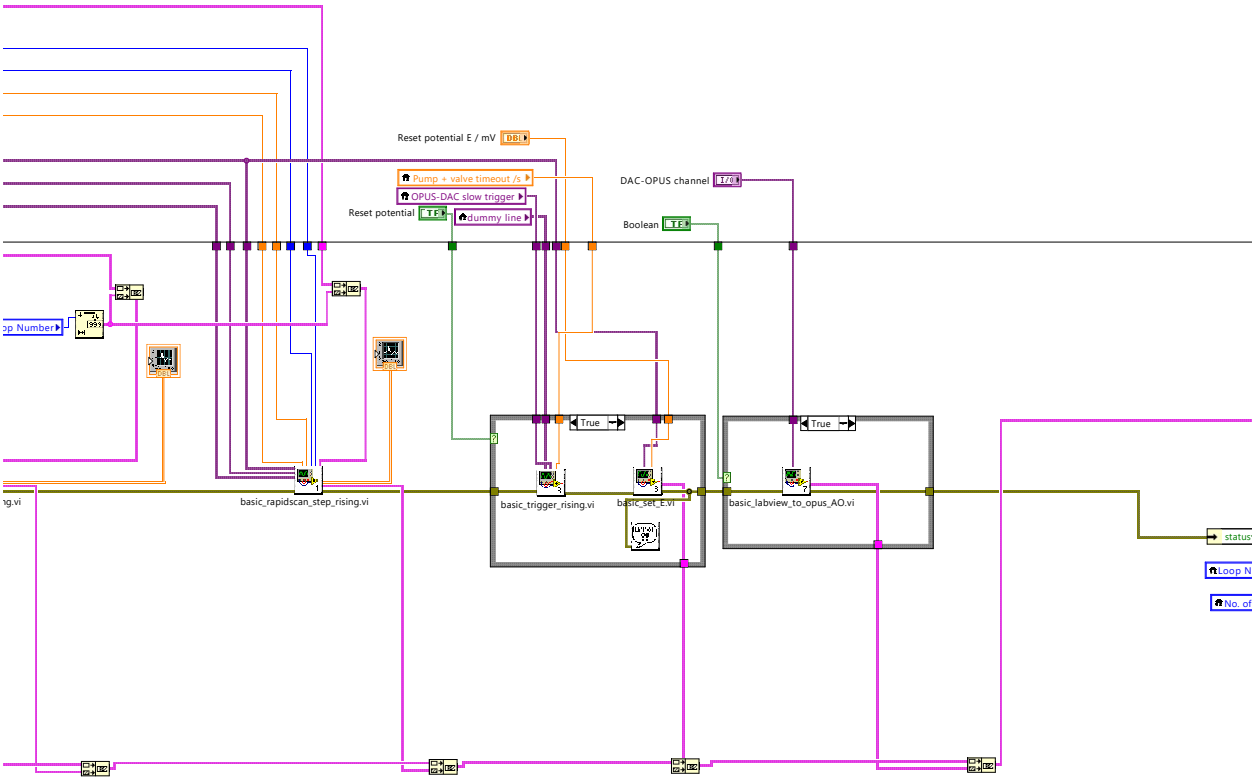

rapidscan_framework_template.vi
Z:\Public Shares\Kaiyang Shared\time resolved FTIR\rapidscan basic components\rapidscan_framework_template.vi
Last modified on 11/18/2019 at 1:38 PM
Printed on 11/18/2019 at 2:47 PM

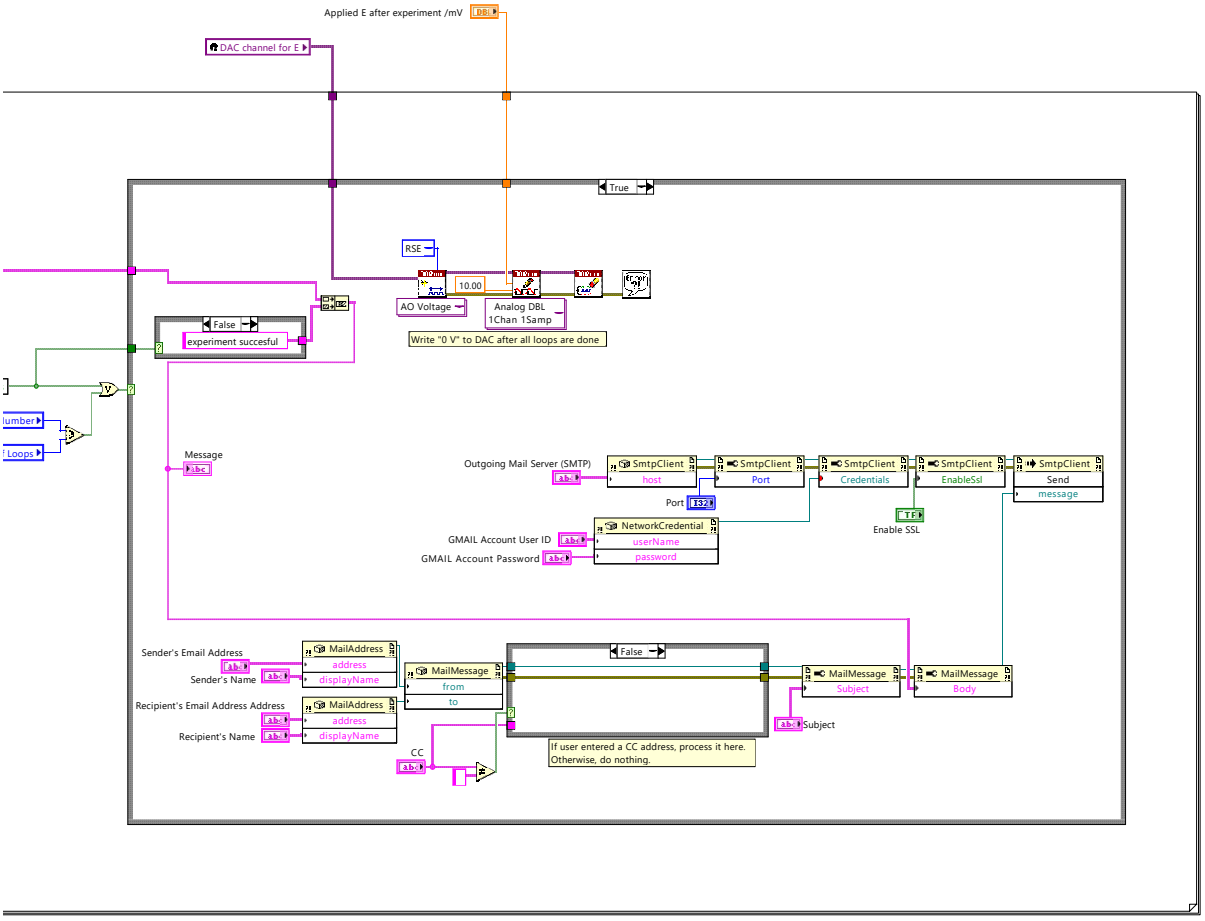

basic_apply_pulse_sequence.vi
Z:\Public Shares\Kaiyang Shared\time resolved FTIR\rapidscan basic components\basic_apply_pulse_sequence.vi
Last modified on 7/20/2019 at 12:23 AM
Printed on 11/18/2019 at 2:47 PM

Block Diagram

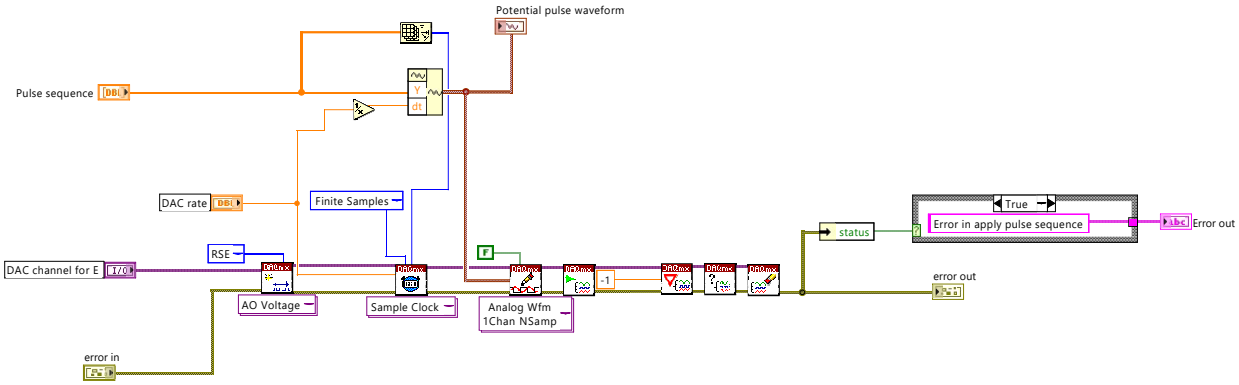

basic_define_pulse.vi
Z:\Public Shares\Kaiyang Shared\time resolved FTIR\rapidscan basic components\basic_define_pulse.vi
Last modified on 7/20/2019 at 12:23 AM
Printed on 11/18/2019 at 2:47 PM

Block Diagram

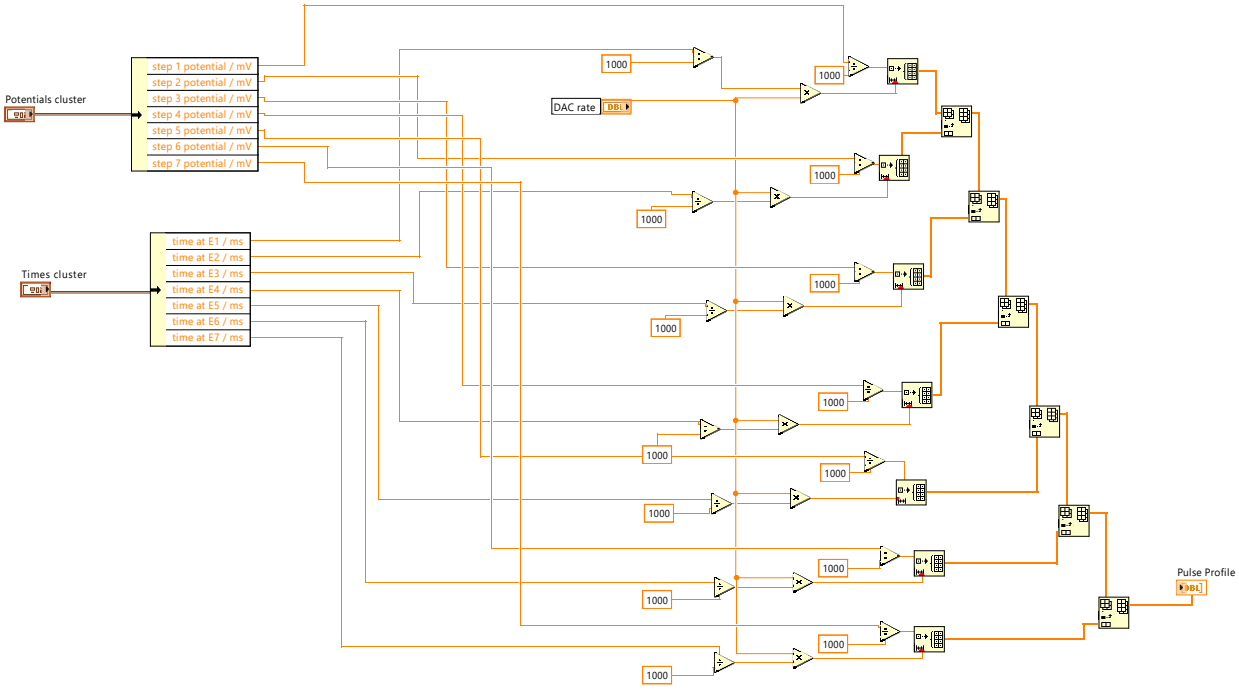

basic_labview_to_opus_AO.vi
Z:\Public Shares\Kaiyang Shared\time resolved FTIR\rapidscan basic components\basic_labview_to_opus_AO.vi
Last modified on 7/20/2019 at 12:23 AM
Printed on 11/18/2019 at 2:47 PM

Block Diagram

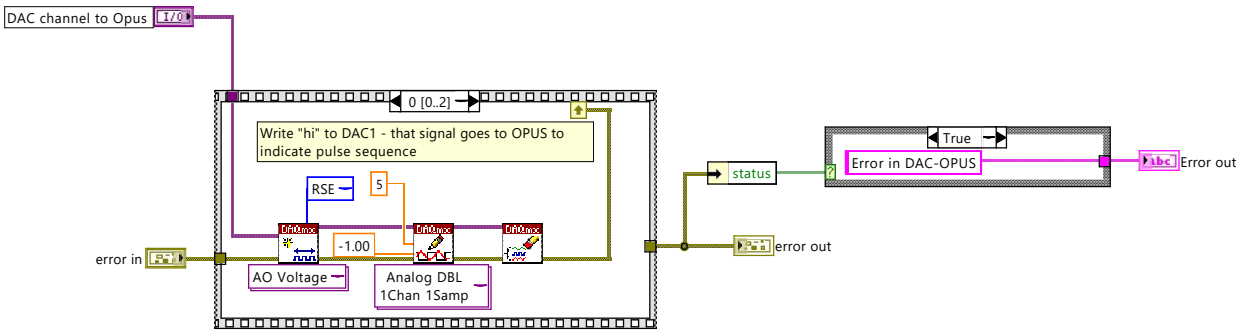

basic_rapidscan_step_falling.vi
Z:\Public Shares\Kaiyang Shared\time resolved FTIR\rapidscan basic components\basic_rapidscan_step_falling.vi
Last modified on 4/29/2016 at 4:35 PM
Printed on 11/18/2019 at 2:47 PM

Block Diagram

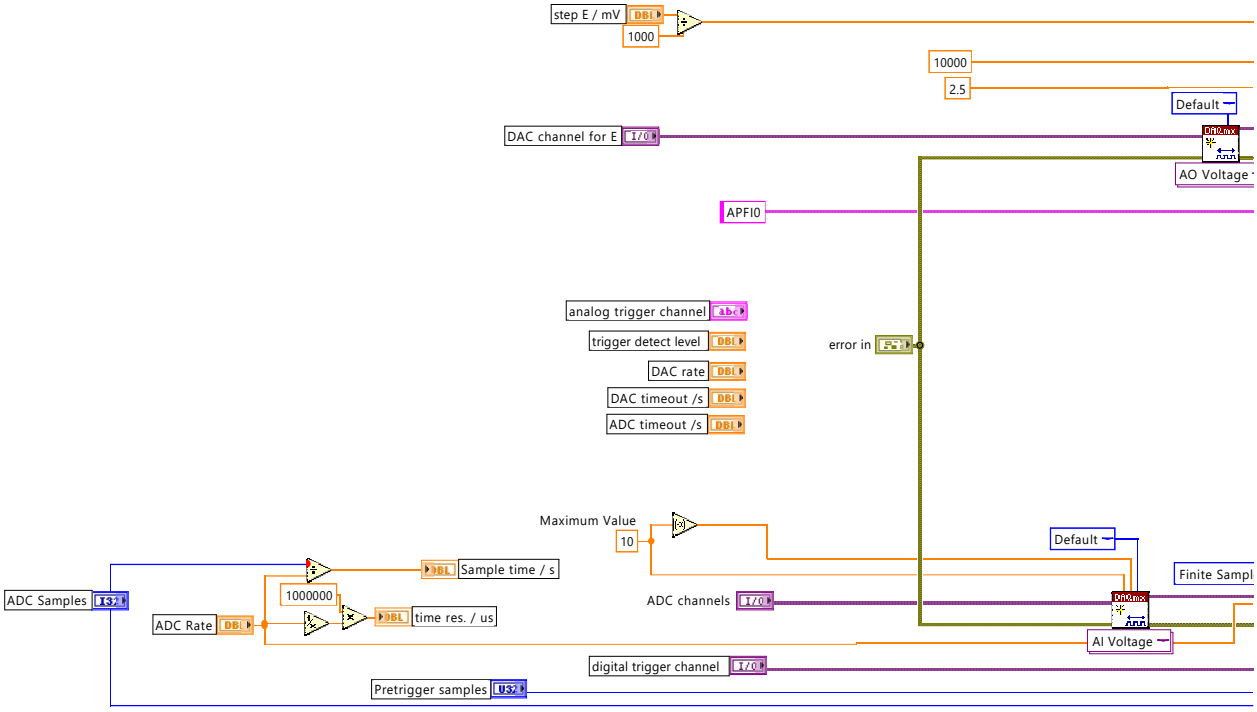

basic_rapidscan_step_rising.vi
Z:\Public Shares\Kaiyang Shared\time resolved FTIR\rapidscan basic components\basic_rapidscan_step_rising.vi
Last modified on 7/20/2019 at 12:23 AM
Printed on 11/18/2019 at 2:47 PM

Block Diagram

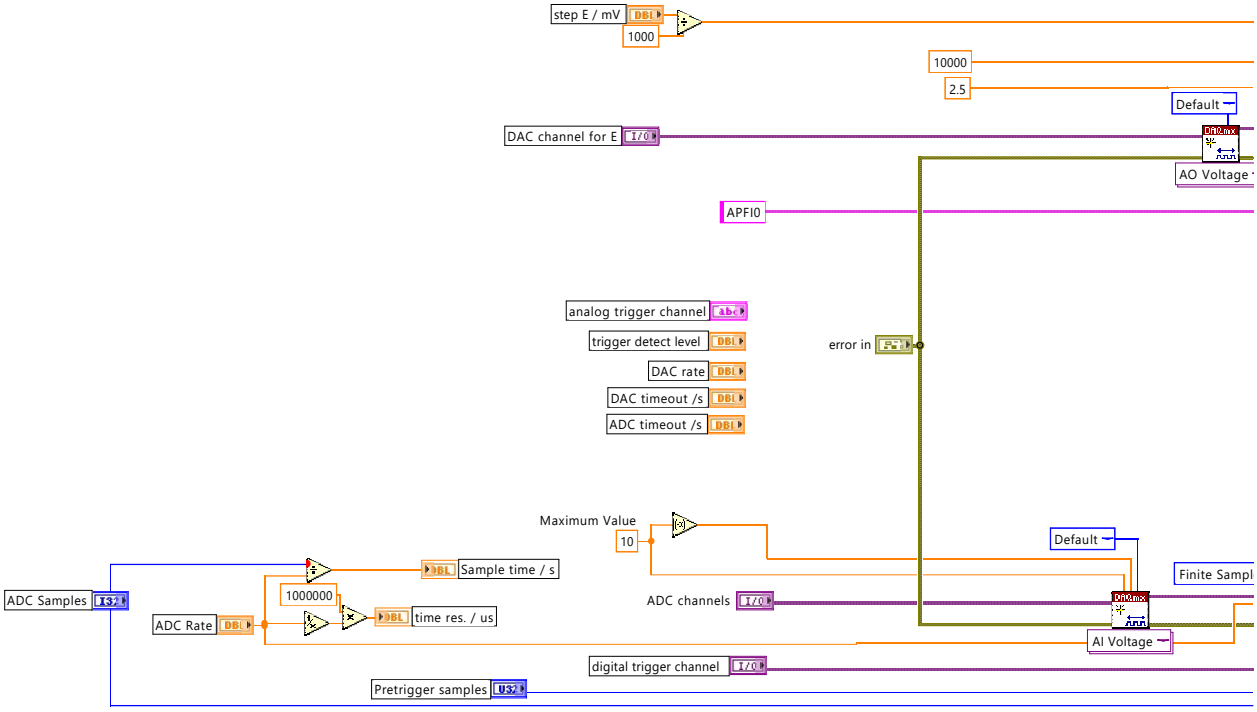

basic_set_E.vi
Z:\Public Shares\Kaiyang Shared\time resolved FTIR\rapidscan basic components\basic_set_E.vi
Last modified on 7/20/2019 at 12:23 AM
Printed on 11/18/2019 at 2:48 PM

Block Diagram

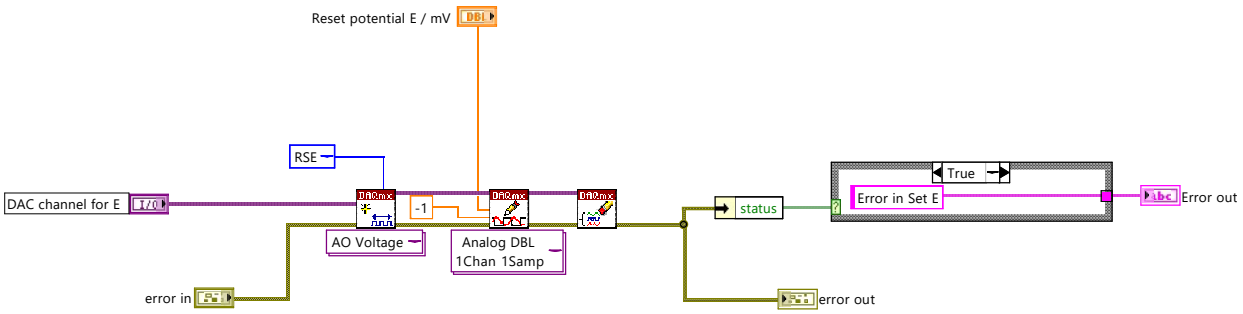

basic_trigger_falling.vi
Z:\Public Shares\Kaiyang Shared\time resolved FTIR\rapidscan basic components\basic_trigger_falling.vi
Last modified on 7/20/2019 at 12:23 AM
Printed on 11/18/2019 at 2:48 PM

Block Diagram

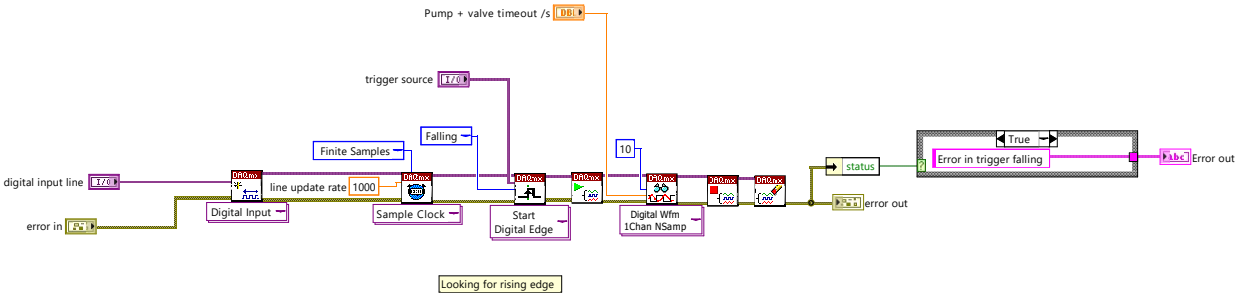

basic_trigger_rising.vi
Z:\Public Shares\Kaiyang Shared\time resolved FTIR\rapidscan basic components\basic_trigger_rising.vi
Last modified on 7/20/2019 at 12:23 AM
Printed on 11/18/2019 at 2:48 PM

Block Diagram

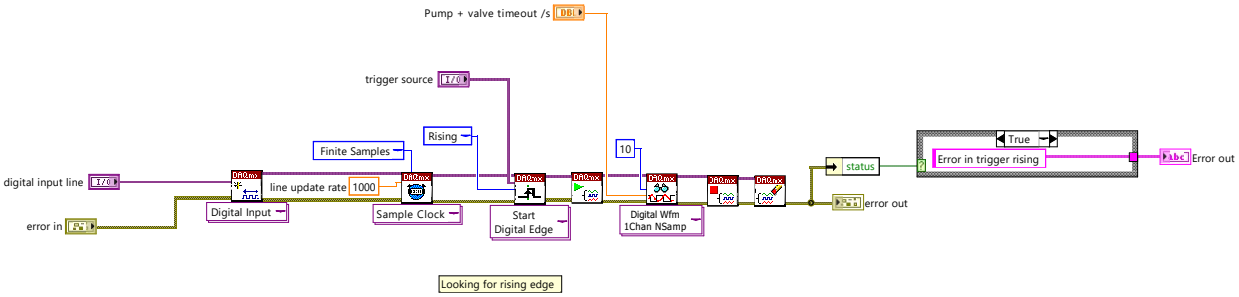

basic_TTL_OFF.vi
Z:\Public Shares\Kaiyang Shared\time resolved FTIR\rapidscan basic components\basic_TTL_OFF.vi
Last modified on 7/20/2019 at 12:23 AM
Printed on 11/18/2019 at 2:48 PM

Block Diagram

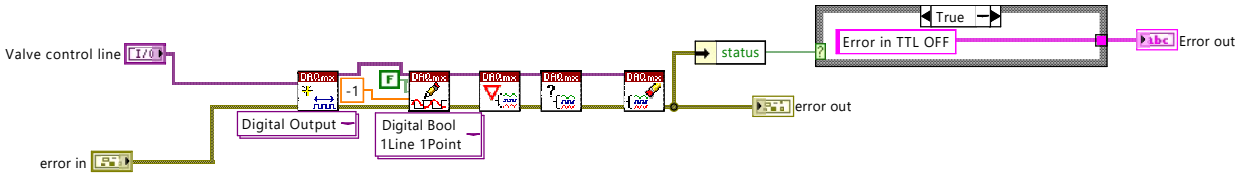

basic_TTL_ON.vi
Z:\Public Shares\Kaiyang Shared\time resolved FTIR\rapidscan basic components\basic_TTL_ON.vi
Last modified on 7/20/2019 at 12:23 AM
Printed on 11/18/2019 at 2:48 PM

Block Diagram

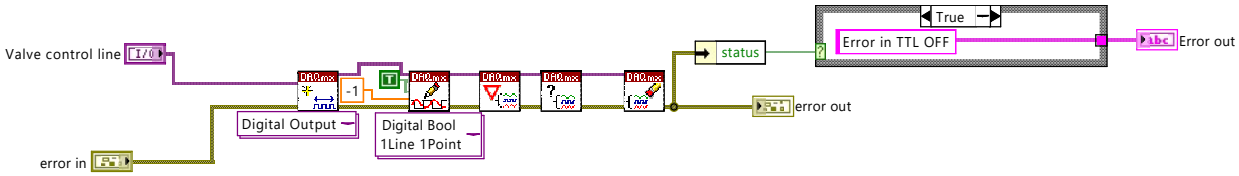

Appendix II: Matlab rapid scan FTIR analysis script

Matlab script to coadd the multiple rapid scan FTIR spectra and calculate their absorbance spectrum.

Input data
The script requires a set of OPUS rapid scan FTIR spectra that are saved as matlab4 files. All files should be located within a single folder and its location addressed in the "path = '...location'; " line within the Matlab script.
The script assumes, that the FTIR spectra are in following format:

wavenumber1, IR signal (reference spectra), IR signal (t_1), IR signal (t_2), ...
wavenumber2, IR signal (reference spectra), IR signal (t_1), IR signal (t_2), ...

Output data
The script creates multiple arrays with the result of the absorbance calculation:

wavenum 1D array with wavenumber values.
absorbance 2D array with calculated absorbance value in following format:

IR absorbance (wavenumber1, t_1), IR absorbance (wavenumber1, t_2), ...
IR absorbance (wavenumber2, t_1), IR absorbance (wavenumber2, t_2), ...

complete 2D array with calculated absorbance value in following format. This is better suited for export as .csv-file:

wavenumber1, IR absorbance (wavenumber1, t_1), IR absorbance (wavenumber1, t_2), ...
wavenumber2, IR absorbance (wavenumber2, t_1), IR absorbance (wavenumber2, t_2), ...

absorbance_collated/complete_collated 2D arrays with time collated absorbance data with similar structure as "absorbance"/"complete" described above. How many time elements are collated depends on the parameter "collation = ...;" set in the beginning of the scrip. "collation" parameter must be a number that is a whole integer divisor of the total time elements of the rapid scan data.

```
%----------------------rapidscan_analysis----------------------%
clear variables
close all
clc
%--------------------------------------------------------------%

path = 'D:\Dropbox\work\reports\thesis\word version\chapter 3 Pt MOR
\figures\MOR rapid scan\raw data\matlab\';
%'filepath of folder with matlab files + \'%

search_path = sprintf('%s*.mat',path);
files = dir(search_path);
filename = sprintf('%s%s',path,files(1).name);
save = load(filename);
[p,q] = size(save.Sc);
timeelements = q-2;
matrixdimension = p;
file_count = 0;
sniftir = zeros(matrixdimension,timeelements);
absorbance = zeros(matrixdimension,timeelements);
sniftir = zeros(matrixdimension,timeelements);
complete = zeros(matrixdimension,timeelements+1);
%zeroes(x,y) ; y has to be the same number as single spectra within
 each%
%rapidscan file%

collation = 2;
collationslice = timeelements/collation;
absorbance_collated = zeros(matrixdimension,collationslice);
complete_collated = zeros(matrixdimension,collationslice+1);

for file = files'
    filename = sprintf('%s%s',path,file.name);
    temp = load(filename);
    data = temp.Sc;

    l = 1;
    collated_counter = 0;

    for j=1:1:timeelements
    %for j=x:y:z ; z has to be the same number as single spectra
 within%
    %each rapidscan file%
        temp_sniftir = (data(:,j+2)-data(:,2))./data(:,2);
        %temp_sniftir = data(:,j+2);
        sniftir(:,j) = sniftir(:,j)+temp_sniftir;
        temp_absorbance = real(-log10(data(:,j+2)./data(:,2)));
        absorbance(:,j) = absorbance(:,j)+temp_absorbance;

        if collated_counter == collation
            l = l + 1;
            collated_counter = 0;
```

```
        end;
        absorbance_collated(:,l) = absorbance_collated(:,l) +
 temp_absorbance;
        collated_counter = collated_counter + 1;

    end;

    file_count = file_count+1;
end;


for i= 1:1:timeelements
    sniftir(:,i) = sniftir(:,i)./file_count;
    absorbance(:,i) = absorbance(:,i)./file_count;
end;


for i= 1:1:timeelements/2
%for i=x:y:z ; z has to be the same number as single spectra within
 each%
%rapidscan file%
    absorbance_collated(:,i) = absorbance_collated(:,i)./file_count;
end;


%rudementary peak fitting
%use?
use = 'n';
%select baseline points around peak
peakpickstart = 959;
peakpickend = 995;

if use == 'y';
    average =
 (absorbance(peakpickstart,:)+absorbance(peakpickend,:))/2;
    for i= peakpickstart:1:peakpickend
        absorbance(i,:) = absorbance(i,:)-average;
    end;
end;

complete(:,1) = temp.Sc(:,1);

for n= 1:1:timeelements
    complete(:,n+1) = absorbance(:,n);
end;

wavenum = temp.Sc(:,1);
```

Published with MATLAB® R2017b

Appendix III: FlexPDE simulation code

Code for FEM simulation in FlexPDE (Lite version), describing the CO_2 diffusion within the PtNi spectroelectroelectrochemical cell for combinatorial screening of MOR in Chapter 4. Detailed descriptions of simulation space (Figure 4.9) and boundary conditions (Table 4.1) can be found in sub chapter 4.4.4.

{ SIMULATION FOR AN EMBEDDED Au ELECTRODE IN A THIN CAVITY CELL - SIMPLE REDOX
This simulation is for the concentration mapping of a simple echem reaction of the form ox + e --> red

It uses a reduced coordinate system as defined below;
The window to window separation in the transmittance cell is h and is set to unity. Normalization is with respect to this parameter.
The un-normalized differential eqns for species ox and red are D_ox(dxx(ox)+dyy(ox)) = dt(ox) ;
D_red(dxx(red)+dyy(red) = dt(red) where D_ox and D_red are the diffusion coefficients for ox and red.
Defining the following normalization parameters...
Ox=MeOH concentration/initial ox concentration ; Red =CO2 concentration/initial ox concentration ; X = x/h ; Y = y/h ;
T = (tD_ox)/h^2 ; D = D_red/D_ox
After normalization the eqns become....dXX(Ox)+dYY(Ox)= dT(Ox), D(dXX(Red)+dYY(Red)) = dT(Red)}

TITLE '2D Diffusion to an embedded gold electrode - simple redox'

COORDINATES cartesian2(x,y) { x - along length of working electrode ; y - normal from working electrode i.e. parallel to the beam path }

VARIABLES { system variables (tolerances) }
Ox (.001), Red (.001)

SELECT { method controls }
TEXTSIZE = 25 { default is 35 - smaller numbers mean bigger font}
ERRLIM = 0.002

DEFINITIONS
XMIN = -100 {distance along shielding to consider in the negative direction}
XMAX = 100 {distance along shielding to consider in the positive direction}
ALLOY = 10 {normalized half width of ALLOY electrode}
B = 1 {normalized width of IR beam}
D = 1 {ratio of Red to Ox diffusion coefficients}
H = 2 {height of thin cavity}

{IROx2=area_Integral (Ox,2); IRRed2=area_Integral (Red,2)}

IROx2=area_Integral (Ox,2); IRRed2=area_Integral (Red,2)
IROx3=area_Integral (Ox,3); IRRed3=area_Integral (Red,3)
IROx4=area_Integral (Ox,4); IRRed4=area_Integral (Red,4)
IROx5=area_Integral (Ox,5); IRRed5=area_Integral (Red,5)
IROx6=area_Integral (Ox,6); IRRed6=area_Integral (Red,6)
IROx7=area_Integral (Ox,7); IRRed7=area_Integral (Red,7)
IROx8=area_Integral (Ox,8); IRRed8=area_Integral (Red,8)
IROx9=area_Integral (Ox,9); IRRed9=area_Integral (Red,9)
IROx10=area_Integral (Ox,10); IRRed10=area_Integral (Red,10)
IROx11=area_Integral (Ox,11); IRRed11=area_Integral (Red,11)
IROx12=area_Integral (Ox,12); IRRed12=area_Integral (Red,12)
IROx13=area_Integral (Ox,13); IRRed13=area_Integral (Red,13)
IROx14=area_Integral (Ox,14); IRRed14=area_Integral (Red,14)
IROx15=area_Integral (Ox,15); IRRed15=area_Integral (Red,15)
IROx16=area_Integral (Ox,16); IRRed16=area_Integral (Red,16)
IROx17=area_Integral (Ox,17); IRRed17=area_Integral (Red,17)
IROx18=area_Integral (Ox,18); IRRed18=area_Integral (Red,18)
IROx19=area_Integral (Ox,19); IRRed19=area_Integral (Red,19)
IROx20=area_Integral (Ox,20); IRRed20=area_Integral (Red,20)
IROx21=area_Integral (Ox,21); IRRed21=area_Integral (Red,21)

{K values without constant Pt area}
{K = 0.000003} {constant}
{K = 0.0001*(X+ALLOY) + 0.0003 } {linear}
{K = 0.0003*exp(0.10*(X+ALLOY))} {exponential}
{K = 0.0003*(1.2)^(X+ALLOY)}

```
{K values with constant Pt area}

K = IF (T < 0)
        THEN 0
        ELSE
          IF (X < 0)
              THEN 0.000012
              ELSE 0.000006 {constant}   {0.0003*(X+5*B) + 0.0003}  {linear}  {0.0003*exp(0.21*(X-4))}  {exponential}



{(1/31.25)*(ALLOY-X)/(2*ALLOY) } {K = 0.003*exp(-0.35*(X+ALLOY))}
{integrate Ox and Red in these regions to mimic IR response}


INITIAL VALUES
Ox = 1
Red= 0

EQUATIONS       { PDE's, one for each variable }
   Ox:dXX(Ox)+dYY(Ox)=dT(Ox)
   Red:D*(dXX(Red)+dYY(Red))=dT(Red)

BOUNDARIES              {natural is essentially the gradient (d/dX + d/dY + d/dZ) of the variable. In the current problem
the gradient only has a non-zero value above the electrode where there is a change in concentration along the Y
direction}
 REGION 1               {this is the total space under consideration}
   START (-2.5*ALLOY, 0)            {start at the centre of the electrode}
      natural (Ox) =-K*Ox
      natural (Red) = -normal(Grad(Ox))
   LINE TO (1*ALLOY,0)
      natural (Ox) = 0                  {no flux along the bottom PVC surface}
      natural (Red) = 0                 {no flux along the bottom PVC surface}
   LINE TO (XMAX,0)       {bottom edge of the diffusion space furthest from the origin}
      value (Ox) = 1                    {semi-infinite conditions along the vertical line linking the two windows}
      value (Red) = 0                   {semi infinited condions along the vertical line linking the two windows}
   LINE TO (XMAX,H)       {top edge of the diffusion space furthest from the origin}
      natural (Ox) = 0              {no flux along the top CaF2 surface}
      natural (Red) = 0                 {no flux along the top CaF2 surface}
   LINE TO (XMIN,H)          {the top edge of the diffusion space above the origin}
      value (Ox) = 1                {semi infinited condions along the vertical line linking the two surfaces}
      value (Red) = 0               {semi infinited condions along the vertical line linking the two surfaces}
   LINE TO (XMIN,0)
      natural (Ox) = 0              {no perpendicular flux above the centre of the electrode}
      natural (Red) = 0                 {no perpendicular flux above the centre of the electrode}
   LINE TO CLOSE          {return to the origin}


{REGION 2 {area above the electrode}
   START(-ALLOY+0*B,0) LINE TO (-ALLOY+20*B,0) LINE TO (-ALLOY+20*B,H) LINE TO (-ALLOY+0*B,H) LINE TO
CLOSE}

REGION 2 {area above the electrode}
   START(-ALLOY+0*B,0) LINE TO (-ALLOY+1*B,0) LINE TO (-ALLOY+1*B,H) LINE TO (-ALLOY+0*B,H) LINE TO
CLOSE
REGION 3 {closest IR region}
   START(-ALLOY+1*B,0) LINE TO (-ALLOY+2*B,0) LINE TO (-ALLOY+2*B,H) LINE TO (-ALLOY+1*B,H) LINE TO
CLOSE
 REGION 4 {next closest IR region}
   START(-ALLOY+2*B,0) LINE TO (-ALLOY+3*B,0) LINE TO (-ALLOY+3*B,H) LINE TO (-ALLOY+2*B,H) LINE TO
CLOSE
```

```
 REGION 5 {next closest IR region}
    START(-ALLOY+3*B,0) LINE TO (-ALLOY+4*B,0) LINE TO (-ALLOY+4*B,H) LINE TO (-ALLOY+3*B,H) LINE TO
CLOSE
 REGION 6 {next closest IR region}
    START(-ALLOY+4*B,0) LINE TO (-ALLOY+5*B,0) LINE TO (-ALLOY+5*B,H) LINE TO (-ALLOY+4*B,H) LINE TO
CLOSE
 REGION 7 {next closest IR region}
    START(-ALLOY+5*B,0) LINE TO (-ALLOY+6*B,0) LINE TO (-ALLOY+6*B,H) LINE TO (-ALLOY+5*B,H) LINE TO
CLOSE
 REGION 8 {next closest IR region}
    START(-ALLOY+6*B,0) LINE TO (-ALLOY+7*B,0) LINE TO (-ALLOY+7*B,H) LINE TO (-ALLOY+6*B,H) LINE TO
CLOSE
 REGION 9 {next closest IR region}
    START(-ALLOY+7*B,0) LINE TO (-ALLOY+8*B,0) LINE TO (-ALLOY+8*B,H) LINE TO (-ALLOY+7*B,H) LINE TO
CLOSE
 REGION 10 {next closest IR region}
    START(-ALLOY+8*B,0) LINE TO (-ALLOY+9*B,0) LINE TO (-ALLOY+9*B,H) LINE TO (-ALLOY+8*B,H) LINE TO
CLOSE
REGION 11 {next closest IR region}
    START(-ALLOY+9*B,0) LINE TO (-ALLOY+10*B,0) LINE TO (-ALLOY+10*B,H) LINE TO (-ALLOY+9*B,H) LINE TO
CLOSE
REGION 12 {next closest IR region}
    START(-ALLOY+10*B,0) LINE TO (-ALLOY+11*B,0) LINE TO (-ALLOY+11*B,H) LINE TO (-ALLOY+10*B,H) LINE
TO CLOSE
REGION 13 {next closest IR region}
    START(-ALLOY+11*B,0) LINE TO (-ALLOY+12*B,0) LINE TO (-ALLOY+12*B,H) LINE TO (-ALLOY+11*B,H) LINE
TO CLOSE
REGION 14 {next closest IR region}
    START(-ALLOY+12*B,0) LINE TO (-ALLOY+13*B,0) LINE TO (-ALLOY+13*B,H) LINE TO (-ALLOY+12*B,H) LINE
TO CLOSE
REGION 15 {next closest IR region}
    START(-ALLOY+13*B,0) LINE TO (-ALLOY+14*B,0) LINE TO (-ALLOY+14*B,H) LINE TO (-ALLOY+13*B,H) LINE
TO CLOSE
REGION 16 {next closest IR region}
    START(-ALLOY+14*B,0) LINE TO (-ALLOY+15*B,0) LINE TO (-ALLOY+15*B,H) LINE TO (-ALLOY+14*B,H) LINE
TO CLOSE
REGION 17 {next closest IR region}
    START(-ALLOY+15*B,0) LINE TO (-ALLOY+16*B,0) LINE TO (-ALLOY+16*B,H) LINE TO (-ALLOY+15*B,H) LINE
TO CLOSE
REGION 18 {next closest IR region}
    START(-ALLOY+16*B,0) LINE TO (-ALLOY+17*B,0) LINE TO (-ALLOY+17*B,H) LINE TO (-ALLOY+16*B,H) LINE
TO CLOSE
REGION 19 {next closest IR region}
    START(-ALLOY+17*B,0) LINE TO (-ALLOY+18*B,0) LINE TO (-ALLOY+18*B,H) LINE TO (-ALLOY+17*B,H) LINE
TO CLOSE
REGION 20 {next closest IR region}
    START(-ALLOY+18*B,0) LINE TO (-ALLOY+19*B,0) LINE TO (-ALLOY+19*B,H) LINE TO (-ALLOY+18*B,H) LINE
TO CLOSE
REGION 21 {next closest IR region}
    START(-ALLOY+19*B,0) LINE TO (-ALLOY+20*B,0) LINE TO (-ALLOY+20*B,H) LINE TO (-ALLOY+19*B,H) LINE
TO CLOSE

TIME 0 BY 0.1 TO 10

MONITORS
{PLOTS}
for T=0 BY 0.1 TO 10

contour (Ox) zoom (-(10+ALLOY),0,4*ALLOY,1)
contour (Red) zoom (-(0.6*ALLOY),-0.25,(1.8*ALLOY),1.5) {painted}
{contour (Ox) zoom (-(10+ALLOY),0,4*ALLOY,1)
contour (Red) zoom (-(5+ALLOY),-0.25,3*ALLOY,1.5)}
```

{elevation (Ox, Red) from (0,0) to (Au,0)
Elevation (Ox,Red) from (0,0) to (Au,0)}

HISTORIES
{history (IRRed2) export format "#t#r#b#i"}
{history (IROx2, IROx3, IROx4, IROx5, IROx6, IROx7, IROx8, IROx9, IROx10, IROx11, IRRed2, IRRed3, IRRed4, IRRed5, IRred6, IRRed7, IRRed8, IRRed9, IRRed10, IRRed11)}
{history (IROx2, IROx3, IROx4, IROx5, IROx6, IRRed2, IRRed3, IRRed4, IRRed5, IRred6) export format "#t#r#b#i"}
history (IRRed2, IRRed3, IRRed4, IRRed5, IRred6, IRRed7, IRRed8, IRRed9, IRRed10, IRRed11, IRRed12, IRRed13, IRRed14, IRRed15, IRRed16, IRRed17, IRRed18, IRRed19, IRRed20, IRRed21) export format "#t#r#b#i"
{history (IROx2, IROx3, IROx4, IROx5, IROx6, IROx7, IROx8, IROx9, IROx10, IROx11, IROx12, IROx13, IROx14, IROx15, IROx16, IROx17, IROx18, IROx19, IROx20, IROx21) export format "#t#r#b#i"}
{history (IRRed10) export format "#t#r#b#i"}
{history (IROx2, IROx3, IROx4, IROx5, IROx6, IROx7, IROx8, IROx9, IROx10) {export format "#t#r#b#i"}}
END

Appendix IV: LabVIEW step scan FTIR program

stepscan_framework_template.vi
Labview Main VI: Main interface that controls the potentiostat and records electrochemical E/I data through the DAC. Generates the TTL-signal from the DAC to the spectrometer to trigger the acquisition of step scan IR data.

basic_set_E.vi
Labview Sub VI: Change the potential applied by the potentiostat through its external potential input channel.

basic_trigger_rising.vi
Labview Sub VI: Waits for a rising edge TTL signal from the spectrometer.

generate_signal 2
Labview Sub VI: Utilized the two waveform generated by the "waveform_generator 2" and applies them to the analog output channels of the DAC. This triggers the simultaneous step scan IR acquisition by the FTIR spectrometer, application of a potential sequence to the spectroelectrochemical cell and the E/I acquisition of the DAC through the sub VI "measure_signal 2".

measure_signal 2
Labview Sub VI: Measures the E/I data coming from the potentiostat into two analog input channels of the DAC. The acquisition is triggered by a rising edge TTL-signal that is generated by the "generate_signal 2" sub VI.

save_data 2
Labview Sub VI: Save E/I data acquired by the "measure_signal 2" sub VI and saves is as a text file.

waveform_generator 2
Labview Sub VI: Generates a two waveforms from two initial 2D array inputs that are later applied through two analog output channels of the DAC by the "generate_signal 2" sub VI. The first waveform contains the rising edge TTL trigger signal for the step scan IR acquisition of the FTIR spectrometer as well as E/I data acquisition. The second waveform contains the potential sequence applied to the WE of the spectroelectrochemical cell through the external potential input channel of the potentiastat.

stepscan_framework_v0.2.vi
Z:\Public Shares\Kaiyang Shared\time resolved FTIR\step scan test v02\
stepscan_framework_v0.2.vi
Last modified on 9/15/2019 at 1:04 PM
Printed on 11/18/2019 at 2:44 PM

Block Diagram

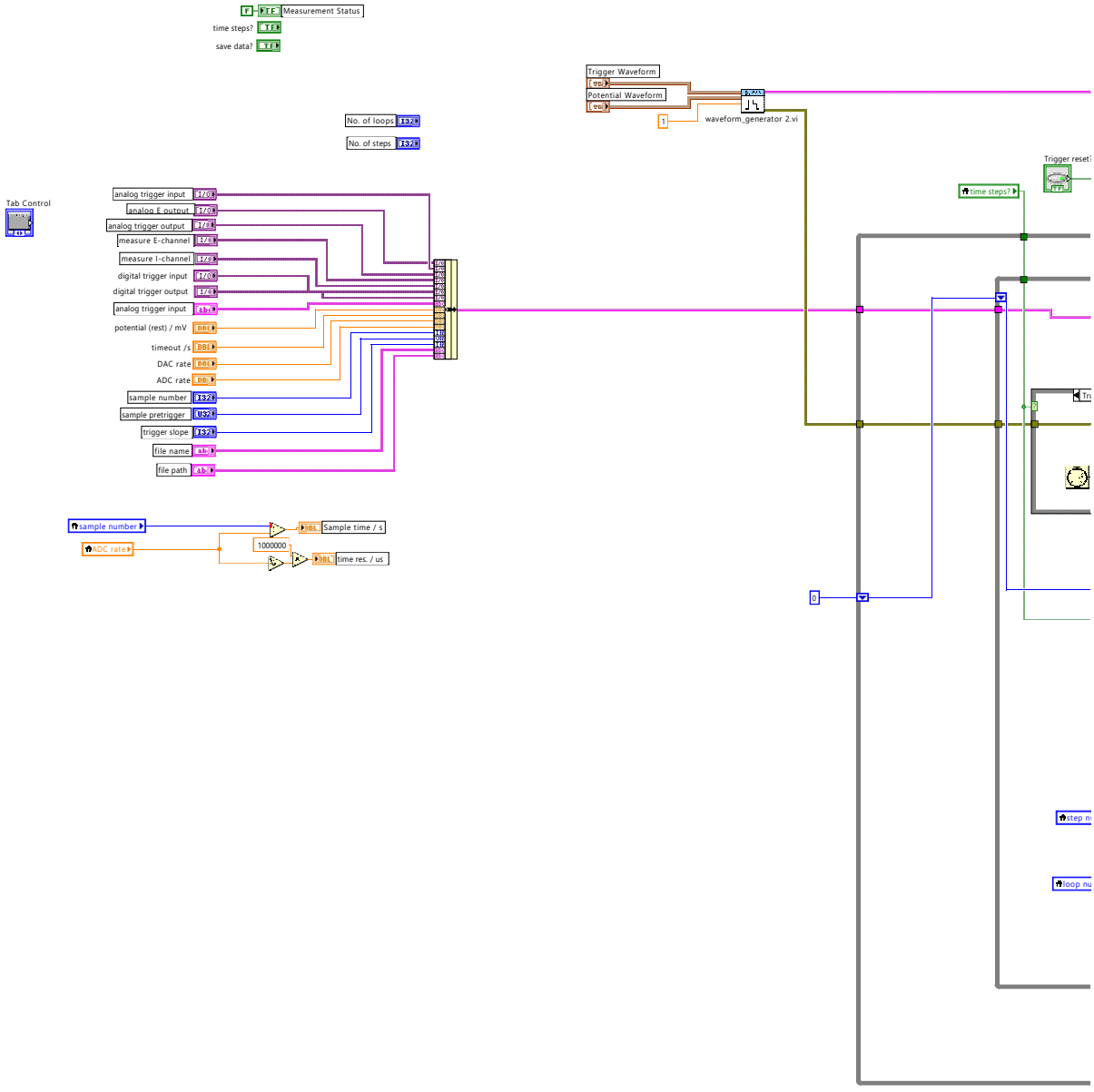

stepscan_framework_v0.2.vi
Z:\Public Shares\Kaiyang Shared\time resolved FTIR\step scan test v02\
stepscan_framework_v0.2.vi
Last modified on 9/15/2019 at 1:04 PM
Printed on 11/18/2019 at 2:44 PM

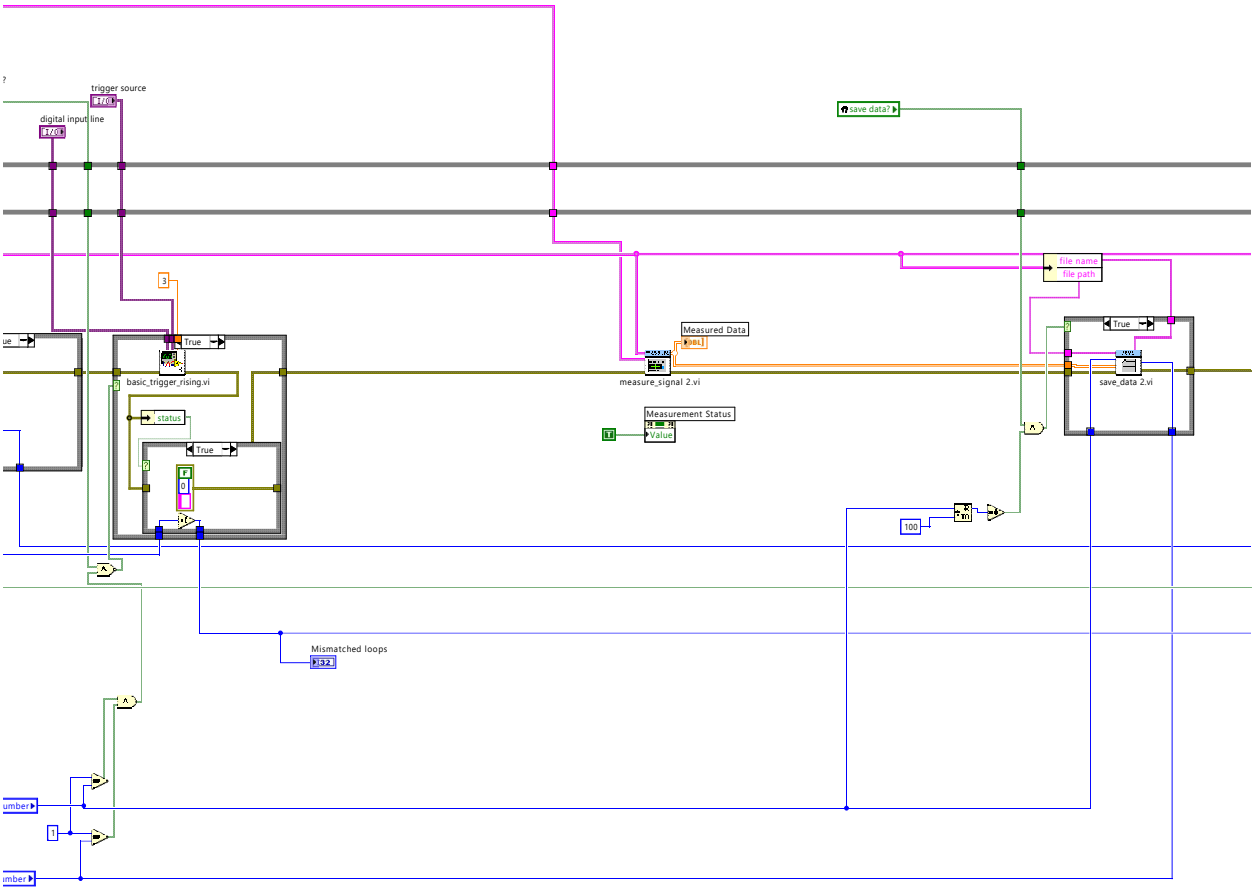

stepscan_framework_v0.2.vi
Z:\Public Shares\Kaiyang Shared\time resolved FTIR\step scan test v02\
stepscan_framework_v0.2.vi
Last modified on 9/15/2019 at 1:04 PM
Printed on 11/18/2019 at 2:44 PM

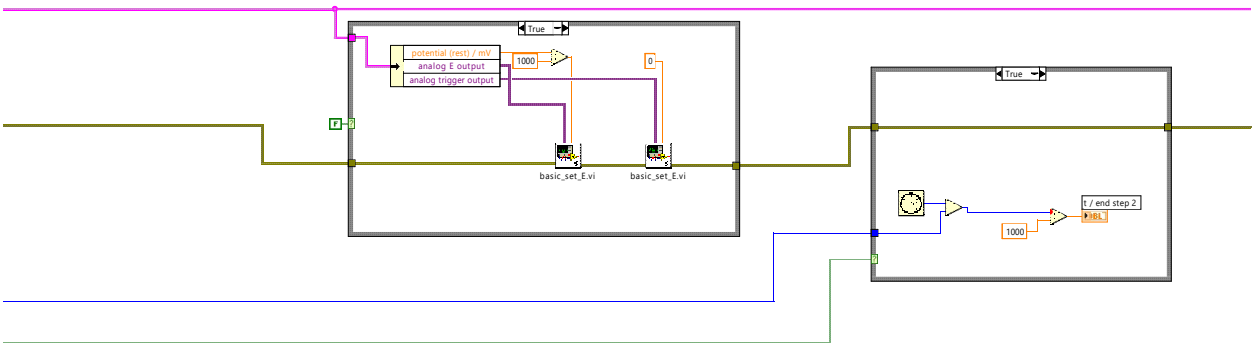

stepscan_framework_v0.2.vi
Z:\Public Shares\Kaiyang Shared\time resolved FTIR\step scan test v02\
stepscan_framework_v0.2.vi
Last modified on 9/15/2019 at 1:04 PM
Printed on 11/18/2019 at 2:44 PM

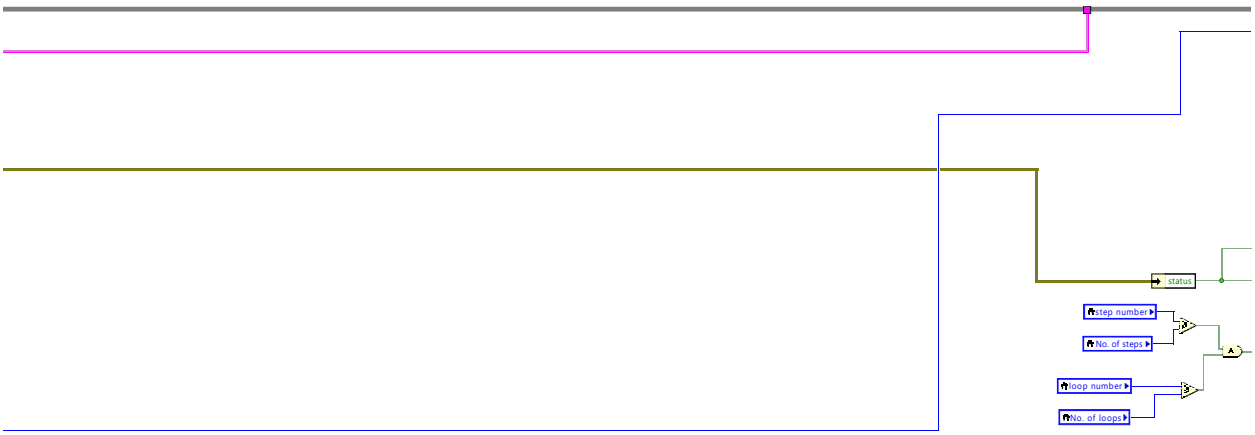

stepscan_framework_v0.2.vi
Z:\Public Shares\Kaiyang Shared\time resolved FTIR\step scan test v02\
stepscan_framework_v0.2.vi
Last modified on 9/15/2019 at 1:04 PM
Printed on 11/18/2019 at 2:44 PM

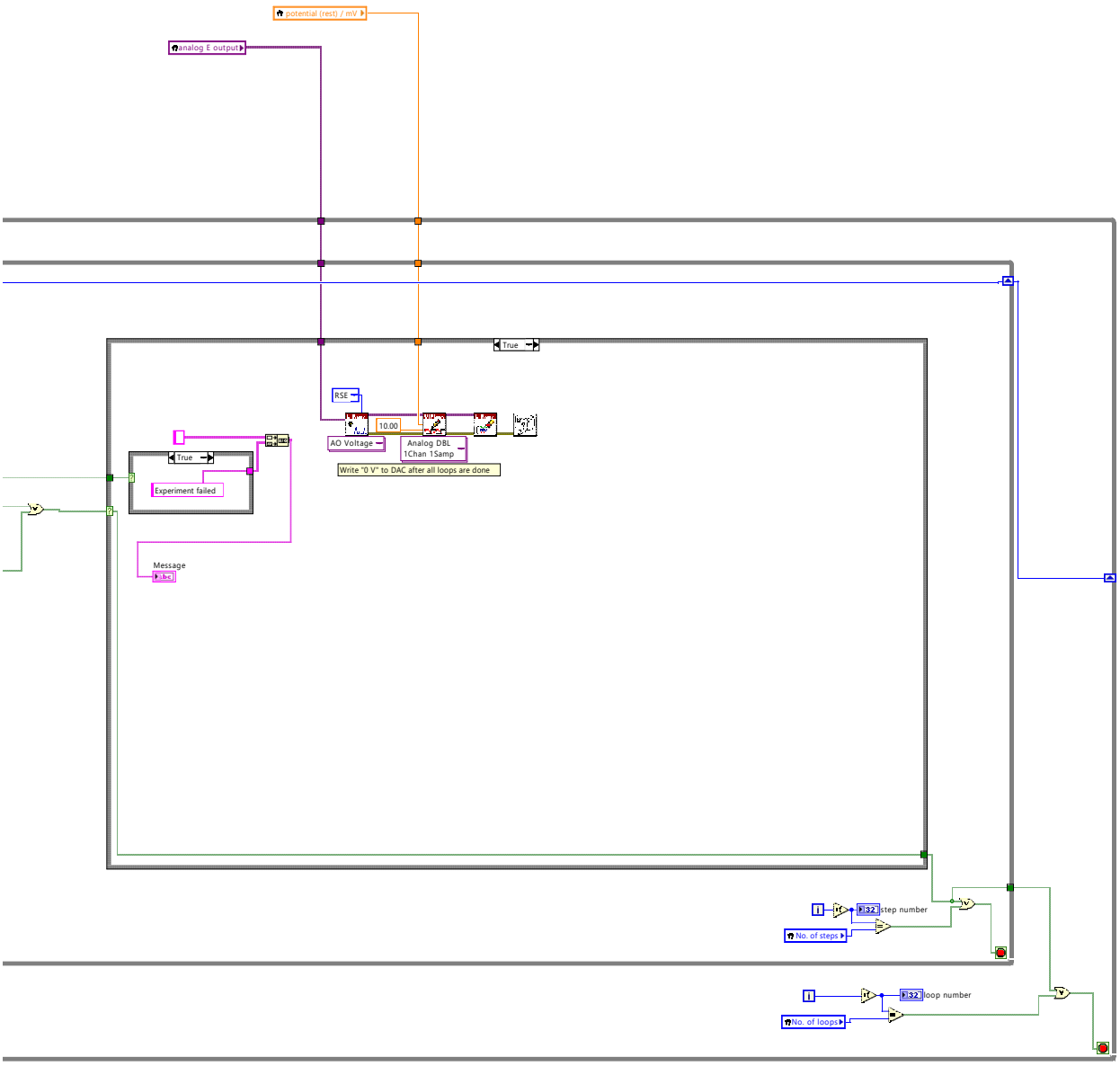

basic_set_E.vi
Z:\Public Shares\Kaiyang Shared\time resolved FTIR\rapidscan basic components\basic_set_E.vi
Last modified on 7/20/2019 at 12:23 AM
Printed on 11/18/2019 at 2:44 PM

Block Diagram

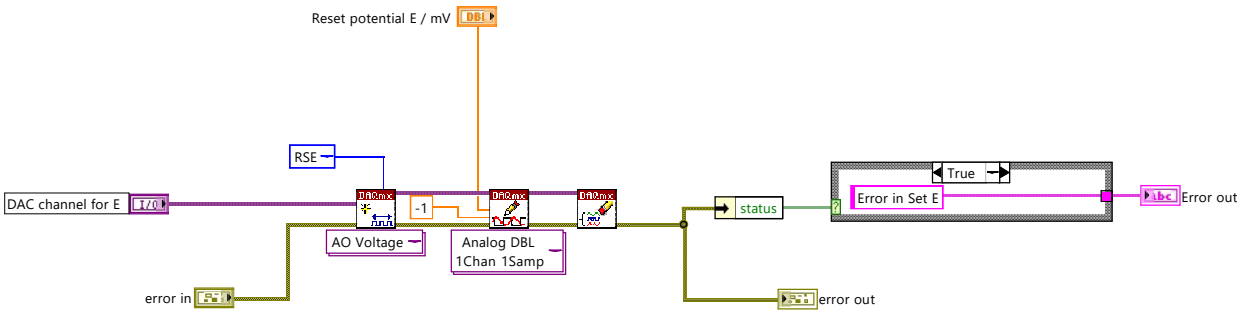

basic_trigger_rising.vi
Z:\Public Shares\Kaiyang Shared\time resolved FTIR\rapidscan basic components\basic_trigger_rising.vi
Last modified on 7/20/2019 at 12:23 AM
Printed on 11/18/2019 at 2:44 PM

Block Diagram

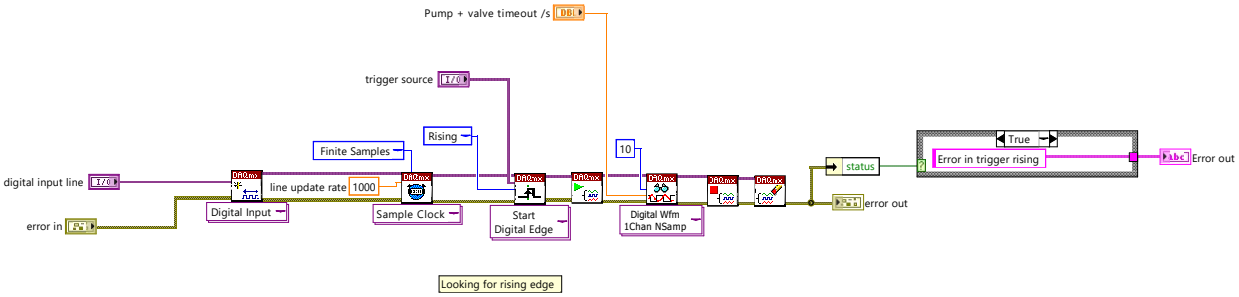

generate_signal 2.vi
Z:\Public Shares\Kaiyang Shared\time resolved FTIR\step scan test v02\
generate_signal 2.vi
Last modified on 9/16/2019 at 11:35 AM
Printed on 11/18/2019 at 2:44 PM

Block Diagram

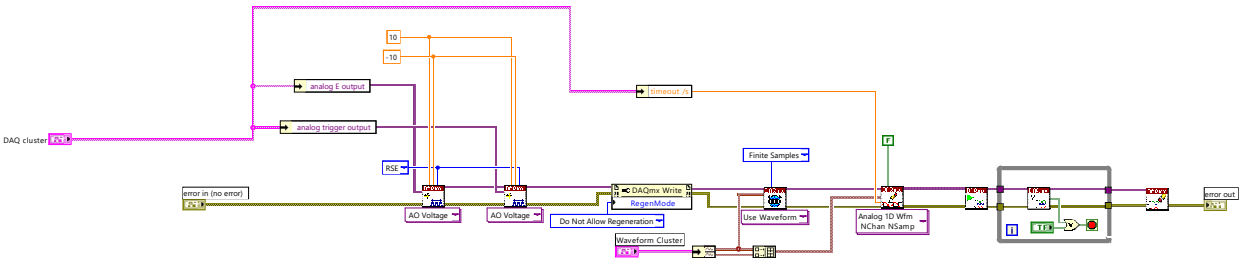

measure_signal 2.vi
Z:\Public Shares\Kaiyang Shared\time resolved FTIR\step scan test v02\
measure_signal 2.vi
Last modified on 9/16/2019 at 11:35 AM
Printed on 11/18/2019 at 2:44 PM

Block Diagram

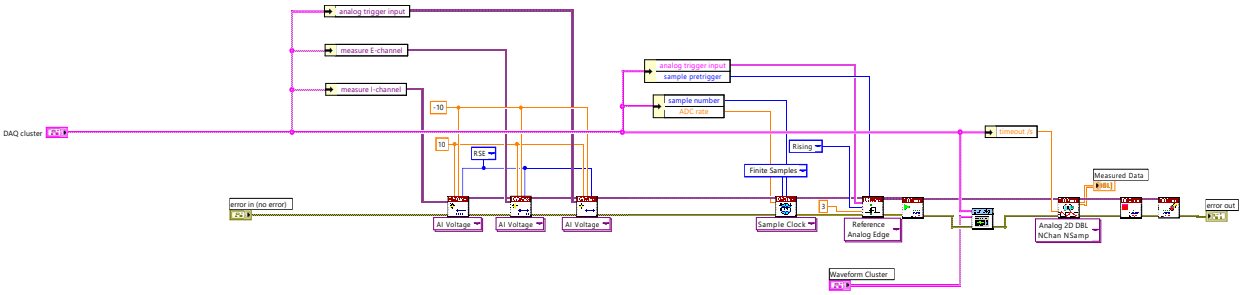

save_data 2.vi
Z:\Public Shares\Kaiyang Shared\time resolved FTIR\step scan test v02\save_data 2.vi
Last modified on 9/16/2019 at 11:35 AM
Printed on 11/18/2019 at 2:44 PM

Block Diagram

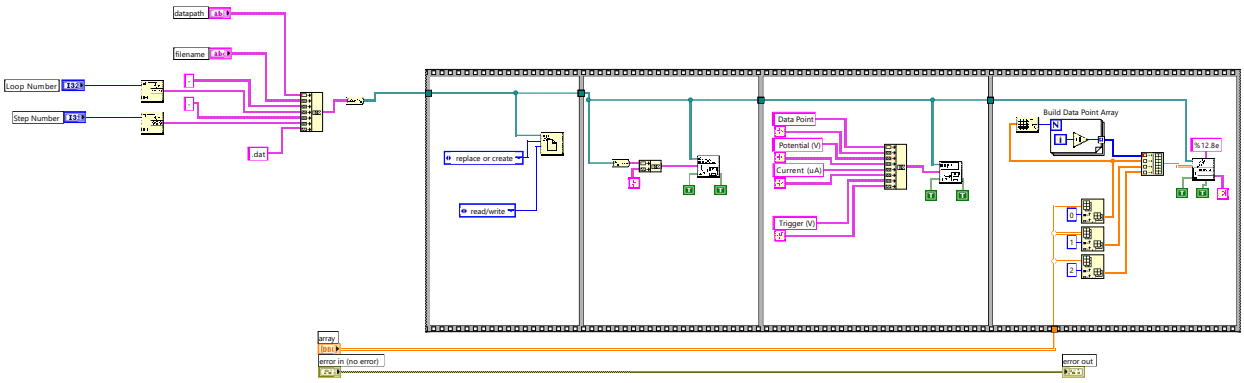

waveform_generator 2.vi
Z:\Public Shares\Kaiyang Shared\time resolved FTIR\step scan test v02\
waveform_generator 2.vi
Last modified on 9/16/2019 at 11:35 AM
Printed on 11/18/2019 at 2:44 PM

Block Diagram

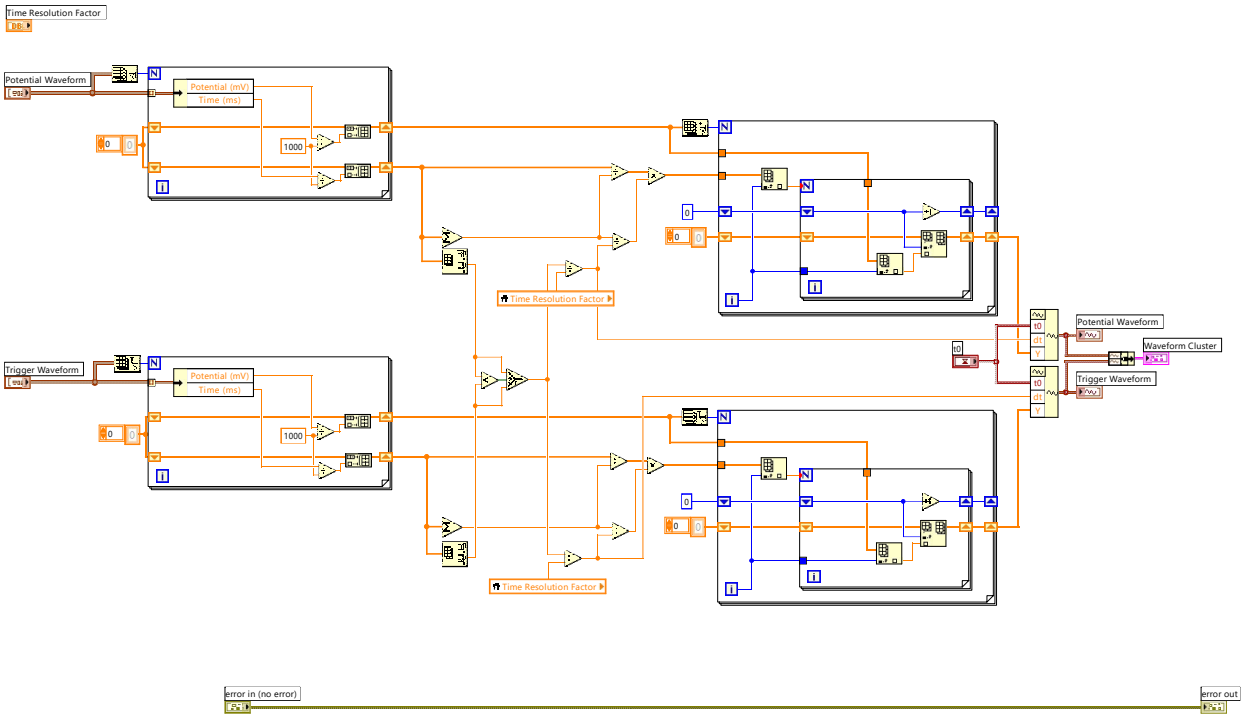

Appendix V: Matlab step scan FTIR analysis script

Matlab script to coadd the multiple step scan FTIR spectra and calculate their absorbance spectrum.

Input data
The script requires a set of OPUS step scan FTIR spectra that are saved as matlab4 files. All files should be located within a single folder and its location addressed in the "path = 'file location'; " line within the Matlab script. The script assumes, that the FTIR spectra are in following format:

wavenumber1, IR signal (reference spectra), IR signal (t_1), IR signal (t_2), ...
wavenumber2, IR signal (reference spectra), IR signal (t_1), IR signal (t_2), ...

Output data
The script creates multiple arrays with the result of the absorbance calculation:

wavenum 1D array with wavenumber values.
absorbance 2D array with calculated absorbance value in following format:

IR absorbance (wavenumber1, t_1), IR absorbance (wavenumber1, t_2), ...
IR absorbance (wavenumber2, t_1), IR absorbance (wavenumber2, t_2), ...

absorbance_collated: 2D arrays with time collated absorbance data with similar structure as the "absorbance" 2D array described above. How many time elements are collated depends on the parameter "collation = ...;" set in the beginning of the scrip. "collation" parameter must be a number that is a whole integer divisor of the (total time elements - background time elements) of the step scan data.

```
%------------------------stepscan analysis-------------------------%
clear variables
close all
clc
%------------------------------------------------------------------%
%

path = 'D:\Dropbox\work\data\20190918-CLS-stepscan\stepscan01\matlab
\';
%'filepath of folder with matlab files + \'%

search_path = sprintf('%s*.mat',path);
files = dir(search_path);
filename = sprintf('%s%s',path,files(1).name);
save = load(filename);
[p,q] = size(save.Sc);

timeelements = q-1;
datapoints = p;
number = 20;
coadd = 20;
backgroundscannumber = number;
timeelementscor = timeelements - backgroundscannumber;
collation = coadd;
collationslice = timeelementscor/collation;

%rudementary peak fitting use? Creates an linear slope between
 manually
%selected peak start and end values, followed by subtracting it from
 the
%calculated basorbance
peakfituse = 'n';
%select baseline points around peak [peak1start peak1end; peak2start
 peak2end; etc...]
peakfit = [388 398];


single_beam = zeros(datapoints,timeelementscor);
absorbance = zeros(datapoints,timeelementscor);
absorbance_collated = zeros(datapoints,collationslice);
background = zeros(datapoints,1);

file_count = 0;
for file = files'
    filename = sprintf('%s%s',path,file.name);
    temp = load(filename);
    data = temp.Sc;
    background = zeros(datapoints,1);
    for k=2:1:backgroundscannumber+1
        background = background+data(:,k);
    end;
    background = background./backgroundscannumber;
```

```
    l = 1;
    collated_counter = 0;
    for j=1:1:timeelementscor
        temp_absorbance = real(-log10(data(:,j+backgroundscannumber
+1)./background(:,1)));
        absorbance(:,j) = absorbance(:,j)+temp_absorbance;
        if collated_counter == collation
            l = l + 1;
            collated_counter = 0;
        end;
        absorbance_collated(:,l) = absorbance_collated(:,l) +
 temp_absorbance;
        collated_counter = collated_counter + 1;
        single_beam(:,j) = single_beam(:,j) + data(:,j
+backgroundscannumber+1);
    end;

    file_count = file_count+1;
end;

single_beam = single_beam./file_count;
absorbance = absorbance./file_count;
absorbance_collated = absorbance_collated./file_count./collation;
wavenum = temp.Sc(:,1);

%----------------------rudementary peak
 fitting-----------------------------
test = 0;
if peakfituse == 'y';
    [k,l] = size(peakfit);
    for j = 1:1:k
        slope = (absorbance(peakfit(j,2),:)-
absorbance(peakfit(j,1),:))/(peakfit(j,2)-peakfit(j,1));
        temp_storage = absorbance(peakfit(j,1),:);
        for i= peakfit(j,1):1:peakfit(j,2)
            absorbance(i,:) = absorbance(i,:)-temp_storage-slope*(i-
peakfit(j,1));
            test = test+1;
        end;
    end;
end;

%----------------------rudementary FT
 filter--------------------------------

use_FT_filter = 'n';
if use_FT_filter == 'y';
    for k = 1:1:datapoints
        absorbance(k,:) = bandstop(absorbance(k,:),[50 120],80000);
    end;
end
```

Published with MATLAB® R2017b

Appendix VI: Python step scan FTIR baseline fitting script

Python script to perform asymmetric least square fitting of large step scan IR data sets. The program requires input of the step scan data as following format:

wavenumber1, IR absorbance (wavenumber1, t_1), IR absorbance (wavenumber1, t_2), ...
wavenumber2, IR absorbance (wavenumber2, t_1), IR absorbance (wavenumber2, t_2), ...

Once data is imported, optimizing the baseline fit for segments of the IR data occurs over the "lam" and "p" parameter. "lam" describes the "smoothness" of the fit can be changed between 1 to 1E6 or more. "p" describes the sensitivity to negative or positive going peaks and ranges between 0 to 1 (>0.5 increasingly ignoring negative peaks and <0.5 for positive peaks).
Once a segment of the IR spectra has undergone baseline fitting it can be transferred to storage variables ("full_export_...). Once all baseline fit are completed, the data can be exported as .csv-files.

Asymmetric Least Squares Fitting-thesis

February 9, 2020

1 Asymmetric Least Squares Baseline Fitting

2017 October
Tyler Morhart
Edits: Kaiyang Tu 24.08.2018

1.1 Introduction

This notebook includes minimum working code to implement Asymmetric Least Squares Baseline Fitting (ALS). Briefly, ALS is an iterative method of finding a baseline under two constraints: smoothness and asymmetry. By varying the two parameters controlling these constraints, a nice baseline can be chosen by eye. The key is that, by choosing the asymmetry parameter carefully, you can force the ALS routine to ignore positive or negative peaks in the data.

For more information on ALS, see Eilers' 2005 paper, available at `dx.doi.org/10.1021/ac034173t`.

In [1]:
```
# ## Importing the correct libraries

# In[3]:

# The next command forces the plotting library, matplotlib, to make graphs
# in the notebook.
get_ipython().magic(u'matplotlib inline')

import numpy as np # used for arrays of data. Very useful library!
import scipy as sci # contains several useful libraries (following three
                    # lines) used in ALS
import toyplot as toyplot # interactive plots
from scipy import stats # statistics library
from scipy import optimize # optimization library for matrix math
from scipy import sparse # sparse matrix math methods
import matplotlib.pyplot as plt # import library of plotting commands
```

1.2 baseline_ALS

The following cell contains two functions. The function `baseline_als` takes the following inputs:

- `input_data` a 1xn-dimensional array of data

- `lam` short for 'lambda'. Lambda is a "smoothness" parameter, and can vary from 1 to 1E6 or more.
- `p` asymmetry parameter. `p` varies from 0 to 1; `p` = 0.5 weights upward and downward peaks easily. `p`> 0.5 will ignore downward peaks. `p` < 0.5 will ignore upward peaks.
- `niter` is the number of iterations to do. The default is 10, and is usually sufficient.

`baseline_als` returns an array of the same dimension as `input_data` which is the calculated baseline. This can then be used for e.g. baseline subtraction.

Good guesses for IR spectra are usually `lam` between 1E2 and 1E6 (try 1E2, 1E3, ... , 1E6 iteratively).

In [2]:
```
# BASELINE CORRECTION.

global exported

# takes an input spectrum (single column vector), a guess at fitting
# parameters labmda and p, and does
# 10 iterations
def baseline_als(input_data, lam, p, niter=10):
    # lam = smoothness parameter
    # p = asymmetry
  y = input_data
  L = len(y)
  D = sparse.csc_matrix(np.diff(np.eye(L), 2))
  w = np.ones(L)
  for i in range(niter):
    W = sparse.spdiags(w, 0, L, L)
    Z = W + lam * D.dot(D.transpose())
    z = sparse.linalg.spsolve(Z, w*y)
    w = p * (p > z) + (1-p) * (y < z)
  return z
```

2 A useful plotting routine

The following block has a handy segment of code. For a given array of data (`y_range`) it will calculate a baseline (`fit`), do a baseline subtraction and plot the original data, the fit, and the subtracted spectrum.

This function needs:

- `y_range` the data you want to plot.
- `x_range` the corresponding horizontal coordinates of the data (usually wavenumber)

In [3]:
```
# Load the correct data. Data should be of dimension (NUMBER OF
# WAVENUMBER POINTS, 64 x 64 spectra)
temp = np.genfromtxt(r'D:\Dropbox\work\reports\thesis\
20190628-ATR-wafer-Au-ferrocene_stepscan01_raw_data', delimiter = ',')

full_export_data = np.zeros ((len(temp),len(temp[0])))
```

```
full_export_fit = np.zeros ((len(temp),len(temp[0])))
full_export_baseline_subtracted = np.zeros ((len(temp),len(temp[0])))

full_export_data[:,0] = temp[:,0]
full_export_fit[:,0] = temp[:,0]
full_export_baseline_subtracted[:,0] = temp[:,0]
```

In [7]:
```
# Define segment to baseline fit
start = 1300
end = 1550

data = temp[start:end, :]

timestart = 0
timeend = 600

timeelements = timeend - timestart+1
export_data = np.zeros ((len(data),timeelements))
export_fit = np.zeros ((len(data),timeelements))
export_baseline_subtracted = np.zeros ((len(data),timeelements))

x_range = data[:,0]
export_data[:,0] = data[:,0]
export_fit[:,0] = data[:,0]
export_baseline_subtracted[:,0] = data[:,0]

for i in range(1, timeelements):

    y_range = data[:,i]

# Define some parameters to pass to baseline_als
    lam = 1E6
    p = 0.05

    fit = baseline_als(y_range, lam, p, niter = 10)

    baseline_subtracted = y_range - fit

    plt.figure(1)
    plt.plot(x_range, baseline_subtracted)
    plt.legend(('baselinesubstracted'))
    plt.title('Fitting')

    plt.figure(2)
    plt.plot(x_range, y_range, x_range, fit)
    plt.legend(('data', 'fit'))
    plt.title('Fitting')
```

```
    export_baseline_subtracted[:,i] = baseline_subtracted
    export_data[:,i] = y_range
    export_fit[:,i] = fit

canvas = toyplot.Canvas(width=300, height=300)
axes = canvas.cartesian()
mark = axes.plot(x_range, export_baseline_subtracted[:,1:timeend])
```

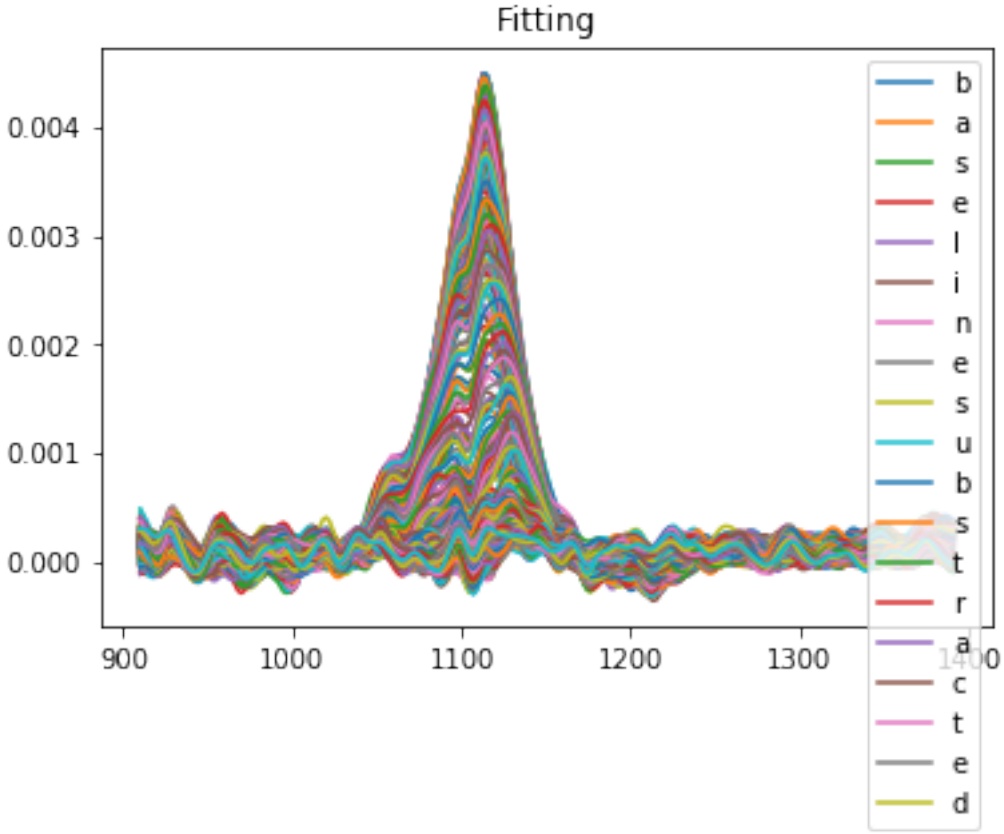

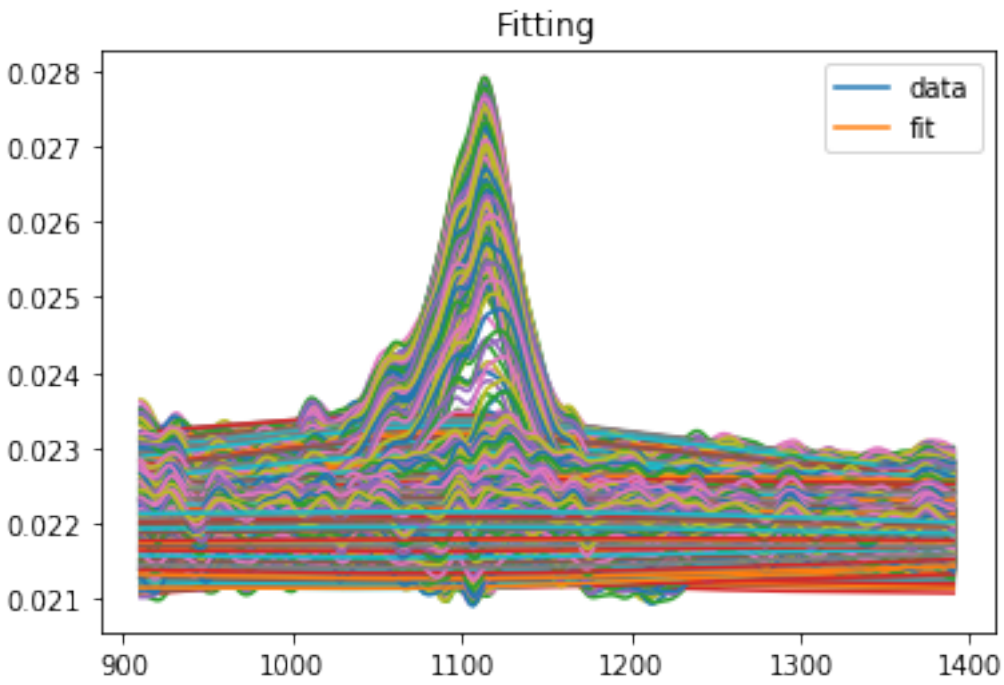

In [8]:
```
# Add segment to full data set

insertstart = 0
insertend = 250

ending = len(temp[0])

for i in range(insertstart, insertend):

    wavenum = export_data[i,0]

    for j in range (0, len(temp)):
        if wavenum == full_export_data[j,0]:
            full_export_data[j,1:ending] = export_data[i,1:ending]
            full_export_fit[j,1:ending] = export_fit[i,1:ending]
            full_export_baseline_subtracted[j,1:ending] = export_
            baseline_subtracted[i,1:ending]
```

In [9]:
```
# Write the data into a file

np.savetxt('20background_filter_data_n-4_cathodic.txt', full_export
           _data, delimiter = ',')
np.savetxt('20background_filter_fit_n-4_cathodic.txt', full_export
           _fit, delimiter = ',')
```

Appendix VII: Matlab 2D-COS analysis script

Matlab scripts to generate 2D-COS maps from step scan IR data. The main script (next two pages) relies on several Matlab functions:

fft2dcor(inputdata) Calculates the synchronous and asynchronous 2D-COS map, based on "inputdata" and outputs these as two 2D arrays [sym, asym]. "inputdata" must be of following format:

IR absorbance (wavenumber1, t_1), IR absorbance (wavenumber1, t_2), ...
IR absorbance (wavenumber2, t_1), IR absorbance (wavenumber2, t_2), ...

delete_section(data_syn, data_asyn, section_info) Deletes sections of the synchronous and asynchronous 2D-cos map that are determined outside of this function to be void of analytical IR signal. Requires the input of the synchronous and asynchronous 2D-COS map as "data_syn" and "data_asyn". The function outputs the 2D-COS maps back in the same format it received. To define the section that need to be deleted, "section_info" needs to be provide in form of a 2D array containing the individual section of interest.

[position of the lowest data point within to-be-deleted section1
position of the highest data point within to-be-deleted section1 ;
start of section2
end of section2 ;
...]

plot2d(syn, asyn, x-axis, syn_n, asyn_n) Matlab function to plot the calculated synchronous and asynchronous 2D-COS maps (input data as "syn" and "asyn") into 2D contour plots. "x-axis" requires a 1D array with wavenumber information to define the axis within plotted maps. y-axis titles are assumed to be identical to x-axis. "syn_n" and "asyn_n" define how many levels the contour map should contain.

```
clear;

temp = csvread('D:\Dropbox\work\reports\thesis\chapter
 5 ferrocene\figure\step scan IR\step scan data
\20background_filter_baseline_subtracted_n-4_cathodic.txt');
temp2 = temp;

timesliceA = 1;
timesliceB = 300;

%should program scale?
autoscaling = 1;
thresshold_value = 0.25;

%plot all data or just section?
data_limitA = 380;
data_limitB = 1500;
%data_limitB = 1310;

%disregard sections of the spectra
%section_info = [44 59;986 1028]; %for filtered full spectra
%section_info = [44 59]; %for filtered without ClO4 peak
section_info = [1 17;42 117;140 761;921 1038;1109 1121]; %for
 unfiltered full spectra
%section_info = [42 117;140 761]; %for filtered without ClO4 peak
[m,n] = size(temp);
data = zeros(m,timesliceB-timesliceA+1);

%better values
data = temp(:,timesliceA+1:timesliceB+1)*1000;
dataT = temp(:,timesliceA+1:timesliceB+1)'*1000;

[m,n] = size(data);

dataE = data;
dataF = dataE;

if autoscaling == 1
    for i = 1:1:m
        m = max(abs(dataE(i,:)));
        if m < thresshold_value;
            dataF(i,:) = dataE(i,:)*0.01;
        else
            dataF(i,:) = dataE(i,:);
        end
    end
end

%2D correlation calc
datacorr = dataF(data_limitA:data_limitB,:);
axis = temp(data_limitA:data_limitB,1);
[syn,asyn] = fft2dcor(datacorr');
```

```
%delete section
[syn,asyn] = delete_section(syn,asyn,section_info);

%plot 2D maps
plot2d(syn,asyn,axis,20,20);
```

```
Error using csvread (line 35)
File not found.

Error in sandbox (line 3)
temp = csvread('D:\Dropbox\work\reports\thesis\chapter
 5 ferrocene\figure\step scan IR\step scan data
\20background_filter_baseline_subtracted_n-4_cathodic.txt');
```

Published with MATLAB® R2017b

```
temp = csvread('D:\Dropbox\work\programs\python\baseline correction
\20background_filter-n-6_baseline_subtracted.txt');
[m,n] = size(temp);
data = zeros(m,n-1);
for i= 1:1:n
    data(:,i) = temp(:,i);
end;
```

```
Error using csvread (line 35)
File not found.

Error in loaddata (line 1)
temp = csvread('D:\Dropbox\work\programs\python\baseline correction
\20background_filter-n-6_baseline_subtracted.txt');
```

Published with MATLAB® R2017b

```
function [syn,asyn] = fft2dcor(inputdata)

[m,n] = size(inputdata);
m2 = floor(m/2)+1;

ibeg = m2;
ifin = m;

corr(1:n,1:n) = zeros(n,n);

Y = fft(inputdata)/sqrt(m);  % Fourier Transform the data along the
 dynamic variable %
for i = 1:n
    for j = 1:n
        corr(i,j) = sum(Y(ibeg:ifin,i).*conj(Y(ibeg:ifin,j))); %
 Univariate Correlation %
    end
end

corr = 2*corr; % correct the correlation to the correct number of
 degress of freedom %
syn = real(corr);
asyn = imag(corr);
end
```

```
Not enough input arguments.

Error in fft2dcor (line 3)
[m,n] = size(inputdata);
```

Published with MATLAB® R2017b

```
function [syn,asyn] = delete_section(data_syn,data_asyn,section_info)

[n,m] = size(section_info);

%delete section
for i = 1:1:n
    data_syn(section_info(i,1):section_info(i,2),:) = NaN;
    data_syn(:,section_info(i,1):section_info(i,2)) = NaN;
    data_asyn(section_info(i,1):section_info(i,2),:) = NaN;
    data_asyn(:,section_info(i,1):section_info(i,2)) = NaN;
end;

syn = data_syn;
asyn = data_asyn;
```

```
Not enough input arguments.

Error in delete_section (line 3)
[n,m] = size(section_info);
```

Published with MATLAB® R2017b

```
function plot2d(syn,asyn,axis,syn_n,asyn_n)
%create axis labels
x_axislabel = axis(:,1);

figure;
[M,c]=contour(x_axislabel,x_axislabel,syn,syn_n);
title('Synchronous');
c.LineWidth = 1;
set(gcf,'Position',[10 10 850 750]);
colorbar;
colormap jet;
% subplot(2,2,2);
%     mesh(syn);
%     title('Synchronous');

figure;
[M,c]=contour(x_axislabel,x_axislabel,asyn,asyn_n,'fill','on');
title('Asynchronous');
c.LineWidth = 1;
set(gcf,'Position',[10 10 850 750]);
colorbar;
colormap jet;
% subplot(2,2,4);
%     mesh(asyn);
%     title('Asynchronous')
```

```
Not enough input arguments.

Error in plot2d (line 3)
x_axislabel = axis(:,1);
```

Published with MATLAB® R2017b